Approved : _____

Timothy A. Shedd, Assistant Professor

Date : _____

© Copyright by Ryan K. Jester, 2007
All Rights Reserved

Aggresive Energy Recovery from the Waste Heat of a Hybrid Automotive Powerplant

by

Ryan K. Jester

A thesis submitted in partial fulfillment of
the requirements for the degree of

Master of Science
(Mechanical Engineering)

at the

UNIVERSITY OF WISCONSIN-MADISON
2007

Aggresive Energy Recovery from the Waste Heat of a Hybrid Automotive Powerplant

Ryan K. Jester, M.S.
Department of Mechanical Engineering
University of Wisconsin-Madison, 2007
Professor Timothy A. Shedd, Advisor

Energy consumption is garnering increased attention in our society as energy costs continue to rise and the environmental impact of emissions from energy production become increasing visible. The transportation industry is under increased scrutiny as it makes up a significant portion of the energy consumption in the Unites States. This has led to the mass development of new designs that stress energy efficiency, such as the gasoline/electric hybrid vehicle. Although these hybrid vehicles offer higher efficiencies, there is still a substantial percentage of energy that is dissipated to the environment through the waste heat. The storage battery in gasoline/electric vehicles allows a location for recovered energy to be stored and utilized for drive power as the system requires. The purpose of this study is to explore the viability of the implementation of various heat recovery systems to a gasoline/electric hybrid vehicle. An analysis of the energy balance of a 2004 Toyota Prius was performed to evaluate the system operation. This analysis was extended to include the theoretical and finite time availability of possible recoverable effluents. The analysis of the Prius data directed heat recovery efforts to the exhaust system and the coolant system. The feasibility of heat recovery from exhaust system was studied through modeling the implementation of a turbine and, separately, a compact heat exchanger in the exhaust stream. The primary focus of the exhaust stream analysis was the development of a correlation between the backpressure effects on engine performance and energy recovered through the heat recovery system. The analysis of waste heat recovery from the coolant system involves an innovative approach using spray cooling for thermal management of the engine. Experiments were conducted to demonstrate the high heat transfer coefficients that can be attained with the spray cooling system. Higher heat transfer coefficients provide the opportunity to run the coolant at a higher temperature, allowing the possibility for higher recovery rates of energy. The spray cooling system offers potential for both energy recovery systems and utilization in typical vehicles for improved engine thermal management.

Acknowledgments

I would first like to thank my advisors, Professors Tim Shedd and Sandy Klein, for their constant support throughout my work at the Solar Energy Laboratory. I have learned more than I ever thought possible during my graduate education at the University of Wisconsin-Madison and would like to thank my advisors for providing me with this opportunity and assisting me along the way. I would also like to thank Professor David Foster for being on my defense committee. I appreciated additional feedback that I received from the other professors in the Solar Energy Laboratory during seminars and summer meetings. I would also like to thank Argonne National Laboratory for assisting with this project.

I would never have made it this far without the loving support of my family. My wife, Laura, has provided me with motivation and loving support throughout my collegiate education, even during times that are tough. My parents, Ron and Bev, have been ideal role models for me to be the best that I can along with providing loving and financial support. My brothers, Cam and Nick, have offered me the camaraderie and support that siblings should have for one another. I would like to thank my grandparents, Axel and Betty Boilesen and Royal and Betty Jester, for their continued loving support of everything I have done from childhood to now. I greatly appreciate my grandfather, Axel, for being the role model of an engineer in the family and to Royal and Betty for their financial support of my education.

I would also like to thank my friends and the rest of my family back in Nebraska. We have been many good times that assisted me in relieving the stresses associated with attaining an engineering education. Also, thanks to all of the new friends that I have made here in Madison; you all have made the moving transition fun and exciting for me. I greatly appreciate all of the Solar Lab Crew, especially Adam, Ben, Brady, Curtis, Diego, Drea, Kate, Paul, Rodrigo, Scott, Steve, Terry, Tyler and Yiaxa. Also a thank you to Nicole, who assisted in the last minute data collection.

Table of Contents

Abstract **i**

Acknowledgments **iii**

Table of Contents **v**

List of Tables **ix**

List of Figures **xi**

Nomenclature **xvii**

1 Introduction **1**

2 Literature Review **5**
2.1 Hybrid Vehicles 5
2.1.1 Introduction 5
2.1.2 Hybrid Vehicle Technology 6
2.1.3 Toyota Hybrid System (THS II) 9
2.1.4 Atkinson Cycle 14
2.2 Waste Heat Recovery 15
2.2.1 Introduction 15
2.2.2 Waste Heat Recovery Cycles 16
2.2.3 Energy Recovery 19
Vehicle Heating 20
Heat Storage 20
Thermoelectrics 21
Vehicle Cooling and Engine Air Pre-Cooling 22
Exhaust Gas Heat Recovery 24
Rankine Cycles for Energy Recovery 25

3 Availability Analysis **29**
3.1 Introduction 29
3.2 Energy Balance 30
3.3 Availability Analysis 35
3.3.1 Availability of Fuel 37
3.3.2 Availability of Exhaust 40
3.3.3 Availability in the Engine Coolant 42
3.3.4 Availability Comparison 44

3.4 Finite Time Analysis . . . 45
3.5 Discussion of Results . . . 60
3.6 Conclusions . . . 61

4 Recovering Waste Energy with a Turbine in the Engine Exhaust 63
4.1 Introduction . . . 63
4.2 GT-Power . . . 64
4.2.1 Background . . . 64
4.2.2 GT-Power Backpressure Model . . . 67
4.2.3 Comparison to Literature . . . 69
4.2.4 Air Standard Otto Cycle Model . . . 71
4.3 Preliminary GT-Power Model . . . 74
4.4 Detailed Prius GT-Power Model . . . 76
4.5 Engine Speed Variation . . . 80
4.6 Parametric Analysis of Engine Parameters . . . 84
4.6.1 Vehicle Survey . . . 85
4.6.2 Compression Ratio . . . 88
4.6.3 Bore . . . 91
4.6.4 Stroke . . . 92
4.6.5 Comparison . . . 94
4.6.6 Atkinson Cycle Considerations . . . 95
4.7 Conclusions . . . 96

5 Analysis of a Compact Heat Exchanger in the Exhaust System 97
5.1 Introduction . . . 97
5.2 Compact Heat Exchanger Model . . . 97
5.3 Conclusions . . . 111

6 Experimental Investigation of Higher Engine Coolant Temperatures 115
6.1 Experimental Exploration of the Redesign of the Engine Coolant System to Optimize Energy Recovery . . . 115
6.1.1 Introduction . . . 115
6.1.2 Spray Cooling . . . 116
6.1.3 Experimental Setup . . . 117
Uncertainty in Measurements . . . 128
6.1.4 Experimental Results . . . 130

7 Conclusions and Recommendations 151

Bibliography 155

Appendix 161

A Compact Heat Exchanger Analysis Results **161**
A.1 Finned-tube surface, Circular Tubes, Circular Fins - 'CF 8.72' 167
A.2 Finned-tube surface, Circular Tubes, Circular Fins - 'CF-7.34' 174
A.3 Finned-tube surface, Circular Tubes, Continuous Fins - '7.75 - 5/8 T' 181
A.4 Finned-tube surface, Flat Tubes, Continuous Fins - '9.29-0.737-SR' 187

List of Tables

3.1 Comparison of Energy Split in the Prius to Typical Values 34
3.2 Integral of Availability of the Exhaust with respect to time 41
3.3 Comparison of the Availability in the Coolant and Exhaust 44
3.4 Finite Time Thermodynamic Analysis 51

4.1 Comparison of Results from Prius Model at 3600 RPM 79
4.2 Comparison of Total Power for Various Engine Speeds 84

List of Figures

2.1 Series Hybrid System Configuration 7
2.2 Parallel Hybrid System Configuration 8
2.3 Series/Parallel Hybrid System Configuration 9
2.4 Schematic of the Toyota Hybrid System II (THS II) [1] 10
2.5 Schematic of the Power Split Device in the THS II [1] 11
2.6 Diagrams of the operation of the Toyota Hybrid System II (THS II) [1] . . . 13
2.7 Rankine Cycle Schematic 17
2.8 Brayton Cycle Schematic 18
2.9 Absorbtion Refrigeration Cycle Schematic 19

3.1 Defined System for the Energy Balance 30
3.2 Histogram of Air/Fuel Ratio over the Drive-Test Data 32
3.3 Variation of the Energy Split as a Function of the Miscellaneous Heat Losses 35
3.4 Mass Flow Rate of Fuel from the Prius data 39
3.5 Exhaust Gas Temperatures prior to the catalytic converter (Precat) and after the catalytic converter (Postcat) 40
3.6 Sensitivity of the Pressure in the Exhaust on the Availability in the Exhaust 42
3.7 Temperature of the Engine Coolant from the Prius Data 43
3.8 Correlation of Coolant Mass Flow Rate and Engine Speed 44
3.9 Carnot Cycle Operating between a Heat Source and Heat Sink [2] 46
3.10 Power Output versus Efficiency [2]] 48
3.11 Sensitivity Analysis on the Cold Side Heat Exchanger Effectiveness 52
3.12 Sensitivity Analysis on the Hot Side Heat Exchanger Effectiveness 54
3.13 Sensitivity Analysis on the Cross Sectional Area of the Radiator 55
3.14 Sensitivity Analysis on the Ambient Temperature 56
3.15 Sensitivity Analysis on the Coolant Temperature 58
3.16 Sensitivity Analysis on the Coolant Mass Flow Rate 59

4.1 Engine Power vs. Backpressure for the Preliminary GT-Power Model at 3600 rpm (Default Engine Parameters and No Catalytic Converter or Muffler . . . 68
4.2 Comparison of Nondimensional Brake Horsepower Parameter and Engine Backpressure at an Engine Speed of 2000 RPM 70
4.3 Comparison of Nondimensional Brake Horsepower Parameter and Engine Backpressure at an Engine Speed of 3000 RPM 70
4.4 Comparison of Nondimensional Brake Horsepower Parameter and Engine Backpressure at an Engine Speed of 4000 RPM 71
4.5 P-v and T-s diagrams of the air-standard Otto cycle 72
4.6 Comparison of GT-Power Model to Air Standard Analysis 74

4.7 Power vs. Backpressure for the Preliminary Model at 3600 rpm in GT-Power (Default Engine Parameters and No Catalytic Converter or Muffler) 75
4.8 Block Diagrams Representing the Three GT-Power Models 77
4.9 Power vs. Backpressure for the Prius model with a Turbine in the PreCat Location at 3600 RPM 78
4.10 Power vs. Backpressure for the Prius model with a Turbine in the PostCat Location at 3600 RPM 78
4.11 Power vs. Backpressure for the Prius Model with a Turbine at an Engine Speed of 1000 RPM 81
4.12 Power vs. Backpressure for the Prius Model with a Turbine at an Engine Speed of 2000 RPM 81
4.13 Power vs. Backpressure for the Prius Model with a Turbine at an Engine Speed of 3000 RPM 82
4.14 Power vs. Backpressure for the Prius Model with a Turbine at an Engine Speed of 4000 RPM 82
4.15 Power vs. Backpressure for the Prius Model with a Turbine at an Engine Speed of 5000 RPM 83
4.16 Engine Speed for a Typical Driving Cycle of the Toyota Prius 85
4.17 Compression Ratio for Various Vehicles 86
4.18 Bore for Various Vehicles 87
4.19 Stroke for Various Vehicles 87
4.20 Power versus Compression Ratio 89
4.21 Percentage in Total Power Change with Compression Ratio 90
4.22 Engine Power versus Bore 91
4.23 Percentage Change in Total Power with Bore 92
4.24 Engine Power versus Stroke 93
4.25 Percentage Change in Total Power with Stroke 93
4.26 Percent Change in Total Power for Percent Change in the Variable 94

5.1 Schematic of the 7.75-5/8T Compact Heat Exchanger Geometry Studied . . 99
5.2 Average Percent Gain in Energy as a Function of the Heat Exchanger Length and Frontal Area 99
5.3 Optimum Heat Exchanger Length as a Function of the Frontal Area 100
5.4 Exhaust Mass Flow Rate as a Function of the Engine Speed for the Prius Data 102
5.5 Reynolds number for the Exhaust Gas as a Function of the Engine Speed for the '7.75-5/8T' Compact Heat Exchanger 102
5.6 Friction factor for the Exhaust Gas as a Function of the Engine Speed for the '7.75-5/8T' Compact Heat Exchanger 103
5.7 Overall Heat Transfer Coefficient-Area Product for the Exhaust Gas as a Function of the Engine Speed for the '7.75-5/8T' Compact Heat Exchanger . 105
5.8 Effectiveness for the Exhaust Gas Side as a Function of the Engine Speed for the '7.75-5/8T' Compact Heat Exchanger 106

5.9 Heat Transfer Rate as a Function of the Engine Speed for the '7.75-5/8T' Compact Heat Exchanger . . . 107
5.10 Pressure Drop as a Function of the Engine Speed for the '7.75-5/8T' Compact Heat Exchanger . . . 108
5.11 Engine Power as a Function of the Backpressure at an Engine Speed of 2000 RPM . . . 109
5.12 Average Percent Power Difference as a Function of the Heat Exchanger Length for the '7.75-5/8T' Compact Heat Exchanger . . . 109
5.13 Power vs. Rankine Cycle Efficiency for a Compact Heat Exchanger with Continuous Fins ('7.75-5/8T') in the Exhaust System with an Engine Speed of 2500 RPM Using Toluene as a Working Fluid . . . 111
5.14 Power vs. Rankine Cycle Efficiency for a Compact Heat Exchanger with Continuous Fins ('7.75-5/8T') in the Exhaust System with an Engine Speed of 3000 RPM Using Toluene as a Working Fluid . . . 112
5.15 Percent Change in Power vs. Rankine Cycle Efficiency for a Compact Heat Exchanger with Continuous Fins ('7.75-5/8T') in the Exhaust System at the Precat location Using Toluene as a Working Fluid . . . 113

6.1 Aluminum Cylinder with Holes Drilled for Theromocouples . . . 119
6.2 Aluminum Nozzle Tube that was Machined for use in the Spray Device . . . 120
6.3 CAD Drawing of the Spray Device Made for the Experimental Work . . . 120
6.4 Top View of the Spray Array Without the Aluminum Cylinder in Place . . . 121
6.5 CAD Drawing of the Teflon piece (Top Cap) . . . 122
6.6 CAD Drawing of the Polyetherimide piece (Bottom Cap) . . . 123
6.7 CAD Drawing of the Entire Spray Device) . . . 124
6.8 Picture of the Assembled Spray Device) . . . 125
6.9 Schematic of the Experimental Setup . . . 126
6.10 Experimental Components (Clockwise Starting from the Upper Left)1)Tank(Reservoir)2)Pump 3)Filter 4)Heat Exchanger 5)Outlet and Inlet Manifolds . . . 127
6.11 Propane Torch Mounted at the Base of the Spray Device . . . 128
6.12 Comparison of the Temperatures Measured from the Thermocouple and the Temperature Bath for the Fluid Outlet Thermocouple . . . 129
6.13 Fluid Temperatures at the Inlet and Outlet of the Spray Device for a Flowrate of 8.5 lpm . . . 132
6.14 Outer Cylinder Surface Temperatures for a Flowrate of 8.5 lpm . . . 132
6.15 Outer Cylinder Surface Temperature Map for a Flowrate of 8.5 lpm . . . 133
6.16 Heat Transfer Rate for the Dataset with a Flowrate of 8.5 lpm . . . 134
6.17 Heat Transfer Coefficient for the Dataset with a Flowrate of 8.5 lpm . . . 135
6.18 Outer Cylinder Surface Temperature Map for a Flowrate of 6.8 lpm . . . 136
6.19 Outer Cylinder Surface Temperature Map for a Flowrate of 10.3 lpm . . . 137
6.20 Outer Cylinder Surface Temperature Map for a Flowrate of 11.5 lpm . . . 137
6.21 Averages Outer Cylinder Surface Temperature Map for as a function of Flowrate 138

6.22 Outer Cylinder Heat Transfer Coefficient as a Function of Flowrate 139
6.23 Outer Cylinder Surface Temperature Map for a Flowrate of 8.5 lpm and a Fluid Inlet Temperature of 40 Degrees Celsius 140
6.24 Outer Cylinder Heat Transfer Coefficient as a Function of Flowrate for a Fluid Inlet Temperature of 40 Degrees Celsius 141
6.25 Outer Cylinder Heat Transfer Coefficient as a Function of Flowrate for a Fluid Inlet Temperature of 50 Degrees Celsius 141
6.26 Relationship Between the Outer Cylinder Heat Transfer Coefficient and the Flowrate at 12 Degrees Celsius 142
6.27 Relationship Between the Outer Cylinder Heat Transfer Coefficient and the Flowrate at 40 Degrees Celsius 143
6.28 Relationship Between the Outer Cylinder Heat Transfer Coefficient and the Flowrate at 50 Degrees Celsius 143
6.29 Relationship Between the Outer Cylinder Heat Transfer Coefficient and the Fluid Thermal Properties at 6.8 lpm 144
6.30 Relationship Between the Outer Cylinder Heat Transfer Coefficient and the Fluid Thermal Properties at 8.5 lpm 145
6.31 Relationship Between the Outer Cylinder Heat Transfer Coefficient and the Fluid Thermal Properties at 10.3 lpm 145
6.32 Calculation of the Coefficient for the New Correlation 146
6.33 Comparison of the Correlation to All of the Experimental Data 147
6.34 Comparison of the Experimental Heat Transfer Coefficient for a 20-80 Mixture of Ethylene Glycol-Water to the Correlation Prediction 148

A.1 Exhaust Mass Flow Rate as a Function of the Engine Speed for the Prius Data 163
A.2 Engine Power as a Function of the Backpressure at an Engine Speed of 2000 RPM 166
A.3 Schematic of the ‘CF-8.72’ Compact Heat Exchanger Studied 168
A.4 Reynolds number as a Function of the Engine Speed for the ‘CF-8.72’ Compact Heat Exchanger 168
A.5 Friction Factor as a Function of the Engine Speed for the ‘CF-8.72’ Compact Heat Exchanger 169
A.6 Effectiveness as a Function of the Engine Speed for the ‘CF-8.72’ Compact Heat Exchanger 169
A.7 Heat Transfer Rate as a Function of the Engine Speed for the ‘CF-8.72’ Compact Heat Exchanger 170
A.8 Pressure Drop as a Function of the Engine Speed for the ‘CF-8.72’ Compact Heat Exchanger 170
A.9 Average Percent of Power Change as a Function of the Heat Exchanger Length for the ‘CF-8.72’ Compact Heat Exchanger 171
A.10 Power as a Function of the Rankine Cycle Efficiency for the ‘CF-8.72’ Compact Heat Exchanger at an Engine Speed of 2000 RPM 171

A.11 Power as a Function of the Rankine Cycle Efficiency for the 'CF-8.72' Compact Heat Exchanger at an Engine Speed of 2500 RPM 172
A.12 Power as a Function of the Rankine Cycle Efficiency for the 'CF-8.72' Compact Heat Exchanger at an Engine Speed of 3000 RPM 172
A.13 Percent Power Change as a Function of the Rankine Cycle Efficiency for the 'CF-8.72' Compact Heat Exchanger 173
A.14 Flow Configuration of Compact Heat Exchanger Studied 174
A.15 Geometry of the Tubes in the Compact Heat Exchanger 175
A.16 Reynolds number for the Exhaust Gas as a Function of the Engine Speed for the 'CF-7.34' Compact Heat Exchanger 175
A.17 Friction factor for the Exhaust Gas as a Function of the Engine Speed for the 'CF-7.34' Compact Heat Exchanger 176
A.18 Pressure Drop as a Function of the Engine Speed for the 'CF-7.34' Compact Heat Exchanger 176
A.19 Effectiveness for the Exhaust Gas Side as a Function of the Engine Speed for the 'CF-7.34' Compact Heat Exchanger 177
A.20 Heat Transfer Rate as a Function of the Engine Speed for the 'CF-7.34' Compact Heat Exchanger 177
A.21 Average Percent Power Difference as a Function of the Heat Exchanger Length for the 'CF-7.34' Compact Heat Exchanger 178
A.22 Power vs. Rankine Cycle Efficiency for a Compact Heat Exchanger with Circular Fins ('CF-7.34') in the Exhaust System with an Engine Speed of 2000 RPM 178
A.23 Power vs. Rankine Cycle Efficiency for a Compact Heat Exchanger with Circular Fins ('CF-7.34') in the Exhaust System with an Engine Speed of 2500 RPM 179
A.24 Power vs. Rankine Cycle Efficiency for a Compact Heat Exchanger with Circular Fins ('CF-7.34') in the Exhaust System with an Engine Speed of 3000 RPM 179
A.25 Percent Change in Power vs. Rankine Cycle Efficiency for a Compact Heat Exchanger with Circular Fins ('CF-7.34') in the Exhaust System at the Precat location 180
A.26 Schematic of the '7.75-5/8T' Compact Heat Exchanger Studied 181
A.27 Reynolds number as a Function of the Engine Speed for the '7.75-5/8T' Compact Heat Exchanger 182
A.28 Friction Factor as a Function of the Engine Speed for the '7.75-5/8T' Compact Heat Exchanger 182
A.29 Effectiveness as a Function of the Engine Speed for the '7.75-5/8T' Compact Heat Exchanger 183
A.30 Heat Transfer Rate as a Function of the Engine Speed for the '7.75-5/8T' Compact Heat Exchanger 183

A.31 Pressure Drop as a Function of the Engine Speed for the '7.75-5/8T' Compact Heat Exchanger . . . 184
A.32 Average Percent of Power Change as a Function of the Heat Exchanger Length for the '7.75-5/8T' Compact Heat Exchanger . . . 184
A.33 Power as a Function of the Rankine Cycle Efficiency for the '7.75-5/8T' Compact Heat Exchanger at an Engine Speed of 2500 RPM . . . 185
A.34 Power as a Function of the Rankine Cycle Efficiency for the '7.75-5/8T' Compact Heat Exchanger at an Engine Speed of 3000 RPM . . . 185
A.35 Percent Power Change as a Function of the Rankine Cycle Efficiency for the '7.75-5/8T' Compact Heat Exchanger . . . 186
A.36 Schematic of the '9.29-0.737-SR' Compact Heat Exchanger Studied . . . 187
A.37 Reynolds number as a Function of the Engine Speed for the '9.29-0.737-SR' Compact Heat Exchanger . . . 188
A.38 Friction Factor as a Function of the Engine Speed for the '9.29-0.737-SR' Compact Heat Exchanger . . . 188
A.39 Effectiveness as a Function of the Engine Speed for the '9.29-0.737-SR' Compact Heat Exchanger . . . 189
A.40 Heat Transfer Rate as a Function of the Engine Speed for the '9.29-0.737-SR' Compact Heat Exchanger . . . 189
A.41 Pressure Drop as a Function of the Engine Speed for the '9.29-0.737-SR' Compact Heat Exchanger . . . 190
A.42 Average Percent of Power Change as a Function of the Heat Exchanger Length for the '9.29-0.737-SR' Compact Heat Exchanger . . . 190
A.43 Power as a Function of the Rankine Cycle Efficiency for the '9.29-0.737-SR' Compact Heat Exchanger at an Engine Speed of 2000 RPM . . . 191
A.44 Power as a Function of the Rankine Cycle Efficiency for the '9.29-0.737-SR' Compact Heat Exchanger at an Engine Speed of 2500 RPM . . . 191
A.45 Power as a Function of the Rankine Cycle Efficiency for the '9.29-0.737-SR' Compact Heat Exchanger at an Engine Speed of 3000 RPM . . . 192
A.46 Percent Power Change as a Function of the Rankine Cycle Efficiency for the '9.29-0.737-SR' Compact Heat Exchanger . . . 192

Nomenclature

Symbol		Description	Units
Symbols			
A	=	cross sectional area	[m^2]
A_c	=	minimum free-flow area	[m^2]
$A_h t$	=	heat transfer area	[m^2]
$A_x s, min$	=	minimum cross sectional area	[m^2]
BTQ	=	brake torque	[kJ]
$\dot{C}$	=	heat capacity rate	[kW K^{-1}]
C_p	=	specific heat	[kJ kg^{-1} K^{-1}]
CR	=	heat capacity ratio	[-]
D_h	=	hydraulic diameter	[m]
f	=	friction factor	[-]
G	=	mass flux	[kg m^{-2} s^{-1}]
g	=	gravitational constant	[m s^{-2}]
h	=	specific enthalpy	[kJ kg^{-1}]
H	=	enthalpy	[kJ]
htc	=	heat transfer coefficient	[W m^{-2} K^{-1}]
I	=	inertia	[kg m^2]
k	=	thermal conductivity	[W m^{-1} K^{-1}]
L	=	length	[m]
m	=	mass	[kg]
$\dot{m}$	=	mass flow rate	[kg s^{-1}]
NTU	=	number of transfer units	[-]
Nu	=	Nusselt number	[-]
P	=	pressure	[kPa]
PR	=	pressure ratio	[-]
Pr	=	Prandtl number	[-]
P_w	=	wetted perimeter	[m]
$\dot{Q}$	=	heat transfer rate	[kW]
R	=	thermal resistance	[K W^{-1}]

Re	=	Reynolds number	[-]
RPM	=	engine speed	[rev min^{-1}]
S	=	entropy	[kJ K^{-1}]
St	=	Stanton number	[-]
T	=	temperature	[K]
u	=	specific internal energy	[kJ kg^{-1}]
UA	=	overall heat transfer coefficient area product	[W K^{-1}]
V	=	velocity	[m s^{-1}]
$\dot{W}$	=	power	[kW]
y	=	mole fraction	[-]
z	=	elevation	[-]

Greek symbols

γ	=	specific heat ratio	[-]
Δ	=	difference	[-]
ϵ	=	effectiveness	[-]
η	=	efficiency	[-]
μ	=	dynamic viscosity	[kg m^{-1} s^{-1}]
ν	=	specific volume	[m^3 kg^{-1}]
ρ	=	density	[kg m^{-3}]
ψ	=	specific availability	[kJ kg^{-1}]
$\dot{\Psi}$	=	availability rate	[kW]
ω	=	crank train acceleration	[rad s^{-2}]

Subscripts and Superscripts

b	=	brake
C	=	cold side
CHE	=	compact heat exchanger
$CoolantIn$	=	coolant inlet stream
$CoolantOut$	=	coolant outlet stream
ct	=	cranktrain
cv	=	control volume
e	=	exit streams
h	=	hot side of heat engine
H	=	hot side, heat source

in	=	inlet
j	=	inlet streams
l	=	cold side of heat engine
L	=	heat sink
max	=	maximum
min	=	minimum
$misc$	=	miscellaneous
o	=	ambient conditions
P	=	products
R	=	reactants
rad	=	radiator
s	=	shaft
$surf$	=	surface
w	=	wall
∞	=	bulk fluid

Chapter 1

Introduction

Energy consumption and efficiency have been of increased interest in our society recently. Concerns over long term energy resource availability have prompted price increases and discussion about policy reform. The energy consumption in the United States makes up approximately 24% of the world energy use [3]. As of 2005, 28% of the United States energy consumption is used for transportation, 60% of which is used for light-duty vehicles [3]. In the United States, energy consumption in the transportation industry is projected to grow 1.4% annually from 2005 to 2030 [3]. This significant amount of energy consumption, along with the diminishing economically viable petroleum resources, has motivated a substantial amount of research in passenger vehicle efficiency.

Emissions concerns, specifically those associated with global warming, are also garnering significant attention. Carbon dioxide emissions have steady risen over the past 50 years to approximately 380 ppm in the atmosphere as of 2006 [4]. Land temperature data shows an increase of $1°C$ over the last 100 years [5]. These data and others have led most scientists to agree that carbon dioxide emissions are a major contributor to global warming. Carbon dioxide emissions from the transportation industry make up 33% of the total carbon dioxide emissions [3]. This has led to a significant push for policy change that would provide a limit to carbon dioxide emitted.

Vehicle manufacturers have been preparing for the new direction that the consumer market will take, whether it be by choice or policy driven. There has been a significant amount of research done to find methods to increase vehicle efficiency, without reductions in vehicle comfort and power that the consumer market has become accustomed to. Gas/electric hybrid vehicles have led the way in vehicle system modification emphasizing fuel economy.

These vehicles use an internal combustion engine and electric motor to simultaneously power the vehicle, optimizing the engine efficiency and generally include new modifications for increasing overall system efficiency, including regenerative braking and aerodynamic design.

Gas/electric hybrid vehicles are superior compared to typical gasoline vehicles in using the available resources to provide the most efficient system. However, even in gas/electric hybrid vehicles, only about 1/4 of the energy in the fuel is used to power the vehicle [6]. The rest of the energy is made up of waste heat that dissipates into the atmosphere. A significant portion of the wasted energy is in the exhaust stream and the coolant system, offering potential for heat recovery. The gas/electric hybrid vehicle is better suited for capturing this energy and putting it to use with the storage battery that is a component of the hybrid configuration. In typical vehicles, a heat recovery system could only power the electrical system of the vehicle, unless substantial modifications to the drive train were made. The hybrid configuration includes a storage battery, which is used to provide additional power to the electric motor and recover the energy from the regenerative braking system. Energy recovered from the cooling or exhaust systems in a hybrid vehicle could not only be used for the electrical system but also to the storage battery which would directly power the vehicle. The addition of energy to the storage battery would lessen the engine load for a given driving cycle, reducing the energy consumed and increasing overall system efficiency.

Research in this area first requires a background literature review, as there have been many designs and ideas in vehicle design. The literature review in Chapter 2 focuses on gas/electric hybrid technology and energy recovery systems. This provides a good understanding of how the vehicle works and systems that can be applied to it to increase system efficiency.

Data from a 2004 Toyota Prius gas/electric hybrid vehicle was obtained from testing performed at Argonne National Laboratory. These data were used to perform a baseline energy balance of the vehicle to determine the best effluents for heat recovery. This analysis,

in Chapter 3 was extended to include availability and finite time considerations for more realistic estimates for energy recovery potential and provided direction for more detailed analysis of heat recovery systems that could be implemented in the cooling system or exhaust system.

Heat recovery from the exhaust system was explored first, with the implementation of a turbine in the exhaust stream (Chapter 4). This analysis was performed in an engine simulation program called GT-Power. The analysis is focused on the effects of backpressure on the engine performance. Parametric analysis of the engine speed and engine parameters are explored.

Chapter 6 begins with an analysis of the effect of backpressure on engine performance with a compact heat exchanger model. This model relates the pressure drop through a compact heat exchanger to the heat transfer and estimates Rankine cycle output power. The negative impact of the heat exchanger motivates an exploration of energy recovery from the cooling system with a new cooling system design. The design uses spray cooling on the outer surface of the engine cylinder to cool the materials. Spray cooling can offer much higher heat transfer performance, allowing additional potential in the cooling system for energy recovery.

Chapter 2

Literature Review

2.1 Hybrid Vehicles

2.1.1 Introduction

Although gasoline/electric hybrid vehicles may seem like a new technology with their recent gain in popularity, the original concept and development actually occurred over a century ago. In 1905, an American engineer named H. Piper filed a patent for a gasoline engine/electric motor powered vehicle [7]. The motive for this design was not to increase fuel efficiency as is the current focus, but rather to increase overall system power. The early 1900s were a time in which many different technologies were competing in the transportation industry. At the time, the number of vehicles sold was approximately a three way split between gasoline, electric and steam powered vehicles. The amount of power that was produced from each of these types of vehicles was very small relative to today's standards. Piper's patent combining the two technologies allowed the vehicle to accelerate from 0 to 25 miles per hour in ten seconds. This was quite an improvement over the typical thirty seconds for the other vehicle types.

The new and competing technologies allowed for many creative and innovative methods for powering vehicles to be developed. However, very few of these ideas, including the petrol/electric vehicle, were mass produced. This was mainly due to the dramatic increase in the technology of the gasoline powered engines. They quickly became powerful enough that the additional power of an electric motor was not needed. This led to the demise of the petrol/electric vehicle, along with many other technologies, including the steam powered car and all electric vehicle.

In the 1970s, the oil crisis created a renewed interest in different vehicle technologies. This brought back the technologies from the early part of the century, only this time for a different reason, reducing fuel consumption. This interest decreased some through the 1980s as the tensions of the oil crisis subsided. However, interest was sparked once again in the 1990s with increasing oil prices and increased awareness of the world's diminishing petroleum resources. Additionally, there is increasing evidence that hydrocarbon emissions significantly contribute to the increase in the temperature of the atmosphere. The prognostication of higher oil prices, increased energy consumption, emissions concerns and the demise of available petroleum resources has led vehicle manufacturers to invest billions of dollars to combat these issues.

2.1.2 Hybrid Vehicle Technology

Honda and Toyota have led the hybrid vehicle technology development with release of their first hybrid vehicles in the late 1990s; as of 2006, these companies still lead the world in sales and development, however, most other vehicle manufacturers are joining with models of their own. There are many different ways in which hybrid technology can be utilized, along with different technologies that can be used in tandem with the hybrid system to increase power and efficiency. Each manufacturer uses different variations of the basic technology and alters them as they see fit. The main difference is the power distribution paths of hybrid systems, of which three main types are currently used. These include the series hybrid system, the parallel hybrid system and the series/parallel hybrid system.

The series hybrid system uses an internal combustion engine to drive a generator, which powers an electric motor that drives the wheels. There is also a battery in the vehicle that is used to store energy recovered from the brakes and power the electric motor. The series name comes from the power flow configuration in which the power flows from the engine to the electric motor to the wheels in series. The advantage of this configuration is that it

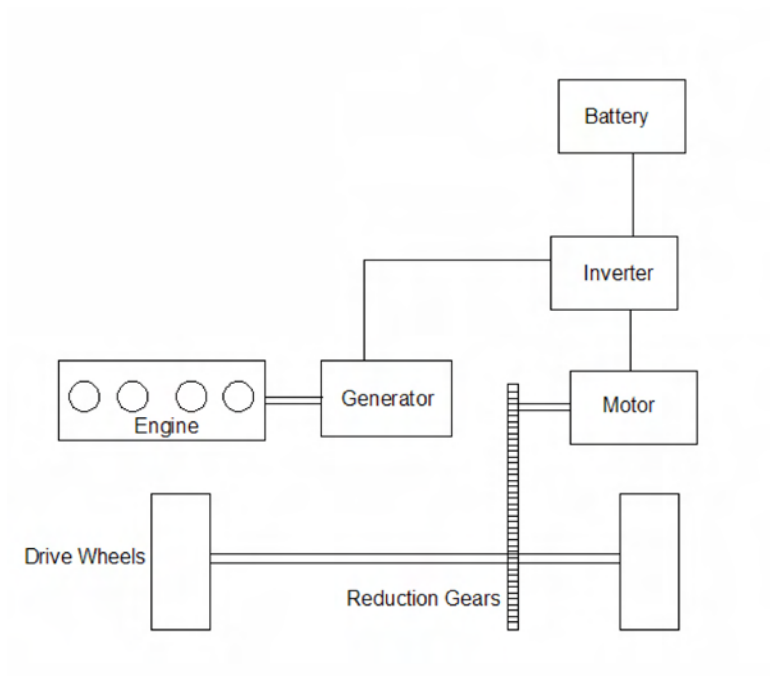

Figure 2.1: Series Hybrid System Configuration

allows the internal combustion engine to run in an efficient operating region for a majority of its operation. The system contains two electric motors; one acts as a generator and the other is an electric motor. This configuration is shown in Figure 2.1.

The parallel hybrid system has a configuration in which the internal combustion engine and electric motor power the wheels in parallel. Both the internal combustion engine and electric motor directly power the wheels, allowing the driving conditions to dictate how much power comes from each source. The internal combustion engine is the prime mover in this configuration, with the electric motor assisting at higher loads where the engine is relatively inefficient. The disadvantage of this configuration is that the electric motor can not simultaneously power the wheels and charge the battery. A schematic of this configuration is shown in Figure 2.2.

The series/parallel hybrid system combines the series and parallel system, allowing the

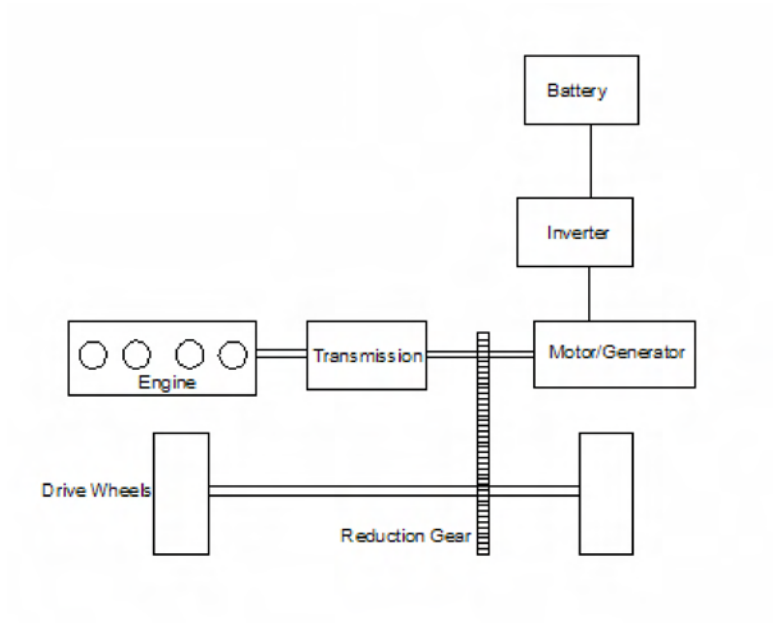

Figure 2.2: Parallel Hybrid System Configuration

advantages of each to be attained. This configuration allows the internal combustion engine to either power the wheels directly or power a generator, which provides power to the electric motor or charges the storage battery. The two motors allow the vehicle to be powered by either the engine or electric motor alone, or some combination thereof. This flexibility allows the system to achieve a higher efficiency by distributing the power in a manner that is optimum for the driving conditions that are experienced. This configuration is shown in Figure 2.3

The series, parallel and series/parallel configurations are the basic power distribution paths that are used for combining an internal combustion engine and electric motor for vehicle propulsion. All three of these configurations can benefit from the addition of regenerative braking. Regenerative braking systems convert the vehicle's kinetic energy into electrical energy to charge the battery. These systems include both a regenerative brake and a hydraulic braking system, with the system favoring the regenerative brake when possible. The system

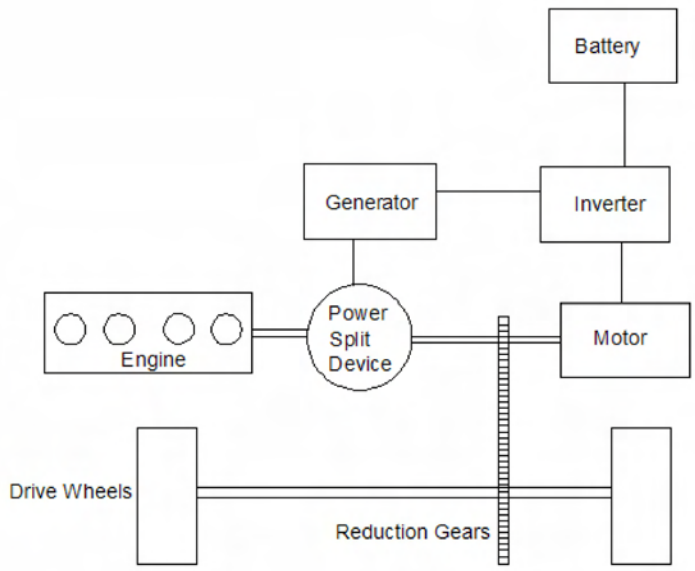

Figure 2.3: Series/Parallel Hybrid System Configuration

is most effective in city driving where there are typically numerous instances of acceleration and deceleration. The system not only recovers energy when the foot brake is used, but also during engine braking. The system reduces the friction loss in the transmission and recovers driving system loss during deceleration. There are many other technologies that are utilized in providing additional energy efficiency for vehicles. These include different types of engines (i.e. the Atkinson Cycle), variable valve timing, variable cylinder management and continuously variable transmission. These technologies are used in both gasoline/electric hybrid vehicles and solely gasoline powered vehicles.

2.1.3 Toyota Hybrid System (THS II)

The many different types and configurations of hybrid electric vehicles make it difficult to describe the details of the vehicle operation. Therefore, in order to provide a detailed description of the manner in which these vehicles operate without confusion, a specific system

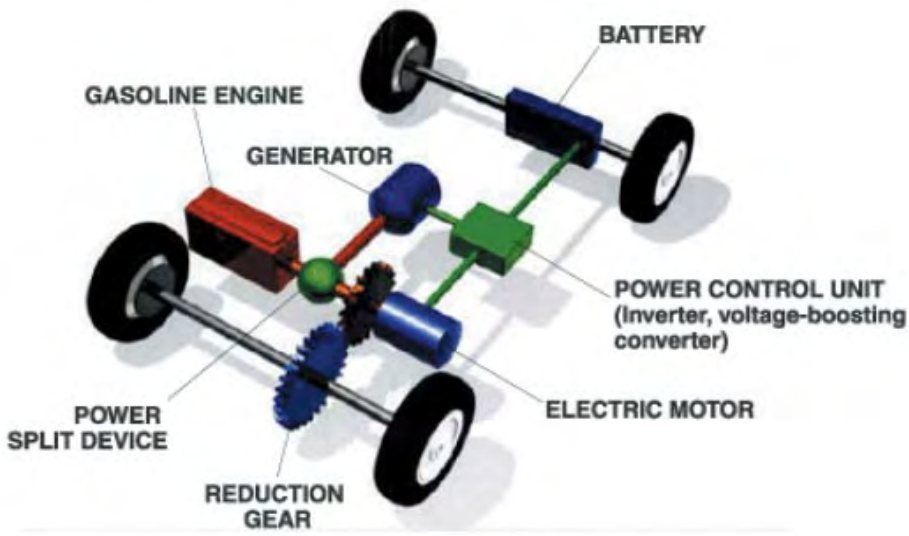

Figure 2.4: Schematic of the Toyota Hybrid System II (THS II) [1]

is chosen for analysis. The system chosen is the Toyota Hybrid System II (THS II) [1]. This was chosen because it has many years of development and is a worldwide leader in sales. Also, it is the same system used in the 2004 Toyota Prius, on which data analysis is based in subsequent chapters.

The THS II uses the series/parallel configuration described above. The internal combustion engine and the electric motor work with one another to optimize the efficiency of the entire system. The system includes a high efficiency engine, a permanent magnet AC synchronous motor, a power split device, a generator, a nickel-metal hydride (Ni-MH) battery and a power control unit. The system is shown in Figure 2.4

The THS II uses a high voltage power circuit for the transfer of electrical energy in the system. The high voltage (500 V) allows a large amount of power to be delivered at a small current, minimizing electrical losses. The electric motor in the system has a power output of 50 kW, which is a substantial increase over the motor in the THS I system. The generator in the system is capable of rotating at high speeds, allowing the output to be significant

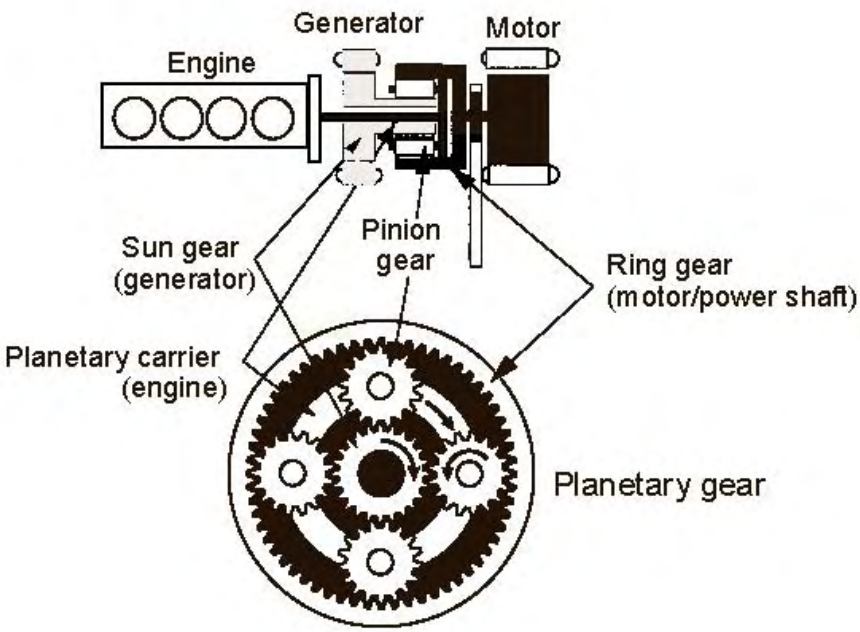

Figure 2.5: Schematic of the Power Split Device in the THS II [1]

enough to power the electric motor. The transmission in the vehicle is made up of the power split device, the generator and the electric motor. The power from the internal combustion engine is distributed by the power split device to the wheels and to the generator. The power split device does this by using a planetary gear system to transmit the power. The engine transmits power to the planetary carrier. The planetary carrier transmits the power via pinion gears to the outer ring gear, which is directly linked to the motor, and the inner sun gear, which is directly linked to the generator. The relationships of the relative speeds of the gears in the power split device is dependent on the driving conditions. This is shown in Figure 2.5

Figure 2.6 shows how the THS II operates when subjected to different driving conditions. The system is powered by solely the battery power and electric motor at startup and low speeds. For typical driving conditions, the internal combustion engine both directly and

indirectly powers the vehicle. Some of the power generated in the engine goes directly to the wheels and the rest goes through a generator to an electric motor, which also provides power to the wheels. The internal combustion engine turns on to directly power the vehicle and power the electric motor for typical driving conditions. A sudden demand for additional power, such as an acceleration, requires that additional power from the battery to be used. The system also includes regenerative braking that is used during vehicle decelerations. Additional charging of the battery is supplied by the engine as required by the driving conditions. The engine will automatically turn off when the vehicle is at rest, reducing the inefficiencies encountered during the idling period of a typical vehicle.

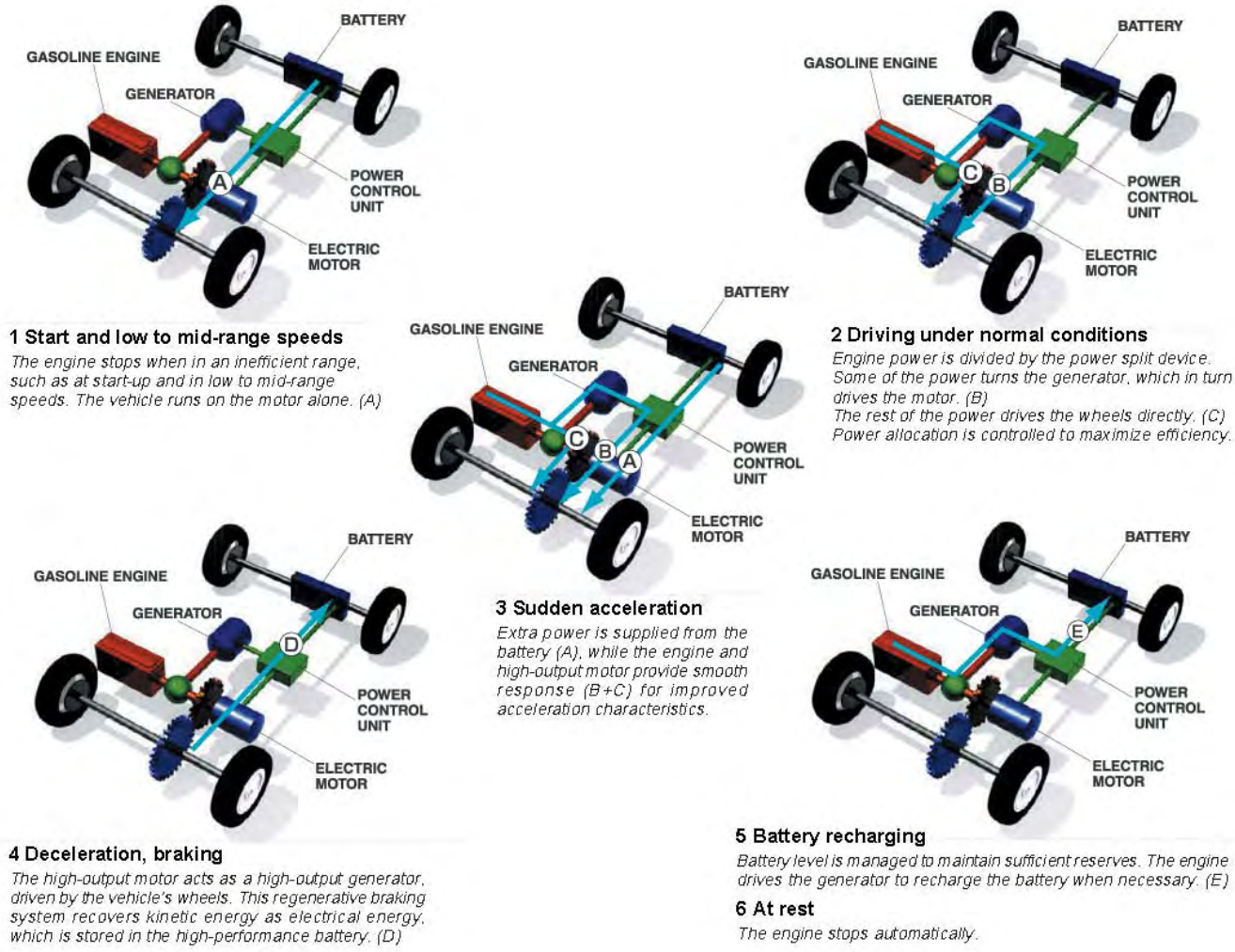

Figure 2.6: Diagrams of the operation of the Toyota Hybrid System II (THS II) [1]

2.1.4 Atkinson Cycle

The 2004 Toyota Prius uses an Atkinson cycle internal combustion engine, as opposed to the Otto cycle engines that are used in most current gasoline powered vehicles [8]. The Atkinson cycle was developed by James Atkinson in 1882, primarily to avoid patent infringement of Nicolaus Otto. The cycle consists of a unique linkage that includes the same four strokes as the Otto Cycle; intake, compression, expansion and exhaust. However, these four strokes are accomplished in one turn of the crankshaft, rather than the two crankshaft turns per cycle in the Otto Cycle. The unique linkage of the system allows the expansion ratio to be greater than the compression ratio. The Otto Cycle requires that these ratios are the same. For increased efficiency, it is desirable to have a larger expansion ratio for more power conversion. Also, the pumping losses are reduced as the expansion ratio is increased, providing greater overall efficiency. The compression ratio of a gasoline vehicle is limited due to engine knock. The limitation of the compression ratio thus restricts the expansion ratio in the Otto cycle, as they must be the same. However, the Atkinson cycle linkage provides a way to achieve a longer power stroke while avoiding the issues associated with engine knock.

The Atkinson cycle also leaves the intake valve open for a longer period of time than the standard Otto cycle, including the first part of the compression stroke. The late intake valve closing results in some of the fuel/air mixture being pushed back into the intake valve. Once the intake valve is closed, the remaining fuel/air mixture is compressed and the cycle continues in a manner similar to that of the Otto cycle. As a result of the late intake valve closure, the effective compression ratio is smaller.

The increased efficiency in the Atkinson cycle comes at the expense of power. The limited power restricted the Atkinson cycle from competing with the Otto cycle in the late 1800s. At that time, the main goal was to increase the power output, with little or no concern for the efficiency of the machine. This cycle is beginning to appear in newer vehicles as society

is becoming more conscious of energy efficiency. The Atkinson cycle is also an ideal fit for the hybrid electric vehicle. The increase in efficiency is obviously desired and the reduction in power is augmented with the additional power of the electric motor.

2.2 Waste Heat Recovery

2.2.1 Introduction

There are many ways in which energy recovery can be accomplished within a vehicle. Regenerative braking is widely used in gas/electric hybrid automotive applications due to the additional generator and storage battery that are a part of the hybrid system. Turbochargers are widely used in Diesel vehicles and high performance gasoline vehicles. A turbocharger is a device that compresses the inlet air to the engine to increase the amount of oxygen in the fuel/air mixture which increases the power. The compressor is driven by the exhaust gas stream. There are also unique ideas for redesigning the engine to optimize energy recovery efforts, such as the Scuderi Air-Hybrid Engine [9].

The Scuderi Air-Hybrid engine has a different engine design that allows for simple additions for energy recovery and increased efficiency. The Scuderi engine is a split cycle engine that uses two cylinders to complete the four strokes. The first cylinder is used for intake and compression, at which point the compressed air is transferred to a second cylinder for combustion and exhaust. The original technology was developed in 1914, however it was not able to compete with other technologies at the time. The Scuderi engine has a unique valve design and firing timing that allows it to overcome previous problems in split cycle engines, such as poor volumetric efficiency and low thermal efficiency. In addition to the reduced emissions and reduced piston friction, the engine can easily include built in supercharging and Miller effect. An air storage tank is added to store the compressed air from the first cylinder for use as an energy storage device. Along with providing compressed air to the

second cylinder for combustion, the air storage device can be used for regenerative braking. A turbocharger can also be used to reduce the amount of compression work done by the engine. Overall, the Scuderi Air-Hybrid engine offers many performance and efficiency benefits for minimal equipment additions and cost.

There are numerous ideas and designs that have been developed that include a completely different mode of power production, such as the Scuderi. The evaluation of these numerous ideas would require a great deal of time due to the variety and complexity, making it necessary for a more narrow definition of the project of the literature review. Therefore, the focus of this review will be energy recovery from typical vehicles that have a substantial consumer market. This makes the probability of implementation in the consumer market higher than it would for nontraditional vehicles. Additionally, the waste heat in exhaust gas and engine coolant are the most significant for energy recovery, creating a primary focus on these effluents. There are many ideas and designs of energy recovery from a typical gasoline vehicle, some of which have been around for over a century. The recent increase in production and popularity of gasoline/electric hybrid vehicles allows for additional designs for energy recovery to be developed.

2.2.2 Waste Heat Recovery Cycles

Bottoming cycles are used to provide additional power generation from the waste heat of the primary power cycle. There are many different types of cycles that are used in power plants and other power generation cycles to increase the overall efficiency of the system. There is the potential for these cycles to be scaled down and modified so that they can be implemented into a vehicle application. These cycles include, but are not limited to, the Rankine cycle, Brayton cycle, absorption refrigeration cycle and Kalina cycle. Each of these cycles operate in a different way and are suitable for different objectives.

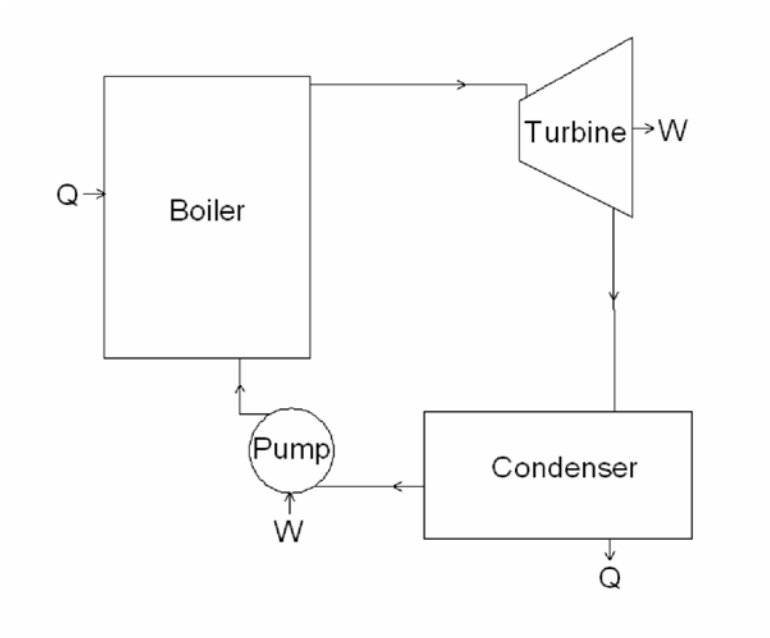

Figure 2.7: Rankine Cycle Schematic

The basic Rankine cycle includes a turbine, condenser, pump and boiler. There are many different working fluids that can be used in Rankine cycles, including water and organic fluids. The working fluid is expanded through the turbine from a high pressure prior to the turbine to a low pressure after the turbine. The turbine provides a net work out of the cycle. The working fluid then enters the condenser where it is cooled at a constant pressure to a saturated liquid state. The fluid then enters the pump, which compresses the liquid to a high pressure. Next, the working fluid enters a boiler, which provides heat to the fluid at a constant pressure. The high temperature, high pressure working fluid then enters the turbine and repeats the cycle. A schematic of a basic Rankine cycle is shown in Figure 2.7 [10].

The Brayton cycle is a power cycle that includes a compressor, turbine and heat exchanger. The system can be an open or closed system, depending on the application. The working fluid enters the compressor and is compressed to a high pressure. At this high pressure, the working fluid enters a heat exchanger, which adds heat at a constant pressure. The

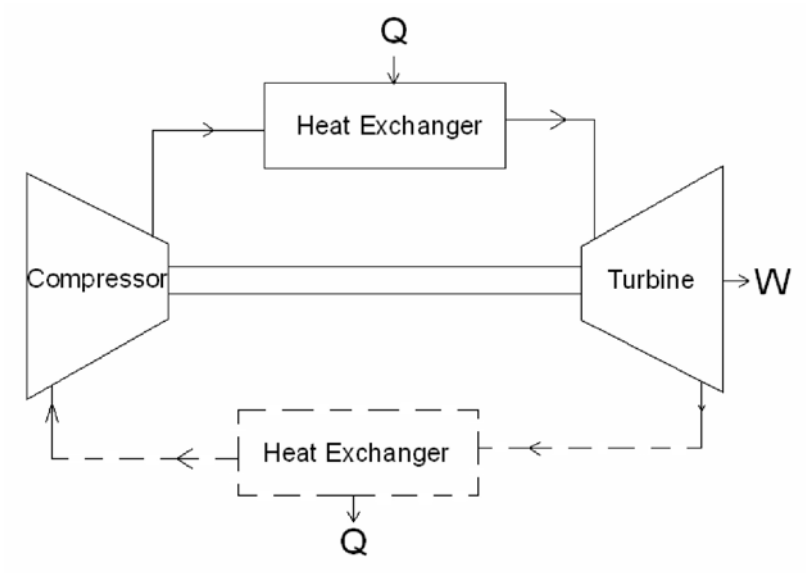

Figure 2.8: Brayton Cycle Schematic

high pressure, high temperature working fluid then is expanded through a turbine, which produces a work output for the cycle. The expanded working fluid is then either exhausted to the surroundings or driven through a heat exchanger and back to the compressor, depending on if it is an open or closed cycle. The compressor is driven by some of the work produced by the turbine. The remainder of the turbine work is the net power out of the cycle. A schematic of a Brayton cycle is shown in Figure 2.8 [10].

An absorption refrigeration cycle consists of an evaporator, condenser, expansion valve, absorber, pump and generator. There are two working fluids required for these systems, a refrigerant and an absorbent. The refrigerant goes through a condenser, expansion valve and evaporator prior to entering the absorber. In the absorber, the refrigerant vapor is absorbed by the absorbent. The refrigerant-absorber mixture enters leaves the absorber and enters a pump, which increases the pressure of the mixture prior to entering the generator. A high temperature source drives the generator, which forces the refrigerant out of the solution and back into the condenser. The remaining, mostly absorbent mixture returns to the absorber.

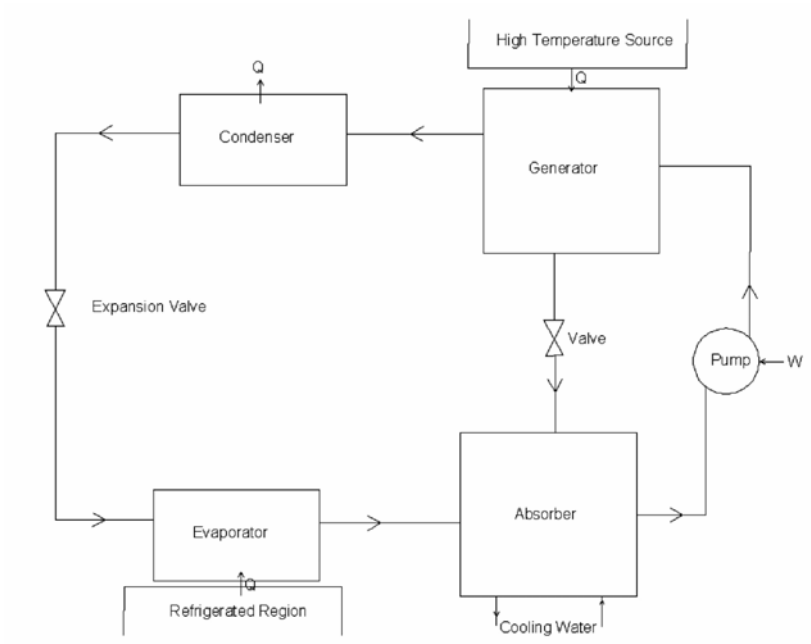

Figure 2.9: Absorbtion Refrigeration Cycle Schematic

The high temperature source drives the cycle, which provides a refrigerated region at the evaporator. The absorption refrigeration cycle is shown schematically in Figure 2.9 [10].

The Kalina Cycle is a combination of a Rankine cycle and an ammonia absorbtion refrigeration cycle [11, 12]. There are many different variations in the configuration, but each of them typically include a turbine, condenser, pump, recuperator and evaporator. The working fluid is an ammonia-water mixture. The fluid mixture allows the fluid to boil and condense at a variable temperature. Thirty to fifty percent more power can be generated from a Kalina cycle than from an Organic Rankine cycle.

2.2.3 Energy Recovery

There are a variety of methods that have been used in recovering waste heat from the exhaust gas. Some of these technologies are in the development stage, which has been prompted by the recent increase in fuel cost and emissions concerns. Other technologies have been around

for a long time, but have never been economical or desired. There are also some technologies that have been widely used in other applications that can be applied for energy recovery from a vehicle.

Vehicle Heating

The heat in the exhaust gas can be used to heat the interior of the vehicle for passenger comfort. Diehl et. al. has developed an Exhaust Heat Recovery System that utilizes the waste heat from the exhaust for cabin heating [13]. The Exhaust Heat Recovery System would also be used to assist in faster engine warm-up times, which would assist the lower fuel efficiency at cold start. Although this system is unique, as it appears to provide better cabin heating than the typical vehicle, the overall fuel efficiency is minimally affected. Yang, Yuan and Lin examined the implementation of a heat pipe heat exchanger to recover the waste heat of the exhaust gas to be used for cabin heating of a bus [14]. This application of the waste heat recovery for internal vehicle heating appears to be viable, however the engine coolant system is generally utilized for this application. Therefore, no additional gains in vehicle efficiency would be obtained.

Heat Storage

The emissions and fuel consumption during a cold start up period are significantly higher than during typical operation. It would be advantageous to find a way to reduce these emissions and fuel consumption during this time period. An obvious solution to these issues is to increase the temperature of the engine block prior to or at the startup time. A system that accomplishes this is already incorporated into the Toyota Hybrid System using a different design of the engine cooling system [1]. The THS engine cooling system includes two loops that are used to provide heat and cooling as desired, by using a thermal storage tank. There have been many other similar designs utilizing a heat storage device in the engine cooling

loop. One design of a cooling loop has been applied to a bus petrol engine [15]. The designed system was numerically modeled and verified with experimental testing. The results appear optimum for a mass transportation vehicle that operates on a standard schedule, such as a bus.

Thermoelectrics

Waste heat recovery from the exhaust stream can also be accomplished by the use of thermoelectrics on the exhaust pipe. Hendricks and Lustbader investigated the use of thermoelectric power systems for light-duty and heavy-duty vehicles [16]. The amount of waste heat recovered by the thermoelectic power system is strongly dependent on the mass flow rate of the exhaust stream and the temperature of the exhaust pipe. It was found that heavy-duty vehicles have 5 times the potential for waste heat recovery over light-duty vehicles. This can result in an additional power production of 5 - 6 kW for heavy-duty vehicles. Anatychuk et al. studied the use of waste heat recovery using thermoelectric generators for use in Diesel engines and gas turbine plants [17]. The temperatures of the systems that were looked at were quite low (200-400 $°C$), resulting in low conversion efficiencies. However, the amount of waste heat is significant enough that the amount of energy recovered is a significant portion (17%) of the mechanical energy output of the engine without heat recovery. Crane, Jackson and Holloway examined the use of a thermoelectric radiator in hybrid vehicles to recharge the battery or provide power to the electrical systems in the vehicle [18]. The thermoelectric radiator was modeled to show that 1 - 2 kW can be recovered. Engine simulations showed that even at low loads, the electrical power needs of the vehicle could be achieved. This could allow the alternator to be removed from the system, which would allow the 5 - 6 kW that generally powers the alternator to go to useful power. Overall, indications are that thermoelectric systems could have potential for waste heat recovery in vehicles if the mass flow rate and temperature of the exhaust stream are significant enough. The economic factor

of utilizing thermoelectric systems for waste heat recovery is also important. Thermoelectric systems can be expensive, but costs are dropping as technologies are improving. The economic viability for these systems in vehicles has not yet been reached.

Vehicle Cooling and Engine Air Pre-Cooling

There are a variety of heat generated cooling systems that could be used in vehicles for air conditioning and engine inlet air pre-cooling. Some of these include metal hydride cooling systems, zeolite heat pumps, thermoacoustic cooling and vapor absorption systems [19]. Metal hydride systems absorbed and release hydrogen, releasing and consuming heat respectively. These systems could be used to recover the waste heat from the vehicle and provide air conditioning inside the vehicle. There are still challenges in reaching coefficient of performance levels that would allow the size of the system to be implemented into a vehicle for the desired cooling load. Zeolite systems work in a manner similar to metal hydride systems. Zeolite attracts water and releases heat, so this process would be reversed for heat recovery. Thermoacoustic systems are based on the correlation of temperatures changes with pressure and velocity changes in a sound wave. All three of these systems have potential for supplying air conditioning in vehicles. However, there are still many research challenges that exist for all three technologies before they can meet the demands of cooling the interior space of a typical vehicle. There are also the challenges of vehicle implementation that exist for the metal hydride, zeolite, and thermoacoustic systems.

There has been a lot of investigation of the using the exhaust gas streams to run vapor absorption systems for air conditioning and pre-cooling the inlet air to the engine. Ballaney, Grover and Kapoor compared ammonia-water and water-lithium bromide vapor absorption systems to run the air conditioning system in a Fiat Car [20]. Ballaney et al. determined that this is a feasible design with the water-lithium bromide solution providing the best results. Exhaust waste heat recovery using an absorption refrigeration cycle with a turbocharged

Diesel engine vehicle was explored by Talbi and Agnew [21]. The system would provide air conditioning and pre cool the inlet air to the engine, providing increased power and efficiency. Talbi and Agnew determined that this design would accomplish the desired results, however an economic analysis still needs to be performed to prove overall feasibility.

Mostafavi and Agnew have explored the use of vapor absorption systems in many types of Diesel powered vehicles [22, 23]. A general investigation of engines found that the system is very dependent on the operating conditions and configuration of the engine. It was found that Diesel cycles with a high power to energy rejection rate ratio will offer the best results for the implementation of this system. Specific applications of the combined Diesel engine - Absorption unit are to a turbocharged engine [24] and a supercharged engine [25]. The initial analysis were used in an engine simulation program to obtain more realistic results. From the analysis, both the turbocharged engine and supercharged engine offer feasible opportunities for the implementation of the absorption units. An increased pressure ratio for both the turbocharged and supercharged engines decreases the cooling capacity.

Atan also investigated the use of an absorption air conditioning system driven by the exhaust waste heat in a passenger vehicle [26]. This system would run on a lithium-bromide and water solution. Preliminary calculations revealed that up to 3 kW could be generated from the recovered energy. Akerman has also looked at absorption air conditioning systems in passenger vehicles, utilizing three different working fluid combinations [27]. These working fluid combinations include water-lithium bromide, ammonia-water and refrigerant 22-dimethyl ether of tetraethylene glycol.

The investigation of vapor absorption systems for the use of interior vehicle air conditioning and pre-cooling the inlet air to the engine provides promise for increasing overall vehicle efficiency. Detailed vehicle analyses still need to be performed to show the viability and economic feasibility for a specific vehicle. There are many issues that need to be addressed, such as additional vehicle mass, location of additional system, reduction in fuel consumption

and cost of the system. Also, most of the literature has focused on the implementation of these systems into Diesel powered vehicles. The viability of these systems in a gasoline powered vehicle still needs to be investigated.

Exhaust Gas Heat Recovery

There are many very unique systems that have been developed to recover the waste heat from the exhaust stream to provide additional power to the vehicle. These systems can be directly connected to the crankshaft of the vehicle, provide power to the auxiliary devices or to a battery in a hybrid vehicle.

Kapich has developed a turbo-hydraulic system to recover the exhaust energy and provide power to the vehicle [28]. Although specific engine parameters were not investigated, it is presumed that this system would work best for heavy-duty Diesel vehicles. The cost of the device will be approximately 15 to 20% of the engine cost. An analysis would have to be done to determine if the reduction in fuel consumption over the life of the car would offset the initial cost of the system for each specific vehicle design.

One of the developing technologies for exhaust gas energy recovery is the Turbo-Generator Integrated Gas Energy Recovery System, or TIGERS [29]. This project is being developed by engineers working under the Society of Motor Manufacturers and Traders Foresight Vehicle research initiative. The TIGERS consists of a turbine that is driven by exhaust gases to drive a generator. The TIGERS is attached to a bypass waste pipe that is connected just below the engine exhaust manifold. A valve is used to allow some flow through the bypass pipe and into the turbine. The bypass valve is controlled so that it allows more flow through at higher engine speeds where more energy can be captured. For lower engine speeds, the engine performance is significantly affected by the backpressure, thus the bypass valve allows minimal flow through. The generated power from the TIGERS can be used to drive the vehicle's electrical system including heating, air conditioning, lighting and electronics. This

power could also be used to drive cam and drive belts and the alternator. In hybrid vehicles this could provide power to drive motors or to the battery. The engineers working on this project estimate a reduced fuel consumption in the range of 5 to 10 percent.

BMW is developing the Turbosteamer, which is a steam powered auxiliary drive [30]. The system uses waste heat in the exhaust gases and cooling system to drive the system. The waste heat from the vehicle goes through expansion units which are directly linked to the crankshaft of the internal combustion engine. BMW claims that the system can provide a fuel consumption reduction of up to 15%, while adding an additional 14 horsepower and 20 Nm of torque. The system is currently set up on a 1.8 liter, four-cylinder engine and is expected to be in volume production by 2015.

Recovering energy from the exhaust system to provide additional system power can have substantial impacts on the efficiency of the system. Exhaust gas temperatures can be significant, thereby providing an excellent opportunity for energy recovery. However, recovering energy from the exhaust system will increase backpressure on the engine, reducing the engine power. The significance of the backpressure on engine performance must be studied further to understand the viability of exhaust gas recovery systems.

Rankine Cycles for Energy Recovery

There are many types of cycles that could be used for energy recovery in a vehicle, however the most common is the Rankine cycle. Rankine cycles have been used in many applications, so the knowledge about their performance is good. There are many other applications in which Rankine cycles are used as bottoming cycles, which make the implementation to a vehicle application easier than other cycles. Water can be used as the working fluid for Rankine cycles, however the temperature extremes that a vehicle would encounter necessitate another fluid. Organic fluids can also be found as working fluids in Rankine cycles and would work for vehicle applications as long as toxicity and flammability requirements could be met.

The recovery of exhaust gas energy using a Rankine cycle has been studied for Diesel engines in stationary applications. Verneau investigated energy recovery form the exhaust gases of a large Diesel engine in a power plant [31]. The energy recovery is accomplished by an organic Rankine cycle with FLORINOL 85 (trifluoroethanol and water) as the working fluid. Recovery results were good, however many issues with corrosion in the filters, evaporator vibrations and equipment failures were encountered. These issues would have to be solved prior to an industry wide implementation of this system. Aly has also studied using Organic Rankine cycles to recover the waste heat from a Diesel engine [32]. The working fluid, R-12, is first heated using the engine coolant and then superheated using the exhaust gases. The working fluid is expanded through a turbine prior to entering a condenser that is air cooled. Utilizing this system, a 15% improvement in engine power can be achieved. Different alternatives of power cycles for waste heat recovery from the exhaust of adiabatic Diesel engines was studied by Bailey [33]. The three cycles analyzed were the stream Rankine, organic Rankine and air Brayton cycles. Benefits were found from all three cycles, however the price of fuel at the time was not enough to provide economic feasibility.

There have been studies done examining Rankine cycles for exhaust gas heat recovery in a vehicle application. Thermo Electron Corporation tested a Diesel-organic Rankine compound engine on Class 8 trucks [34]. The Diesel engines that power these trucks are relatively efficient, however a significant amount of energy is wasted in the exhaust stream. Dynamometer tests on one of these vehicles demonstrated a 16% improvement in efficiency and emissions. The implementation of this bottoming cycle could save over a billion dollars annually for the trucking industry in the United States.

Oomori and Ogino studied the use of a Rankine bottoming cycle for the recovery of waste heat from an evaporative engine cooling system [35]. This target application of this system is compact passenger cars, with a main goal of increasing fuel efficiency. Using simulations and experimental data, Oomori et. al. found that recovered energy can be up to 3% in

engine output energy with the system.

Chammas and Clodic investigated the implementation of a Rankine cycle in a hybrid vehicle for waste heat recovery [36]. An energy balance of a typical vehicle showed that most potential for heat recovery from the exhaust stream. An analysis of different working fluids for use in the Rankine cycle compared organic fluids to water. Organic fluids have higher boiling points and lower freezing temperatures than water, however these fluids come with other concerns such as toxicity and flammability. Although the backpressure effects were acknowledged in this analysis, detailed investigation was not performed. Also, the effects of a hybrid configuration were not considered by Chammas and Clodic. In using the organic fluids, the possibility exists to also recover energy from the cooling system. Utilizing the organic fluids with the exhaust and cooling system, Chammas and Clodic estimate a 23% fuel economy improvement.

The use of a Rankine bottoming cycle in a vehicle appears to have potential. The recovery of heat from the exhaust gas would again need to be analyzed to see if the backpressure would impact engine performance significantly. Application to a specific vehicle would require system redesign to fit all of the system components in the vehicle. The additional vehicle mass and system cost would need to be determined show economic feasibility.

Chapter 3

Availability Analysis

3.1 Introduction

Automotive vehicle efficiency is an issue that is becoming increasingly important in our world. Since a significant amount of energy is lost to waste heat in automotive vehicles, it is of interest to investigate the viability and methods of waste heat recovery in current vehicles. Gas/electric hybrid vehicles have some of the highest efficiencies of any automobile on the road today. Further increasing the efficiency of these vehicles through waste heat recovery could accomplish the goal of significantly reducing the energy consumption and emissions from automobiles. Additionally, recovered energy can easily be stored as useful energy in the battery of the hybrid vehicle. This first part of the waste heat recovery analysis provides direction to where the best location(s) are to recover energy.

The data used for this analysis were recorded from a 2004 Toyota Prius at Argonne National Laboratory during a pre-defined driving cycle that is designed to simulate a typical usage pattern. This data acquisition was part of comprehensive vehicle testing on the Prius vehicle at the laboratory. The Prius data were taken every tenth of a second for approximately 24 minutes, during which the Prius was placed under a variety of driving conditions including idling, accelerating to and driving at highway speeds, as well as city driving conditions.

The Prius data are first used in an energy balance to determine how the incoming fuel energy is being divided. The results of this analysis are compared with typical values for the fractions of fuel energy existing at each of the locations. Next, an availability analysis was performed to provide an upper bound for the amount of work that can be obtained

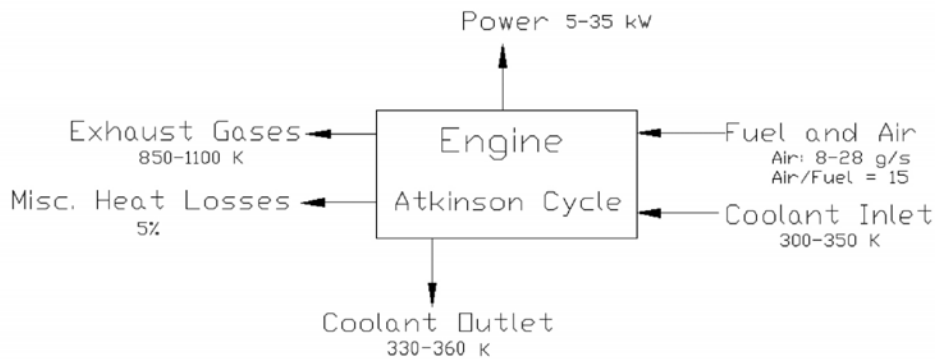

Figure 3.1: Defined System for the Energy Balance

from the effluents. Finally, a finite time analysis was applied to provide an estimate of the actual energy that can be recovered. Since these data did not include all of the parameters necessary to complete the energy balance and availability analysis for the system, values were assumed or computed for the unknowns. A sensitivity analysis was used to verify that the assumed values were within a reasonable range.

3.2 Energy Balance

An energy balance was performed on the data taken from the Prius. The energy balance is used to evaluate the energy split from each of the effluents and compare them to typical values. The general equation for a control volume energy rate balance is shown in Equation 3.1 [10].

$$\frac{dE}{dt} = \dot{Q}_{cv} - \dot{W}_{cv} + \sum_{j}^{\#inlets} \dot{m}_j(h_j + \frac{V_j^2}{2} + gz_j) - \sum_{e}^{\#exits} \dot{m}_e(h_e + \frac{V_e^2}{2} + gz_e) \tag{3.1}$$

The application of Equation 3.1 first requires the definition of a system. The system for this analysis is chosen to be the engine, which is an open system control volume. Figure 3.1 shows the definition of the system for this analysis.

As shown in Figure 3.1, the mass that enters the system will include fuel, air and coolant. Exhaust gases and coolant will exit the system along with shaft power out. There is also an additional heat loss from the engine and its associated components to the surrounding air. Kinetic and potential energy terms shown in Equation 3.1 are assumed to be negligible. The left-hand side of the general equation for a control volume energy rate balance is assumed to be zero corresponding to steady state operation. The temperature and pressure of the fuel and air entering the engine are assumed to be at ambient conditions. The coolant is assumed to be incompressible and have a constant specific heat. Also, the coolant is assumed to be 40% ethylene glycol and 60% water. The pressure of the gases in the exhaust pipe was assumed to be one atmosphere. For the evaluation of properties, the ideal gas assumption was made for all of the gas species in the exhaust. Using these assumptions, the energy balance from Equation 3.1 is simplified as shown in Equation 3.2.

$$0 = -\dot{W}_b + \dot{m}_{Fuel} h_{Fuel} + \dot{m}_{Air} h_{Air} - \dot{m}_{ExhGas} h_{ExhGas} - \dot{m}_{Coolant}(h_{CoolantOut} - h_{CoolantIn}) - \dot{Q}_{Misc} \tag{3.2}$$

In Equation 3.2, the $\dot{W}_b$ term is the work output of the system and was calculated from the engine torque and engine speed from the Prius data. The $\dot{m}_{Fuel}$ and $\dot{m}_{Air}$ terms are the mass flow rates of fuel and air respectively, and are directly from the Prius data. The specific enthalpies are denoted with the symbol h and are evaluated from the temperature of each specific substance. The lower heating value of octane was used for the enthalpy of the fuel. This value was found to be 44430 kJ/kg [10]. The $\dot{Q}_{Misc}$ term accounts for the miscellaneous heat losses from the engine. Typical values for this term are between 3 and 10% of the fuel energy [6]. For this analysis, the miscellaneous heat losses were assumed to be 5% of the fuel energy.

This leaves Equation 3.2 with only the $\dot{m}_{ExhGas}$ term and the $\dot{m}_{Coolant}$ term, which are

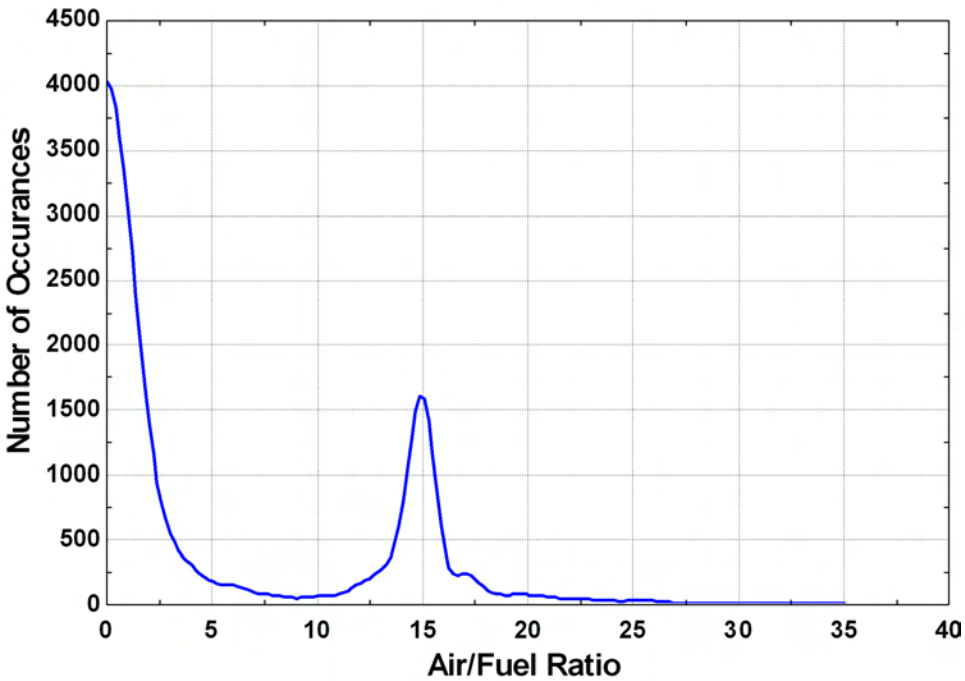

Figure 3.2: Histogram of Air/Fuel Ratio over the Drive-Test Data

the mass flow rate of exhaust gas and mass flow rate of coolant, respectively. The Prius data do not include the mass flow rate for the exhaust gases, so it had to be estimated from a combustion analysis of the fuel. The fuel flow and air flow rates into the engine were recorded, however the Air-Fuel ratio (A/F) that is calculated directly from these data is very erratic. This inconsistency is partially due to a timing offset in the measurements of the two parameters. Also, there are values that are recorded near zero when the engine is off that cause values of the A/F to be abnormally small. Therefore, the A/F was assumed to be 15 based on an analysis of averages and offsets of the fuel flow and air flow data. The results of this analysis show that an A/F of 15 is a good estimate for a variety of driving conditions of the Toyota Prius, as seen in Figure 3.2. The large spike of data near zero is due to the error from the erratic behavior of the engine turning on and off as described above, and thus can be ignored.

The Air/Fuel ratio found from this analysis is very close to the stoichiometric value. Therefore, for ease of computation, the chemical reaction used for this analysis is the stoichiometric value, as shown in Equation 3.3.

$$C_8H_{15} + 12.4(O_2 + 3.76N_2) \longrightarrow 8CO_2 + 7.5H_2O + 46.62N_2 + 0.65O_2 \tag{3.3}$$

The chemical reaction in Equation 3.3 relates the molar flow rates of the fuel and the products. The mass flow rate of the fuel is included in the Prius data, which allows the evaluation of the flow rates of each of the products in the exhaust. The mass flow rates of these products were summed to obtain the mass flow rate of the exhaust stream.

Using the measured and calculated data together with the above assumptions, the mass flow rate of the coolant is the only unknown in the energy balance shown in Equation 3.2. Unfortunately, the coolant mass flow rate is not included in the Prius data and has to be found through the energy balance. This ensures that the fractions of energy solved for in the energy balance will sum to 1.

The energy split was determined by evaluating the terms from Equation 3.2 over the entire cycle of the Prius data. These terms were integrated over the cycle to find values that can be easily compared to one another. Percentages were calculated by dividing the integrals of the exiting energy terms by the integral of the incoming fuel and air. These percentages were then compared to typical values for the energy split, as shown in Table 1 [6].

Table 3.2 shows that the power is a larger than typical percentage of the total energy. Also, the exhaust is a smaller than typical portion of the total energy. This variation is due to the nature of the Atkinson cycle engine that exists in the Toyota Prius, as opposed to the more common Otto cycle engine. The longer expansion stroke of the Atkinson cycle allows more useful work to be obtained from the process, thereby using energy that would have gone to the exhaust and causing the exhaust gas temperatures to be lower. The longer

Table 3.1: Comparison of Energy Split in the Prius to Typical Values

	Integrated Value (kJ)	**Percent of Fuel**	**Typical Values (Heywood)**
Fuel/Air ($\dot{m}_{Fuel}h_{Fuel} + \dot{m}_{Air}h_{Air}$)	14106		
Work ($\dot{W}_b$)	4564	32.36%	25-28%
Exhaust Gas ($\dot{m}_{ExhGas}h_{ExhGas}$)	1958	13.88%	36-50%
Coolant ($\dot{m}_{Coolant}(h_{CoolantOut} - h_{CoolantIn})$)	6878	48.76%	17-26%
Misc ($\dot{Q}_{Misc}$)	705.3	5%	3-10%

expansion stroke also increases the amount of time that the hot gases are in the combustion chamber, allowing more energy to be captured in the coolant. There have been studies of internal combustion engines that show the dependence of the engine speed and percent load on the energy split [37]. At higher engine speeds, less energy is directed to the coolant. Also, at larger engine loads, the energy in the coolant tends to decrease. The Prius data are at relatively low engine speeds and loads, resulting in a higher percentage of energy in the coolant. This is typical of the Prius, as the engine speed and load tend to be relatively small for typical driving conditions. The power split device in the Prius controls the engine speed and loading to values that optimize the efficiency and performance of the vehicle. These values are typically lower than those of a gasoline-only powered vehicle, as the electric motor power is utilized to provide additional power to supplement the internal combustion engine. Thus, values for the Prius in Table 1 deviate from the typical values provided by Heywood due to these differences that the Prius has from a typical vehicle.

The assumption of the percentage of energy that is due to miscellaneous heat losses was explored further in a sensitivity analysis. The assumption was made for the miscellaneous heat losses value to be 5% of the fuel energy, as typical values from Heywood suggest that it should be between 3% and 10%. The actual value will be dependent on the type of engine and driving conditions, among other factors. Figure 3.3 shows how the variation of the miscellaneous heat losses affects the energy split.

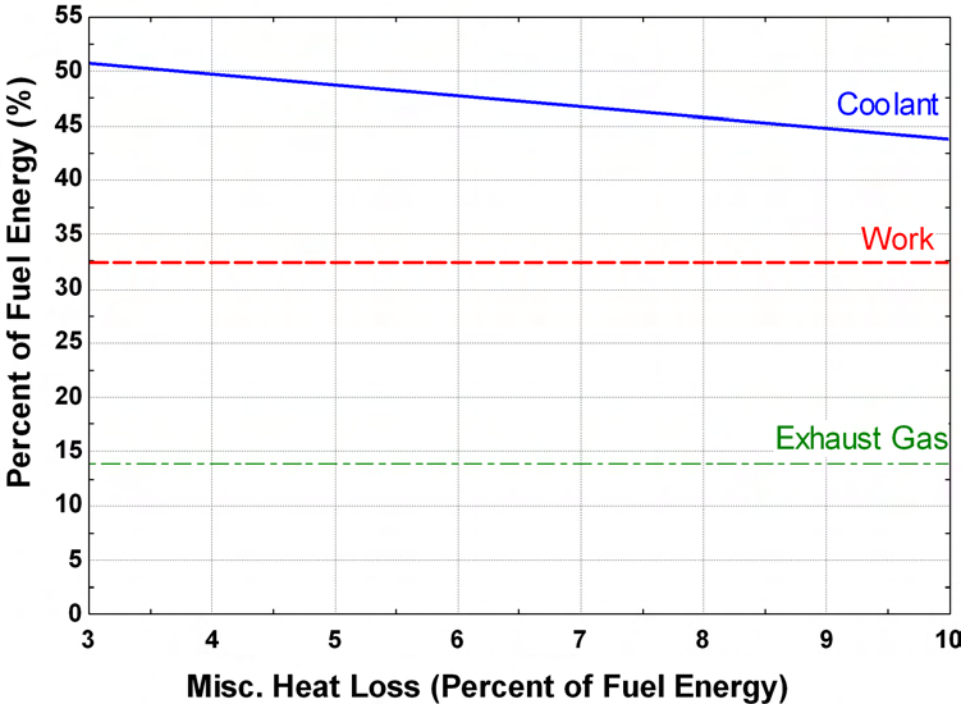

Figure 3.3: Variation of the Energy Split as a Function of the Miscellaneous Heat Losses

The variation in the miscellaneous heat loss assumption had no effect on the energy that powers the vehicle (work) or the energy in the exhaust gas. This is because the energy from the work and exhaust gas were calculated directly from the Prius data. This means that the coolant energy is the only flow that is dependent on the miscellaneous heat loss assumption. The mass flow rate was computed through the energy balance and is dependent on the miscellaneous heat loss assumption. This sensitivity analysis shows that the energy in the coolant is between 43.7% and 50.8% of the fuel energy for the miscellaneous heat losses in the 3-10% range.

3.3 Availability Analysis

An availability analysis is a calculation of the maximum theoretical work that a given system can do on its surroundings. It is derived from the first and second laws of thermodynam-

ics. The availability of a system is determined by the comparison of the thermodynamic properties of the system at its given state to the properties of the same system if it were at the state of the surroundings. The maximum theoretical work that a system can produce corresponds to the system changing from its original state to a state of thermal equilibrium with the surrounding environment in a completely reversible process.

An availability analysis was utilized to provide direction and expectations for heat recovery analysis. This analysis should indicate where the greatest potential for energy recovery lies in the vehicle (i.e., the coolant, the exhaust, or some combination of the two) and what the maximum theoretical availability is. The knowledge of the relative maximum magnitudes for each recovery option will give an idea of which options are best suited for further exploration.

The evaluation of availability is based on thermodynamic properties of the system. The specific availability,ψ , of a system is defined in Equation 3.4 [10].

$$\psi = h - h_o - T_o(s - so) + \frac{V^2}{2} + gz \tag{3.4}$$

The kinetic and potential energy contributions are shown in Equation 3.4, but they are subsequently neglected as they are not significant for the case that is analyzed. The equation does include the specific enthalpy and specific entropy of the system at the given state, which are denoted by h and s respectively. The rest of the terms in the equation are evaluated at the reference state and are denoted with a '0' subscript. T_o is the temperature of the surroundings. The terms h_o and s_o are the specific enthalpy and specific entropy, respectively, of the system contents evaluated at the reference state conditions. The availability rate,$\dot{\Psi}$, is evaluated as shown in Equation 3.5, where $\dot{m}$ is the mass flow rate of the system.

$$\dot{\Psi} = \dot{m}\psi \tag{3.5}$$

The specific availability and availability rate equations were used to perform an availability analysis on the coolant and exhaust systems of a Toyota Prius. This analysis is used to gain a better understanding of which effluents are best suited for energy recovery. The availability analysis also requires the definition of the reference state conditions. The reference state conditions include the temperature and pressure of the environment and are defined as:

$$T_o = 298K$$

$$P_o = 101.325kPa$$

3.3.1 Availability of Fuel

As a baseline, the availability of the fuel is computed to determine the magnitude of availability entering the engine. This value is then compared to the values for the exhaust and engine coolant streams to establish the percentage of initial availability that exists in each of the various thermal flows out of the engine. The availability rate in the fuel, $\dot{\Psi}_{Fuel}$, was calculated by applying the mass flow rate of fuel $\dot{m}_{Fuel}$ and the specific availability of gasoline $\psi_{C_8H_{15}}$ to Equation 3.5. The specific availability of gasoline was calculated using the thermodynamic definition of availability for a fuel shown in Equation 3.6.

$$\psi_{C_8H_{15}} = (H_R - H_P) - T_o(S_R - S_P) \tag{3.6}$$

The H_R and S_R terms are the enthalpy and entropy, respectively, of the reactants in the combustion equation. The enthalpy and entropy of the products in the combustion equation are denoted as H_P and S_P, respectively. Evaluating the variables in Equation 3.6 requires the chemical equation for the complete combustion of the fuel into combustion products with stoichiometric air, as derived previously in Equation 3.3.

The enthalpy of the products is found by multiplying the enthalpy of formation values for each chemical species by its respective number of moles from the combustion equation. For the combustion equation shown in Equation 3.3, the enthalpy of the reaction terms includes gasoline, oxygen and nitrogen. The values for the enthalpy of formation for these species were retrieved from thermodynamic tables [10] and multiplied by the number of moles of the chemical species according to the combustion equation shown in Equation 3.3. The enthalpy of the products was calculated in a similar manner.

The entropy terms are determined in a way that is similar to that of the enthalpy terms. For the reactants, the evaluation of the entropy terms requires the pressure of the substance. This is the partial pressure of the substance in the surroundings. The partial pressure of each of the products was found by multiplying the total pressure (atmospheric in this case) by the molar fraction. The entropy used for the gasoline found in the reactants was found by looking up the value of absolute entropy for octane in a thermodynamic table [10]. The product equations required the molar fractions, which are the fraction of the substance that exists in the atmosphere. The mole fractions of gas species in the environment were assumed to be:

$$y_{CO_2} = .000375$$

$$y_{H_2O} = .008$$

$$y_{O_2} = .209$$

$$y_{N_2} = .782625$$

The computation of the variables H_R, H_P, S_R, S_P and T_O allows for the computation of the specific availability in octane according to Equation 3.6. The specific availability of gasoline was calculated from this equation as 5,433,106 kJ/kmol or 47,565 kJ/kg.

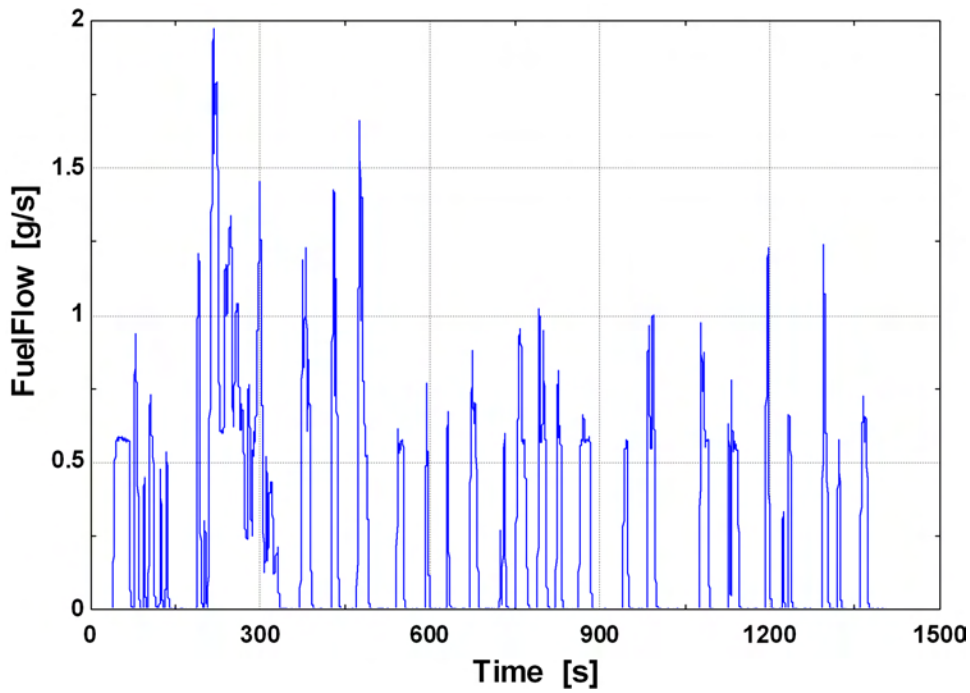

Figure 3.4: Mass Flow Rate of Fuel from the Prius data

Next, the availability rate of the fuel was calculated for the driving cycle of the Prius using Equation 3.5. The mass flow rate of fuel, $\dot{m}_{Fuel}$, which is included in the Prius data, was used in conjunction with the specific availability to find the availability rate of fuel. The mass flow rate of the fuel from the Prius data is plotted in Figure 3.4.

The specific availability of the fuel is a constant value. Therefore, the availability rate for the fuel calculated from Equation 3.5 reflects the same trends as the mass flow data. The integrated value of the availability rate over the driving cycle was calculated from these data to be 13724 kJ, which is useful for comparison purposes when examining the availability in the exhaust and engine coolant.

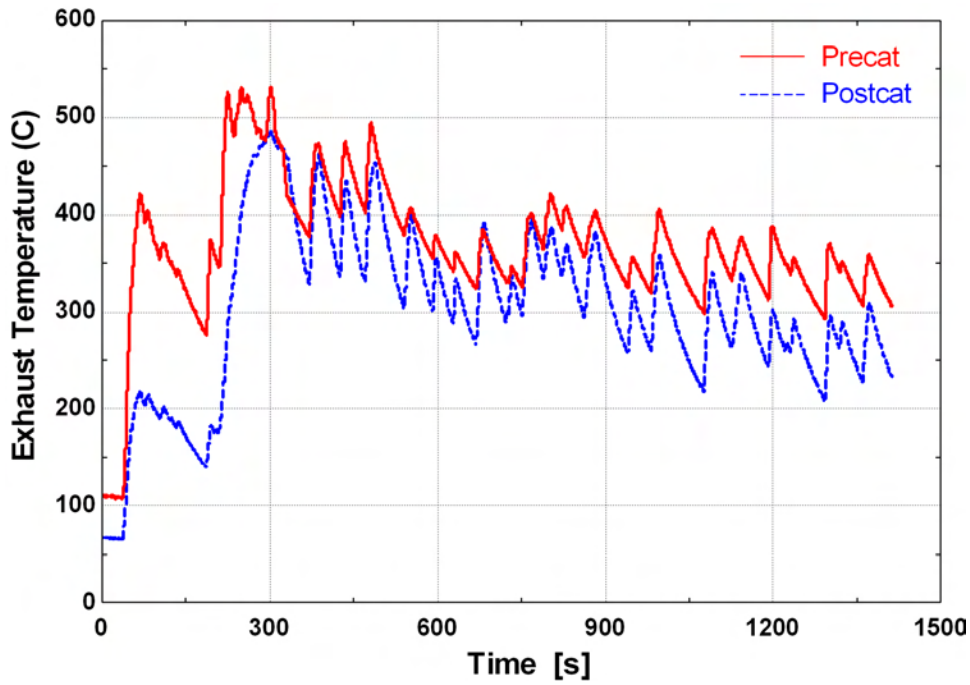

Figure 3.5: Exhaust Gas Temperatures prior to the catalytic converter (Precat) and after the catalytic converter (Postcat)

3.3.2 Availability of Exhaust

The availability in the exhaust was computed using the measured temperature and the mass flow rate of the exhaust gases and applying them to the specific availability and availability rate equations. The Prius data include three different temperatures in the exhaust system. The temperature readings were taken prior to, after and between the catalytic converters. These exhaust temperatures were taken with type K thermocouples that measured the temperatures of the exhaust gas inside the exhaust gas pipe. The temperatures between the catalytic converters are similar to the temperatures prior to the catalytic converters, so they will provide similar results in this analysis. Therefore, only the temperatures prior to and after the catalytic converter (Precat and Postcat, respectively) will be considered in the availability analysis. Figure 3.5 is a plot of these temperatures from the Prius data.

The availability of each of the gas species in the products of the combustion equation

Table 3.2: Integral of Availability of the Exhaust with respect to time

Location in Exhaust	$\int \dot{\Psi} dt$ **(kJ)**
Precat	1176
Postcat	944.6

shown in Equation 3.3 were evaluated individually. The mass flow rate was compared for each of the gas species in the products of the combustion equation. This mass flow rate is denoted as $\dot{m}_i$, where the subscript i refers to the specific gas that is being evaluated. These mass flow rates and the associated specific availability were applied to Equation 3.5 to find the availability rate for each species, which were then summed to find the availability rate of the exhaust gas.

Using the data and assumptions described above, the availability rate was computed at the Precat and Postcat locations. The Precat data were typically near 3.5 kW and the Postcat data were near 2.5 kW. The plots of the availability rate across the driving cycle have the same trends as the mass flow rate of fuel shown in Figure 3.4, and therefore are not shown here. Instead, a more important value is the integral of the availability rate over the driving cycle was calculated. The integrated values give a way to compare the results of the data analysis. The integrals of the availability rates for the Precat and Postcat locations in the exhaust stream are shown in Table 3.2.

There were many assumptions that were made in order to obtain these results. For example, the pressure of the exhaust stream was assumed to be at ambient pressure, but the addition of a heat recovery system in the exhaust will most likely increase the pressure in the exhaust pipe. Therefore, a sensitivity analysis was performed by calculating the integrated availability as the pressure in the exhaust increased from ambient pressure to 50% above ambient pressure. The results are shown in Figure 3.6.

As shown in Figure 3.6, the availability values increase by approximately 15% as the

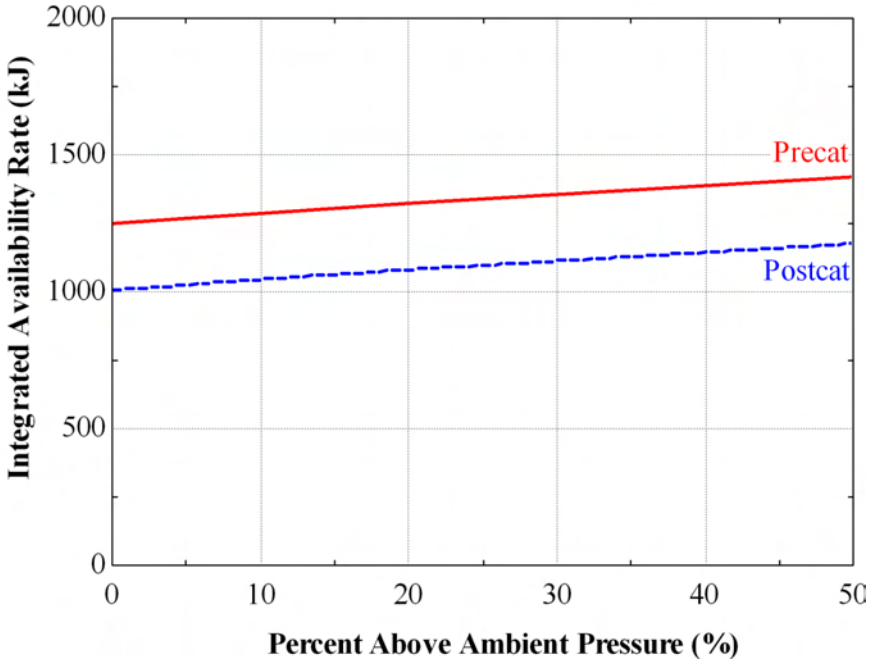

Figure 3.6: Sensitivity of the Pressure in the Exhaust on the Availability in the Exhaust

pressure in the exhaust is increased from ambient pressure to 50% above ambient pressure. The sensitivity analysis of the pressure shows that pressure differences have some effect on the availability, but the original assumption appears to be adequate. However, implementing a heat recovery device into the exhaust system will increase this pressure, possibly significantly which will have effects on the engine performance as discussed in detail in Chapter 4.

3.3.3 Availability in the Engine Coolant

The specific availability and availability rate in the coolant were calculated from the temperatures in the coolant and the mass flow rate of the coolant according to Equations 3.4 and 3.5, respectively. The Prius data include temperatures of the coolant in and out of the engine, which are shown in Figure 3.7. The specific availability was found by applying these temperatures to Equation 3.4.

Since the mass flow rate of coolant was not measured in the Prius data, a correlation was

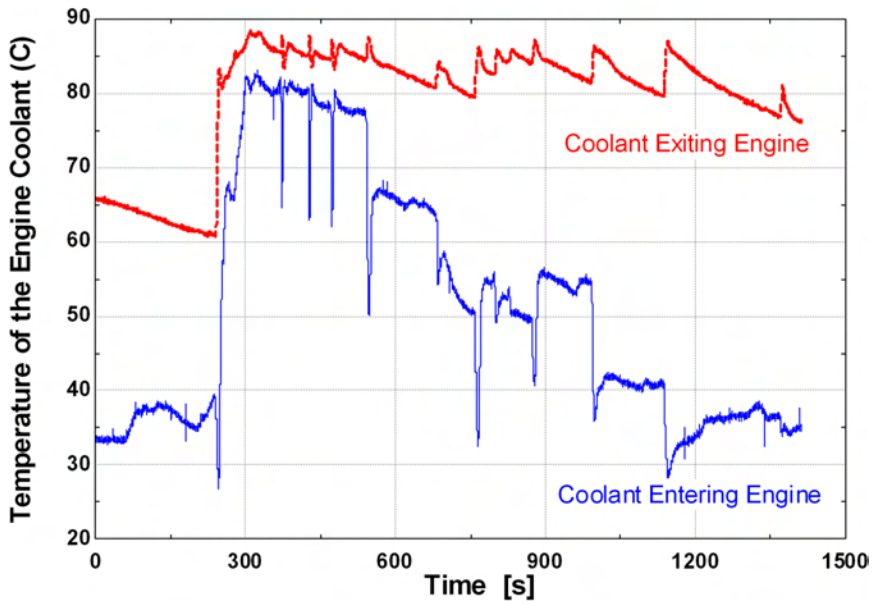

Figure 3.7: Temperature of the Engine Coolant from the Prius Data

developed to predict the flow rate based on the values computed in the energy balance. The water pump is driven by the engine when in operation, therefore causing the coolant flow rate to be dependent on the engine speed. Locations of relatively constant engine speed were found within the dataset. The engine speed for each of these locations was averaged over the timeframe where the engine speed remained relatively constant. This was correlated with the average of the coolant flow rate predicted from the energy balance over the same time frame. The plot of the engine speeds and coolant mass flow rates is shown in Figure 3.8.

As shown in Figure 3.8, an approximately linear trend relating the coolant mass flow rate and engine speed could be found. The mass flow rate of coolant predicted from the correlation and specific availability of coolant were used to equate the availability rate of coolant for the entire set of the Prius data, in a manner similar to that of the exhaust. The resulting availability rate was integrated over the driving cycle to obtain the availability for the entire cycle. This value can be easily compared to the other results in this analysis.

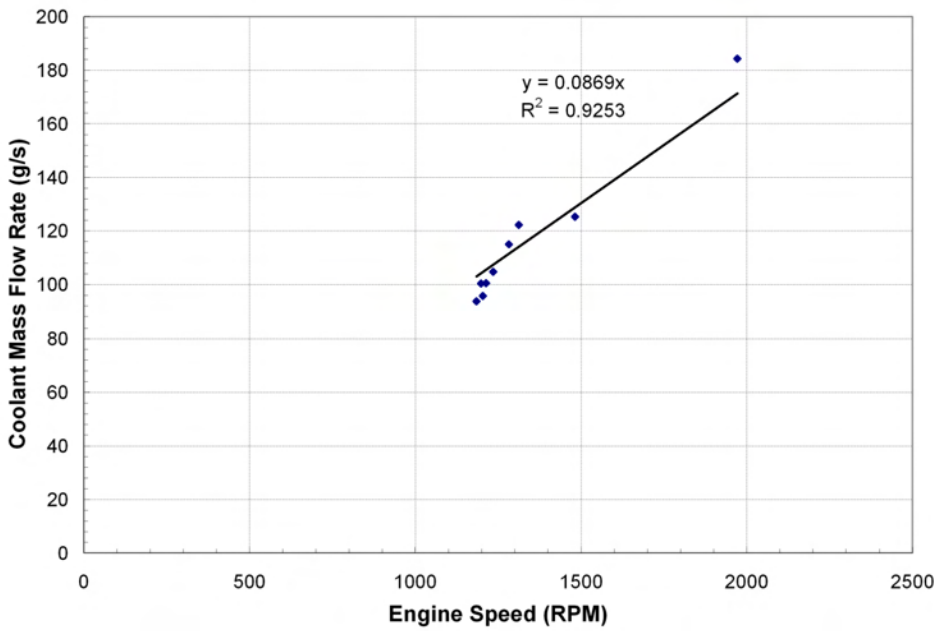

Figure 3.8: Correlation of Coolant Mass Flow Rate and Engine Speed

3.3.4 Availability Comparison

The integrated values of availability over the driving cycle have been calculated for the fuel, exhaust and coolant. These values were computed to compare the availability at each of the effluents and determine a percentage of fuel availability that exists at each of these locations. The comparison of the availability computed over the driving cycle for the coolant and exhaust and the associated percentage of fuel availability is shown in Table 3.3.

The data in Table 3.3 show that the availability in the coolant and the availability in

Table 3.3: Comparison of the Availability in the Coolant and Exhaust

	$\int \dot{\Psi} dt$ **(kJ)**	**Percent of Fuel**
Fuel/Air	13724	
Coolant	1222	8.9%
Exhaust Gas Precat	1176	8.6%
Exhaust Gas Postcat	944.6	6.9%

the exhaust are very similar to one another. The results show that there is 8.9% of the fuel availability in the coolant and 8.6% in the exhaust. Even though there was a significantly larger amount of energy in the coolant, the quality of this energy flow is low when compared to the exhaust. This is reflected in the relatively similar values of availability for the coolant and exhaust flows.

3.4 Finite Time Analysis

The availability analysis found the maximum theoretical work that could be obtained if a reversible heat power cycle was placed between the heat source and heat sink. The availability analysis doesn't consider the irreversibilities that occur in a practical heat engine that is placed between the heat source and heat sink. For a system to produce the amount of power found in the availability analysis, an infinite amount of time is required to execute a reversible cycle. This is obviously not a practical scenario, thus providing motivation for the investigation of the power output that can be achieved in a finite amount of time.

The efficiency for a Carnot cycle is dependent on only the temperatures of the heat source and heat sink. This completely reversible process assumes infinitesimal temperature differences between the heat engine and reservoirs to be reversible. For a cycle to be practical, it must take a finite amount of time to complete, thus reducing the efficiency to a point lower than the Carnot efficiency. It is of interest to find the efficiency at the maximum power, as the power output is generally what is desired. The investigation of finite time thermodynamics, specifically the efficiency at maximum power, has been studied previously [38]. This analysis assumes that all irreversibilities occur in the transfer of heat to and from the power cycle. The power cycle itself is considered reversible. For a cycle to have a power output greater than zero, there must be temperature differentials between the heat source/heat sink and the power cycle, as shown in Figure 3.9 [2].

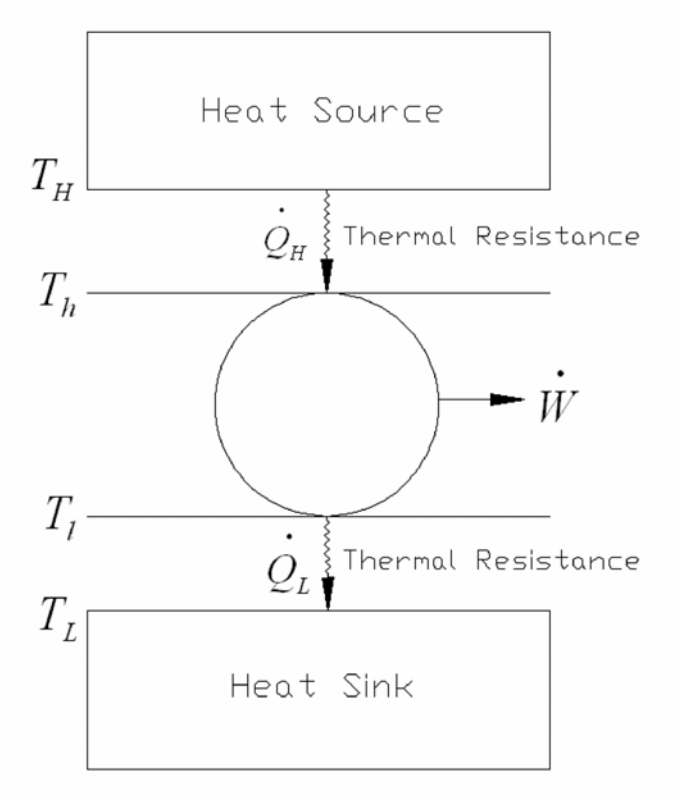

Figure 3.9: Carnot Cycle Operating between a Heat Source and Heat Sink [2]

As shown in Figure 3.9, a temperature difference between the heat source and power cycle has been created to introduce a driving force for the thermal energy. In a similar manner, a temperature difference has been introduced between the heat sink and the power cycle. This will result in a positive overall output power ($\dot{W}$). The heat transfer rates between the heat source/heat sink and the power cycle are a function of the effectiveness(ϵ), heat capacity rate($\dot{C}$) and temperature difference. The heat transfer rates on the hot ($\dot{Q}_H$) and cold ($\dot{Q}_C$) sides of the power cycle are shown in Equations 3.7 and 3.8, respectively. The following equations include the subscripts, H and L, which respectively stand for the heat source side and heat sink side of the power cycle.

$$\dot{Q}_H = \epsilon_H \dot{C}_H (T_H - T_h) \tag{3.7}$$

$$\dot{Q}_L = \epsilon_L \dot{C}_L (T_l - T_L) \tag{3.8}$$

The temperature difference shown in Equations 3.7 and 3.8 is the difference between the heat source or heat sink temperature and the temperature of the power cycle on the respective side of the power cycle. The temperatures on either side of the power cycle are denoted with the lower case letter of the specific side of the power cycle. An energy balance on the power cycle yields Equation 3.9.

$$\dot{W} = \dot{Q}_H - \dot{Q}_L \tag{3.9}$$

Equation 3.9 shows that the power output is equal to the difference in the heat transfer from the heat source and the heat transfer to the heat sink. As stated previously, the power cycle itself is considered to be completely reversible, thus allowing the application of the Carnot efficiency to be applied as in Equations 3.10 and 3.11.

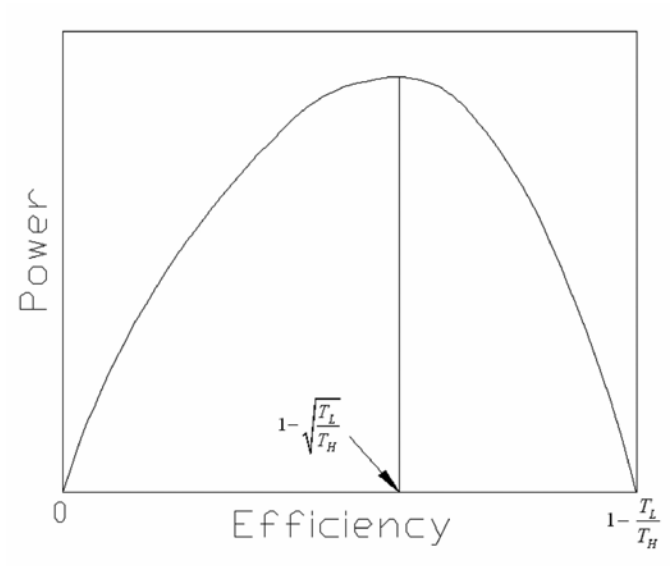

Figure 3.10: Power Output versus Efficiency [2]]

$$\eta = \frac{\dot{W}}{\dot{Q}_H} \tag{3.10}$$

$$\eta = 1 - \frac{T_l}{T_h} \tag{3.11}$$

Equation 3.10 is the definition of efficiency: the work output from the system divided by the heat input to the system. Equation 3.11 is the Carnot efficiency applied to the temperatures immediately surrounding the reversible power cycle. The five above equations (Equations 3.7 through 3.11) contain the following twelve variables: $\dot{Q}_H$,$\dot{Q}_L$,ϵ_H ,ϵ_L ,$\dot{C}_H$,$\dot{C}_L$,T_H ,T_L ,T_h ,T_l ,$\dot{W}$ and η. Assuming six of these variables can be determined from the conditions of the specific system that is to be analyzed (ϵ_H ,ϵ_L ,$\dot{C}_H$,$\dot{C}_L$,T_H ,T_L), the remaining six variables need one more equation to be solved. Using the above five equations, the efficiency was varied from zero to the Carnot efficiency. A plot of the cycle power versus the efficiency resulting from this analysis is shown in Figure 3.10.

This analysis showed that the efficiency (η) at the maximum power point for a given

cycle is only dependent on the temperatures of the heat source and heat sink, as shown in equation 3.12.

$$\eta = 1 - \sqrt{\frac{T_L}{T_H}} \tag{3.12}$$

The efficiency at the maximum power point shown in Equation 3.12 has been shown to be a very good approximation for many different types of cycles [2] and that the efficiency at maximum power is independent of the power cycle that is used. The efficiency calculated from this analysis is a very good estimate of the efficiency that can actually be achieved for the given conditions, which provides a tool that is very simple, yet quite accurate for an initial system analysis.

Equation 3.12 provides the sixth equation for the finite time analysis. This leaves six equations and six unknowns, which allows all of the variables to be determined.

The finite time approximation was utilized in the analysis of the Prius data. The temperatures of the coolant and exhaust streams were applied to the T_H variable in the above system of equations. The hot side heat capacity rate, $\dot{C}_H$, was found by taking the product of the mass flow rate of the coolant/exhaust (from the Prius data) and the specific heat of that substance at a temperature, T_H. The cold side of the cycle is assumed to be similar to the radiator cooling system that is typical in automobiles today. This results in a lower effectiveness due to the fact that a gas (air) is the cooling mechanism. The temperature of the heat sink is the ambient temperature. The following assumptions were made to complete the analysis.

$$\epsilon_H = .5$$

$$\epsilon_L = .5$$

$$T_L = 298K$$

These variables are validated with a sensitivity analysis later in the report. Additionally, the heat capacity rate on the cold side ($\dot{C}_L$) needs to be determined. This is defined as the product of the mass flow rate and the specific heat. The cold side fluid is air, so the specific heat can be determined based on the temperature of the heat sink. The fluid used for this analysis is a 50-50 mixture of ethylene glycol and water. The mass flow rate is dependent on the velocity of the vehicle. The relative motion of the vehicle with respect to the surrounding air creates a dynamic pressure that forces air through the radiator. This pressure difference, ΔP , is shown in Equation 3.13.

$$\Delta P = \frac{\rho_{air} V_{vehicle}^2}{2} \tag{3.13}$$

Equation 3.13 includes the density of air and velocity of the vehicle which are denoted as ρ_{air} and $V_{vehicle}$, respectively. The pressure drop in Equation 3.13 is set equal to the friction pressure drop ($\Delta P_{friction}$) experienced as the air flows through the radiator as shown in Equation 3.14. This gives a relationship between the velocity of the vehicle, which is included in the Prius data, and the velocity of air through the radiator.

$$\Delta P_{friction} = f\left(\frac{L}{D_h}\right)\rho_{air} V_{rad}^2 \tag{3.14}$$

Equation 3.14 includes the variable f, which is the friction factor. The friction factor is dependent on the Reynolds number. The radiator is assumed to be of plate-fin geometry, thus for laminar flow the friction factor can be found from the correlation for laminar flow between flat plates (Incropera and DeWitt, 2002). For turbulent flow, the Churchill correlation was used (Churchill, 1977). The variables, L and D_h , found in Equation 3.14 are the length of the radiator and the hydraulic diameter, respectively. These variables are dependent on the geometry of the radiator. The radiator geometry was defined to be 50 cm x 24 cm x 10 cm (WxHxL). The fin pitch and fin thickness were defined to be 1.2 mm and .2 mm, respectively.

Table 3.4: Finite Time Thermodynamic Analysis

	$\int \dot{\Psi} dt$ **(kJ)**	**Percent of Fuel**
Fuel/Air	14106	
Coolant	165.4	1.2%
Exhaust Gas Precat	226.7	1.6%
Exhaust Gas Postcat	154.2	1.1%

These geometrical definitions allow for the calculation of the length and hydraulic diameter variables in Equation 3.14. Based on the geometry defined above, the cross sectional area (A) that the air flows through as it passes through the radiator is calculated as .1 m^2. This value is modified in the sensitivity analysis to see how it affects the results of the finite time analysis. The definition of the flow area and the calculation of the velocity of air through the radiator allow the mass flow rate to be computed. This is shown in Equation 3.15.

$$\dot{m}_c = \rho_{air} V_{rad} A \tag{3.15}$$

The calculation of the mass flow rate of air allows the heat capacity on the cold side ($\dot{C}_L$) to be calculated. This is the final variable that is necessary for the finite time analysis to be completed. These variables were then applied to the Equations 3.7 - 3.12, resulting in six equations with six unknowns. This process was applied to the coolant, exhaust precat and exhaust postcat data and the work output over the Prius data was found by evaluating the system of equations for each of the data sets. The work output values were then integrated over the Prius data and compared to the integrated value of fuel to find a percentage of energy that could realistically be recovered. These results are shown in Table 3.4.

As discussed previously, the calculation of the values in Table 3.4 required the estimation of the ambient temperature, the cross sectional area of the radiator and the effectiveness on both the hot and cold stream sides. A sensitivity analysis was performed on each of these

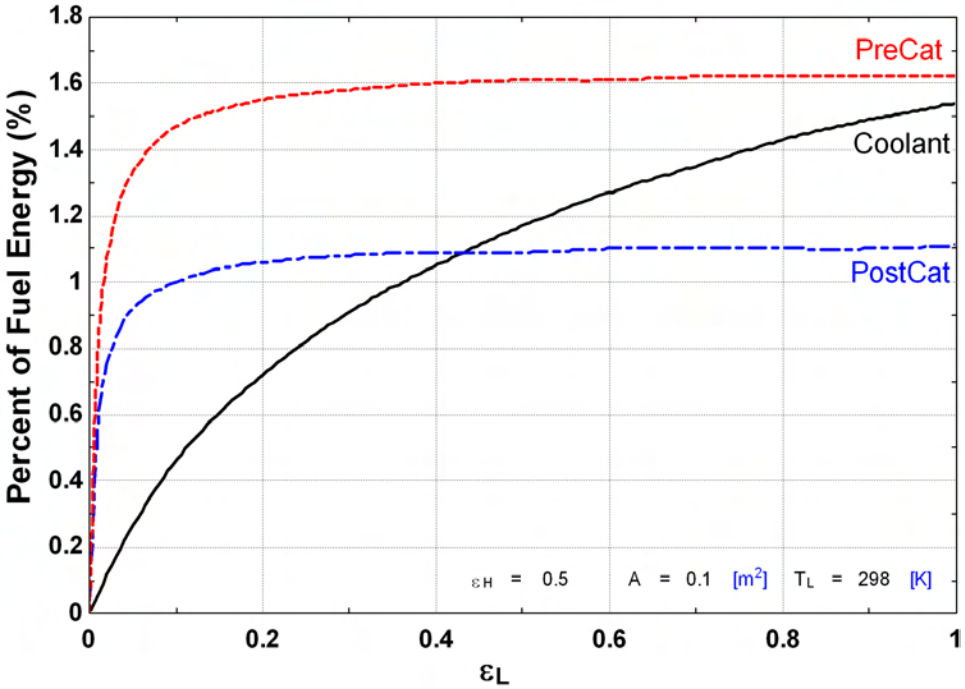

Figure 3.11: Sensitivity Analysis on the Cold Side Heat Exchanger Effectiveness

parameters to see how their variation affects the integrated work output shown in Table 3.4. In the sensitivity analysis, each of the variables were studied independently. As one of the parameters was varied, the remaining variables were kept constant at the values originally assumed. This allows the investigation of the effects that each of the variables independently has on the work output of the system.

The effectiveness on the cold stream side was assumed to be 0.5, due to the limitations imposed by a heat exchanger containing a gas as one of the heat transfer fluids. This value was varied down to a lower limit of 0, which allows the effects of 0.5 being an overestimate to be investigated. The range of data studied includes values up to 1 for the cold side effectiveness to show how the effects of making improvements to the heat exchanger will affect performance.

Figure 3.11 shows the percent of fuel values calculated for the finite time analysis as

a function of the cold side heat exchanger effectiveness. The plot shows that as the heat exchanger effectiveness is increased, the amount of energy recovered increases as well. The variation of the cold side heat exchanger effectiveness from 0 to 1 had drastic results on the recovered energy from the coolant. A large increase in the exhaust values occurred in the 0 - 0.1 range of effectiveness values. Raising effectiveness values to values larger than 0.3 had minimal effects on the percent of fuel energy recovered. On the coolant side, a continuous rise occurs as the effectiveness value is increased. Therefore, the investigation of increasing the cold side heat exchanger effectiveness appears to be worth looking into.

With a good design, the heat exchanger effectiveness on the hot side can reach high values due to the given boundary conditions and fluids that are used. This resulted in an assumption of 0.5 for the hot side heat exchanger effectiveness. For the actual design, this value may be different, so the sensitivity analysis varied the hot side heat exchanger effectiveness from 1 down to 0. The effect of this variation on the values obtained in the finite time analysis is shown in Figure 3.12.

As shown in Figure 3.12, the higher heat exchanger effectiveness values result in higher percentages of energy recovered. The coolant had a similar trend with the variation of the hot side effectiveness that it did with the cold side effectiveness. An analysis for a liquid to two-phase heat exchanger using Flatplate select showed that an effectiveness of 0.5 or higher is possible for the coolant side conditions [39]. For the exhaust, the variation of the hot side heat exchanger effectiveness had a linear trend with the percent of fuel recovered, which has significant effects on the exhaust data. Chapter 5 includes effectiveness calculations for a heat exchanger in the exhaust stream which show that an effectiveness of 0.5 can be attained. Therefore, it would be beneficial to design the system in a manner that maximizes the heat exchanger effectiveness on the hot side.

The cross sectional area, and thus size of the radiator, was assumed in the calculation of the values in Table 3.4. The sensitivity analysis investigated the variation in the cross

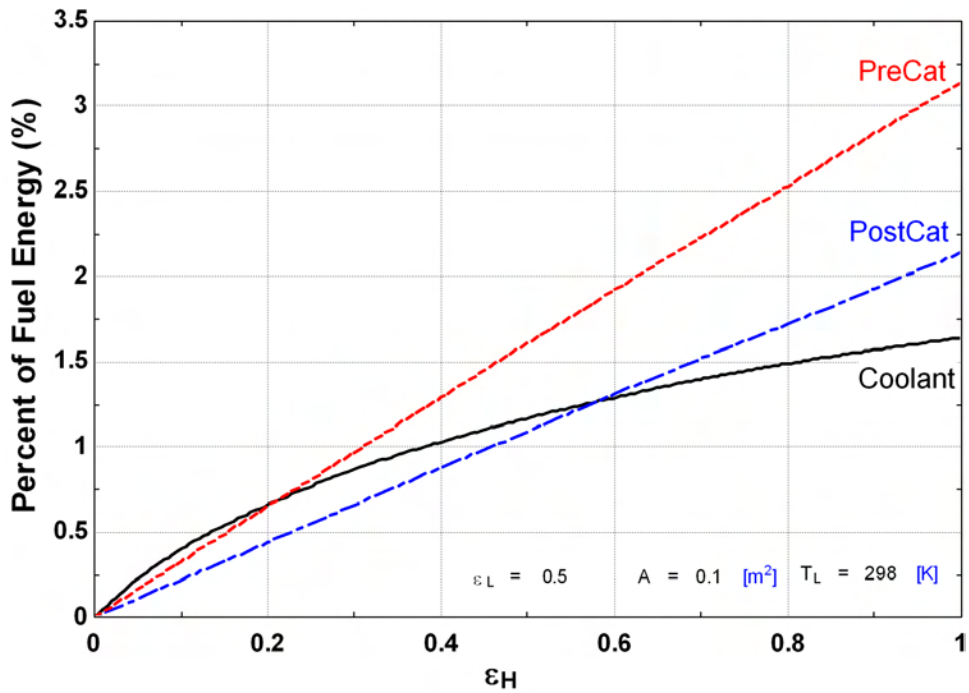

Figure 3.12: Sensitivity Analysis on the Hot Side Heat Exchanger Effectiveness

sectional area and how it affects the values of energy recovered. The results of this sensitivity analysis are shown in Figure 3.13.

Figure 3.13 shows that as the cross sectional area of the radiator is increased, the amount of energy that is recovered increases as well. Obviously, there are space constraints in an automobile, which limit the size of the radiator. The slope of the plots decrease as the area is increased, limiting the energy recovered as the cross sectional area is increased. The best solution for this system is to find a point where the size of the radiator is within the space constraints of the vehicle, yet still realizing a significant amount of energy recovered. This point appears to be near 0.1 m^2 for the exhaust as the slope becomes relatively constant at areas larger than this. The slope of the coolant doesn't diminish as quickly, leaving open the possibility for increasing the area even more.

The ambient temperature was assumed to be $298K(25°C)$ for the finite time analysis.

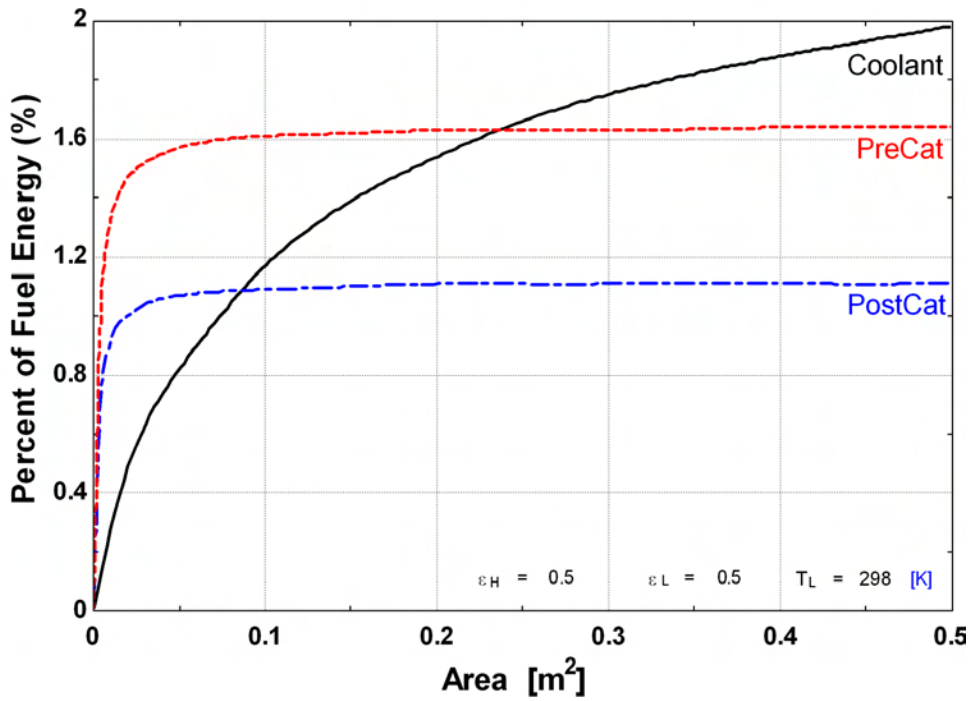

Figure 3.13: Sensitivity Analysis on the Cross Sectional Area of the Radiator

Geographical location and weather conditions dictate the value of the ambient temperature, the variation of which can be quite significant. The sensitivity analysis examined the effects of the change in ambient temperature on the amount of recovered energy. These results are shown in Figure 3.14.

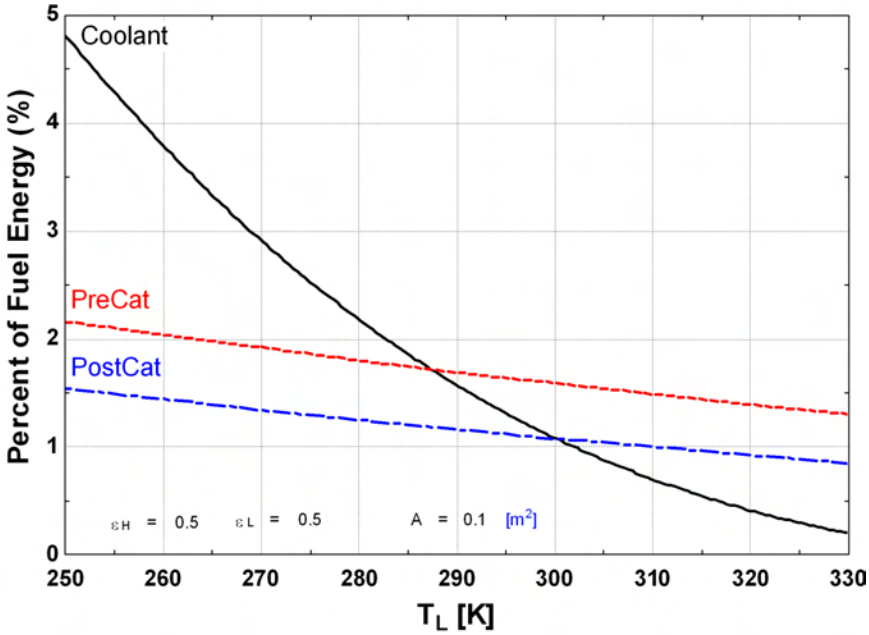

Figure 3.14: Sensitivity Analysis on the Ambient Temperature

As shown in Figure 3.14, an increase in the ambient temperature results in a significant decrease in the amount of energy recovered from all of the effluents. The power cycle will recover more power when the heat sink is at a lower temperature. The ambient temperature has an effect on both the coolant and the exhaust, however the coolant has a much higher sensitivity to the ambient temperature, as seen from the larger slope. There isn't a way to control this, other than choosing the geographical location of the vehicle operation. This does give an idea of the dependence of the energy recovery system performance on the local climatic conditions.

It is of interest to see how the energy recovered from the coolant behaves as the temperature of the coolant in the system is raised. There are many other factors that need to be studied before such a change could be made, such as combustion effects, boiling of the fluid, use of other fluids and material failure. For this analysis, the motivation is to see how much of a difference a raised coolant temperature will make on the total energy recovered. If the amount of energy that can be recovered significantly increases, it would provide motivation to further explore these other issues so that such a device could be designed. For the analysis in Table 3.4, the coolant temperatures were taken from the Prius data. These temperatures were typically in the $80°C$ range, so the sensitivity analysis investigated temperatures in the $60°C$ to $150°C$ range. The results of this sensitivity analysis are shown in Figure 3.15.

Figure 3.15 shows that the percentage of fuel energy recovered significantly increases as the coolant temperature is increased. Although there are a significant number of additional variables that this would affect in an internal combustion engine, the results show that they may be worth investigating.

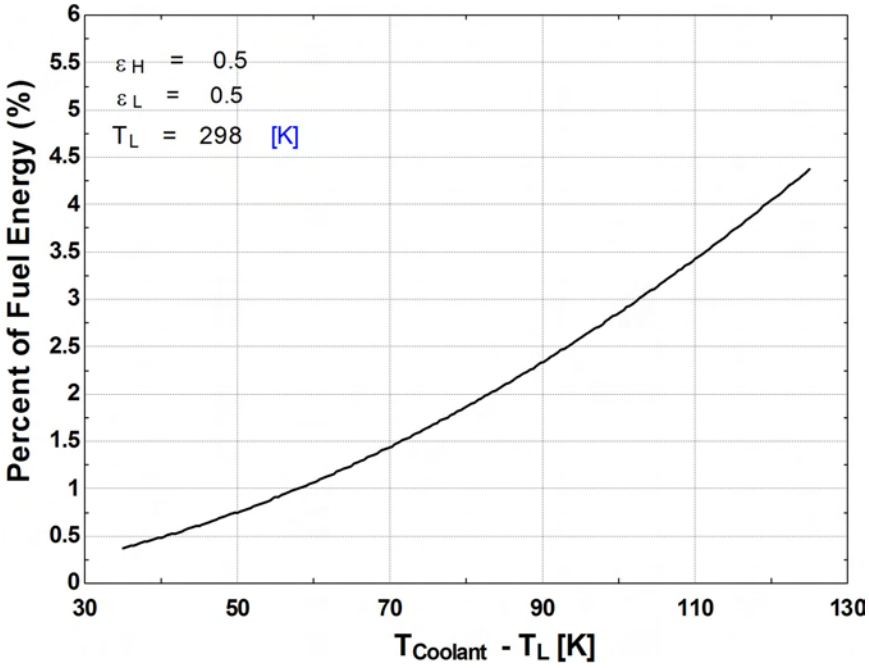

Figure 3.15: Sensitivity Analysis on the Coolant Temperature

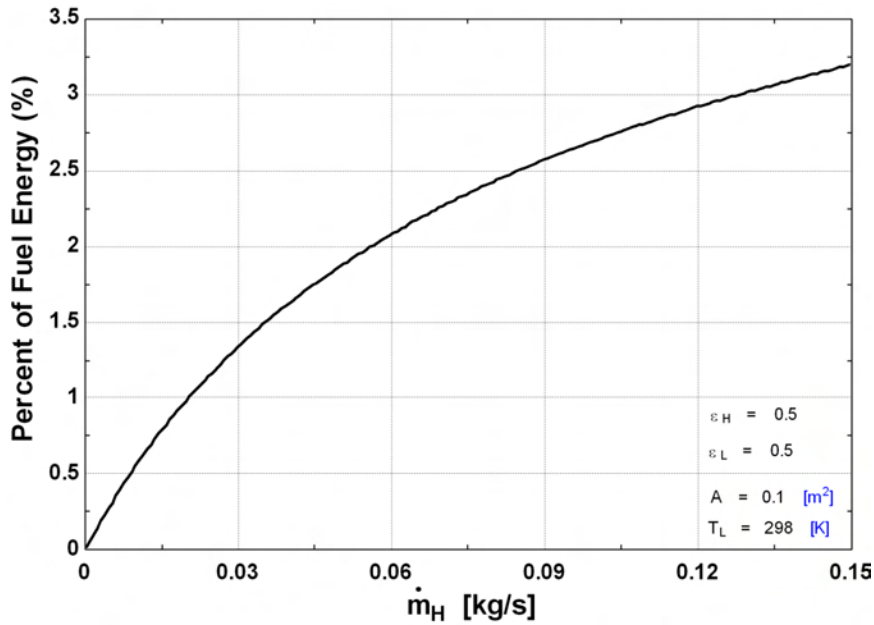

Figure 3.16: Sensitivity Analysis on the Coolant Mass Flow Rate

Finally, the investigation of the mass flow rate of coolant was performed. For all of the above analysis, the mass flow rate of coolant that was used was derived from the correlation with engine speed that was obtained out of the energy balance. This had an average value of 0.025 $\frac{kg}{s}$. This investigation varied the coolant flow rates to constant values in the 0 to $0.15\frac{kg}{s}$ range. The results are shown in Figure 3.16.

Figure 3.16 shows that as the mass flow rate of coolant increases, the percent of fuel energy recovered also increases. As the flow rate is increased, the increase in fuel energy recovered decreases. This leads to an optimization of pumping power and recovered energy that must be done to determine the best flow rate for a given system.

3.5 Discussion of Results

The main goal of this analysis was to compare the availability that remains in each of the various effluents. Examining the energy balance reveals that the energy coming into the system is distributed among the exhaust, coolant, power and miscellaneous heat losses. The energy that provides the power to the crankshaft is not of interest, as this is already going to useful work. The miscellaneous heat losses can not be practically recovered and therefore do not provide any useful availability. This leaves the availability in the coolant and the exhaust, both of which have been determined. The comparison of the availability in the coolant and exhaust yields a direction for future heat recovery analysis.

The method of extraction for the exhaust will be important, as heat transfer from a gas is difficult. Additionally, the effects that a heat recovery device will have on the exhaust gas temperatures in after treatment devices must be considered. The exhaust gas temperatures must be high enough at the location of the after treatment devices to ensure the effectiveness of the after treatment operation. If the desired level of effectiveness cannot be reached, then the heat recovery device must be placed after the catalytic converters where the availability has been diminished to 6.9%.

The finite time analysis gives realistic percentages that can be recovered from the coolant and exhaust. This analysis showed that 1.6% of the fuel energy can practically be recovered in the exhaust, while 1.2% can be recovered from the coolant. However, a sensitivity analysis showed that raising the temperature of the coolant or increasing the mass flow rate of the

coolant will allow the recovered energy from the coolant to be comparable or greater than that of the exhaust. The values that can be recovered from the coolant and exhaust are thus both significant and therefore should both be investigated further. The relatively similar amounts of recoverable energy in the coolant and exhaust, reveals that the best option could be using a heat recovery system that takes advantage of both of these heat sources. A combination of the use of these sources could yield a recovery of over 5% of the fuel energy.

3.6 Conclusions

As the use of energy becomes of greater concern, efficiency in automotive vehicles is becoming increasingly important. A significant amount of energy is lost through waste heat in the exhaust and coolant. An energy balance and availability analysis was performed using data from a 2004 Toyota Prius. A hybrid vehicle was chosen as the recovered energy could easily be converted to useful energy that is stored in the battery. The results of this analysis provide direction for the best locations and methods of heat recovery that should be investigated.

The energy balance reveals that the Prius has a significant amount of energy in the coolant (48.8% of fuel) and much less in the exhaust (13.9% of fuel). These numbers deviate from typical values due to the use of the Atkinson cycle engine in the Prius. However, the availability analysis revealed that the coolant and exhaust contain similar quantities of availability, 8.9% and 8.6% of fuel availability, respectively. A finite time analysis gave a realistic recovered power estimate of 1.6% and 1.2% in the exhaust and coolant, respectively. However a redesign of the coolant system could result in a larger portion of the energy being recovered.

The results of this analysis show that both the exhaust and coolant should be explored in future heat recovery analysis. Although the coolant has a large portion of the energy, the relatively low temperatures limit the availability that exists in the coolant. The effects of

backpressure on the engine and temperatures in the after treatment devices must be taken into consideration when implementing a heat recovery device in the exhaust stream. Taking these issues into consideration a heat recovery device that utilizes the waste heat of the exhaust, coolant or combination of exhaust and coolant may be investigated.

Chapter 4

Recovering Waste Energy with a Turbine in the Engine Exhaust

4.1 Introduction

A method by which the waste energy in the exhaust can be recovered in a hybrid automotive power plant is by placing a turbine directly in the exhaust system. The exhaust stream drives the turbine, which can then be used to power a generator. The energy recovered by the generator can be used to charge the battery that exists in the hybrid automobile. The charging of the battery from the waste heat recovery turbine will increase the state of charge of the battery, which results in decreased time that the engine is used to charge the battery. The decrease of the use of the engine leads to a decrease in fuel consumption and exhaust emissions for given driving conditions.

A major limitation of the proposed implementation of the turbine in the exhaust stream is the effect of backpressure that will be imposed on the engine; any backpressure on the engine will reduce the performance of the engine. Therefore, the placement of a turbine in the exhaust stream is only a viable option if the power recovered from the turbine is greater than the reduction in power of the engine caused by the backpressure.

The backpressure effects imposed by the turbine are explored by GT-Power, an engine simulation program. A verification of the accuracy of the GT-Power model is first performed by comparing results to literature and a simple air standard model. GT-Power is then used to explore the feasibility of placing a turbine in the exhaust stream of a hybrid automobile. The specifications for a 2004 Toyota Prius were used in the GT-Power model, as this is the data of particular interest for this analysis. The backpressure effects are studied further by

varying the engine speed. Finally, a parametric analysis was performed on some of the engine parameters to determine the degree of influence that each parameter has on the results.

4.2 GT-Power

4.2.1 Background

The feasibility of the turbine in exhaust system was studied by creating a model in GT-Power [40], an engine simulation program. GT-Power includes built in templates for all components of an engine such as the battery, cylinder, manifold, catalytic converter, pipes, etc. An engine system is modeled by first assigning specific attributes to the templates so that they become objects that model the system components according to the desired specifications. These objects are then placed in the project map and are linked together in a manner that represents the engine system. The simulation of the engine system can then be performed, followed by an analysis of the results. The results of the engine simulation are viewed in an associated software program called GT-Post. The results include parameters such as the temperature, pressure, flow rate, efficiency, power, etc., throughout the system.

GT-Power simulations are based on one-dimensional gas dynamics. The simulations represent the combustion in the cylinders, the mechanical transfer of energy and the heat and flow through the piping and other components of the engine system. The fluid flow model uses the continuity, momentum and energy equations to obtain a solution. They are solved using a one-dimensional approximation, generally using mass flow, density and internal energy as the variables. Pipes are simulated by using various correlations for friction losses, pressure losses and heat transfer. Three dimensional conservation of momentum equations are used for flow splits. For flow connections, various correlations for orifices, throttles, pressure loss, discharge connections etc. are given. Heat exchangers are modeled from steady state experimental performance data.

The origin of the data obtained from GT-Power that is of interest for the calculations in this report was investigated. It is of importance to understand how these data are computed to verify the accuracy of the model. The engine power was found from the engine crank train template. The engine crank train template models the crankshaft and crank slider mechanisms that are converting the power from the pressures in the engine cylinders to the crankshaft output torque. The engine power, in kW, is calculated as shown in Equation 4.1.

$$EnginePower = (BTQ)(RPM)\left(\frac{2\pi}{60000}\right) \tag{4.1}$$

In this equation BTQ stands for the brake torque and RPM is the engine speed. The brake torque and associated equations are calculated as shown in Equation 4.2 and Equation 4.3 respectively.

$$BTQ = \frac{\oint T_b(t)dt}{\oint dt} \tag{4.2}$$

$$T_b(t) = T_s(t) - I_{ct}\omega_{ct}(t) \tag{4.3}$$

The instantaneous brake torque is given by the variable $T_b(t)$. The variable represented as I_{ct} in Equation 4.3 is the crank train inertia and the variable, $\omega_{ct}(t)$, is the instantaneous crank train acceleration. The shaft torque is symbolized as $T_s(t)$.

The backpressure that the turbine imposes on the engine is acquired from the turbine template. The pressure used for comparison in this analysis was the pressure at the inlet of the turbine. This pressure was constant from the exhaust ports of the engine cylinders up through the inlet of the turbine. The average inlet pressure was calculated as shown in Equation 4.4. The integration in Equation 4.4 is the integration over one cycle.

$$P_{in,ave} = \frac{\int \dot{m}P_{in}dt}{\int \dot{m}dt} \tag{4.4}$$

The speed of the turbine and the pressure ratio across the turbine were calculated for each time step in the simulation. These values are used along with other values that are looked up in the turbine map to solve for the pressures, temperatures, and the power of the turbine. The turbine map is a multidimensional map that includes turbine specifications. GT-Power allows users to create their own map or use the default. For the simulation that was performed in this analysis, the default map was used. The power of the turbine is calculated by the enthalpy change of the combustion products across the turbine. The enthalpy at the outlet and associated equations are shown in Equations 4.5 and 4.6.

$$h_{out} = h_{in} - \Delta h_s \eta_s \tag{4.5}$$

$$\Delta h_s = c_p T_{in}(PR^{\frac{\gamma-1}{\gamma}}) - 1) \tag{4.6}$$

The variable definitions in Equation 4.5 and Equation 4.6 are as follows.

$$h_{in} = inlet\ enthalpy$$
$$h_{out} = outlet\ enthalpy$$
$$\Delta h_s = isentropic\ enthalpy\ change$$
$$\eta_s = efficiency\ (.8)$$
$$PR = pressure\ ratio$$
$$C_p = specific\ heat\ of\ incoming\ gas$$
$$T_{in} = inlet\ total\ temperature$$
$$\gamma = specific\ heat\ ratio\ of\ incoming\ gas$$

The power of the turbine (P) is then calculated as shown in Equation 4.7, where $\dot{m}$ is the mass flow rate of the exhaust gases through the turbine.

$$P = \dot{m}(h_{in} - h_{out}) \tag{4.7}$$

4.2.2 GT-Power Backpressure Model

GT-Power has the option of analyzing the effects of modifying defined variables in the model. The parameters in the templates can be set as variables, which are then defined in the case setup menu for each case that is to be analyzed. The power of the turbine is dependent on the pressure drop across the turbine. The pressure drop is a function of the mass flow rate of exhaust through the turbine and the turbine orifice diameter. The mass flow rate of the exhaust stream is significantly dependent on the engine loading. Thus the orifice diameter variable defines the pressure drop over the turbine for a given engine cycle. The turbine template has a parameter defined as the 'orifice diameter'. A decrease in the orifice diameter results in an increase in the power output from the turbine and an increase in the pressure drop over the turbine. An increase in pressure drop in the exhaust system causes a decrease in engine performance. As the pressure drop increases, the engine power will decline and the turbine power will rise. Therefore, the summation of the engine power and the turbine power should have an optimum value at some orifice diameter.

The optimum orifice diameter was found by running the GT-Power simulation over a range of values for the orifice diameter. A specific value of the orifice diameter directly corresponds with a specific backpressure that is imposed on the engine for a particular engine configuration. Therefore, all plots were based on the engine backpressure.

A preliminary GT-Power model was created without the catalytic converter and muffler. The engine parameters used in this model were the default values set by GT-Power. The goal of the preliminary model was to see the effects of the backpressure on engine performance. The model was run at the default engine speed of 3600 rpm for these plots. The effect of

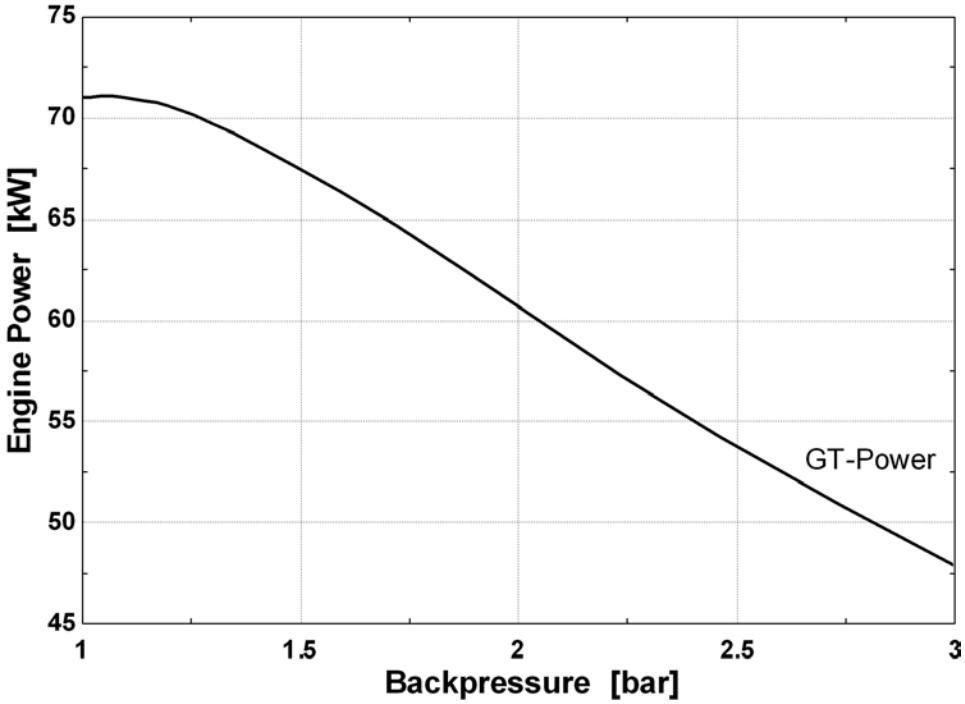

Figure 4.1: Engine Power vs. Backpressure for the Preliminary GT-Power Model at 3600 rpm (Default Engine Parameters and No Catalytic Converter or Muffler

the variation in the engine speed is studied later. All other variables were kept constant so that the effects of backpressure on the engine could be analyzed. The plot of engine power versus backpressure is shown in Figure 4.1.

The plot of engine power in Figure 4.1 shows that as the backpressure rises, it has an increasingly detrimental effect on the engine power. These results are encouraging as it appears that there is a negligible effect on the engine power for pressures in the 1.0 - 1.3 bar range. However for pressures larger than 1.3 bar, the engine power decreases dramatically. It would be difficult for a turbine to make up and exceed the power loss from the engine in this range. Therefore as long as the turbine causes a backpressure in the range where the backpressure effects are not very significant, there is will be opportunity for placing a turbine in the exhaust to be a viable option.

4.2.3 Comparison to Literature

In order to confirm the GT-Power estimate of engine backpressure effects on performance, the results were compared to models found in literature. Bolt, Bergin, and Vesper studied the effects of backpressure on the engine performance of a 1971 Ford 351-W V8 engine [41]. They found that the backpressure effects on engine performance have a significant dependence on engine speed and therefore collected data at various engine speeds. Adams found a similar dependence on engine speed as he looked at the effects of exhaust system design on engine performance [42]. Adams used experimental data from a Ford V-8 5.0L engine. Both of the studies found engine power as a function of backpressure.

The data from GT-Power, Bolt et al. and Adams were all taken from different engines. The engine power varies in magnitude between the data sets. A dimensionless engine power parameter was created from the data to allow for a comparison of the datasets. The nondimensional power parameter is defined as 1 at a backpressure of 1 bar. The plots shown in Figure 4.2 through Figure 4.4 are the comparisons of the data from the above literature sources to the results of the GT-Power model. These comparisons were made for 1000 rpm increments from 2000 rpm to 4000 rpm.

The Bolt, Bergin and Vesper dataset for 3000 RPM deviates from the Adams data and GT-Power model at higher backpressures [41, 42]. Otherwise, the comparison plots show that the general trends for all of the data are similar. There is overall agreement between the data from Bolt et al. and Adams with the GT-Power model, providing confidence in the current model. Overall, the results from GT-Power model are consistent with those of experiment studies on the engines of automobiles.

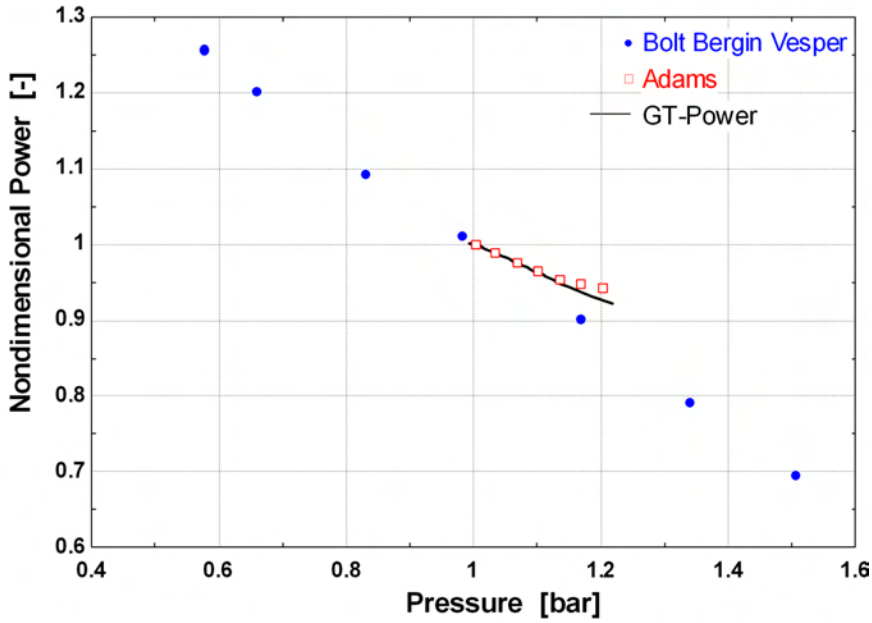

Figure 4.2: Comparison of Nondimensional Brake Horsepower Parameter and Engine Back-pressure at an Engine Speed of 2000 RPM

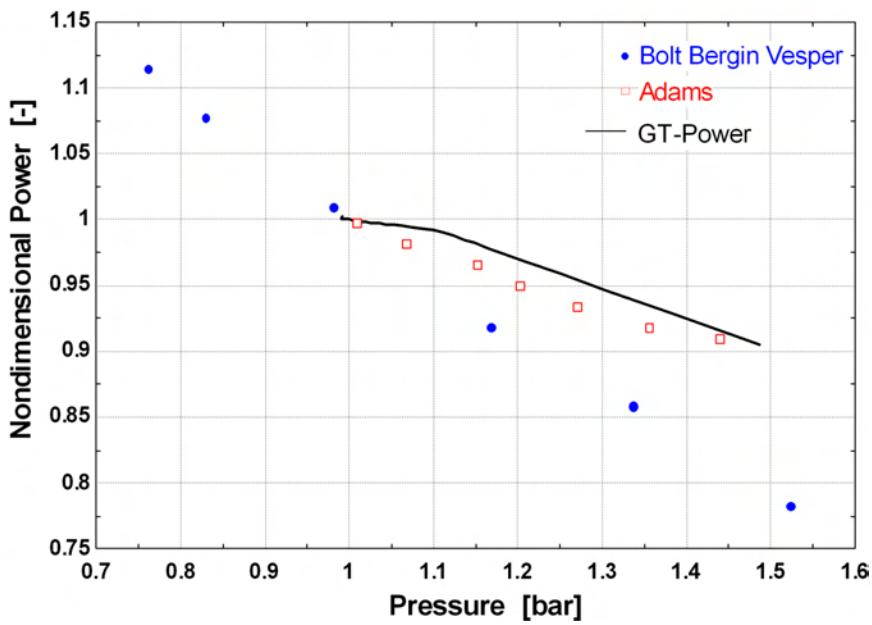

Figure 4.3: Comparison of Nondimensional Brake Horsepower Parameter and Engine Back-pressure at an Engine Speed of 3000 RPM

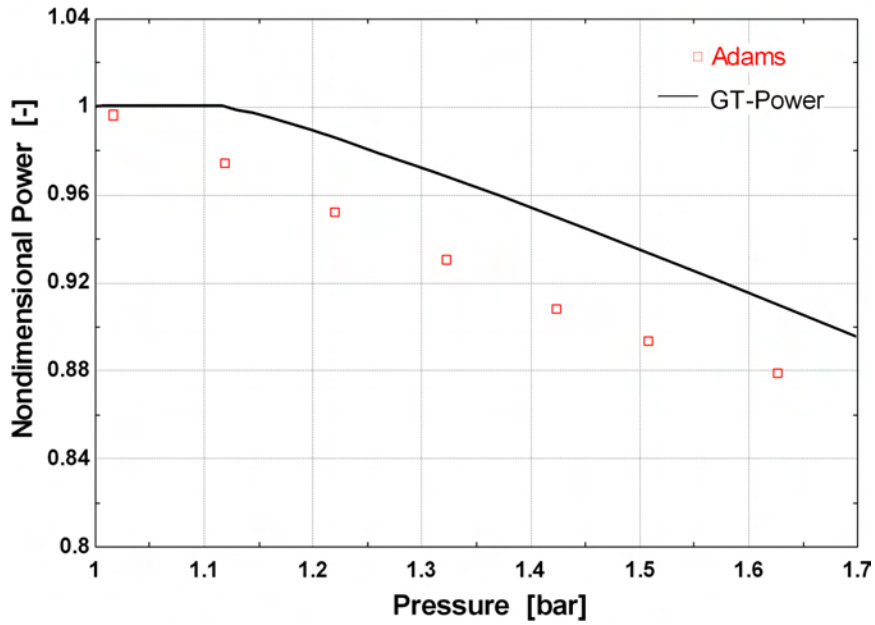

Figure 4.4: Comparison of Nondimensional Brake Horsepower Parameter and Engine Backpressure at an Engine Speed of 4000 RPM

4.2.4 Air Standard Otto Cycle Model

For additional verification the GT-Power backpressure model was compared with an air standard Otto cycle model developed in EES. An air standard analysis is a significant simplification of the processes that occur in an internal combustion engine, air is the working fluid of the system and it is modeled as an ideal gas. The combustion process in the air standard cycle is modeled as a heat transfer from an outside source and the exhaust stroke of the cycle is modeled as a heat transfer to the environment that occurs when the piston is at bottom dead center. In addition, all processes are considered to be internally reversible and to have constant specific heats. Although there are many simplifications and assumptions made with the air standard analysis, the overall trends remain the same. This provides a useful tool to confirm the validity of the GT-Power model.

The air standard analysis model created in EES is based upon the equations and methods

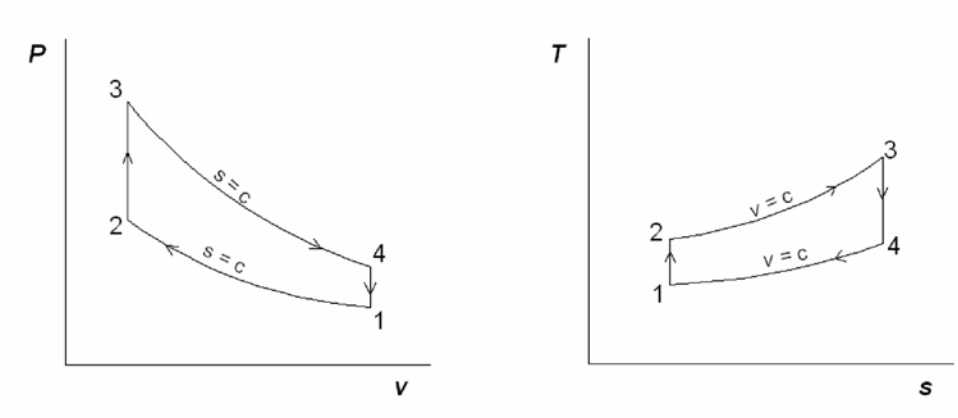

Figure 4.5: P-v and T-s diagrams of the air-standard Otto cycle

in Moran and Shapiro, 2000. The cycle contains four processes that model the work and heat transfer of an Otto cycle. The Pressure-Specific Volume and Temperature - Entropy plots for this process are shown in Figure 4.5.

The process from state 1 to state 2 models the isentropic compression of the air during the compression phase of the cycle. Process 2-3 is a heat transfer to the air while the air is constant volume when the piston is at top dead center. The process from state 3 to state 4 consists of an isentropic expansion of the air. Process 4-1 is a heat transfer rejection that occurs at a constant volume while the piston is at bottom dead center. These processes are assumed to only have either a work term or heat transfer term. For processes 1-2 and 3-4 there is work but no heat transfer whereas processes 2-3 and 4-1 contain heat transfer but no work. By reducing these energy transfers to a closed systems energy balance and neglecting kinetic and potential energy effects expressions for these energy transfers can be derived in terms of the internal energy (u) at each state, as shown in Equations 4.8 through 4.11.

$$\frac{W_{12}}{m} = u_2 - u_1 \tag{4.8}$$

$$\frac{W_{34}}{m} = u_3 - u_4 \tag{4.9}$$

$$\frac{Q_{23}}{m} = u_3 - u_2 \tag{4.10}$$

$$\frac{W_{41}}{m} = u_4 - u_1 \tag{4.11}$$

The net work of the cycle can then be computed as shown in Equation 4.12.

$$\frac{W_{cycle}}{m} = \frac{W_{34}}{m} - \frac{W_{12}}{m} \tag{4.12}$$

Relationships for the isentropic processes 1-2 and 3-4 are shown in Equations 4.13 and 4.14.

$$v_2 = \frac{v_1}{r} \tag{4.13}$$

$$v_4 = v_3 r \tag{4.14}$$

This model was used to create a relationship between the work output of the cycle and the backpressure imposed on the engine. A dimensionless work variable was computed so that results from the GT-Power model and the air standard model could be directly compared. The dimensionless work variable was defined as having a value of 1 for the dimensionless work at a backpressure of 1 bar. A plot of the comparison of the dimensionless work versus backpressure for the air standard analysis model and the GT-Power model is shown in Figure 4.6.

As shown in Figure 4.6, the GT-Power model contains an initial stage where the backpressure has a negligible effect on the work output. Following this initial stage, the effects of backpressure are quite dramatic. On the other hand, the air standard analysis model shows a linear dependence between the work output and engine backpressure. As discussed previously, the air standard analysis is a considerable simplification of the processes that occur

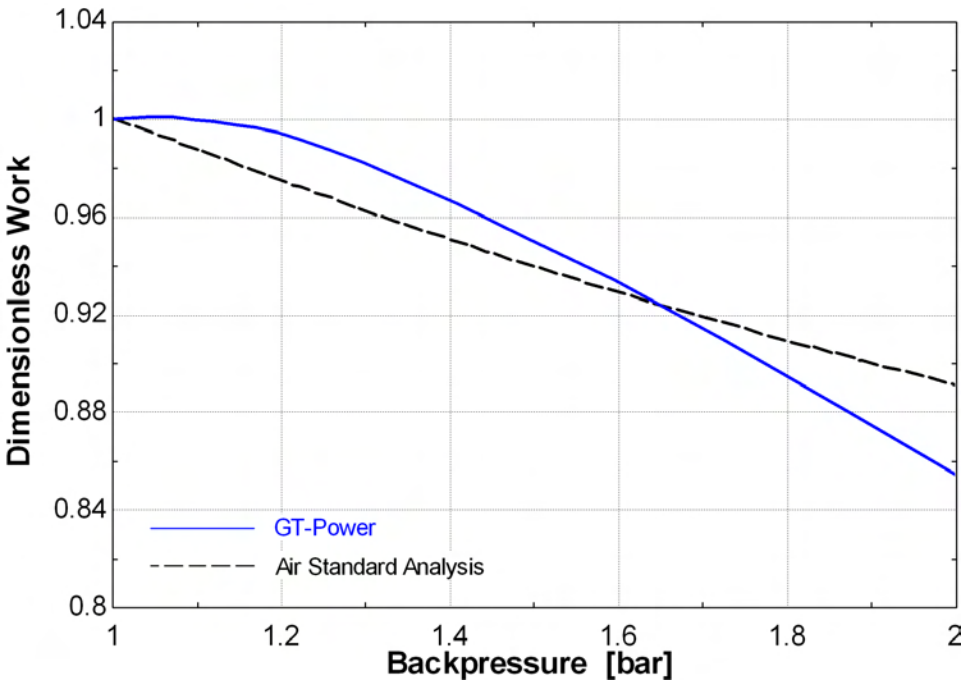

Figure 4.6: Comparison of GT-Power Model to Air Standard Analysis

in an internal combustion engine. Therefore, not all of the details of the actual process are seen here. The actual data are modeled much more accurately with an engine simulation program, such as GT-Power. In examining the results shown in Figure 4.6, it can be seen that the trends of the GT-Power model and the air standard analysis are similar, thus the usefulness and validity of GT-Power has been justified by the comparison to the air standard model along with the literature.

4.3 Preliminary GT-Power Model

As discussed previously, for the turbine in the exhaust to be a feasible alternative, the magnitude of power gain must be significant enough to outweigh the engine power lost due to increased backpressure. The GT-Power results of engine power versus backpressure for the preliminary model are shown again in Figure 4.7, as they were in Figure 4.1, with the

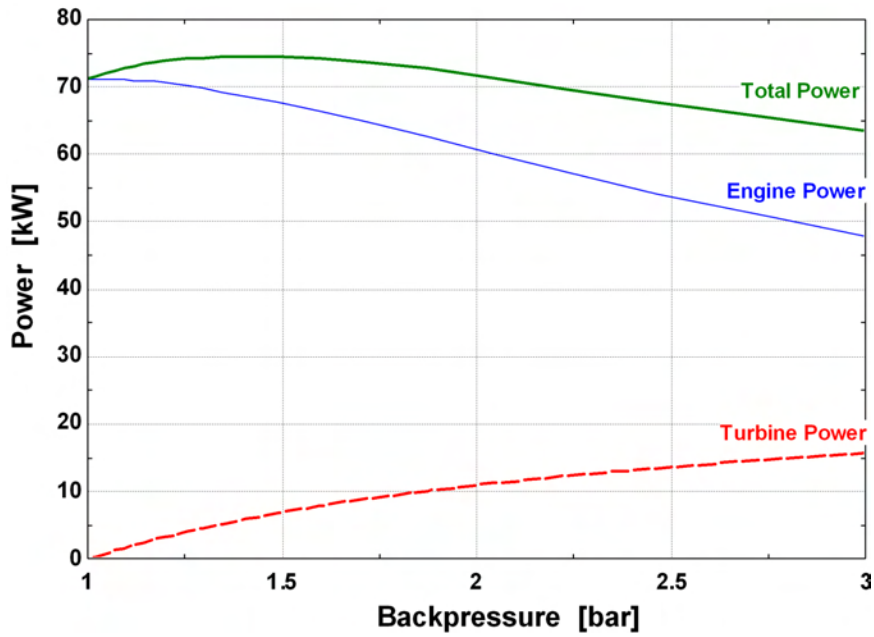

Figure 4.7: Power vs. Backpressure for the Preliminary Model at 3600 rpm in GT-Power (Default Engine Parameters and No Catalytic Converter or Muffler)

addition of plots of turbine power and total power versus backpressure.

Figure 4.7 shows that as the backpressure is increased the power produced by the turbine increases as well. The power produced by the turbine is over 10 kW when the pressure is at 2 bar and over 4 kW at 1.3 bar. The magnitude of the power produced by the turbine appears to be in the range that will assist the engine power to achieve considerable gains in overall power. The key to realizing the optimum gain in power is to find the point at which a maximum power exists. The plot of total power (Engine Power + Turbine Power) vs. backpressure in Figure 4.7 shows that a maximum total power of 74.5 kW is attained at a point where the backpressure is 1.41 bar. At this point, an overall increase in power of approximately 3.5 kW is achieved, or 4.7% greater than with the engine alone. The appreciable gains calculated from the preliminary model show potential for the turbine in exhaust system.

4.4 Detailed Prius GT-Power Model

The preliminary GT-Power model was then further developed so that it accurately reflected the Toyota Prius system. Although not all of the specifications were known for this vehicle, the most significant parameters were known and implemented into the model. The engine parameters, which include the bore, stroke and compression ratio, were changed to match those of the Toyota Prius; GT-Power default values were used for the parameters that were not found in the Toyota Prius specifications. The exhaust system in the Prius includes a catalytic converter and a muffler as shown in the No Turbine model of Figure 4.8.

The intake system, catalytic converter and muffler were added to the GT-Power model. The implementation of the more detailed exhaust system allows for experimentation of the location of the turbine. The turbine was placed in various positions in the exhaust system to examine the effects that position had on the pressures, temperatures, etc., throughout the system and the power output. There may be issues with the proper temperature at the catalytic converter for proper operation if the turbine is placed prior to it. The temperature of the exhaust gas must be high enough for the catalyst to be effective, so the examination of temperatures through the system is important. The model was processed for the turbine placed prior to the catalytic converter (PreCat), after the catalytic converter (PostCat) and absent from the system (No Turbine). Figure 4.8 shows a block diagram representing the GT-Power layout of the engine and exhaust system with all three turbine configurations.

The GT-Power models shown in Figure 4.8were run with an engine speed of 3600 RPM, as in the preliminary model. The effect of the variation in engine speed is studied later in this chapter. The engine power, turbine power and total power for the PreCat and PostCat condition were plotted and analyzed. The result from the model with no turbine was plotted on both the PreCat and PostCat plots for comparison. The power versus backpressure plots for the PreCat and PostCat situations are shown in Figure 4.9 and Figure 4.10 respectively.

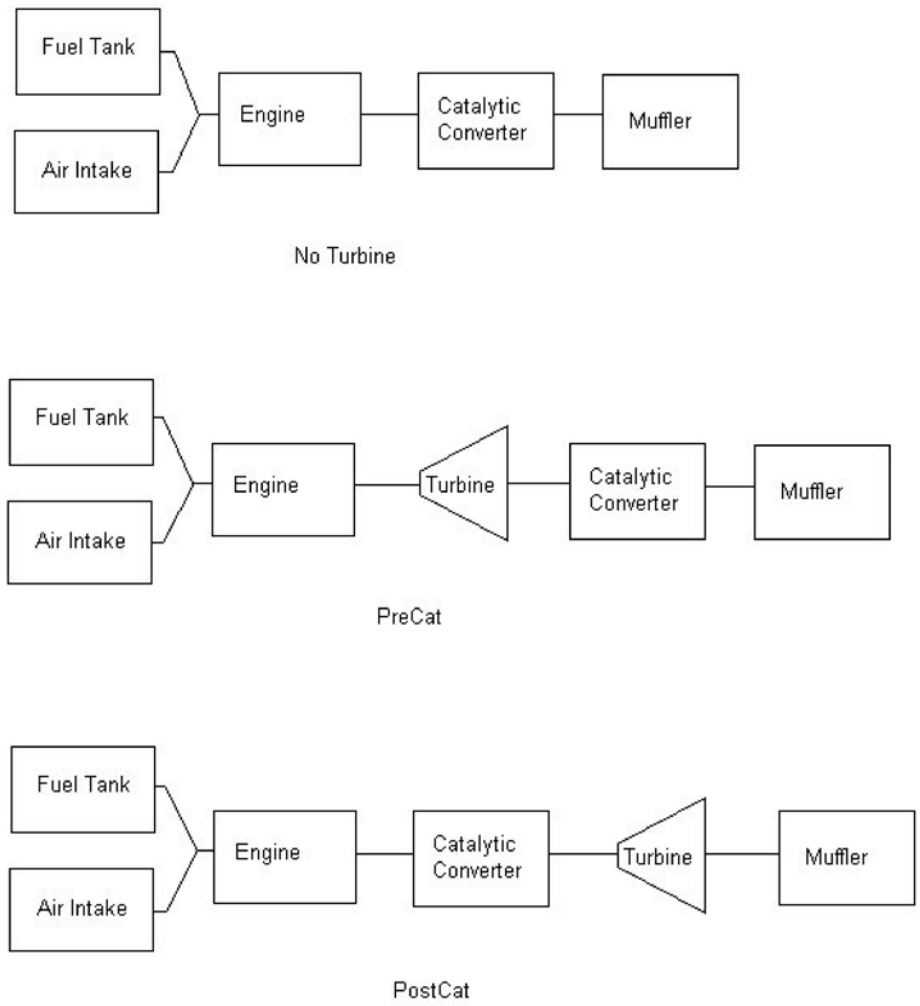

Figure 4.8: Block Diagrams Representing the Three GT-Power Models

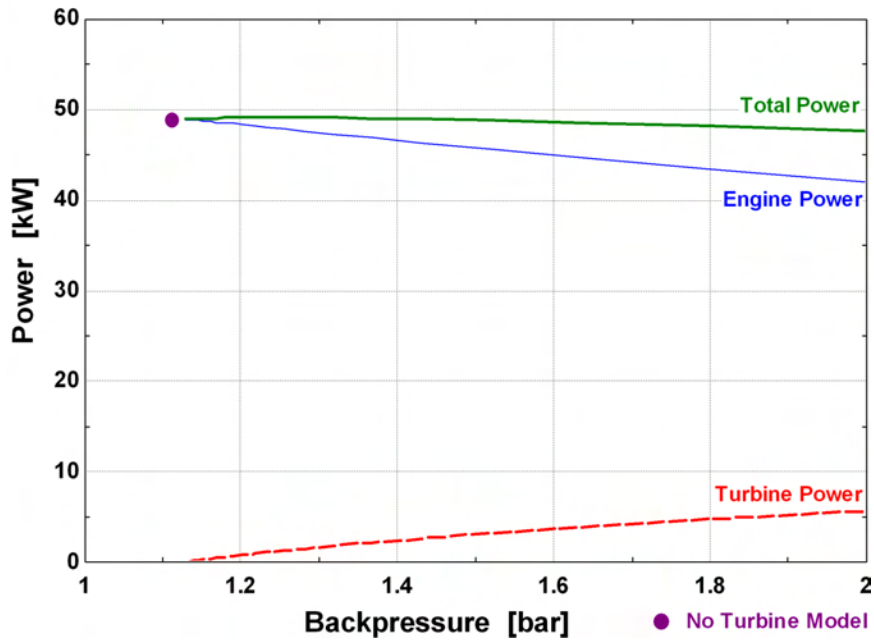

Figure 4.9: Power vs. Backpressure for the Prius model with a Turbine in the PreCat Location at 3600 RPM

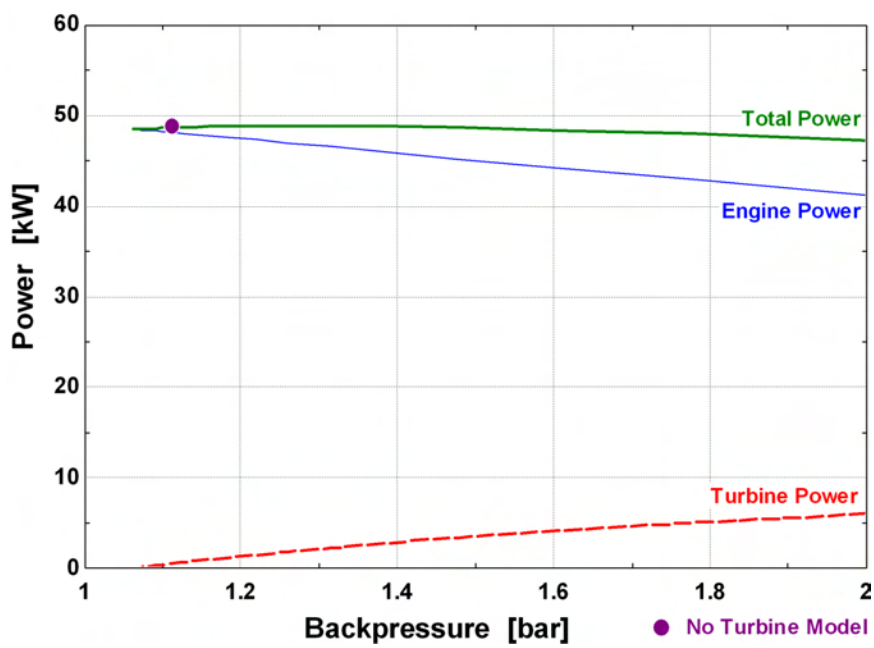

Figure 4.10: Power vs. Backpressure for the Prius model with a Turbine in the PostCat Location at 3600 RPM

Table 4.1: Comparison of Results from Prius Model at 3600 RPM

	No Turbine	**PostCat**	**PreCat**
Power (kW)	48.94	48.86	49.16
Difference (%)		-0.15%	0.45%

The plots shown in Figure 4.9 and Figure 4.10 contain similar trends for the engine and turbine power to that of the initial model. There is a slight shift in the magnitudes of the PreCat and PostCat plots, but both have similar behavior. The implementation of the catalytic converter, muffler and Prius engine parameters had significant effects on the total power increase over the engine system alone. The GT-Power model shows only a marginal increase in the overall system power for the Toyota Prius with the addition of a turbine for the PreCat turbine location and a loss for the PostCat turbine location.

A peak total power of 48.86 kW was calculated with the turbine placed after the catalytic converter and 49.16 kW for the turbine placed after the catalytic converter. These results are compared to the simulation of the no turbine model, which resulted in a power of 48.94 kW. The post catalytic converter model resulted in a .15% decrease in power whereas the pre catalytic converter model had a .45% increase in power. These results are summarized in Table 4.4.

The results in Table 4.4 are discouraging, especially after the promising results obtained with the preliminary model. Some of the negative effects are due to the addition of the catalytic converter and muffler. These devices impose additional backpressure on the engine, taking away opportunity for the turbine to achieve maximum benefits. However, it is necessary to perform parametric analysis of engine parameters to see if any detrimental effects occur due to the parameters specific to the Prius. First, the variation of the engine speed is explored, as it was kept constant for both the preliminary model and the detailed Prius model. Next, the effects of engine parameters such as the bore, stroke and compression ratio

are examined.

4.5 Engine Speed Variation

The engine speed is a significant parameter in the engine and turbine power and thus is very important to this analysis. The engine speed was varied from 1000 rpm to 5000 rpm in 1000 rpm increments. A plot of engine power, turbine power and total power at each engine speed for the PostCat location was created. The data for the PreCat location was also calculated for comparison, but is not shown on the plot as it has similar magnitudes and trends to that of the PostCat model. The results of the PostCat and PreCat models at the varying engine speeds are summarized in Table 4.5. The plots of power versus backpressure for engine speeds of 1000 rpm, 2000 rpm, 3000 rpm, 4000 rpm and 5000 rpm are shown in Figure 4.11 through Figure 4.15, respectively.

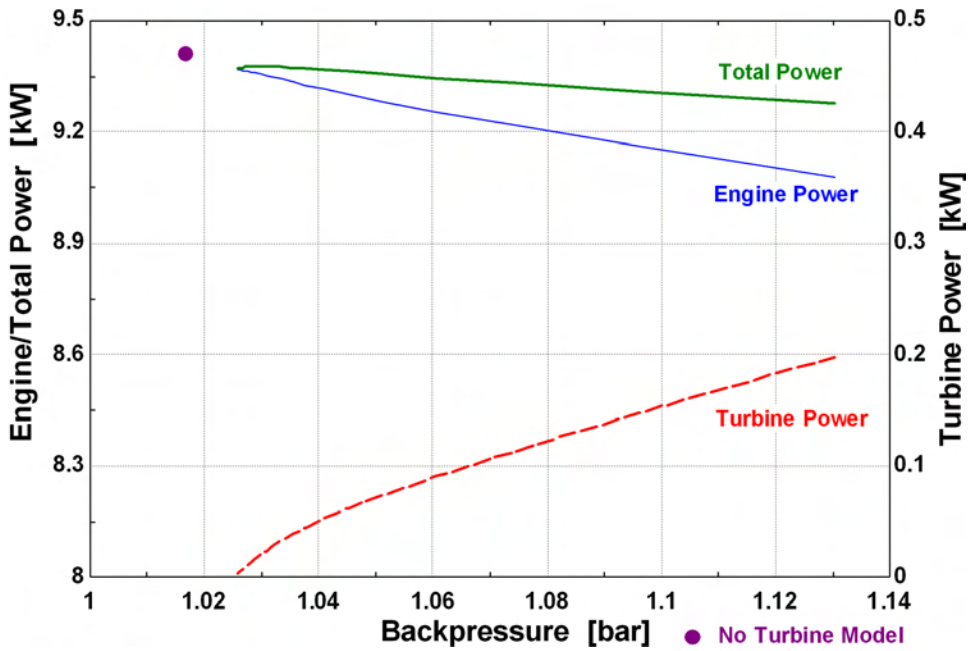

Figure 4.11: Power vs. Backpressure for the Prius Model with a Turbine at an Engine Speed of 1000 RPM

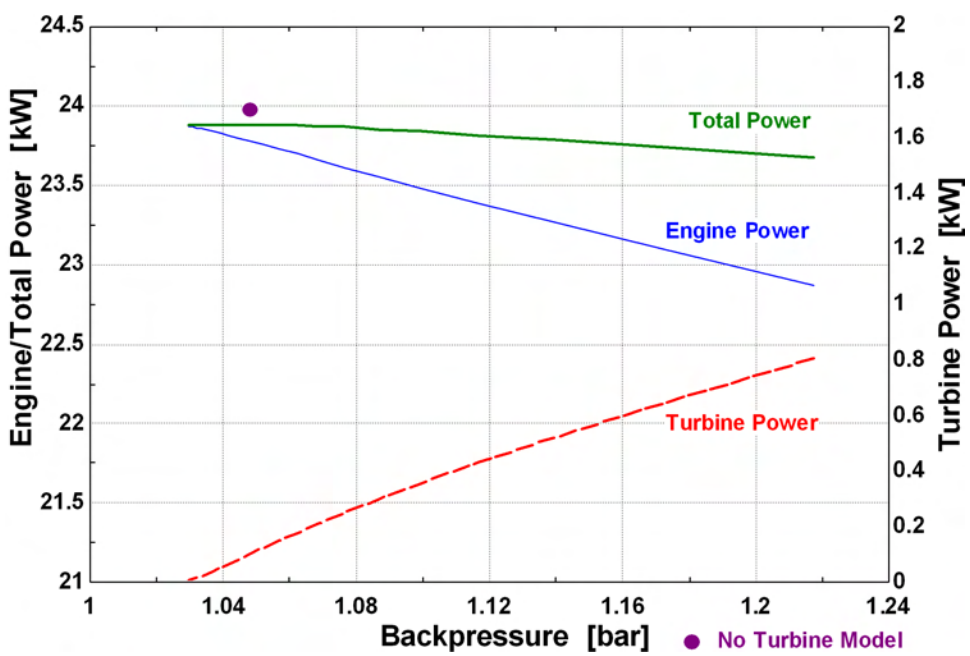

Figure 4.12: Power vs. Backpressure for the Prius Model with a Turbine at an Engine Speed of 2000 RPM

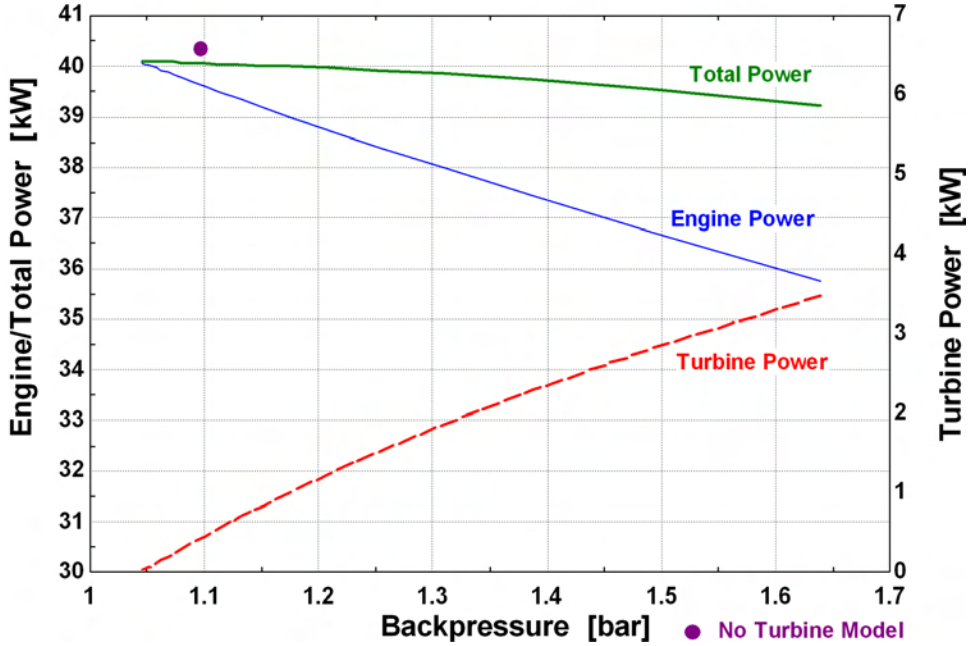

Figure 4.13: Power vs. Backpressure for the Prius Model with a Turbine at an Engine Speed of 3000 RPM

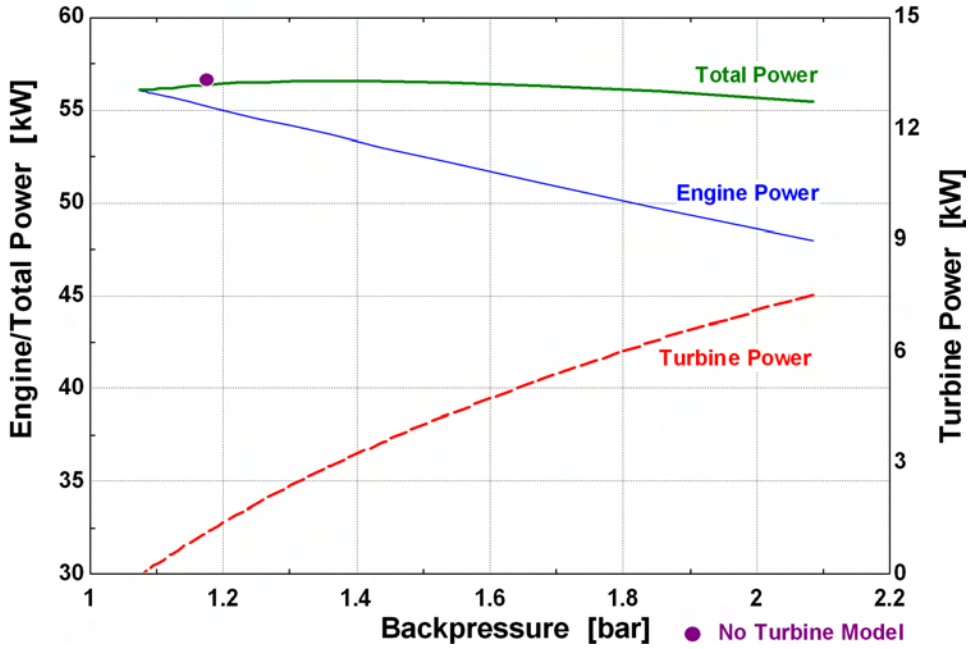

Figure 4.14: Power vs. Backpressure for the Prius Model with a Turbine at an Engine Speed of 4000 RPM

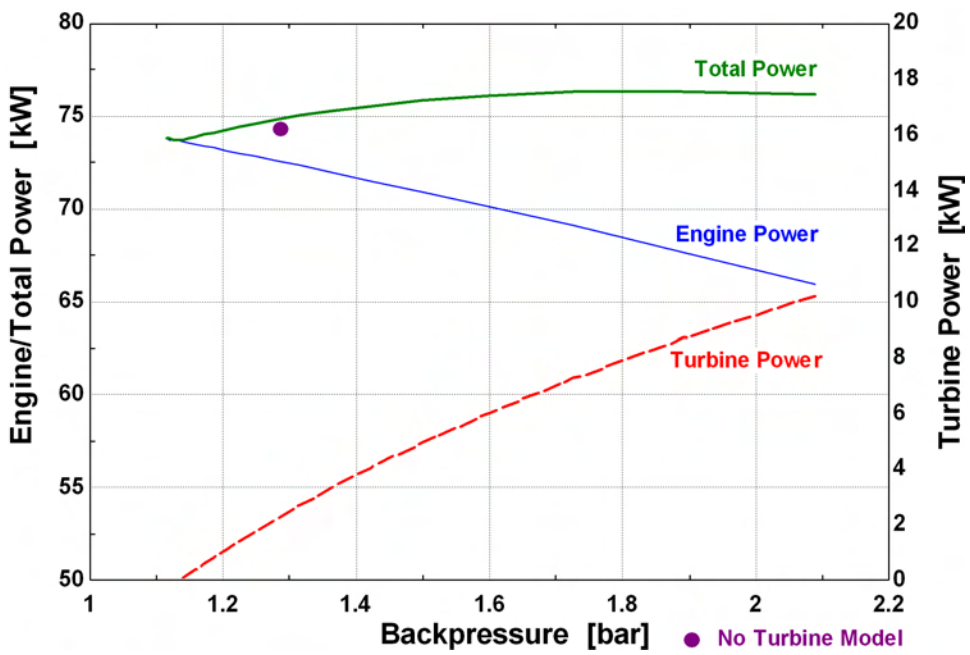

Figure 4.15: Power vs. Backpressure for the Prius Model with a Turbine at an Engine Speed of 5000 RPM

Table 4.2: Comparison of Total Power for Various Engine Speeds

RPM	No Turbine	PostCat	PostCat %	PreCat	PreCat %
1000	9.41	9.38	-0.36%	9.46	-0.38%
2000	23.97	23.88	0.47%	23.97	0.00%
3000	40.32	40.08	-0.59%	40.71	0.96%
4000	56.62	56.58	-0.07%	56.76	0.24%
5000	74.28	76.36	2.80%	76.38	2.82%

The plots in Figure 4.11 through Figure 4.15 show that as the engine speed is increased, the total power benefits over the no turbine model are also increased. Marginal results are achieved at speeds of 2000 rpm or less. As the engine speed is increased to the 3000 - 5000 rpm range, the increased benefits from the turbine contribute to the more drastic total power peaks. These results are shown in Table 4.5.

The parametric analysis of the effect of varying engine speed demonstrated that appreciable benefits for the turbine in exhaust system are only realized in the 5000 rpm range for the Toyota Prius. This range of engine speed is uncommon for most vehicles, including the Prius. A plot of the engine speed for a typical driving cycle of the Toyota Prius is shown in Figure 4.16.

As shown in Figure 4.16, the operating range of the Prius is generally less than 3000 rpm. Therefore the gains realized by the implementation of a turbine in the exhaust stream would be minimal. Although better overall performance is realized through the addition of a turbine in the exhaust stream, the small magnitude of power increase would be difficult to justify economically.

4.6 Parametric Analysis of Engine Parameters

Preliminary calculations using default engine parameters had shown more promise than the results that were obtained by the GT-Power model for the Prius. A parametric analysis was

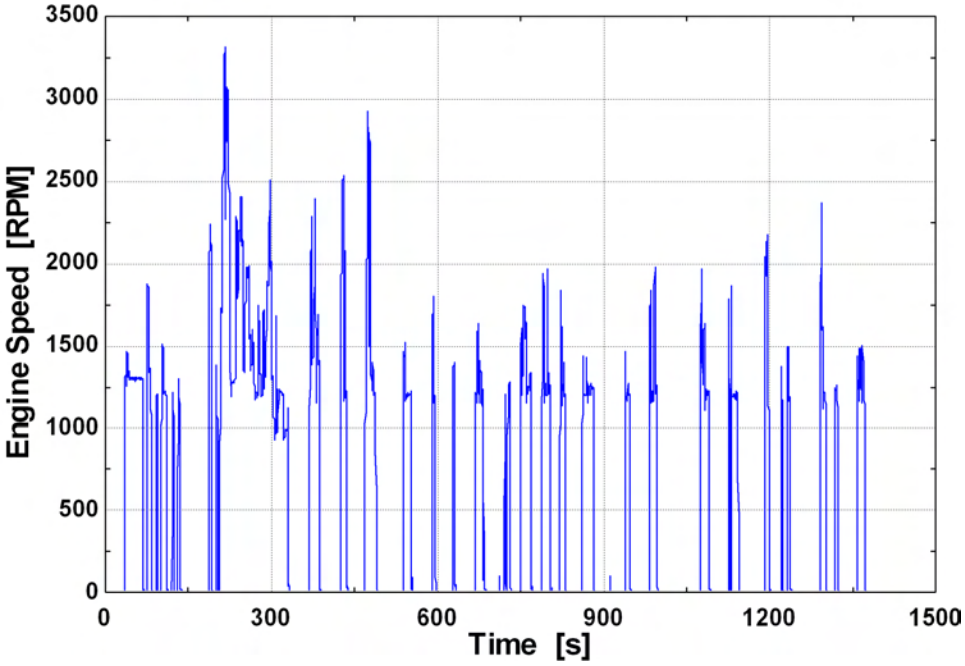

Figure 4.16: Engine Speed for a Typical Driving Cycle of the Toyota Prius

performed on some of the engine specifications to see how significant they are on the turbine in exhaust design. This analysis considered the compression ratio, bore and stroke of the engine. The parametric analysis kept all other variables the same as in the Prius model with the engine speed at 3600 rpm. The analysis was performed for the designs with the turbine placed prior to the catalytic converter, after the catalytic converter and with no turbine.

4.6.1 Vehicle Survey

A survey of fifty-four current vehicles was performed to find the range of compression ratio, bore and stroke to examine for the parametric analysis. A select number of these vehicles were chosen to compare on a plot. The vehicles chosen for the plot demonstrate the full range of values obtained from the analysis. The Toyota Prius is highlighted with a diagonal pattern on these plots to show how it compares to the industry average. The plots of compression ratio, bore and stroke for the selected vehicles are shown in Figure 4.17, Figure 4.18, and

Figure 4.19, respectively.

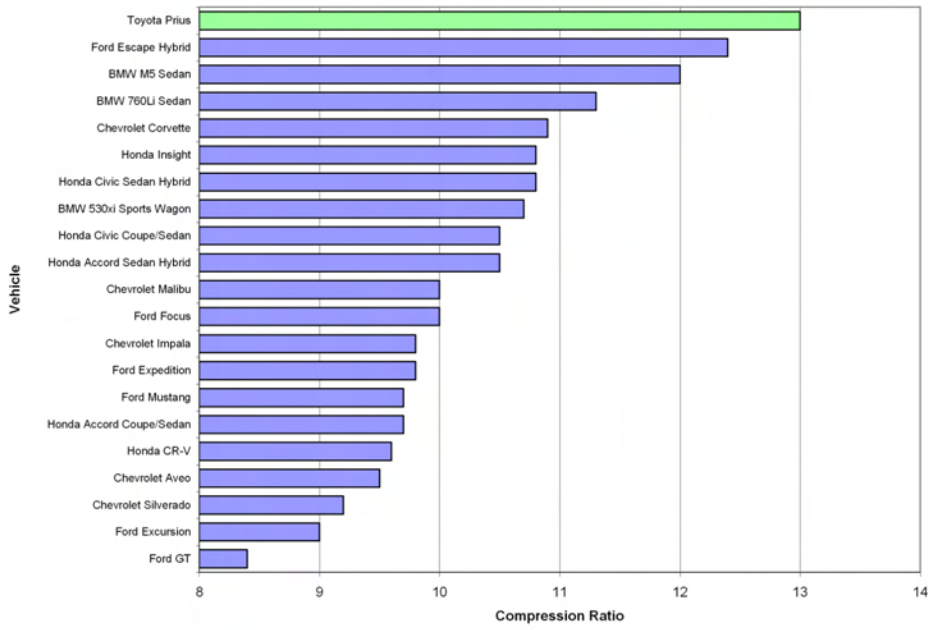

Figure 4.17: Compression Ratio for Various Vehicles

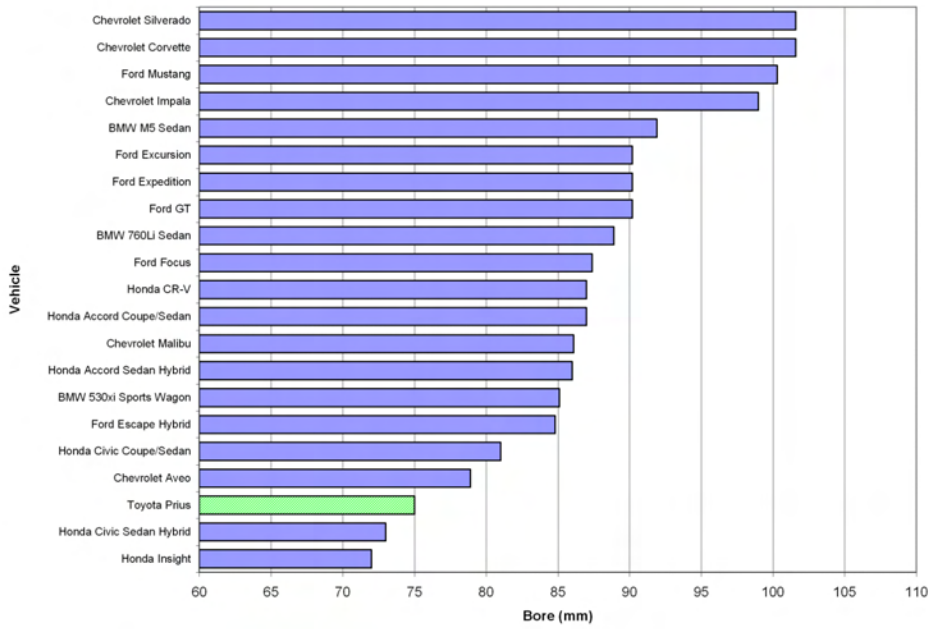

Figure 4.18: Bore for Various Vehicles

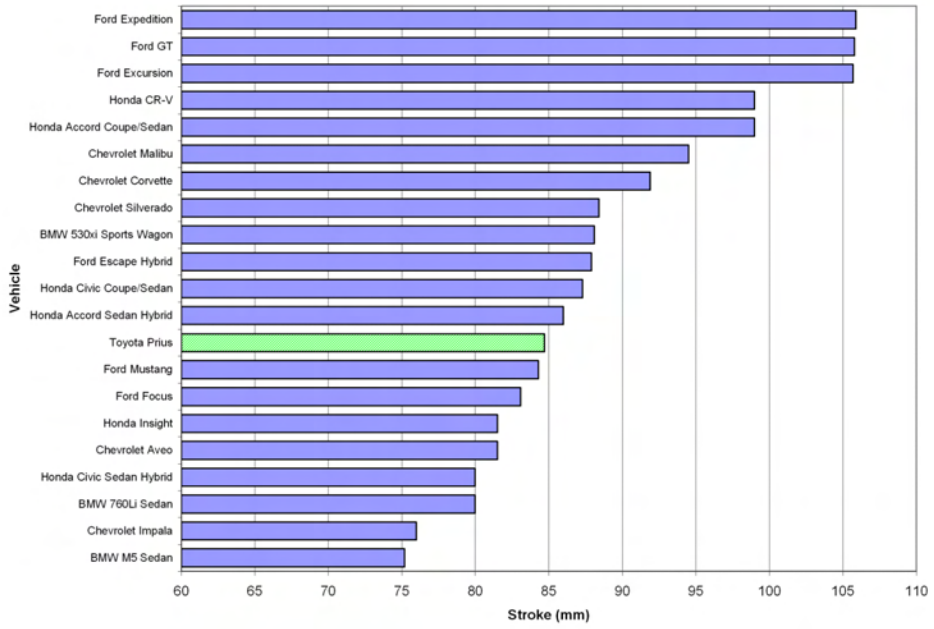

Figure 4.19: Stroke for Various Vehicles

From the values collected in the survey, the compression ratio was found to have a range of 8.4 to 13 with an average value of 10.2. The Toyota Prius has a compression ratio of 13, which is the largest of the vehicles in the survey. The bore of the Toyota Prius is 75 mm, which is on the lower side of the average that was calculated to be 89.5 mm. The bore from the vehicles surveyed was found to have a range of 72 mm to 101.6 mm. The vehicle data had a range for the stroke of 75.2 mm to 105.9 mm with and average value of 89.3 mm. The Prius was on the lower side of the average with a value of 84.7 mm.

The results of the vehicle survey show that the Toyota Prius has unique engine parameters when compared to industry averages. The compression ratio is by far the largest found in the industry and the bore is among the smallest. The stroke is closer to the industry norm but is still on the lower side of the industry average. A parametric analysis was performed to see if these values have a significant effect on the performance achieved when a turbine is placed in the exhaust. These results could produce potential viability for other vehicles to utilize placing a turbine in the exhaust system.

4.6.2 Compression Ratio

The compression ratio was varied from 8 to 14 for the parametric analysis. These values were chosen as they represent the full range that was found from the survey of current vehicles being sold. The plot of engine power, turbine power and total power versus compression ratio for the PostCat turbine location is shown in Figure 4.20. The PreCat and PostCat conditions were both studied for this analysis and resulted in the same trends with similar magnitudes.

The plot in Figure 4.20 shows that more power from the engine is achieved with a larger compression ratio, keeping all other parameters the same. However, as the compression ratio increases, the turbine power decreases. The decrease in power of the turbine is less than the

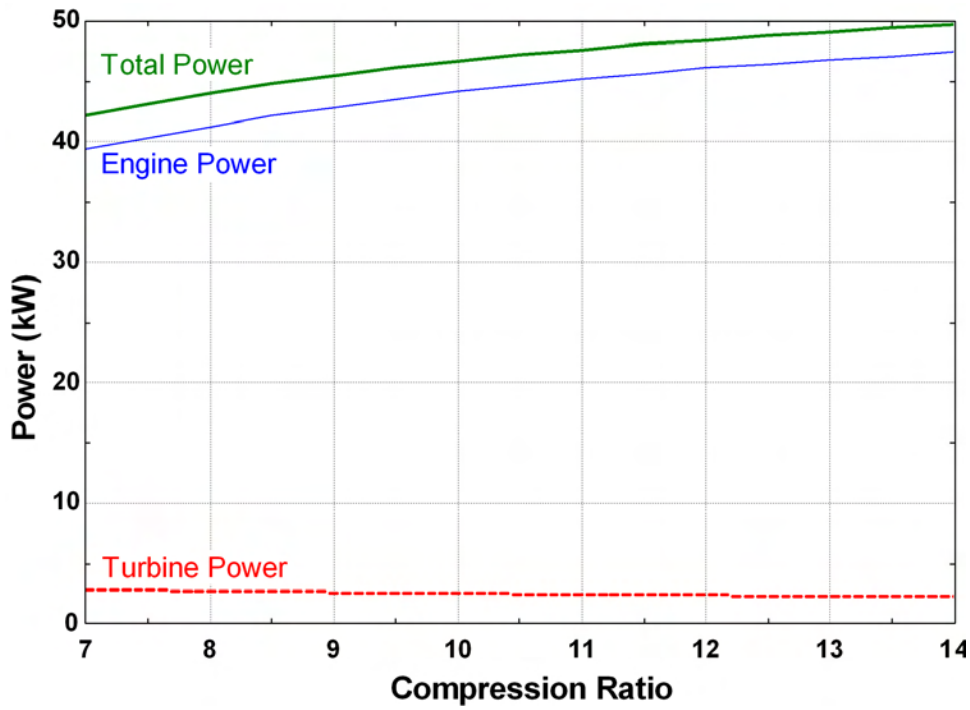

Figure 4.20: Power versus Compression Ratio

gain in engine power which results in a modest increase in total power as the compression ratio is increased. A plot of the percentage change in total power versus compression ratio was created and is shown in Figure 4.21. This plot compares the total power achieved at each compression ratio over the range to the power achieved with a compression ratio of the average from the survey. Figure 4.21 shows a 12% change in total power over the range of compression ratios. The Prius is at the high end of the compression ratio spectrum, so it is benefiting from the marginal increase in power for the higher compression ratio.

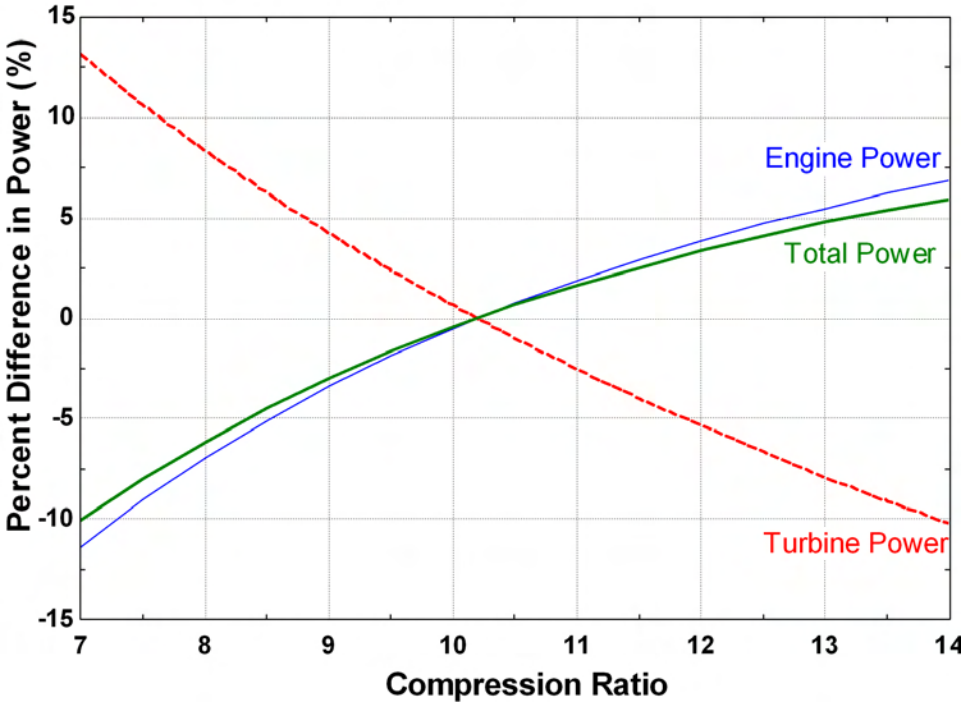

Figure 4.21: Percentage in Total Power Change with Compression Ratio

4.6.3 Bore

The bore was varied from 70 mm to 100 mm for the parametric analysis. The plot of engine power, turbine power and total power versus bore is shown in Figure 4.22.

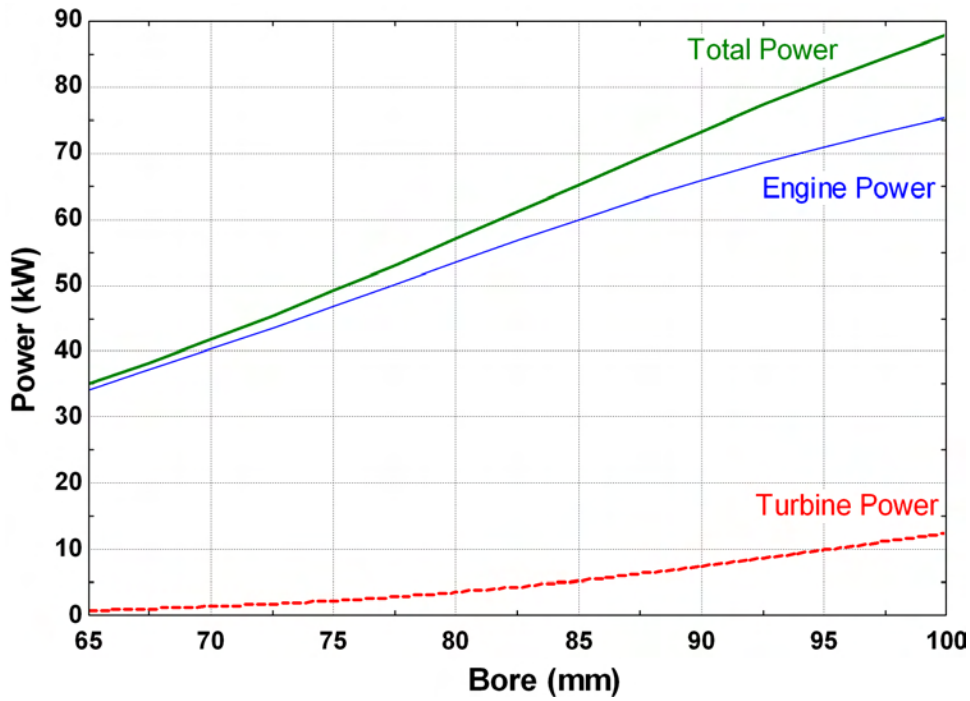

Figure 4.22: Engine Power versus Bore

Figure 4.22 shows that the engine power and turbine power both drastically increase as the bore increases. The total power, calculated as the sum of the engine power and turbine power, has a more or less linear dependence on the bore, as shown in Figure 4.22. A plot of the percentage change in power was created to show the trends in the effects of the variation of the bore. This plot, which is shown in Figure 4.23, compares the power achieved at each bore over the range of values to the power achieved with the average bore obtained in the survey. A change in total power of over 60% is attained over the range of bores, as shown in Figure 4.23. The Prius is at the low end of the bore values, which doesn't allow it to take advantage of the increase in power that is realized from vehicles with larger bores.

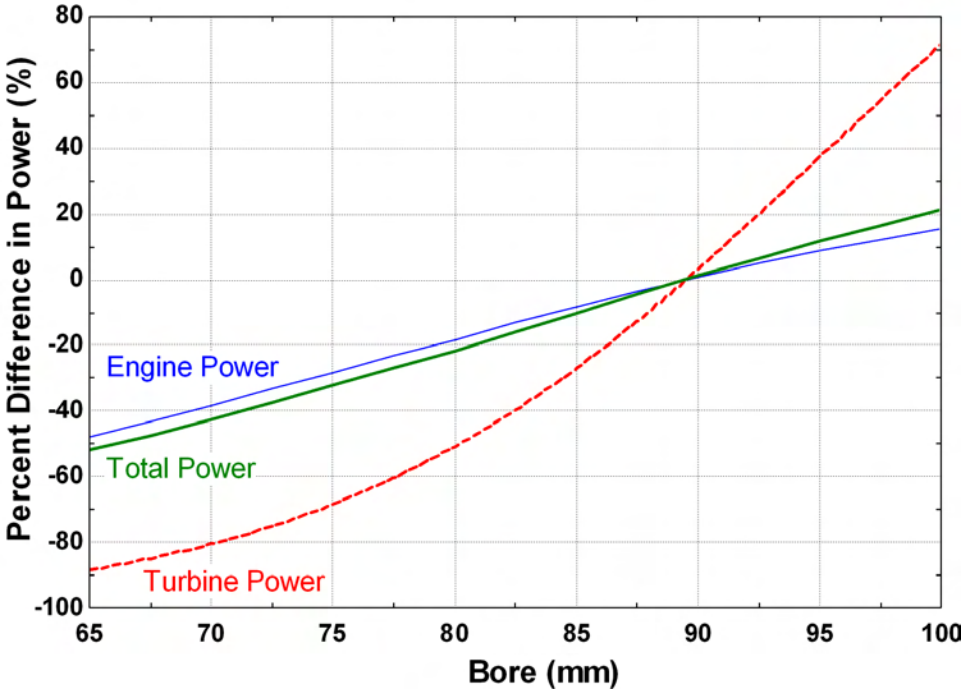

Figure 4.23: Percentage Change in Total Power with Bore

4.6.4 Stroke

The stroke was varied from 75 mm to 105 mm for the parametric analysis. The plot of engine power, turbine power and total power versus stroke is shown in Figure 4.24.

Figure 4.24 shows an increase in engine power and turbine power as the stroke is increased. The engine power increases in a linear fashion, while the turbine power increases in an exponential manner. However the turbine power is small when compared to the total power, which results in keeping the total power more or less linear. A plot of the percentage increase in total power versus the stroke is shown in Figure 4.25. This plot shows a variation of over 30% in total power over the range of strokes.

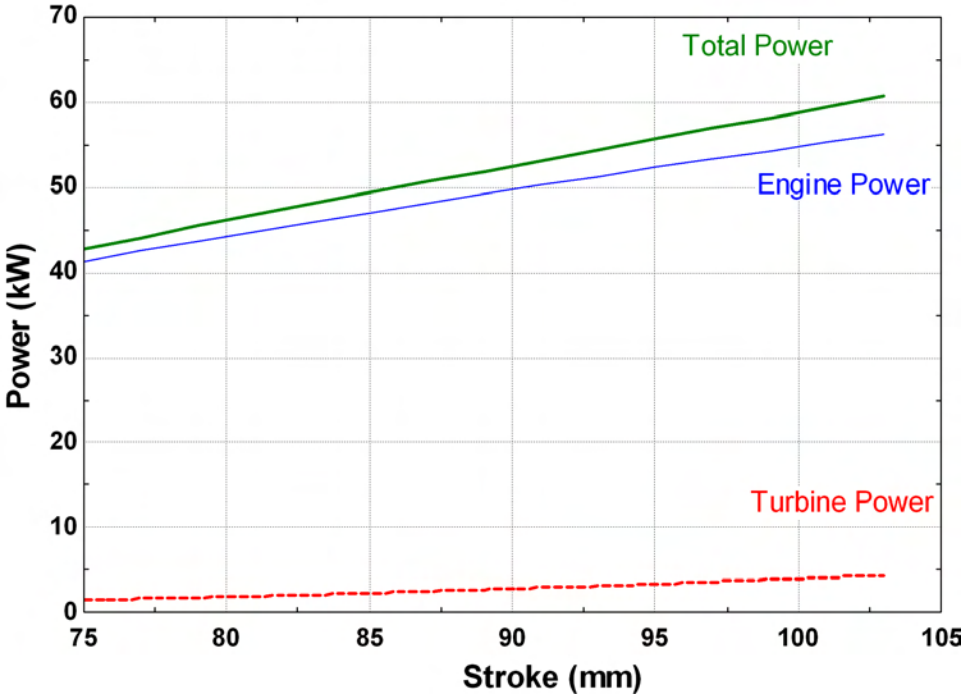

Figure 4.24: Engine Power versus Stroke

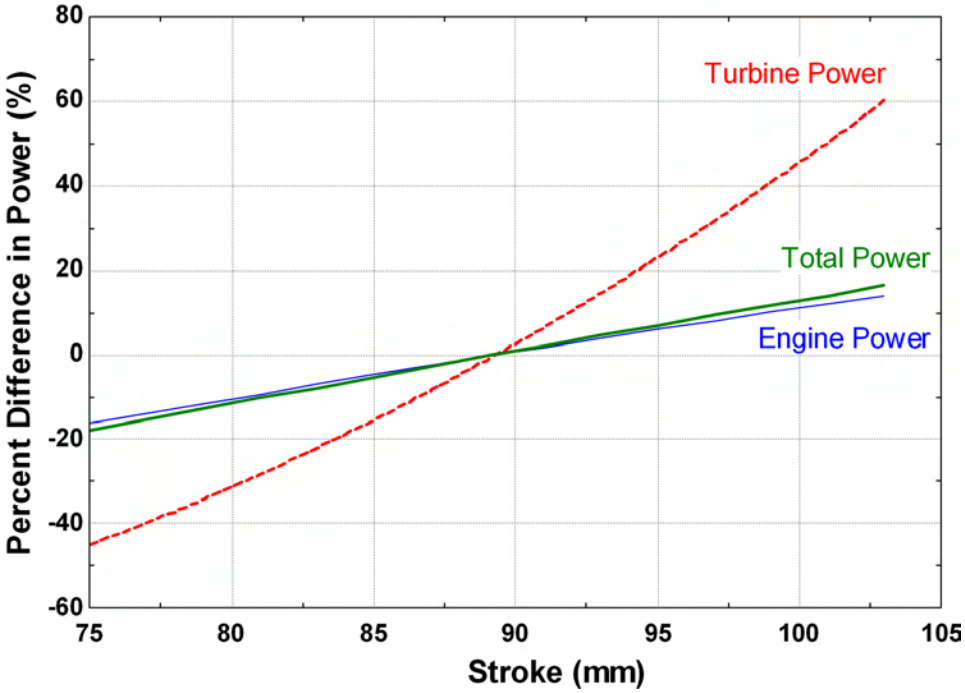

Figure 4.25: Percentage Change in Total Power with Stroke

4.6.5 Comparison

The variations in the power that were achieved for the change in compression ratio, bore and stroke were studied further. In order to compare the variables in a similar manner, the percent change in total power versus the percent change in the variable (compression ratio, bore or stroke) was investigated. This is shown in Figure 4.26, where all of three of the variables are compared against one another.

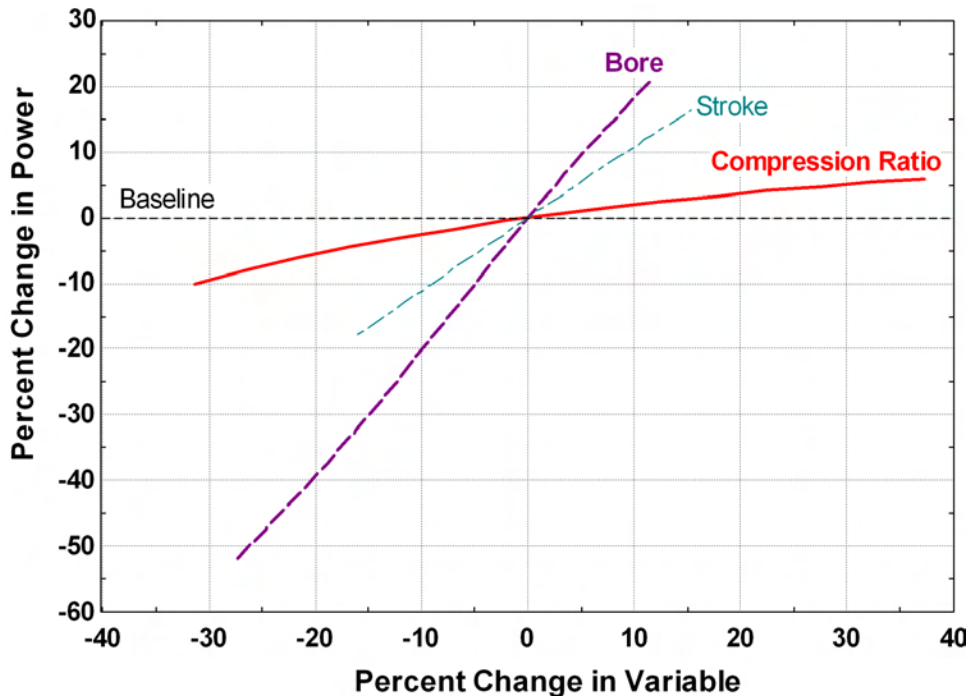

Figure 4.26: Percent Change in Total Power for Percent Change in the Variable

Figure 4.26 shows that the bore has the largest slope, followed by the stroke and the compression ratio. A larger slope means that a change in the variable results in a larger variation in the total power. Therefore the bore is the most significant variable affecting the total power. The stroke is also significant; however, the variation of the compression ratio has a negligible effect when compared to the other variables. The Prius has minor benefits in total power from its high compression ratio. However, the detrimental effects of

the low values of bore and stroke on energy recovery by a turbine outweigh the gains realized from the high compression ratio. Therefore, the Toyota Prius appears to be deficient in the parameters that would make the system optimal for achieving benefits from the turbine in exhaust system. In spite of this, there is potential for the feasibility of the turbine in exhaust system in another vehicle. The sensitivity analysis shows that a larger bore and stroke will have significant effects on the total power that is achieved from the system. Therefore a vehicle with a larger bore and stroke could attain benefits from the turbine in exhaust system. However, this would have to be independently analyzed to determine the magnitude of benefit for the particular vehicle of interest.

4.6.6 Atkinson Cycle Considerations

The Toyota Prius is also unique as it utilizes the Atkinson cycle rather than the more traditional Otto cycle. The details of the Atkinson cycle are discussed in Chapter XX. The major difference that is important for this analysis is the late intake valve closing. The late intake valve closing of the Atkinson cycle results in a lower effective compression ratio than the compression ratio given in the technical specifications. The effective compression ratio is the compression ratio that is actually seen by the components in the engine. The compression ratio for the Prius is 13, which is what was used in the model. However the effective compression ratio, due to the use of the Atkinson cycle would actually be less than this. The parametric analysis looked at the effect of compression ratio on performance of the turbine and engine system. It was determined that the compression ratio has an effect on the performance, but it is small compared to the other variables analyzed. Therefore, it seems appropriate to assume that the effect of the effective compression ratio and differing expansion ratio would have little effect on the results of the analysis. The GT-Power model did not take into consideration that the Prius is actually an engine that uses the Atkinson

cycle. GT-Power assumes the Otto cycle for all spark ignition engines. The actual magnitudes will vary slightly due to the use of the Atkinson cycle, however the general trends have been captured in this analysis. It is assumed that the Atkinson cycle engine would have negligible effects on the overall results and conclusions of turbine in exhaust analysis that was simulated in GT-Power.

4.7 Conclusions

It has become apparent that the implementation of a turbine in the exhaust stream of a Toyota Prius is not very practical. The unique engine parameters and driving cycle of the Prius limit the effectiveness of such a design. The Toyota Prius has a relatively small engine that cycles on and off due to the nature of the hybrid system. These parameters contribute to the limitations observed in this analysis. However, it does appear that this could be a viable option for a different vehicle. It seems that benefits could be attained in vehicles with a larger engine, but this would need further analysis.

Chapter 5

Analysis of a Compact Heat Exchanger in the Exhaust System

5.1 Introduction

The analysis of the implementation of a turbine in the exhaust system (Chapter 4) showed overall negative results for the Toyota Prius system due to the backpressure. Significant gains were only achieved at very high engine speeds, where the Prius rarely operates. These results showed that placing a turbine in the exhaust system is not a viable option for energy recovery, however they do not provide conclusive evidence for other methods of heat recovery utilizing the exhaust stream. Thus, it is of interest to obtain a general relationship between heat recovered and the resulting backpressure.

5.2 Compact Heat Exchanger Model

A compact heat exchanger analysis was performed to provide a general relationship between heat recovered and pressure drop. The analysis was done using the equations, methods and tables from Kays and London [43]. The data from Kays and London [43] have been implemented as a routine in a software program called Engineering Equation Solver (EES) [44]. Additionally, a GT-Power model that examined the backpressure effects on engine performance was created. The resulting data from the compact heat exchanger analysis and GT-Power model were coupled to obtain a total system power. The total system power ($\dot{W}_{total}$) is the sum of the engine power for the given backpressure ($\dot{W}_{engine}$) and the resulting power generated from the heat recovered. The heat recovered is used to drive a Rankine

cycle to produce usable power for the system. Thus, the power generated from the heat recovered is the product of the heat recovered from the compact heat exchanger ($\dot{Q}_{CHE}$) and the Rankine cycle efficiency ($\eta_{Rankine}$). The equation for the total system power is shown in Equation 5.1.

$$\dot{W}_{total} = \dot{W}_{engine} + \eta_{Rankine}\dot{Q}_{CHE} \tag{5.1}$$

The total system power shown in Equation 5.1 was then compared to the engine power computed without any heat recovery system in the exhaust system. This allows for a determination of the viability of a heat recovery system in the exhaust system.

The compact heat exchanger analysis utilized was a compact circular tube bundle with continuous fins. The surface designation abbreviation for flow across the tubes for this configuration is '7.75-5/8T' for which the data are provided in the circular tubes with continuous fins section in Kays and London [43]. The geometry of the tube size and spacing is shown in Figure 5.1.

There are some assumptions that need to be made for the geometry of the heat exchanger prior to the analysis, including the frontal area and length. An optimization of the frontal area and length was performed to determine the best values for this geometry. The length and frontal area were varied simultaneously to show how these values affect the average percent gain in energy. The contour plot in Figure 5.2 shows the average percent gain in energy as a function of the heat exchanger length and frontal area.

Figure 5.2 shows that as the heat exchanger length and frontal area are increased, the average percent gain in energy also increases. For small frontal areas and long lengths the pressure drop is high and has negative effects on the engine and overall performance. For configurations with large frontal areas, the Reynolds number becomes small enough that the correlations are not applicable. Therefore, frontal areas larger than 0.003 m^2 were not

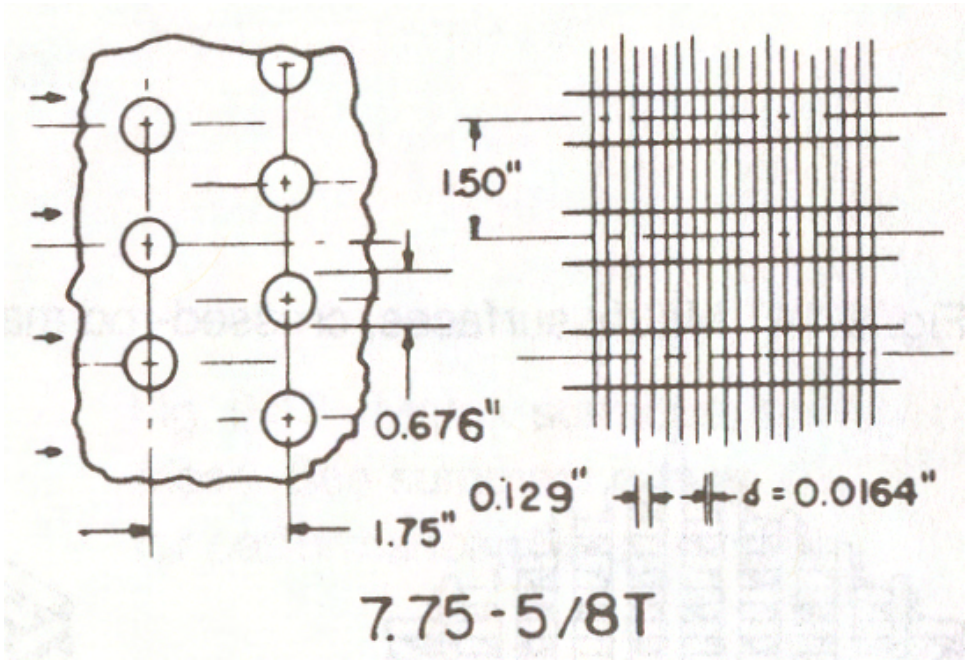

Figure 5.1: Schematic of the 7.75-5/8T Compact Heat Exchanger Geometry Studied

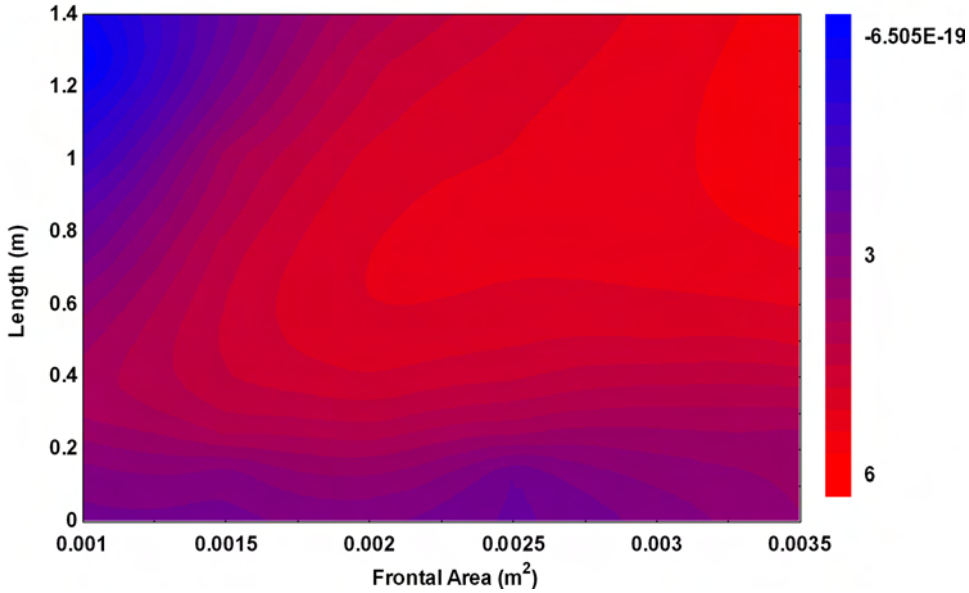

Figure 5.2: Average Percent Gain in Energy as a Function of the Heat Exchanger Length and Frontal Area

studied. Each frontal area has a corresponding optimum length at which the average percent gain in energy is optimum, which is plotted in Figure 5.3.

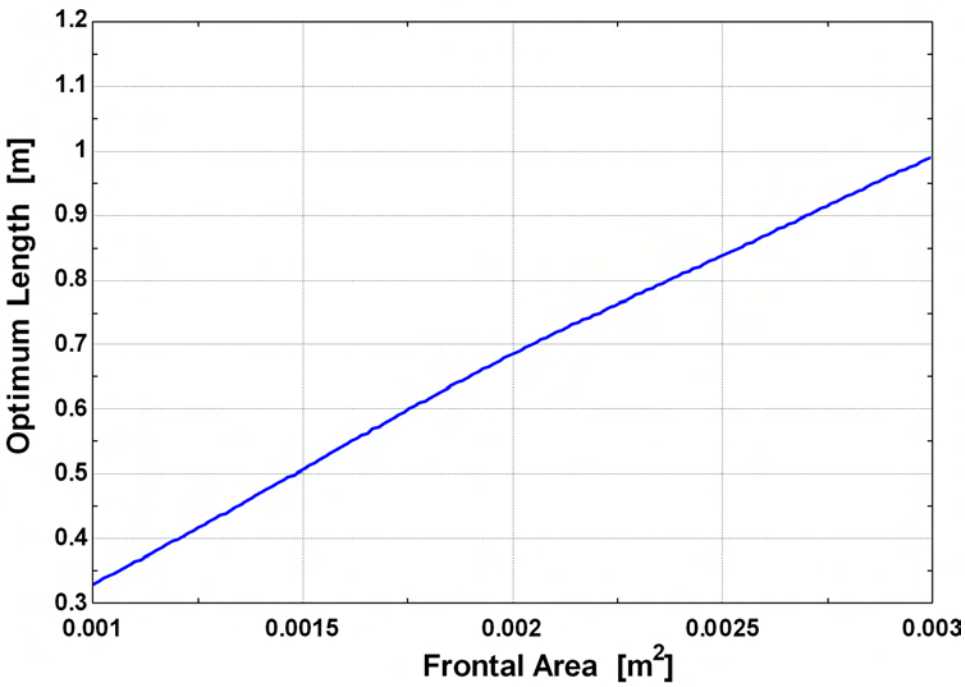

Figure 5.3: Optimum Heat Exchanger Length as a Function of the Frontal Area

As shown in Figure 5.3, the optimum heat exchanger length increases with increasing frontal area. The heat exchanger is to be used in a vehicle where space is limited, creating some additional constraints for the system. Lengths larger than 1 meter could present space complications for the implementation of the heat exchanger in the vehicle. Therefore a frontal area of the heat exchanger is chosen to be 0.0025 m^2, i.e. 0.05m $\times$ 0.05m. The length of the heat exchanger is initially assumed to be the optimum length of .84m that was determined in this analysis. Also for this analysis, it was assumed that the fluid within the tubes is toluene. The heat recovered from the compact heat exchanger would be used directly in a Rankine cycle. Toluene has been found to be a good fluid for low temperature organic Rankine cycles, considering thermal stability, toxicity, flammability and cost [45].

The Reynolds number for the exhaust gas was then determined as shown in Equation 5.2 using the geometry defined above in Figure 5.1.

$$Re = \frac{GD_h}{\mu} \tag{5.2}$$

The mass flux of the exhaust gas (G), viscosity (μ) and the hydraulic diameter (D_h) are needed for the Reynolds number equation. The mass flux is calculated using the mass flow rate and the minimum free flow area (A_c) as shown in Equation 5.3. The hydraulic diameter is found from the correlations in Kays and London [43].

$$G = \frac{\dot{m}}{A_c} \tag{5.3}$$

The mass flow rate of the exhaust stream was found as a function of the engine speed from the Prius data. A linear fit for the mass flow rate of exhaust was calculated from the Prius data as shown in Figure 5.4.

The Reynolds number computed for the exhaust gas was used to find the heat transfer rate and the pressure drop of the heat exchanger. The Reynolds number for the exhaust side is shown in Figure 5.5 as a function of the engine speed for the geometry of the '7.75-5/8T' compact heat exchanger.

The friction factor (f) for a given Reynolds number for various geometries was found from the EES routine, which can be used to determine the pressure drop. Figure 5.6 shows the friction factor as a function of the engine speed for the '7.75-5/8T' configuration.

The EES routine that includes the friction factor also includes the product of the Prandtl number raised to the $\frac{2}{3}$ power and the Stanton number. This dimensionless number is used to find the heat transfer coefficient(htc). The Prandtl (Pr) and Stanton (St) dimensionless numbers are defined in Equations 5.4 and 5.5.

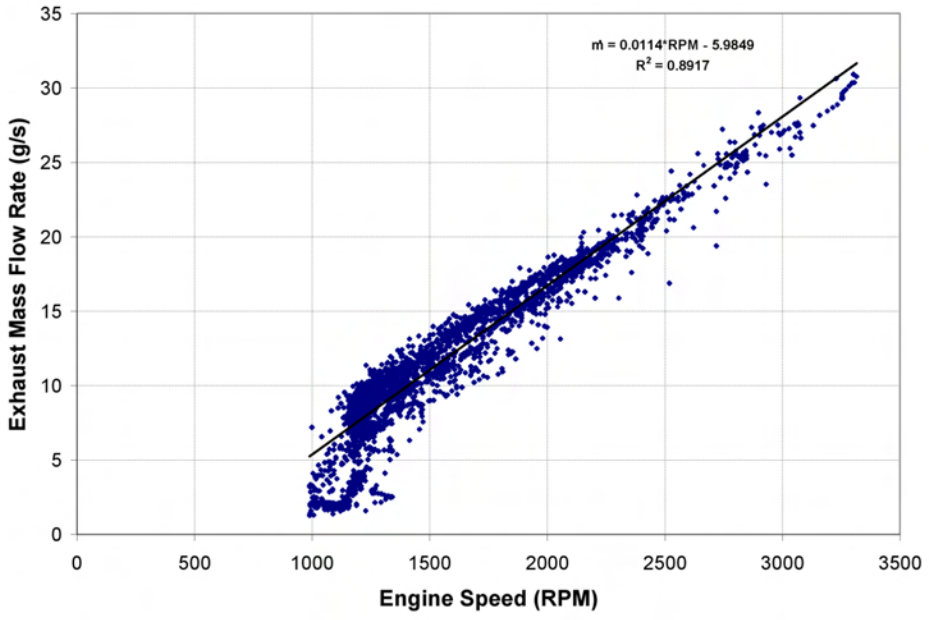

Figure 5.4: Exhaust Mass Flow Rate as a Function of the Engine Speed for the Prius Data

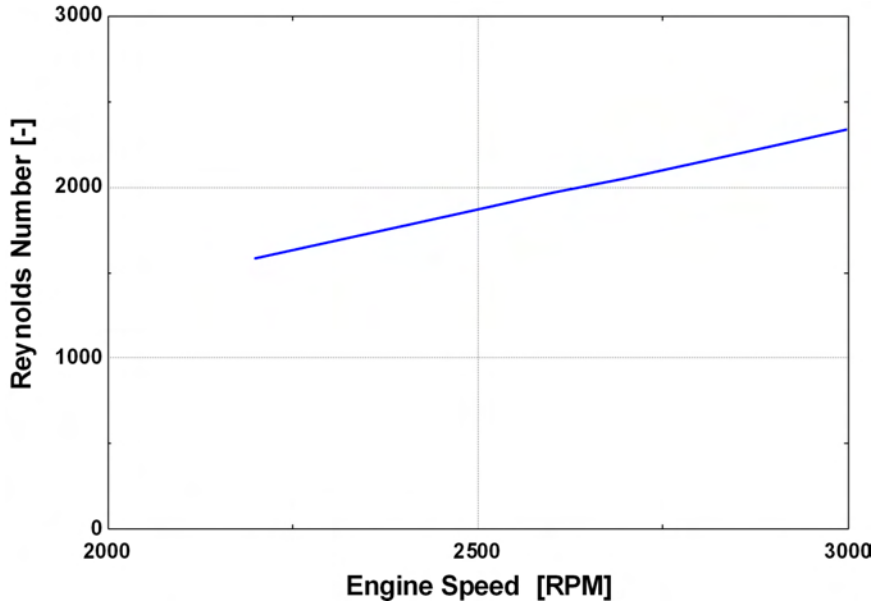

Figure 5.5: Reynolds number for the Exhaust Gas as a Function of the Engine Speed for the '7.75-5/8T' Compact Heat Exchanger

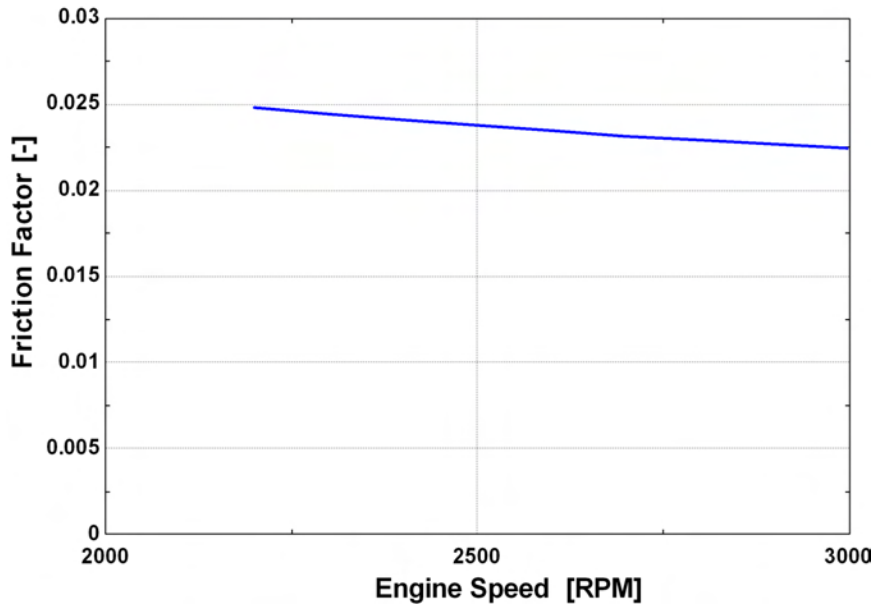

Figure 5.6: Friction factor for the Exhaust Gas as a Function of the Engine Speed for the '7.75-5/8T' Compact Heat Exchanger

$$Pr = \frac{c_p \mu}{k} \tag{5.4}$$

$$St = \frac{htc}{\rho V c_p} \tag{5.5}$$

Previously undefined variables in Equations 5.4 and 5.5 include the thermal conductivity and the specific heat, which are denoted by k and c_p, respectively. Combining these dimensionless numbers into the form for which data is given results in Equation 5.6.

$$StPr^{\frac{2}{3}} = \left(\frac{htc}{\rho V c_p}\right)\left(\frac{c_p \mu}{k}\right)^{\frac{2}{3}} \tag{5.6}$$

The left side of Equation 5.6 is found from the tables in Kays and London [43] for a computed Reynolds number. The right side of Equation 5.6 includes the velocity, which is known, and values that are properties of the fluid that can be found for the given condi-

tions. The only unknown in Equation 5.6 is the heat transfer coefficient, which can then be evaluated.

The heat transfer coefficient on the toluene side was found from a correlation for two-phase flow developed by Gungor and Winterton [46]. The compact heat exchanger would be utilized as an evaporator in the Rankine cycle, requiring the use of a two-phase correlation for evaporation heat transfer to the working fluid.

The heat transfer coefficients found for the exhaust gas and toluene sides were used to compute the overall heat transfer coefficient area product (UA). The thermal resistances (R) were calculated using the heat transfer coefficients found for the toluene and exhaust sides using Equation 5.7.

$$R = \frac{1}{htcA_{ht}} \tag{5.7}$$

In Equation 5.7, A_{ht} denotes the heat transfer area, or the contact area of the two fluids. For the chosen geometry this area was found to be 0.4573 m^2. The calculation of the thermal resistances allows for the computation of the overall heat transfer coefficient area product as shown in Equation 5.8 and is shown as a function of the engine speed in Figure 5.7.

$$UA = \frac{1}{R_{toluene} + R_{wall} + R_{exhaust}} \tag{5.8}$$

The overall heat transfer coefficient area product was then applied to find the number of transfer units (NTU), as in Equation 5.9.

$$NTU = \frac{UA}{\dot{C}_{min}} \tag{5.9}$$

In Equation 5.9, the $\dot{C}_{min}$ term is the minimum of the exhaust and toluene capacity rates, defined as the product of the mass flow rate and the specific heat of a fluid. Additionally,

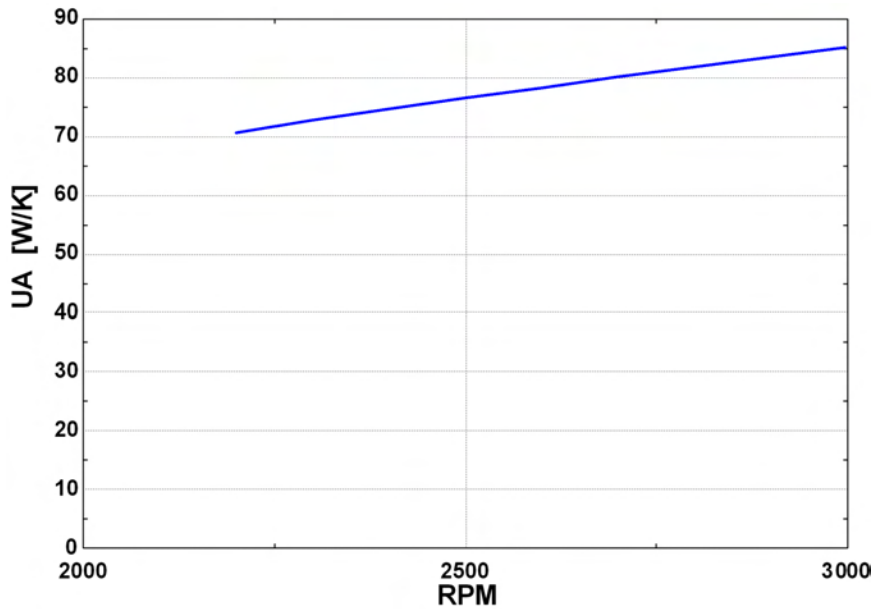

Figure 5.7: Overall Heat Transfer Coefficient-Area Product for the Exhaust Gas as a Function of the Engine Speed for the '7.75-5/8T' Compact Heat Exchanger

the heat capacity rate ratio CR was computed as in Equation 5.10.

$$CR = \frac{\dot{C}_{min}}{\dot{C}_{max}} \tag{5.10}$$

The number of transfer units and heat capacity rate ratio were then used together to obtain the effectiveness (ϵ) by tables in Kays and London [43]. The effectiveness as a function of the engine speed is shown in Figure 5.8 for the '7.75-5/8T' configuration.

The effectiveness is the ratio of the actual heat transfer rate ($\dot{Q}$) to the maximum possible heat transfer rate ($\dot{Q}_{max}$) for a given system, as shown in Equation 5.11.

$$\epsilon = \frac{\dot{Q}}{\dot{Q}_{max}} \tag{5.11}$$

The maximum heat transfer rate is defined as the product of the minimum heat capacity rate and the difference of the temperatures of the inlet streams, as shown in Equation 5.12.

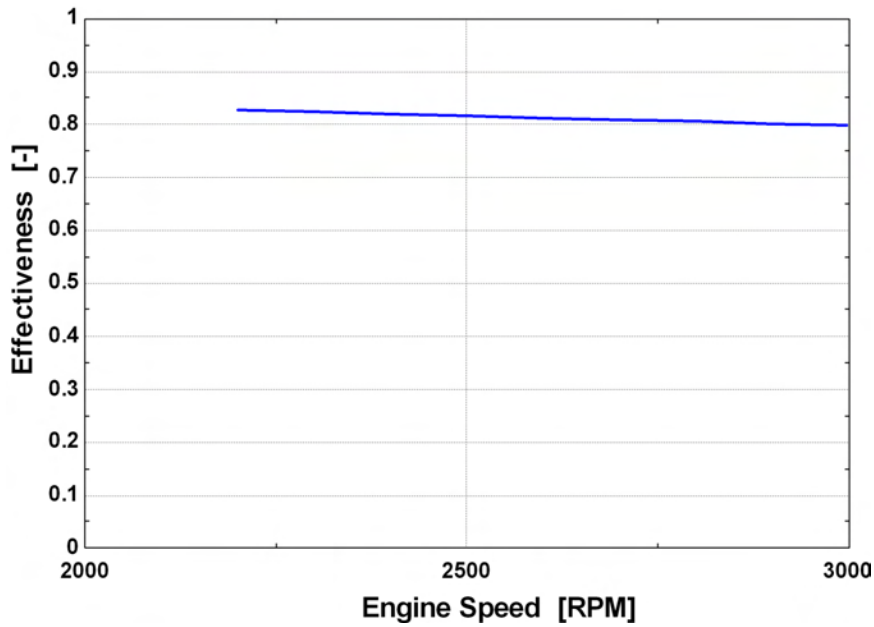

Figure 5.8: Effectiveness for the Exhaust Gas Side as a Function of the Engine Speed for the '7.75-5/8T' Compact Heat Exchanger

$$\dot{Q}_{max} = \dot{C}_{min}(T_{exhaust,inlet} - T_{toluene,inlet}) \tag{5.12}$$

Thus, $\dot{Q}_{max}$ can be found since the variables in Equation 5.12 are all known from the GT-Power model or the assumptions. Therefore, the heat transfer rate for the system can be computed using Equation 5.11. This provides a solution for how much heat can be recovered utilizing a typical compact heat exchanger in the exhaust system. The heat transfer rate for the '7.75-5/8T' configuration is shown in Figure 5.9 as a function of the engine speed.

The pressure drop on the exhaust side of the heat exchanger can then be calculated using the friction factor found from the tables in Kays and London that relate the Reynolds number to the friction factor for various heat exchanger types and geometries. The pressure drop equation is shown in Equation 5.13.

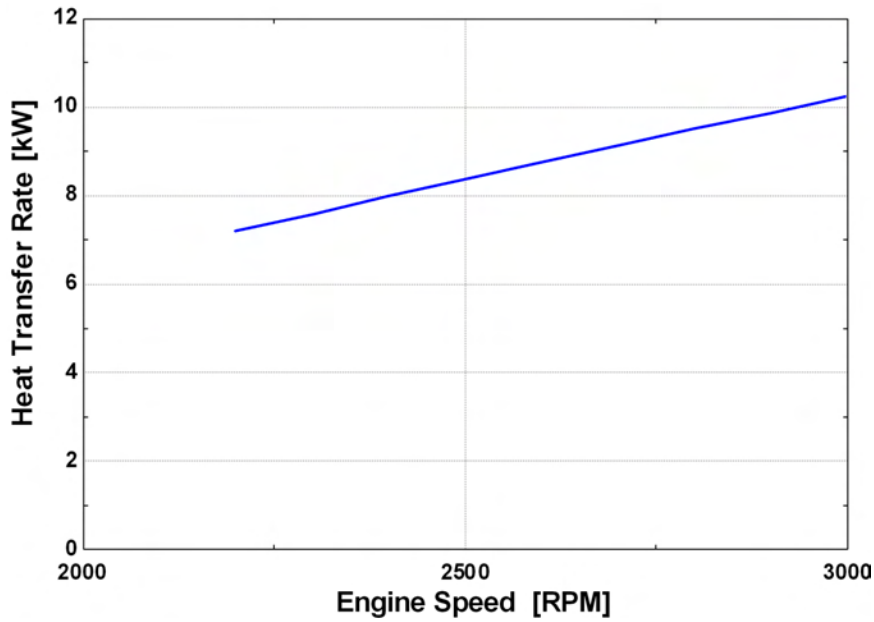

Figure 5.9: Heat Transfer Rate as a Function of the Engine Speed for the '7.75-5/8T' Compact Heat Exchanger

$$\Delta P = \left(\frac{\dot{m}}{A_{xs,min}}\right)^2 (\nu)(f)2\left(\frac{L}{D_h}\right) \tag{5.13}$$

In Equation 5.13, $A_{xs,min}$ is the minimum cross sectional area for the flow of exhaust gas, which was found to be 0.0012 m^2, and ν is the specific volume of the exhaust gas. The pressure drop for the '7.75-5/8T' compact heat exchanger as a function of the engine speed is shown in Figure 5.10

The resulting pressure drop calculated from Equation 5.13 is then compared to results from the Prius model to obtain correlations for the backpressure effects on the engine power. The GT-Power model used in this analysis was the same Detailed Prius model that was used in Chapter 4. The cross sectional area of an orifice in the exhaust system was modified until the backpressure was similar to the pressure drop obtained from Equation 5.13. This provided an engine power given the backpressure constraints due to the compact heat exchanger

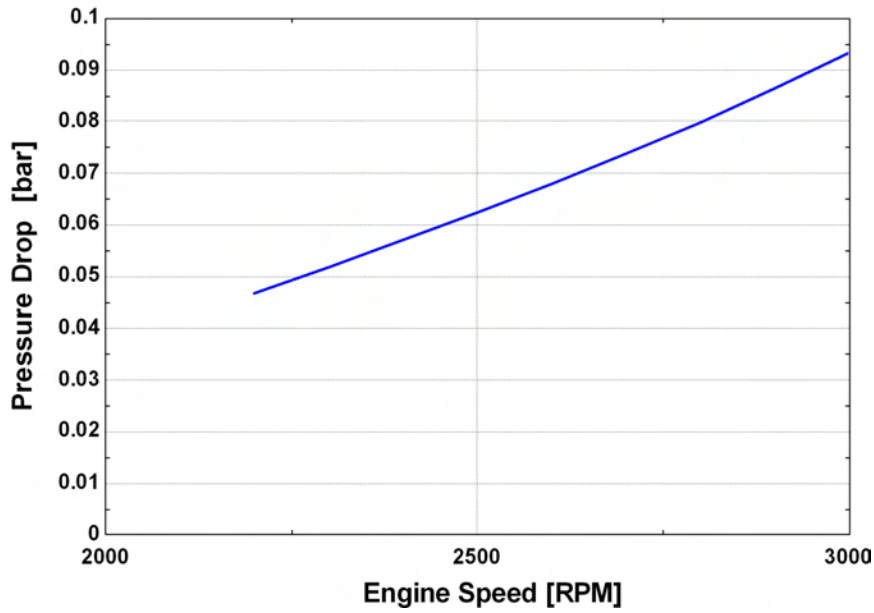

Figure 5.10: Pressure Drop as a Function of the Engine Speed for the '7.75-5/8T' Compact Heat Exchanger

in the exhaust system. The plot of engine power as a function of backpressure, as modeled in GT-Power for an engine speed of 2000 RPM, is shown in Figure 5.11.

The engine power obtained from the GT-Power simulation was summed with the power that could be generated from the heat recovered from the compact heat exchanger. This total system power was then compared to the engine power that results without any heat recovery device obstruction in the exhaust stream to determine the practicality of heat recovery from the exhaust system.

The results for the total system power are then optimized by varying the length of the heat exchanger. The total system power requires the Rankine cycle efficiency, which was assumed to be 0.25. This value was used only in the optimization of the length. These results are shown in Figure 5.12. The average percent power difference is the percentage difference between the total system power (Engine and Heat Exchanger) and the engine without a heat exchanger.

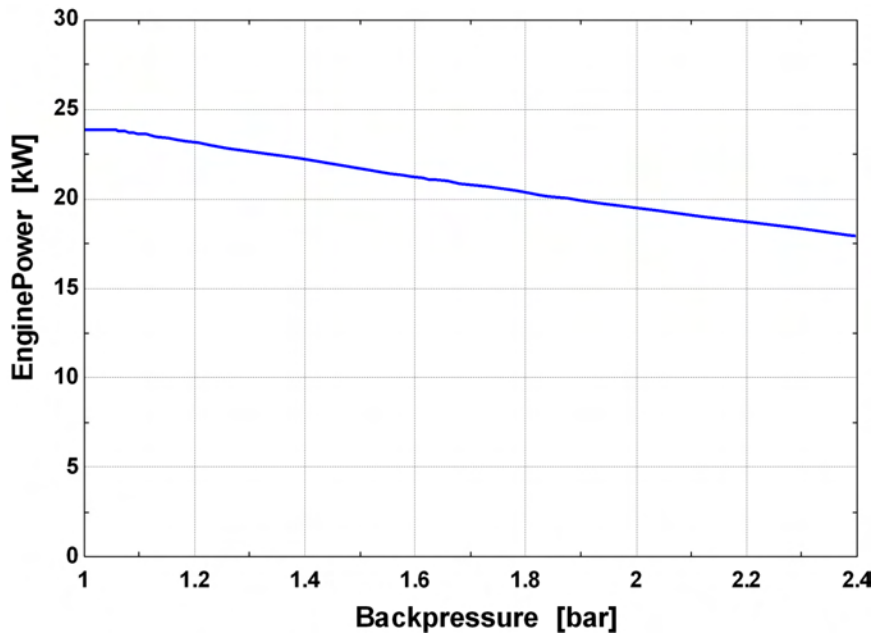

Figure 5.11: Engine Power as a Function of the Backpressure at an Engine Speed of 2000 RPM

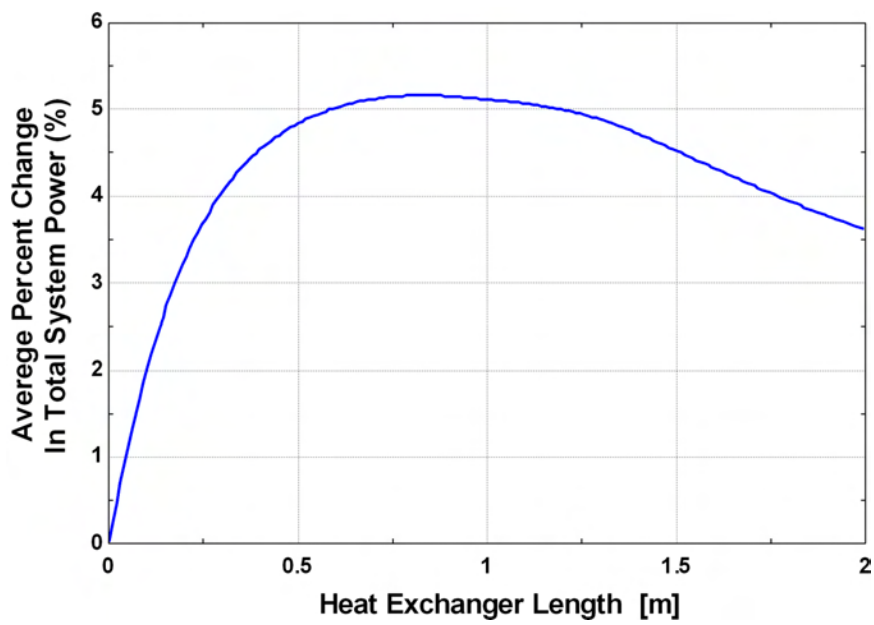

Figure 5.12: Average Percent Power Difference as a Function of the Heat Exchanger Length for the '7.75-5/8T' Compact Heat Exchanger

As shown in Figure 5.12, the optimum length for the '7.75-5/8T' compact heat exchanger is 0.83 m. At heat exchanger lengths larger than 0.83 m, the backpressure effects on the engine begin to diminish the overall system power. For lengths shorter than 0.83 m, there is still opportunity to recover more heat, thus a length of 0.83 m is ideal for the '7.75-5/8T' heat exchanger.

The power that can be generated from the heat recovered was calculated as the product of the heat transfer rate found in Equation 5.11 and a Rankine cycle efficiency. The Rankine cycle efficiency was estimated to be between 0.1 to 0.4, as this is a typical to optimistic range for efficiencies of the Rankine cycle.

The total system power was calculated as a function of the Rankine cycle efficiency. This analysis examined engine speeds in 500 RPM increments from 2000 RPM to 3000 RPM, which are shown in Figures 5.13 through 5.14. These plots show the engine baseline power, which is the power for the engine without any exhaust obstructions, the engine power including the backpressure effects of the compact heat exchanger and the total power (engine power and power from compact heat exchanger) as a function of the Rankine cycle efficiency.

The results are further explored in Figure 5.15, which shows the percent change in power with reference to the baseline power for all of the engine speeds studied at the Precat location.

As shown in Figure 5.15, gains in total system power are achieved at all engine speeds. A similar analysis was performed on other configurations of compact heat exchangers for comparison. The details of these results are shown in Appendix A. The results from the other heat exchanger analysis provided similar results, with variations in the magnitude of power recovered for each heat exchanger configuration.

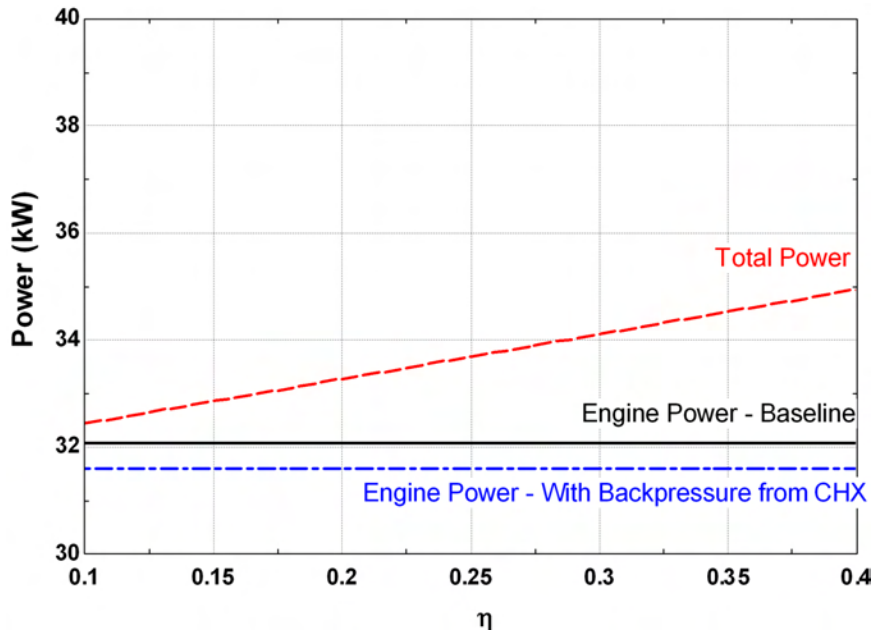

Figure 5.13: Power vs. Rankine Cycle Efficiency for a Compact Heat Exchanger with Continuous Fins ('7.75-5/8T') in the Exhaust System with an Engine Speed of 2500 RPM Using Toluene as a Working Fluid

5.3 Conclusions

This analysis shows that significant gains can be achieved by implementing a compact heat exchanger system in the exhaust system that drives a Rankine cycle to produce additional power. The pressure drop due to the compact heat exchanger designs are much smaller than for the turbine studied in Chapter 4, allowing for heat recovery without drastic effects on the engine power. All of the compact heat exchangers designs that were analyzed, first used water as the working fluid for comparison purposes as shown in Appendix A. Each one of these designs provided gains in overall system power. The '7.75-5/8T' compact heat exchanger provided the best results and was studied in this chapter using toluene as the working fluid. Toluene is used in organic Rankine cycles and might be a good fit for the conditions of a passenger vehicle heat recovery system. The results of this analysis show that heat recovery from the exhaust system is a possibility in gas/electric passenger vehicles

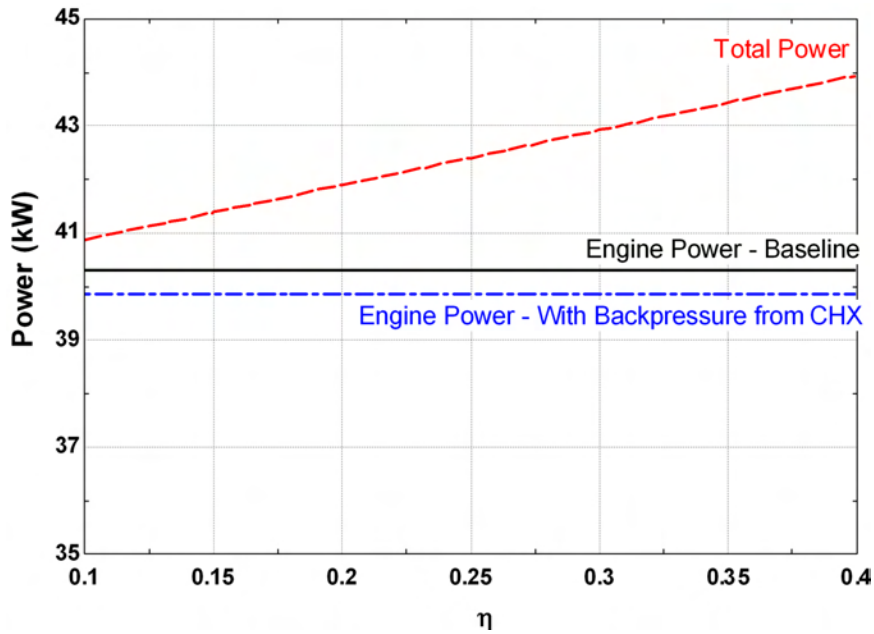

Figure 5.14: Power vs. Rankine Cycle Efficiency for a Compact Heat Exchanger with Continuous Fins ('7.75-5/8T') in the Exhaust System with an Engine Speed of 3000 RPM Using Toluene as a Working Fluid

such as the Toyota Prius.

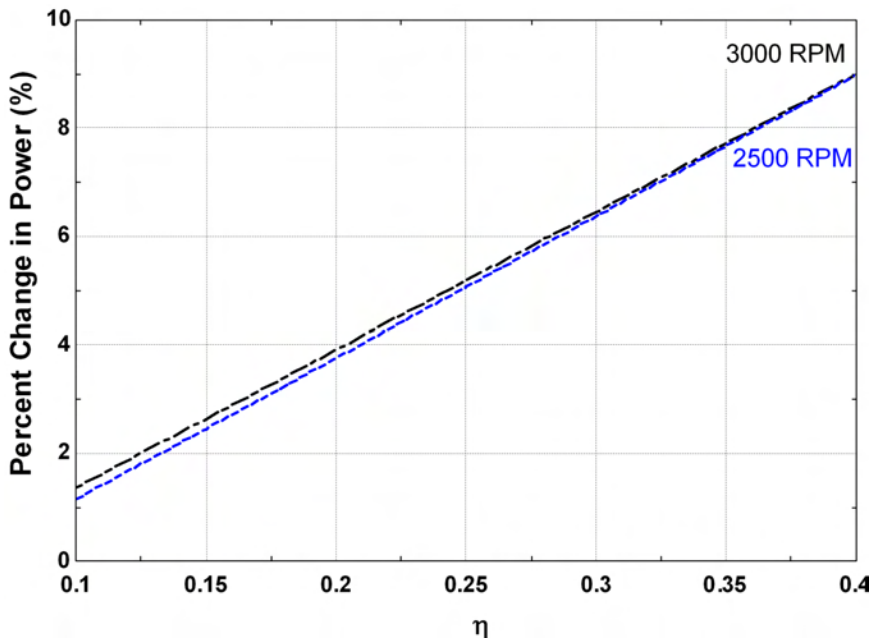

Figure 5.15: Percent Change in Power vs. Rankine Cycle Efficiency for a Compact Heat Exchanger with Continuous Fins ('7.75-5/8T') in the Exhaust System at the Precat location Using Toluene as a Working Fluid

Chapter 6

Experimental Investigation of Higher Engine Coolant Temperatures

6.1 Experimental Exploration of the Redesign of the Engine Coolant System to Optimize Energy Recovery

6.1.1 Introduction

The theoretical and finite time availability analyses (Chapter 3) showed that the coolant and exhaust effluents provide approximately equal opportunity for waste heat recovery. Additional exploration of the finite time relationship to the maximum power possible showed additional opportunity for the coolant system with increased coolant temperatures. An innovative engine cooling system design that optimizes the conditions for energy recovery is investigated experimentally.

As shown in Chapter 3, the availability in the coolant was 8.9% of the fuel energy. The finite time analysis revealed a potential of 1.2% of the fuel energy for energy recovery. However, the parametric analysis on the finite time calculation of the coolant temperature demonstrated that increasing the coolant temperature would provide significant increases for energy recovery. Therefore, the exploration of new coolant system designs is of interest.

For the combustion process to occur in a manner that is similar to current typical operation, the heat removed through the coolant needs to be the same. Equation 6.1 is for the heat rate, $\dot{Q}$, for a convective process.

$$\dot{Q} = (htc)(Area)(T_{surf} - T_{\infty}) \tag{6.1}$$

The variables htc and $Area$ in Equation 6.1 are the average heat transfer coefficient and the heat transfer area, respectively. The temperatures in Equation 6.1 are the temperature of the surface (T_{surf}) and the temperature of the bulk fluid (T_∞).

By applying Equation 6.1 to an engine cylinder, the T_{surf} variable is the temperature on the outside of the cylinder wall and the T_∞ variable is the coolant temperature. The $Area$ term is the area of the outer wall of the engine cylinder that is in contact with the engine coolant. For the redesign of the coolant system, it is assumed that the heat transfer area (cylinder design) stays the same. If the coolant temperature (T_∞) is increased, then the heat transfer coefficient must also rise for the heat rate ($\dot{Q}$) to stay constant. Therefore the main focus is to find a way to increase the heat transfer coefficient for the energy transfer between the cylinder wall and the engine coolant. One method could be the use of spray cooling techniques on the outside surface of the engine cylinder.

6.1.2 Spray Cooling

The use of sprays for cooling has found success in high heat flux applications. High heat transfer performance has been demonstrated with the use of spray cooling, which offers a solution for cooling electronic devices where the performance of the device is currently limited by the heat removal system. Spray cooling also offers an opportunity to replace existing cooling systems to increase heat removal performance and efficiency. A spray cooling system is designed with an array of nozzles that are positioned so that flow through the nozzles will impact the surface that is generating heat. Fluid droplets are atomized as they exit the nozzles and impact the heated surface with a high velocity. A turbulent thin film develops on the heated surface as the fluid particles impact the heated surface. It has been demonstrated that heat transfer coefficients of 10,000 $\frac{W}{m^2K}$ or more can be attained for the turbulent thin film conditions that develop on the heated surface in spray cooling applications [47].

The application of spray cooling to engine cooling applications offers an opportunity to achieve better overall cooling performance and system efficiency. Additionally, spray cooling may offer greater potential for energy recovery from the engine coolant. Multiphase cooling has been attempted in internal combustion engines, however much difficulty has been encountered with providing even cooling throughout the system. The use of spray cooling allows for an even distribution of coolant throughout the engine cooling system. The higher heat transfer performance of the spray cooling techniques would allow the cooling system to utilize less space and liquid than traditional engines, which would reduce the size and weight of the engines. The system could be controlled simply and reliably, as the heat transfer performance has been correlated with coolant flow rate [48].

6.1.3 Experimental Setup

The experimental investigation of spray cooling for use in the engine coolant system began with the simulation of an engine cylinder. A 30.5 cm tall cylinder with a 2.5 cm cap welded on top was used to model an engine cylinder, which is made of aluminum alloy 6061. The cylinder has a 8.9 cm diameter with a 0.64 cm wall thickness. The heat from the combustion process is simulated with a propane torch that heats the inside of the cylinder. Four 0.64 cm diameter holes were drilled in the top of the cap to provide an exit for the exhaust gases. Type T thermocouples were embedded in the cylinder wall at four locations. These locations are approximately 5.1 cm and 12.7 cm down from the top of the cylinder on two sides of the cylinder. At each location, there are 3 thermocouples; one on the inner cylinder surface, one on the outer cylinder surface and one in the middle. These holes are drilled at a 45° angle so that the ends of the thermocouples will be horizontally inline within the cylinder. Additionally, 8 thermocouples were attached to the various locations on the outside of the cylinder to obtain a good estimate of the outer cylinder wall temperature. A picture of the

aluminum cylinder with the thermocouple holes is shown in Figure 6.1.

A spray device was built to surround the engine cylinder with spray nozzles. The spray nozzles were made with aluminum tubing with a 0.48 cm outside diameter and a 0.89 mm wall thickness. The nozzles were made by cutting 0.64 mm thick slots at a 45° angle into the tubing to a depth just above the inside of the tube. A 0.5 mm drill bit was then used to produce the hole in the slot through to the inside surface of the tube. The slots were placed 5 mm apart on the tube with every other one placed at a 30° offset around the tube. This allows the sprays to be distributed more evenly on the surface of the cylinder. Each aluminum tube was made with 25 nozzles, which provides a spray area of approximately 8 cm vertically. The top of the aluminum tubes were cut off at a 45° angle so the fluid would be distributed with minimal pressure drop. A picture of one of the nozzle tubes is shown in Figure 6.2.

A 0.95 cm O.D. copper tube was used as the fluid distribution manifold. The copper tube was formed in a circle of approximately 10.2 cm diameter. This gives the spray device enough room to fit around the aluminum cylinder. Two of these circular shaped copper tubes were made and had holes drilled in them so that the nozzle tubes could be joined vertically between them. The nozzle tubes were placed around the entire circumference of the copper tube circle, except for the two locations where the fluid inlet tubes are located. The fluid inlet tubes are the same material and diameter as the nozzle tubes, but the wall thickness is only 0.56 mm. These tubes are placed on opposing sides of the copper tube circle with two tubes on each side. The fluid inlet tubes run entirely through the bottom copper tube where they connect to the fluid inlet manifold outside of the spray device system. These tubes run up to the top copper tube where the fluid is distributed to the entire array of nozzle tubes. The aluminum nozzle tubes were connected to the copper tubes with epoxy. A 3D CAD drawing of the spray device is shown in Figure 6.3.

A picture showing the top view of the spray array is shown in Figure 6.4. This picture

Figure 6.1: Aluminum Cylinder with Holes Drilled for Theromocouples

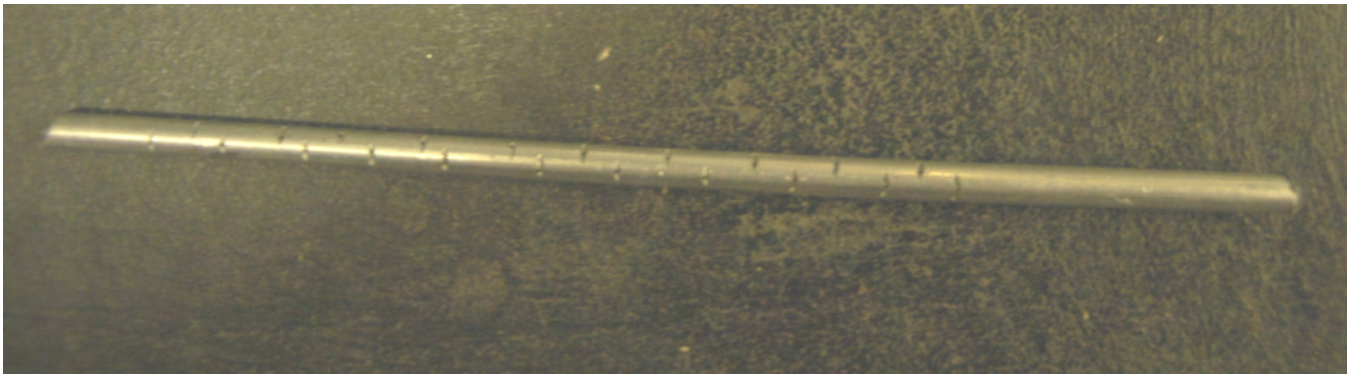

Figure 6.2: Aluminum Nozzle Tube that was Machined for use in the Spray Device

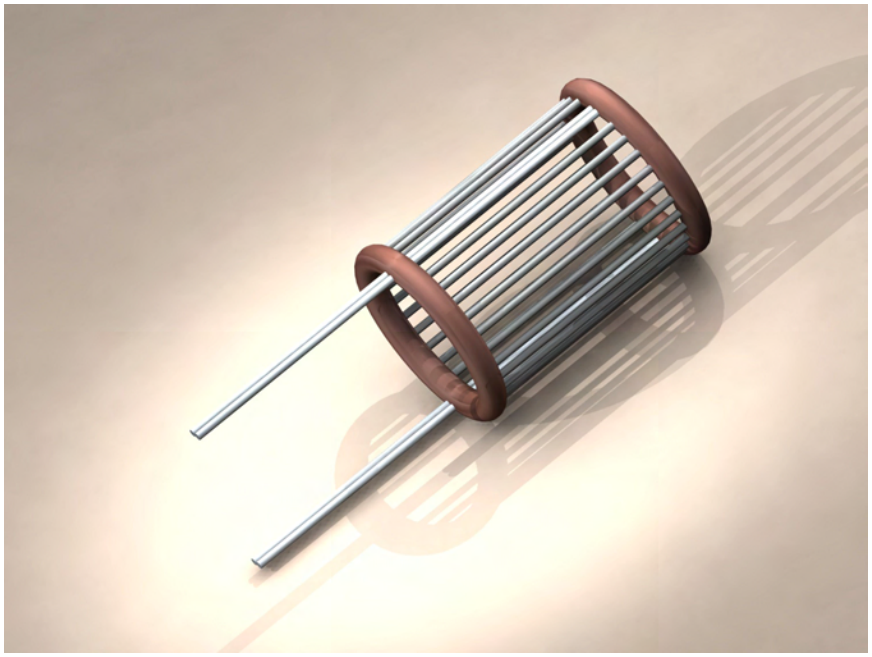

Figure 6.3: CAD Drawing of the Spray Device Made for the Experimental Work

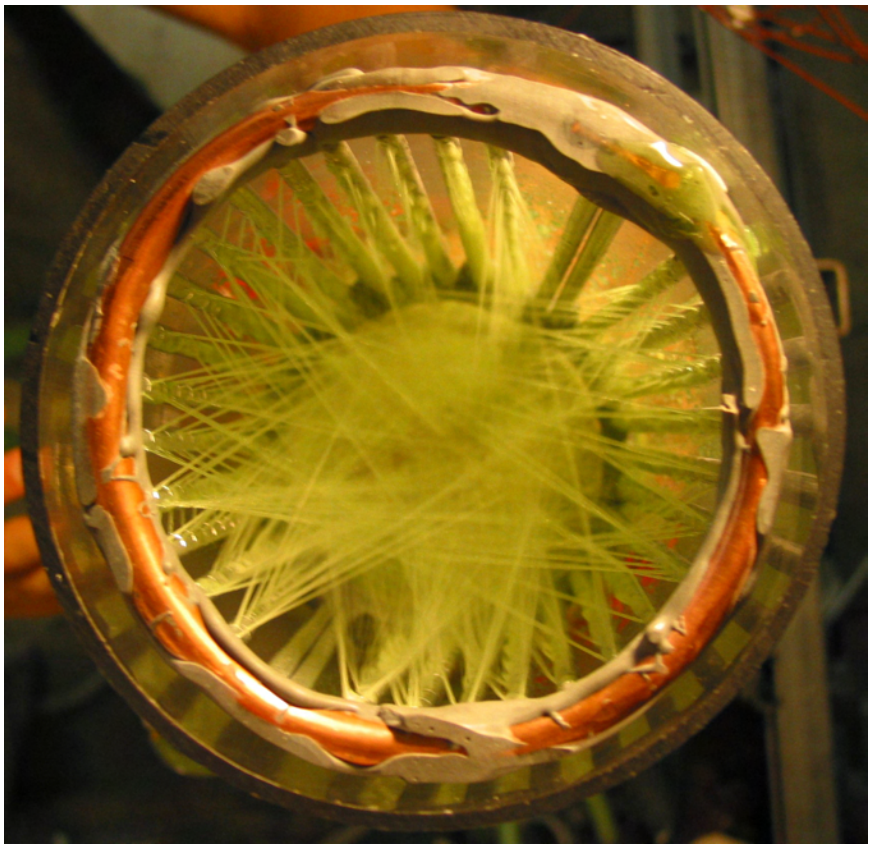

Figure 6.4: Top View of the Spray Array Without the Aluminum Cylinder in Place

does not include the aluminum cylinder, which was placed inside the spray array during testing.

The aluminum cylinder is surrounded by the spray device, which is surrounded by a 12.7 cm outer diameter, 3.2 mm thick polycarbonate cylinder. This allows all of the coolant to be kept inside the polycarbonate cylinder, while allowing visualization of the spray performance. The aluminum cylinder, spray device and polycarbonate cylinder are capped on the top with a 15.2 cm $\times$ 15.2 cm $\times$ 1.9 cm piece of PTFE and on the bottom with a 15.2 cm $\times$ 15.2 cm $\times$ 1.3 cm piece of polyetherimide. These two pieces were machined so that aluminum cylinder and polycarbonate cylinder can be sealed with O-rings. The entire device is then held together with four $\frac{1}{4}$" threaded rods that go through the corners of the

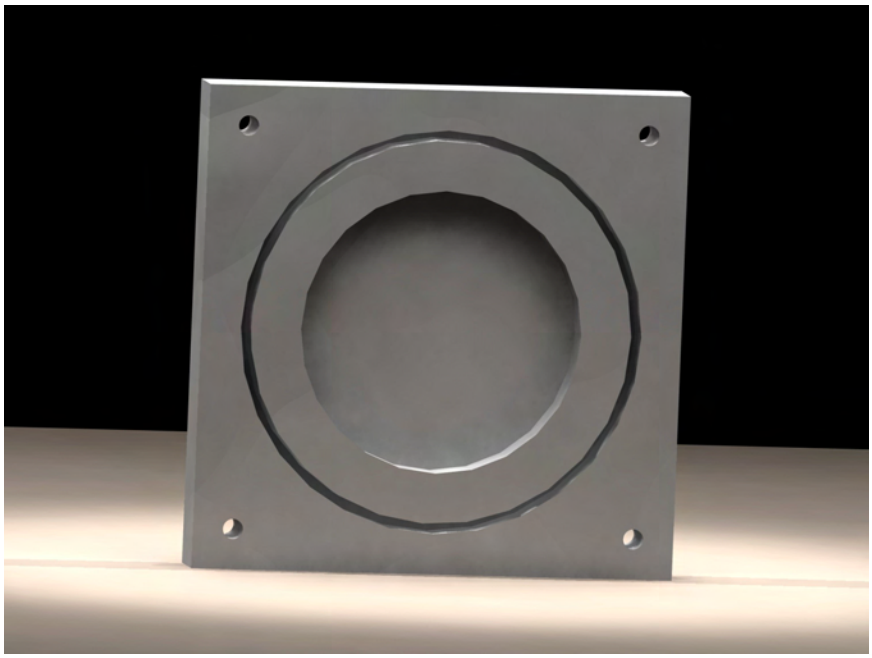

Figure 6.5: CAD Drawing of the Teflon piece (Top Cap)

Teflon and polyetherimide and are secured with wing nuts. CAD drawings of the Teflon and polyetherimide pieces are shown in Figures 6.5 and 6.6.

The square piece of teflon also has four holes that line up with the holes in the aluminum cylinder for the exhaust products to exit the system. The square piece of polyetherimide includes six $\frac{3}{8}$"NPT holes for draining the coolant from the system. Additionally, four $\frac{3}{16}$" holes are included in the polyetherimide piece for the fluid inlet tubes to enter for the spray device.

When in operation, the fluid enters the spray device via the inlet tubes on the outside of the polyetherimide piece. The fluid enters these tubes, which carries it to the top circular copper tube. The copper tube distributes the fluid around to the top of all of the nozzle tubes. The fluid then enters the nozzle tubes at the top and is carried out the spray nozzles onto the aluminum cylinder surface. Next, the fluid runs down the side of the aluminum cylinder surface, where it falls to the polyetherimide piece and out the drains. A CAD

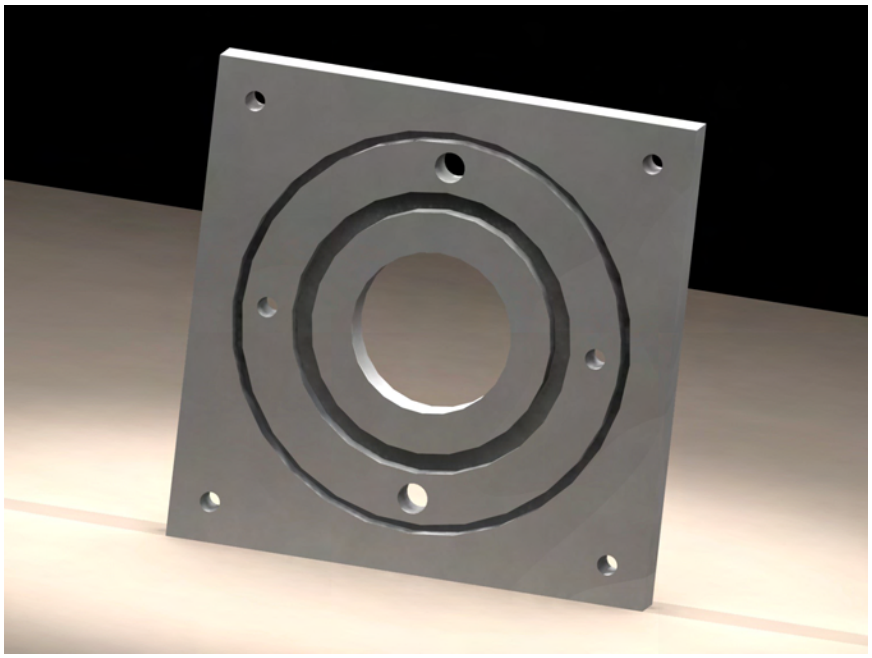

Figure 6.6: CAD Drawing of the Polyetherimide piece (Bottom Cap)

drawing of the entire spray device is shown in Figure 6.7, and a picture of the assembled spray device is shown in Figure 6.8.

The six drains in the bottom of the polyetherimide piece are connected using compression fittings, which are attached to $\frac{3}{8}$" O.D. FEP tubing. These tubes are connected to an aluminum distribution manifold which attaches to the $\frac{1}{2}$" drain tube. The drain tubes use gravity to drain the fluid back into a tank. The fluid is pumped out of the tank using a gear pump. The liquid is then pumped through a filter and a plate heat exchanger to remove the heat from the fluid using city water. The heat transfer fluid continues through a flowmeter and into the inlet manifold, which distributes the fluid to four $\frac{3}{16}$" FEP tubes that connect to the aluminum inlet tubes of the spray device. Additionally, a differential pressure gauge is connected between an inlet and outlet FEP tube to obtain the pressure drop through the device. There are also thermocouples in the inlet and outlet manifolds that measure the incoming and exiting fluid temperature. A schematic of the experimental setup is shown

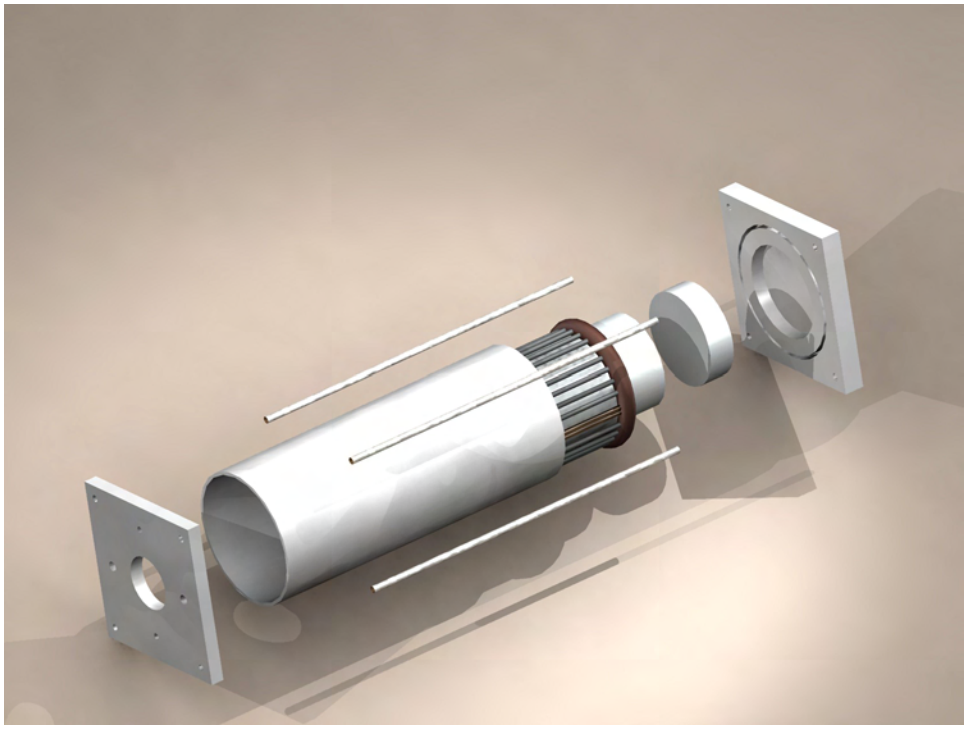

Figure 6.7: CAD Drawing of the Entire Spray Device)

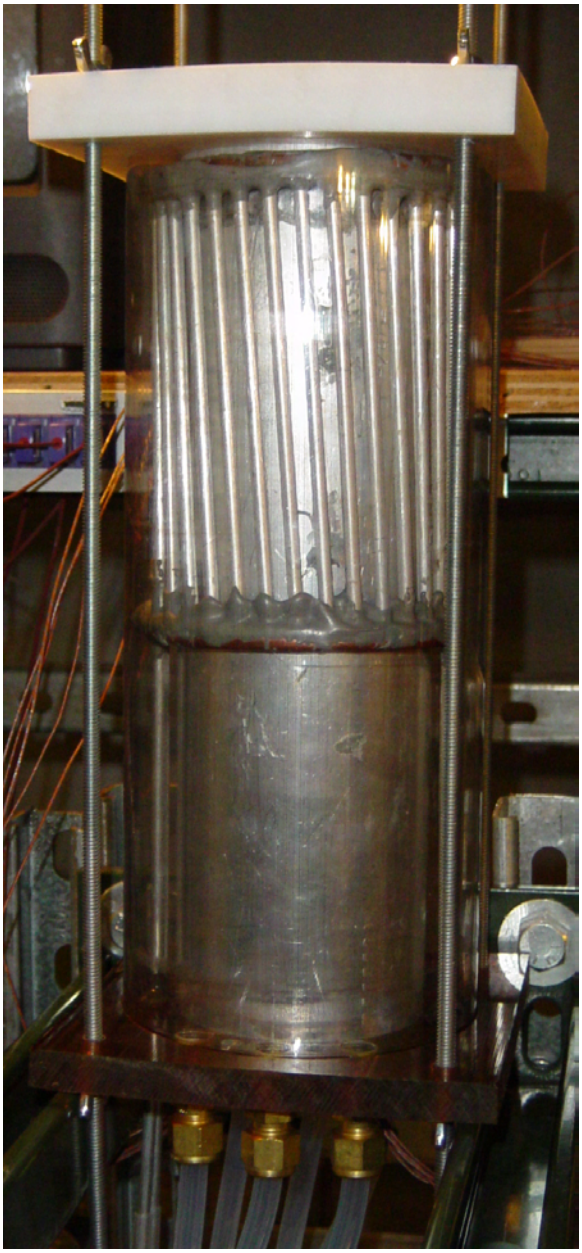

Figure 6.8: Picture of the Assembled Spray Device)

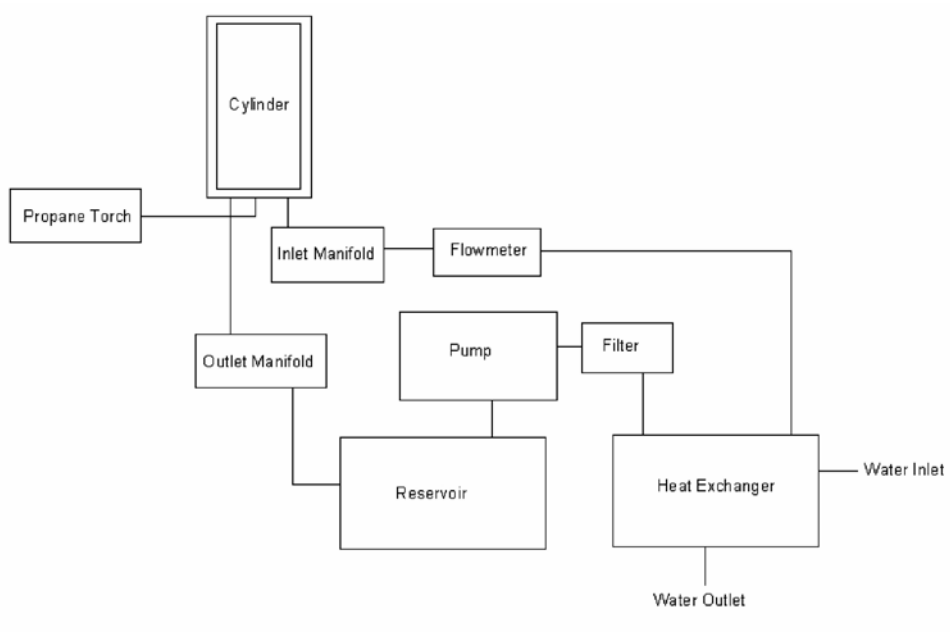

Figure 6.9: Schematic of the Experimental Setup

in Figure 6.9. A picture of the components making up the experimental setup is shown in Figure 6.10.

The fluid used in this experiment is pure ethylene glycol (antifreeze). The boiling point of ethylene glycol diminishes as water is added to the mixture [49]. Since this experiment is investigating higher coolant temperatures, it is best to use pure ethylene glycol. Other fluids, such as those used in Organic Rankine cycles, could be investigated in the future should this experiment produce favorable results.

The heat from the combustion process is modeled with a propane torch that is mounted so that the flame is inside the cylinder. The torch is fed with propane from a tank that sits on a scale. The scale is used to measure the rate at which the propane is consumed. A picture of the propane torch mounted at the base of the spray device is shown in Figure 6.11.

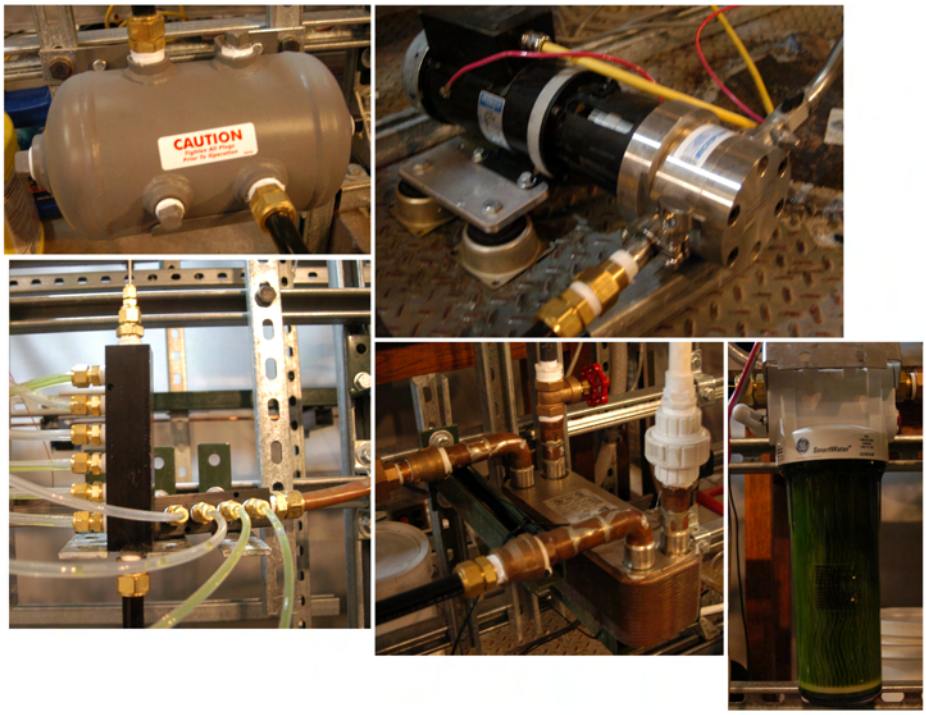

Figure 6.10: Experimental Components (Clockwise Starting from the Upper Left)1)Tank(Reservoir)2)Pump 3)Filter 4)Heat Exchanger 5)Outlet and Inlet Manifolds

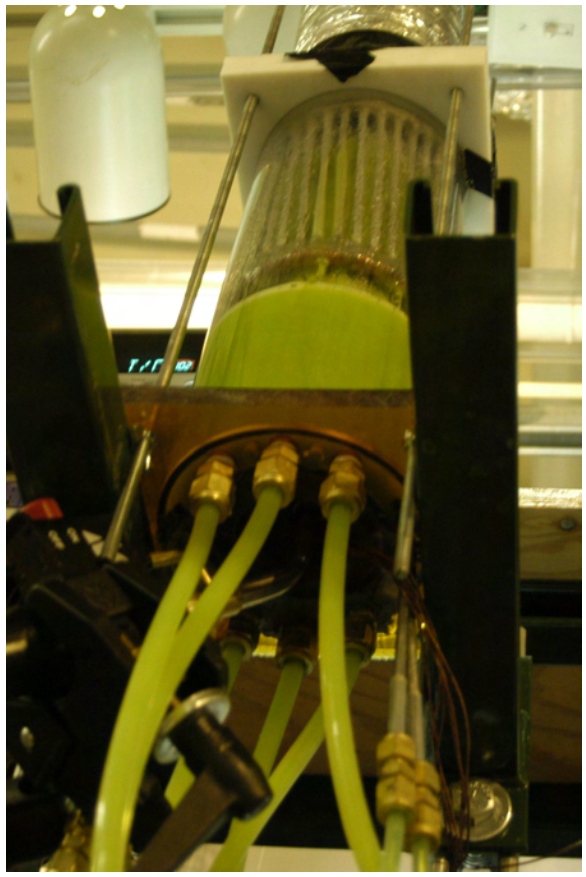

Figure 6.11: Propane Torch Mounted at the Base of the Spray Device

Uncertainty in Measurements

As with all types of experimental work, the measurements taken for this experiment have some uncertainty. The method of the uncertainty propagation that was used for analyzing the data in this experiment is described in NIST Technical Note 1297 [50]. This method of uncertainty propagation is built in to Engineering Equation Solver (EES) [44], which was used for the data analysis and uncertainty propagation.

All of the thermocouples used for the temperature measurements were calibrated using a NIST traceable temperature bath, accurate to $0.01°C$. The thermocouples were calibrated using the same wires and data acquisition system that were used during the data collection.

The temperature measurements from the thermocouples were compared to the temperature bath measurements as shown in Figure 6.12, which shows the data for the thermocouple used to measure the fluid outlet temperature.

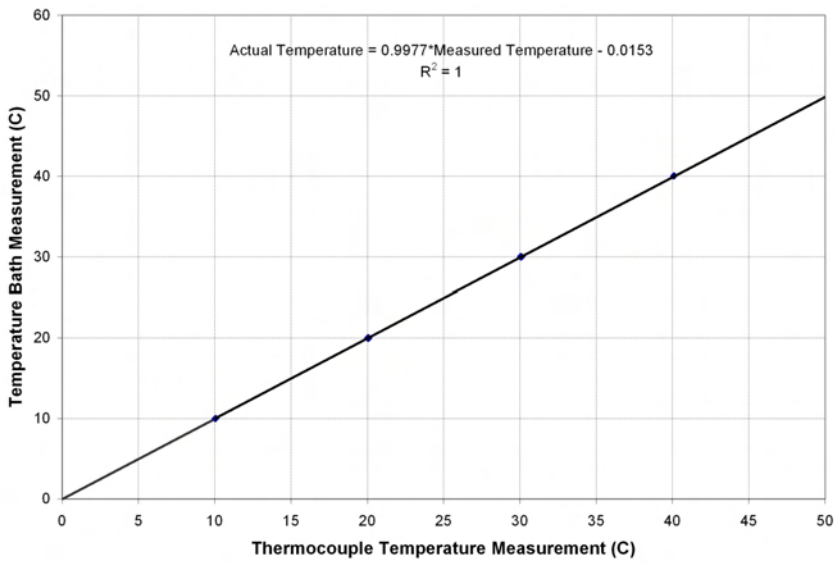

Figure 6.12: Comparison of the Temperatures Measured from the Thermocouple and the Temperature Bath for the Fluid Outlet Thermocouple

Figure 6.12 shows that there is a slight offset in the thermocouple measurement and the temperature bath measurement. This offset was compensated for by using the linear fit equation shown in Figure 6.12. The resulting maximum error after adjusting for the offset was $0.06°C$. The sum of the maximum error found from the calibration and the temperature bath is then $0.07°C$, which is considered to be the total uncertainty of the temperature measurements of the fluid. This procedure was used to calibrate all of the thermocouples.

The cylinder surface temperatures have an additional uncertainty. The placement of the thermocouples onto the cylinder surface required a small divot in the cylinder surface. The divot was drilled to be approximately 75 microns larger than the thermocouple bead. The thermocouple bead was then forced in the hole so that it was in contact with the cylinder

and held in place on its own. Cyanoacrylate glue was then applied on the outer surface of the bead to shield it from measuring the fluid temperature. This measurement technique results in an additional uncertainty due to the measurement being taken at a slightly smaller radius than the outer cylinder. An absolute uncertainty of $0.5°C$ was used for the measurements of the cylinder surface temperature.

Uncertainty also exists in the flowrate measurement, which was made by a NIST traceable gear flow meter with an accuracy of 0.5% of reading. Thus, the uncertainty used for the flowrate measurements for data collection was 0.5%. The heat transfer area for the heat transfer from the cylinder to the fluid was used in the analysis of the data collected. The heat transfer area includes all of the area that is in contact with the fluid. The outside cylinder area for the cylinder which is 0.3 m tall and 0.09 m in outer diameter was calculated to be 0.085 m^2. However, portions of this area, such as the very top of the cylinder are not in contact with fluid. Thus, the uncertainty in the area used for the calculations is 5%.

Additionally, thermal properties are used in the data analysis, including the specific heat and density of ethylene glycol. These values are based on the temperature and concentration of the ethylene glycol. The calculated values of the density and specific heat were found using the fluid temperature measurements and 100% concentration of ethylene glycol. The concentration of the ethylene glycol is guaranteed to be at least 94.5%, and as described above the temperature measurements are accurate to $0.07°C$. Calculating the change in density and specific heat for these variations results in a difference of 0.6% and 4.3%, respectively. These values were used for the uncertainty calculation of the data that was analyzed.

6.1.4 Experimental Results

The pump used for this experiment provided a maximum flow rate of approximately 12 lpm for the experimental setup shown in Figure 6.9. The properties of the fluid at these

conditions don't allow for the liquid to disperse from the nozzles in a spray pattern; instead a jetting stream is produced by the nozzles. As the flow rate is increased from 0 lpm to 12 lpm, the jet stream force increases from a dribble to a strong impingement on the cylinder surface. The flow rates that were tested in this experiment ranged from 6.5 lpm to 11.5 lpm.

Data were collected by first adjusting the pump speed to the desired flow rate and then starting the torch inside the cylinder. The cooling water valve was opened to allow heat to be removed from the system. The fluid circulated through the system with the water, ethylene glycol and fuel flow rates constant until the temperatures on the cylinder approached steady state. At this point, the data collection began; this was a process that lasted approximately five minutes. The analysis of the data used averaged values collected during this interval.

The first set of data examined the variation of the flow rate. The cooling water valve was completely opened, which cooled the ethylene glycol to approximately $12°C$ prior to the heat addition to the cylinder. The fluid temperature entering the spray device would rise 1 or $2°C$ from this point as the system approached steady state. The inlet and outlet fluid temperatures for data collected at 8.5 lpm is shown in Figure 6.13.

Figure 6.13 shows a sharp increase in the fluid temperatures at 740 seconds, which is the point at which the propane torch inside the cylinder was turned on. The point of sharp decrease in fluid temperature at 950 seconds is the point at which the heat addition ceased. The fluid temperatures from 850 to 950 seconds are relatively constant, as the system has reached steady state, which is where the data were averaged for the heat transfer performance calculations. The outer cylinder surface temperatures for the same dataset show similar behavior, as shown in Figure 6.14.

The outer cylinder surface temperatures level off between $17°C$ and $27°C$ for the conditions of this dataset. The variation is due to the different locations of the temperature measurements. Some of the measurements were taken in an area of high nozzle density and others were taken where there is no direct impact of fluid, only a thin film of liquid that is

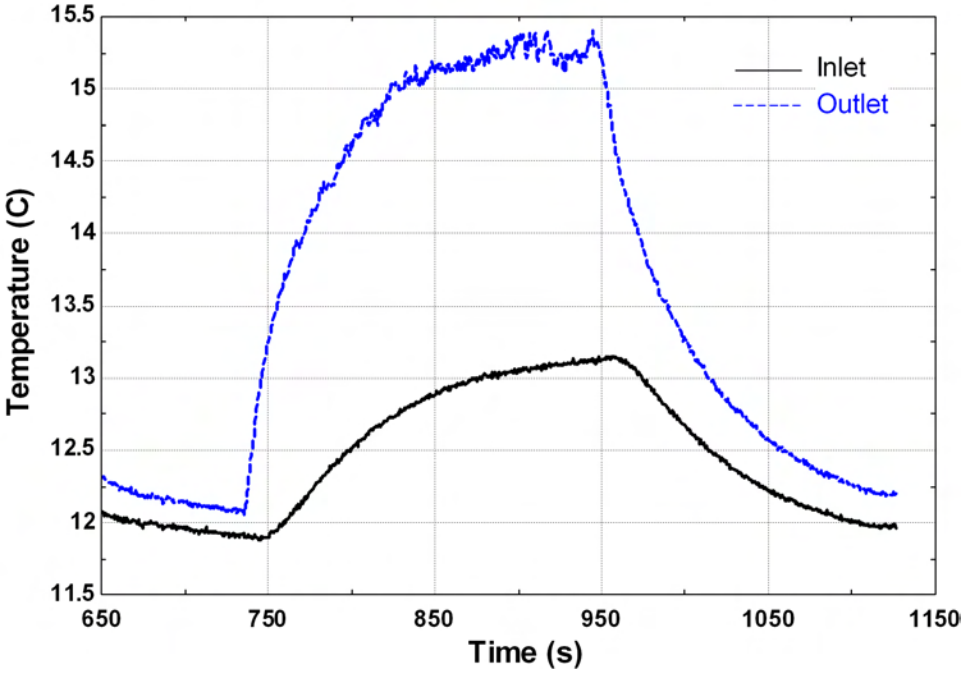

Figure 6.13: Fluid Temperatures at the Inlet and Outlet of the Spray Device for a Flowrate of 8.5 lpm

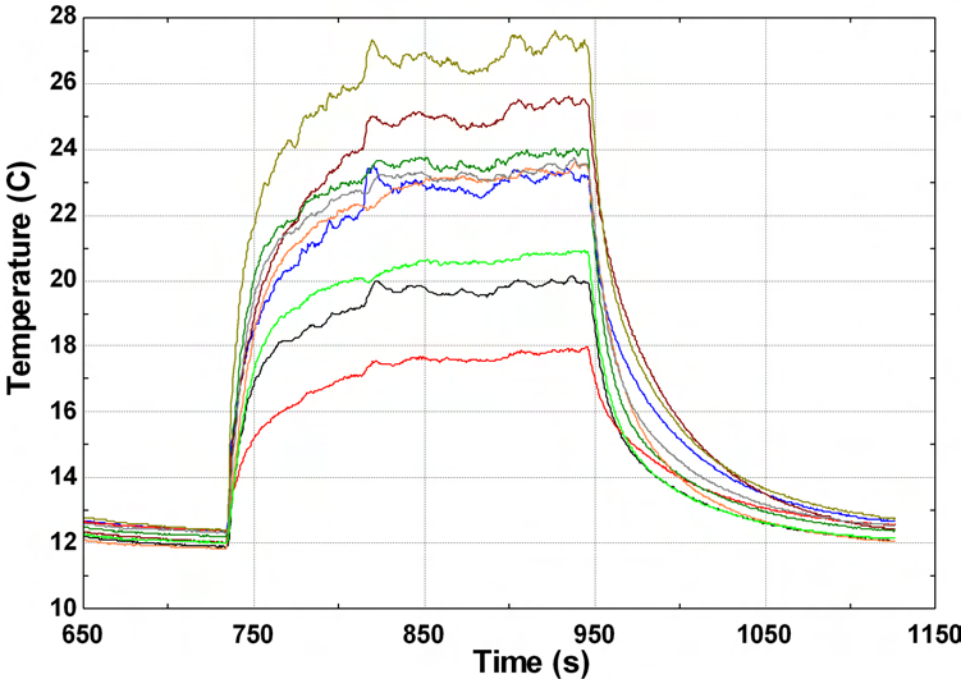

Figure 6.14: Outer Cylinder Surface Temperatures for a Flowrate of 8.5 lpm

draining. A temperature map was created, as seen in Figure 6.15, to show the temperature distribution on the cylinder surface. The y-axis refers to the vertical displacement along the cylinder and the x-axis refers to the distance around the cylinder. This map shows about $\frac{2}{3}$ of the distance around the cylinder. The dashed black lines in Figure 6.15 show the area of the cylinder that the sprays are directly impacting. The vertical black lines show the area where the fluid inlet tubes are located, as there are no nozzles at this location.

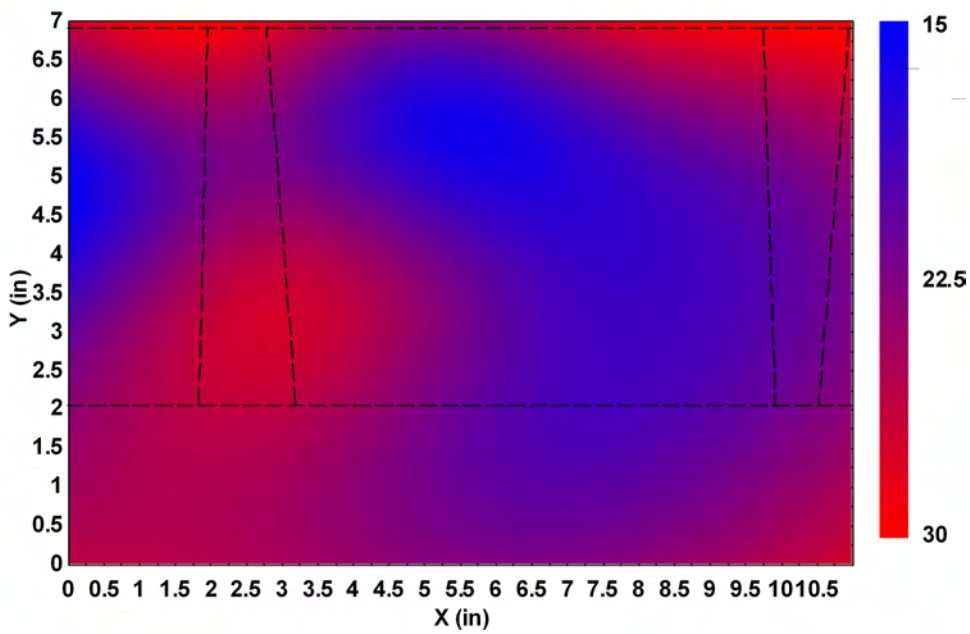

Figure 6.15: Outer Cylinder Surface Temperature Map for a Flowrate of 8.5 lpm

Figure 6.15 shows that the area directly impacted by the fluid is generally at lower temperatures than the area where nozzles are not located. The heat transfer rate, Q, of the flame of the propane torch to the fluid is shown for the 8.5 lpm dataset in Figure 6.16. The uncertainty of the heat transfer rate calculation ranged from 7.9% to 8.5% during the time when the torch was on. The uncertainty calculation was propagation based on the uncertainties of the temperature, area, fluid density, fluid specific heat and flowrate measurements. The average uncertainty of the heat transfer rate calculation during this

time was computed as 8.1%. Raising the uncertainty in the temperature measurements to $0.2°C$ results in an increase of the heat transfer rate uncertainty to 13.5%.

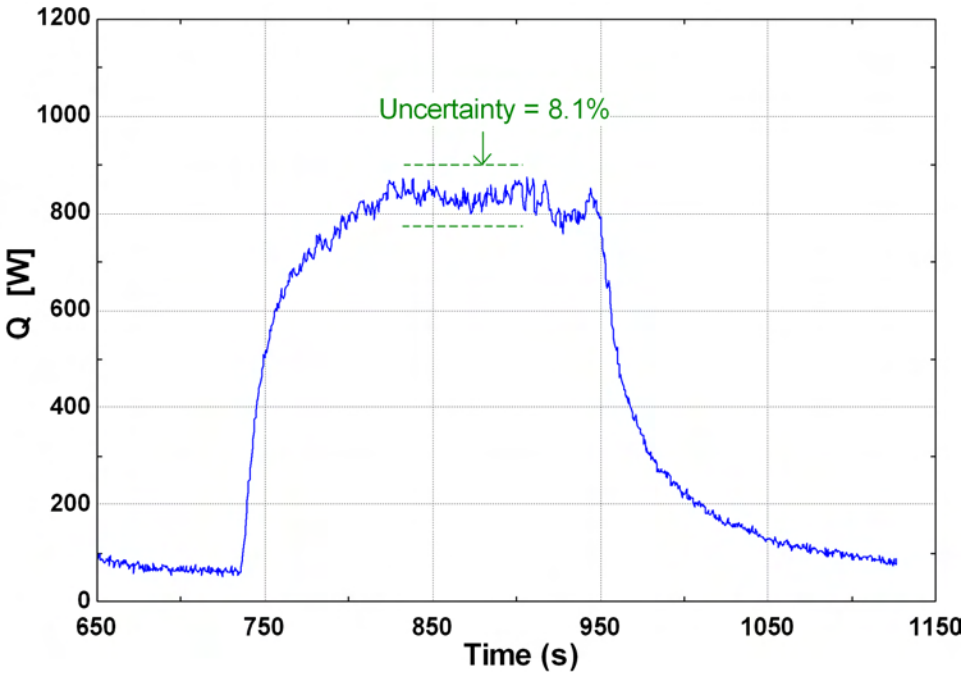

Figure 6.16: Heat Transfer Rate for the Dataset with a Flowrate of 8.5 lpm

Additionally, the heat transfer coefficient for the ethylene glycol fluid being sprayed on the outside of the cylinder was calculated and shown in Figure 6.17. The uncertainty of the heat transfer coefficient is a function of the uncertainty of the heat transfer rate and the temperature measurements. During the time when the torch was on, the range of uncertainty of the heat transfer coefficient was 9.3% to 9.8%, with and average of 9.4%. The heat transfer coefficient is compared to a correlation developed by Ashwood for spray cooling which is shown in Equation 6.2 [47].

$$htc = 0.129\frac{k}{\nu}Pr^{0.5}q''^{0.5} \tag{6.2}$$

Averages of the heat transfer rate and heat transfer coefficient shown in Figures 6.16 and

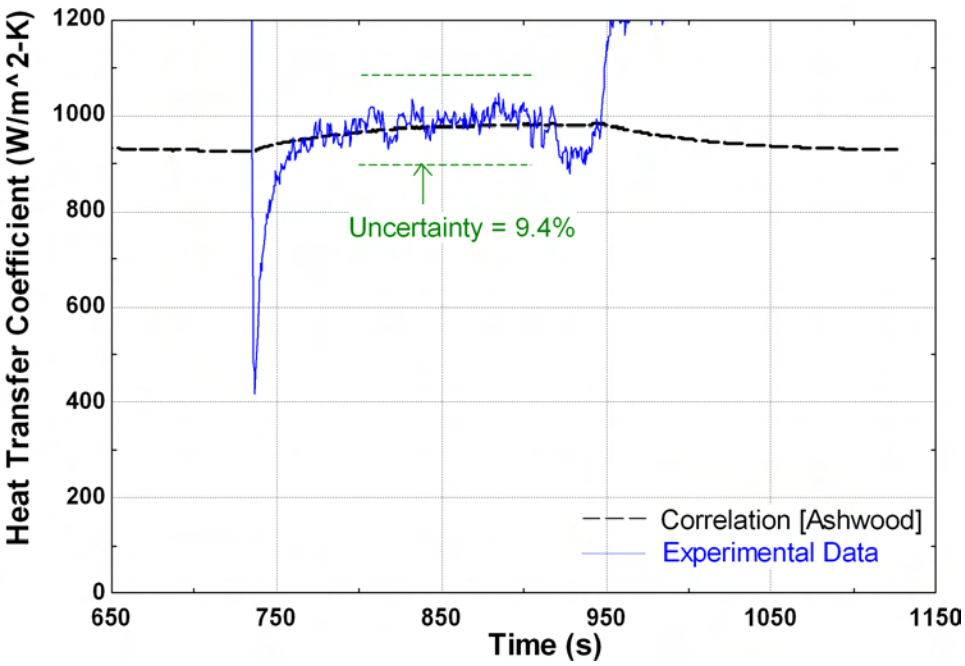

Figure 6.17: Heat Transfer Coefficient for the Dataset with a Flowrate of 8.5 lpm

6.17 were calculated to be 844 W and 998 $\frac{W}{m^2K}$. Data were collected in the same manner for flowrates of 6.8, 10.3 and 11.5 lpm. The temperature maps for these datasets are shown in Figures 6.18 - 6.20.

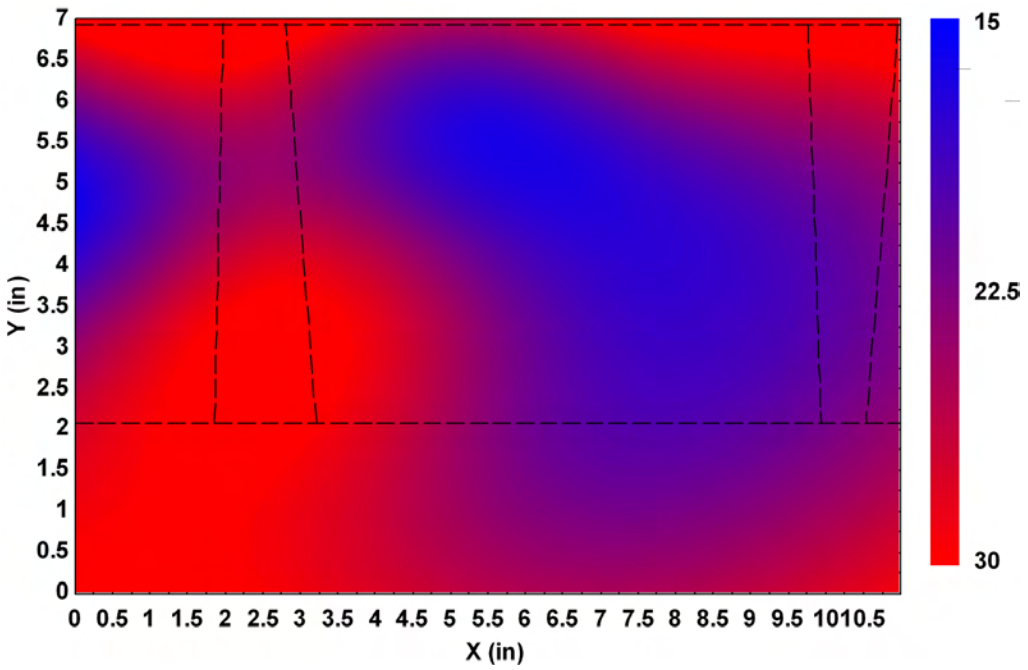

Figure 6.18: Outer Cylinder Surface Temperature Map for a Flowrate of 6.8 lpm

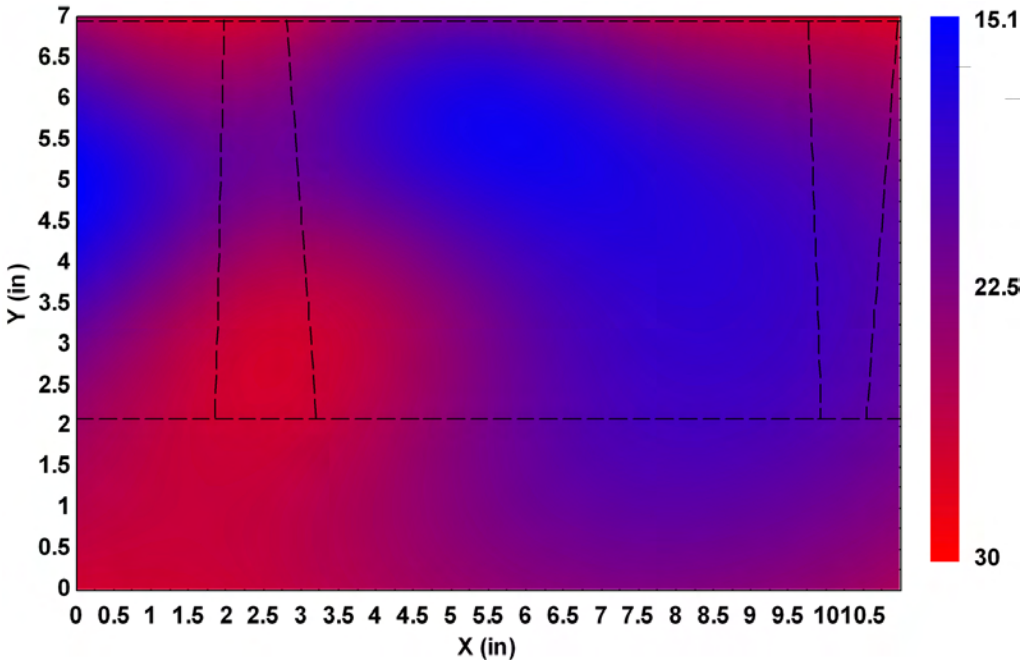

Figure 6.19: Outer Cylinder Surface Temperature Map for a Flowrate of 10.3 lpm

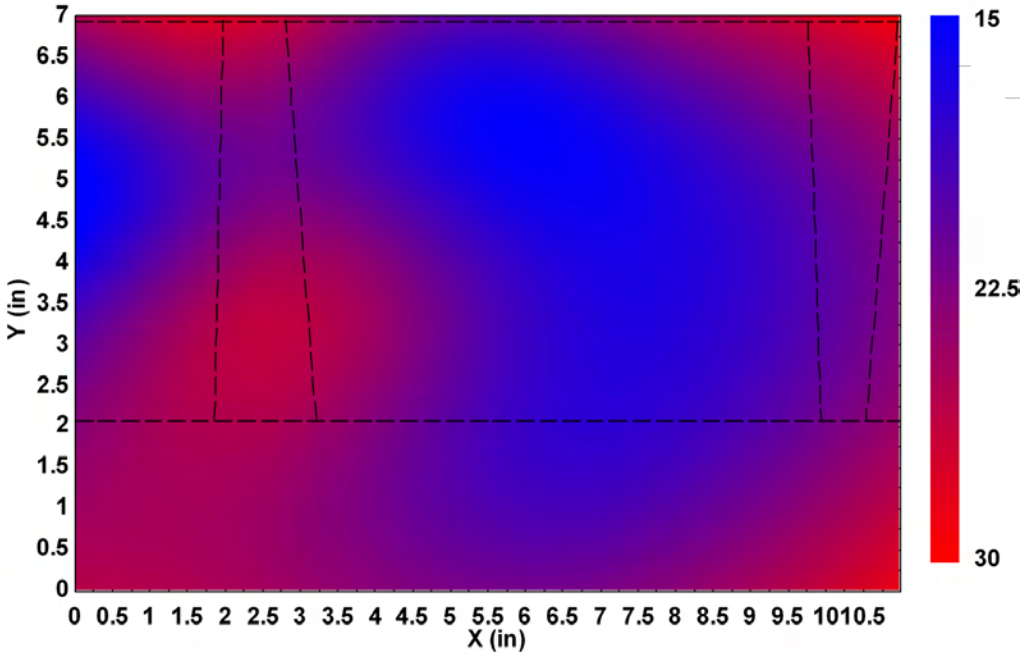

Figure 6.20: Outer Cylinder Surface Temperature Map for a Flowrate of 11.5 lpm

Examination of the temperature map figures shows that as the flowrate is increased, the outer surface temperatures are lower. This can be seen further by examining the average surface temperature of the cylinder as a function of flowrate, as shown in Figure 6.21.

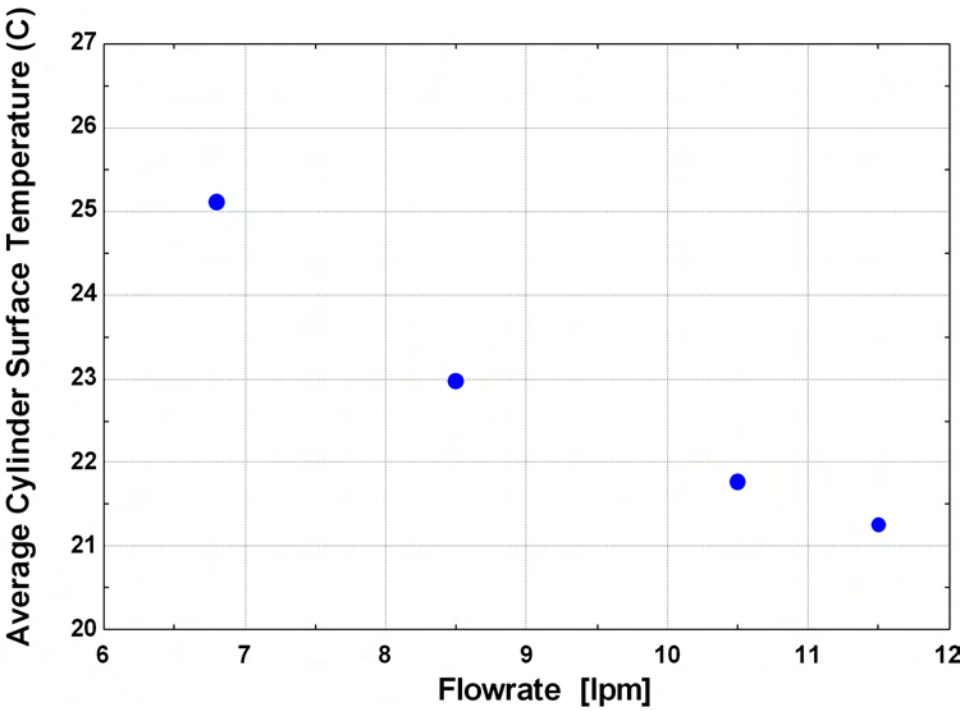

Figure 6.21: Averages Outer Cylinder Surface Temperature Map for as a function of Flowrate

The heat transfer coefficient on the outside surface of the cylinder was calculated for all of the flowrates measured. As shown in Figure 6.22, the heat transfer coefficient increases with increasing flowrate.

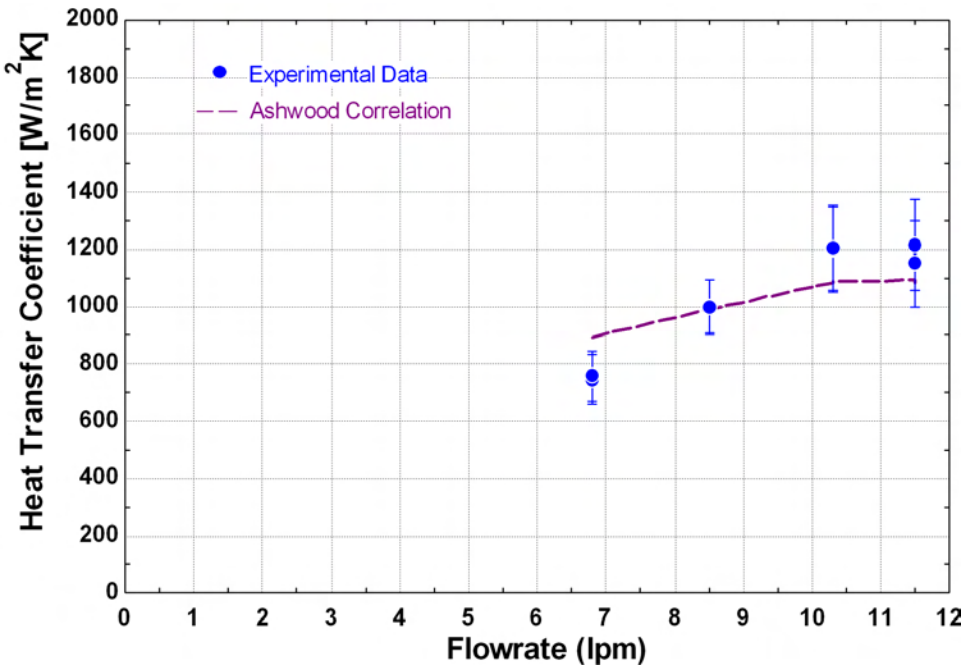

Figure 6.22: Outer Cylinder Heat Transfer Coefficient as a Function of Flowrate

The next investigation was the effect of increasing the fluid temperature on heat transfer performance. These trials were taken in a similar manner to the pervious trials, except the cooling water was adjusted so that the ethylene glycol temperature at the inlet of the spray device was constant. The data were recorded once the temperatures in the system reached a steady state. Data were collected for fluid inlet temperatures of $40°C$ and $50°C$, at flowrates of 6.8, 8.5 and 10.5 lpm. A temperature map of the outer cylinder surface for flow at 8.5 lpm with a fluid inlet temperature of $40°C$, as shown in Figure 6.23, reveals a similar pattern to the previous temperature maps, except for the change in temperature scale.

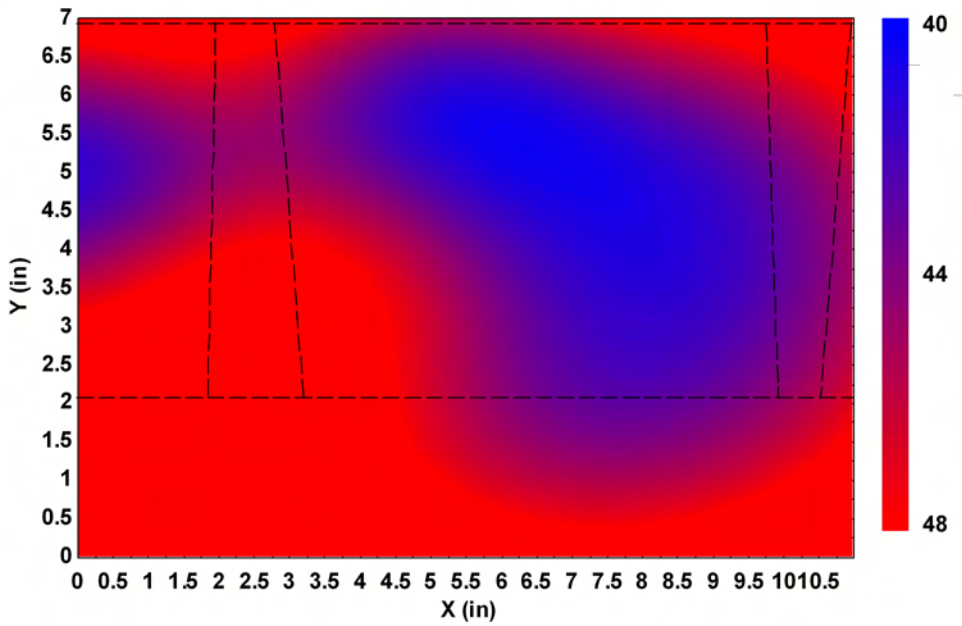

Figure 6.23: Outer Cylinder Surface Temperature Map for a Flowrate of 8.5 lpm and a Fluid Inlet Temperature of 40 Degrees Celsius

The data collected for the higher temperatures were analyzed by plotting the heat transfer coefficient versus flowrate in a similar manner to the analysis of the first dataset. The Ashwood correlation is compared to the experimental results to see if there is agreement [47]. The plots of heat transfer coefficient as a function of flowrate for the datasets at $40°C$ and $50°C$ are shown in Figures 6.24 and 6.25.

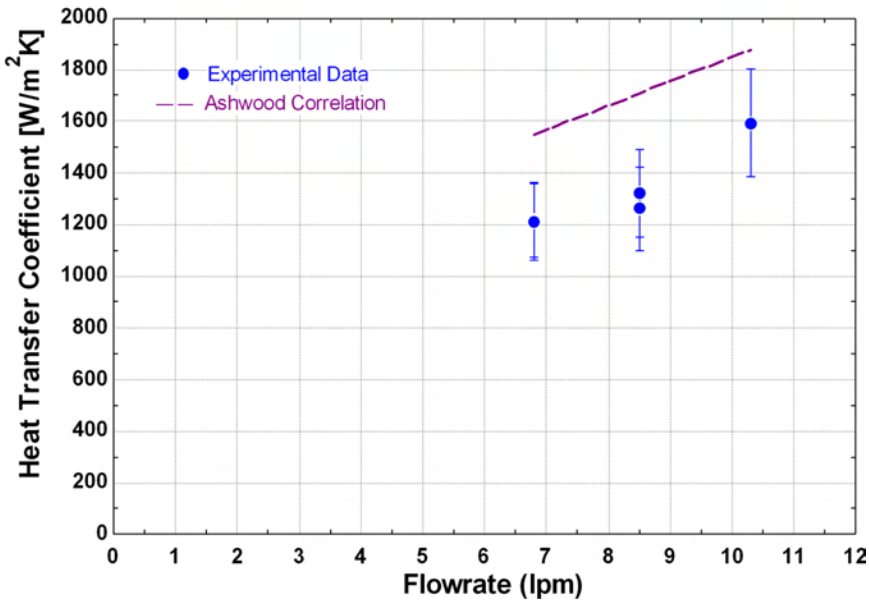

Figure 6.24: Outer Cylinder Heat Transfer Coefficient as a Function of Flowrate for a Fluid Inlet Temperature of 40 Degrees Celsius

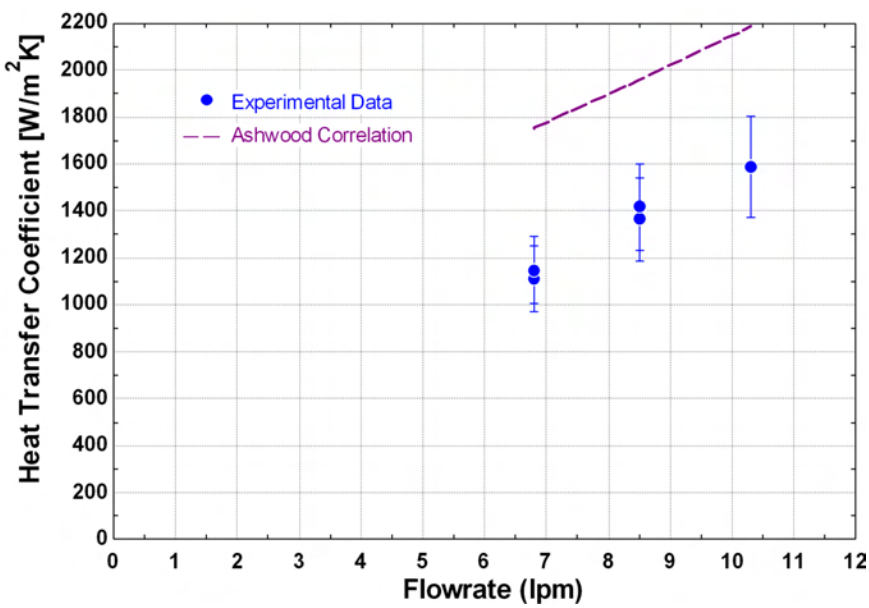

Figure 6.25: Outer Cylinder Heat Transfer Coefficient as a Function of Flowrate for a Fluid Inlet Temperature of 50 Degrees Celsius

The comparison of the Ashwood correlation to the experimental data at the higher temperatures shows that the Ashwood correlation over predicts the experimental results of the heat transfer coefficient. Therefore, a new correlation based on similar principles to the Ashwood correlation is proposed [47]. The data that have been collected includes the heat transfer coefficient as a function of the fluid flowrate and the fluid temperature. The development of the correlation begins with the examination of the heat transfer coefficient as a function of flowrate. The Ashwood correlation shows that the heat transfer coefficient is dependent on the volumetric flow rate per unit area (q'') to the 0.5 power. The validity of the application of this relationship to the experimental data is explored in Figures 6.26 through 6.28.

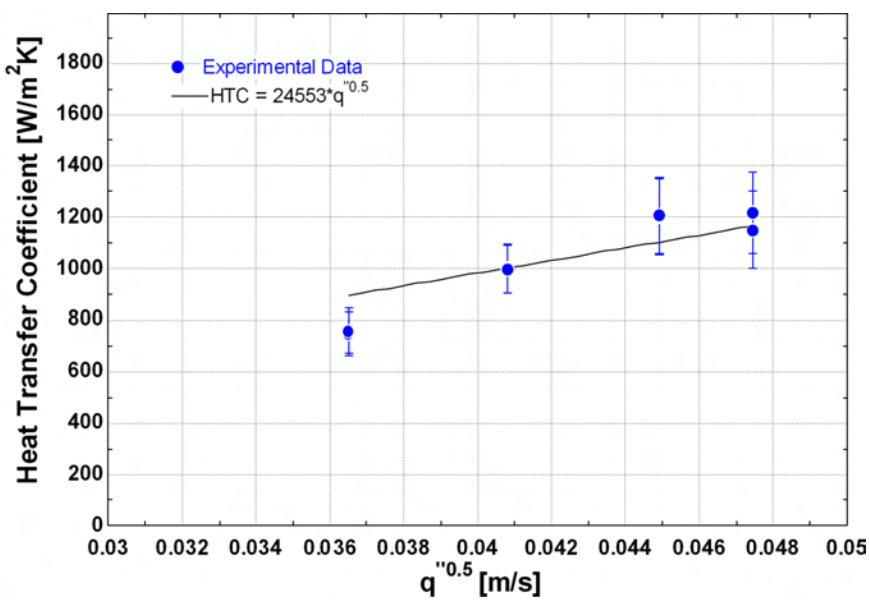

Figure 6.26: Relationship Between the Outer Cylinder Heat Transfer Coefficient and the Flowrate at 12 Degrees Celsius

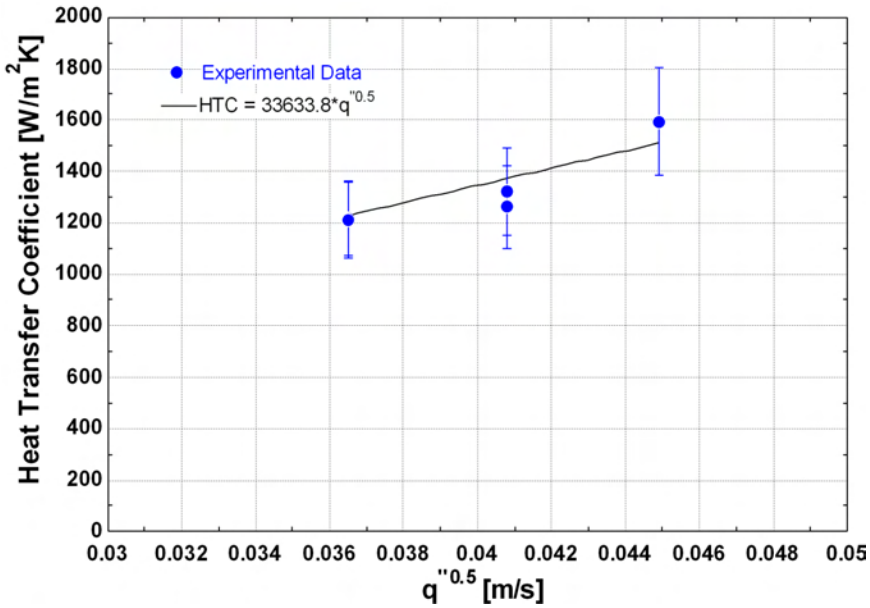

Figure 6.27: Relationship Between the Outer Cylinder Heat Transfer Coefficient and the Flowrate at 40 Degrees Celsius

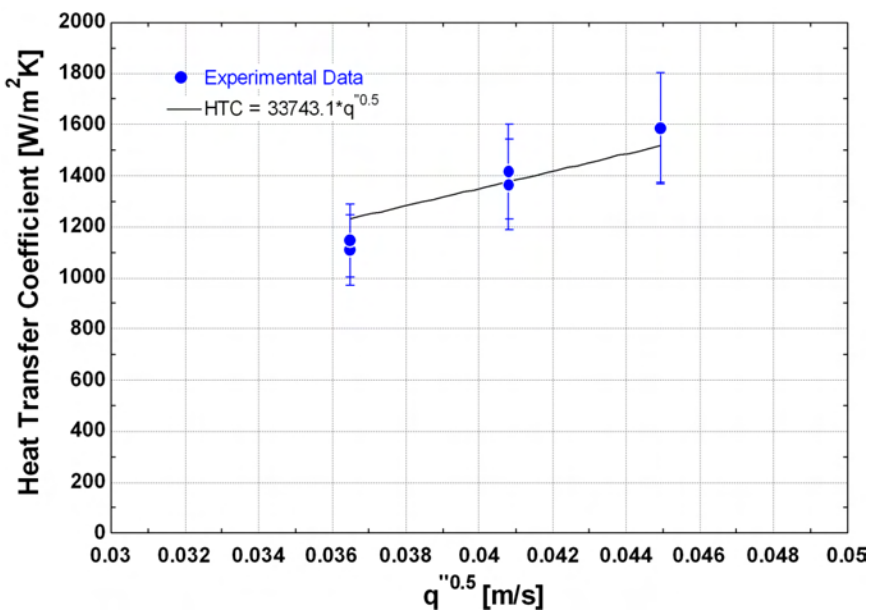

Figure 6.28: Relationship Between the Outer Cylinder Heat Transfer Coefficient and the Flowrate at 50 Degrees Celsius

These plots show a similar linear relationship for the heat transfer coefficient to the volumetric flow rate per unit area to the 0.5 power. Therefore, this dependence is assumed valid and will be kept in the new correlation. The other variable that needs to be determined for the correlation is the temperature. The variation of temperature affects the properties of the fluid such as the thermal conductivity (k), specific heat (C_p), and kinematic viscosity (ν). The heat transfer coefficient at different temperatures should be some function of these properties. A relationship of the heat transfer coefficient to temperature is explored by computing the dependence on the product of the thermal conductivity and specific heat divided by the kinematic viscosity ($\frac{kC_p}{\nu}$) which is based on Equation 6.2 [47]. This relationship is shown in Figures 6.29 through 6.31.

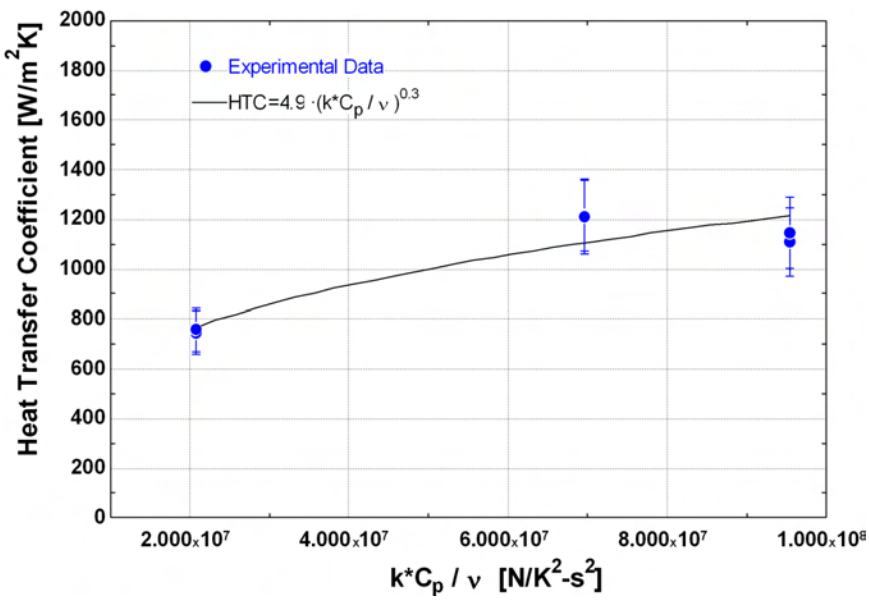

Figure 6.29: Relationship Between the Outer Cylinder Heat Transfer Coefficient and the Fluid Thermal Properties at 6.8 lpm

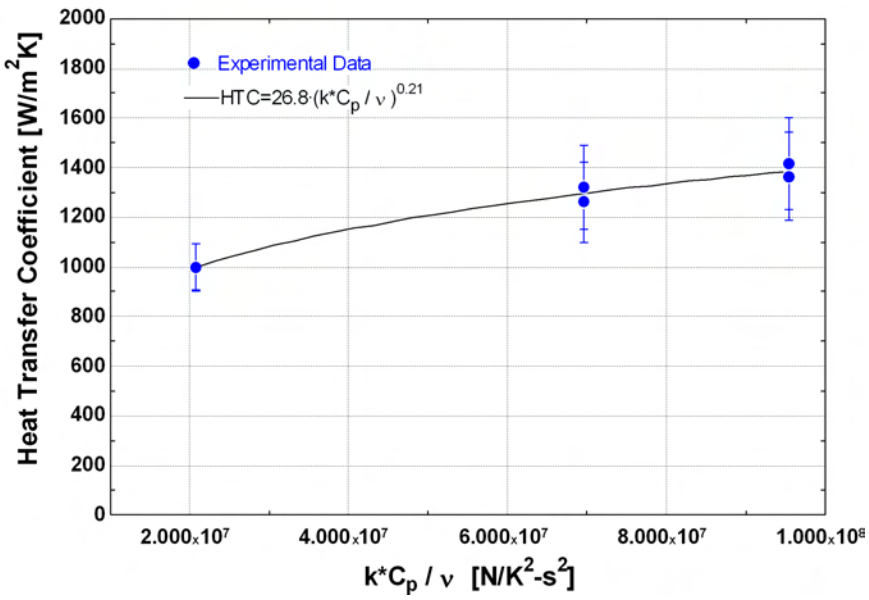

Figure 6.30: Relationship Between the Outer Cylinder Heat Transfer Coefficient and the Fluid Thermal Properties at 8.5 lpm

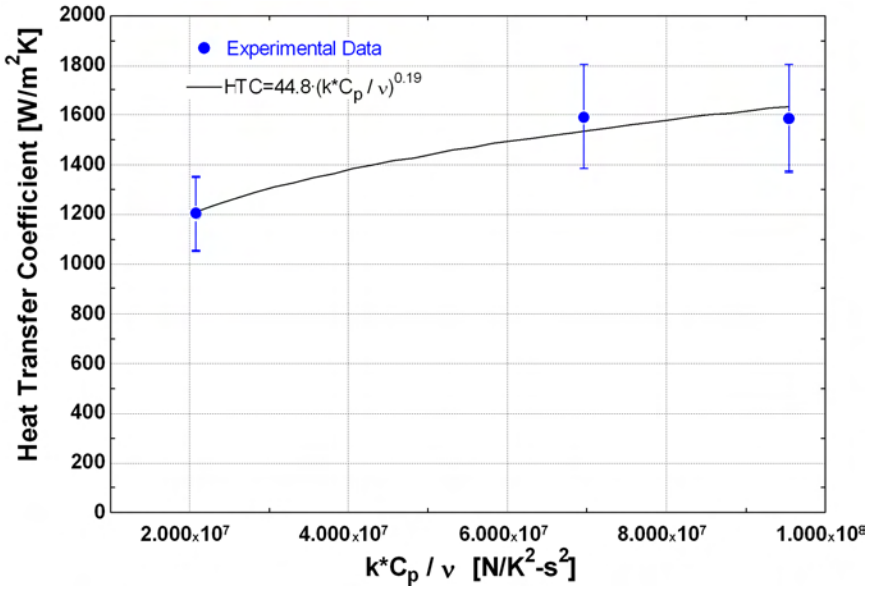

Figure 6.31: Relationship Between the Outer Cylinder Heat Transfer Coefficient and the Fluid Thermal Properties at 10.3 lpm

The data in Figures 6.29 through 6.31 follow a power law relationship. An exponential value was obtained from each of the 3 flowrates and averaged to obtain a value of 0.237, which is the exponent in the new correlation. Finally, the heat transfer coefficient is plotted against the product of the volumetric flow rate per unit area to the 0.5 power and the thermal properties grouping ($\frac{kC_p}{\nu}$) to the 0.237 power. This allows the determination of a coefficient for the correlation by computing the slope, which as shown in Figure 6.32 is found to be 449.

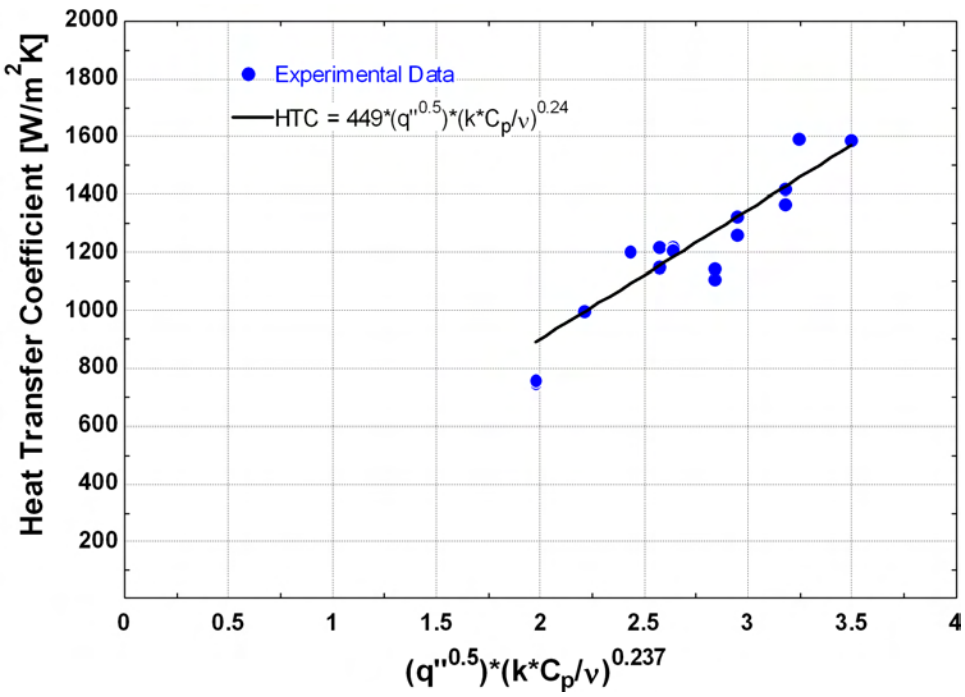

Figure 6.32: Calculation of the Coefficient for the New Correlation

The correlation shown in Figure 6.32 is verified by applying it to the data that was collected. Figure 6.33 includes the comparison of all of the data collected to the correlation prediction for the corresponding conditions. The 20% error lines that are shown in the plot contain all of the data that was collected.

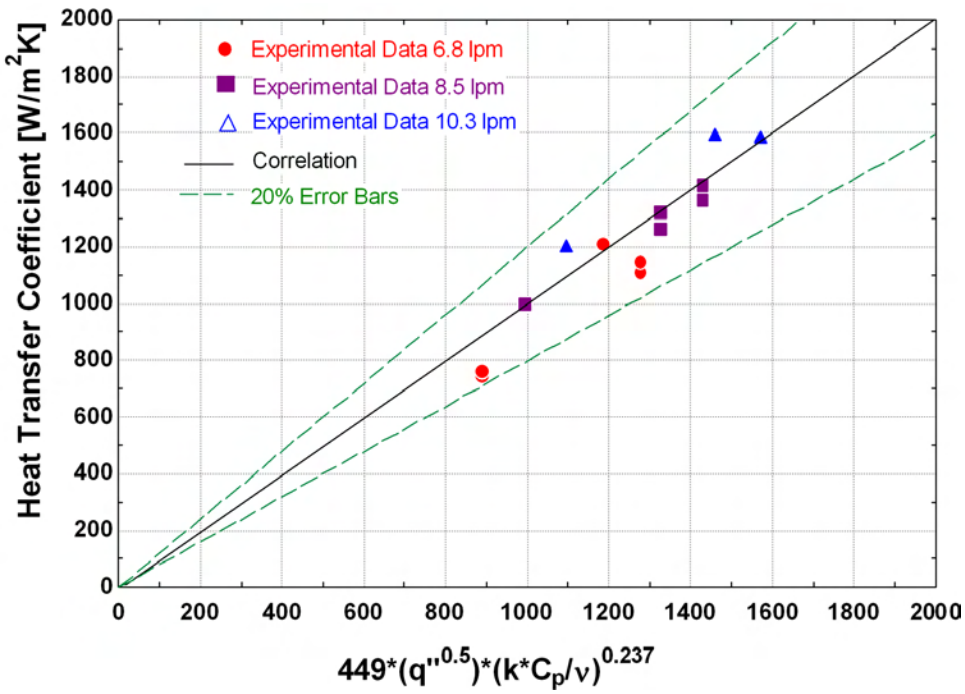

Figure 6.33: Comparison of the Correlation to All of the Experimental Data

Figure 6.33 shows that the correlation developed works quite well for all of the data collected. All of the data were within 10% of the expected values except for two of the datasets at the 6.8 lpm flowrate, both of which were within 20%. The 6.8 lpm flowrate was the smallest flowrate tested and visual inspection of the flow during operation showed weak jet streams. The lack of intensity of the jets at this flowrate could explain the deviation from the expected values of heat transfer performance. The success of the correlation leads to the exploration of applicability to varying concentrations of the ethylene glycol solution with water. An experimental test was done with a 20% ethylene glycol, 80% water solution at 7 lpm. Figure 6.34 shows the measured heat transfer coefficient from the experiment with the mixture to the predicted heat transfer coefficient from the correlation.

Examining the data in the heat addition zones of Figure 6.34 shows that the correlation under predicts the heat transfer coefficient by approximately 30% for the given conditions.

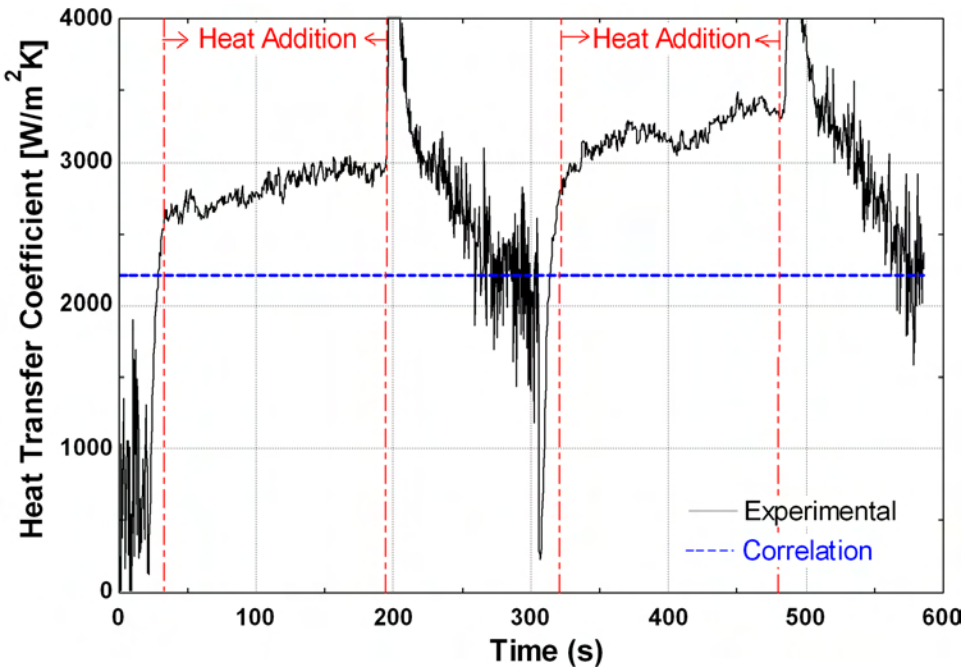

Figure 6.34: Comparison of the Experimental Heat Transfer Coefficient for a 20-80 Mixture of Ethylene Glycol-Water to the Correlation Prediction

Therefore, the correlation is only good for the parameters specified above, not variation in concentration. However, the correlation is quite accurate for the experimental data for pure ethylene glycol and has the potential to be useful for these specific applications. Further analysis is necessary for application to parameters outside of those for this experimental setup.

The pressure drop across the spray device was measured using a differential pressure gauge. At a flowrate of 8.5 lpm, the pressure drop was 40 psi. The pressure drop was used to calculate an approximate pump power that is necessary for the system, as shown in Equation 6.3.

$$\dot{W}_{pump} = \dot{m}\nu\Delta P \tag{6.3}$$

A flowrate of 8.5 lpm results in a pump power requirement of 39 W. During typical

vehicle operation for the Toyota Prius where the coolant is approximately 80 $°C$, the finite time analysis (Chapter 3) showed that a system can achieve between .2 kW and .5 kW of power. Therefore, between 8% and 19% of the power generated from the system would be used to drive the pump. However, if the coolant temperature is increased to 150 $°C$, the system can produce between 1 kW and 2.5 kW of power during engine operation. For this scenario the pump only requires between 1.5% and 3.9% of the system output power.

The data from the ethylene glycol mixture can be compared to an estimate of the heat transfer performance in a typical engine cooling system. An estimate of the heat transfer performance inside a typical engine was made by first estimating the Reynolds number of the flow. The coolant mass flow rate ($\dot{m}_{coolant}$) was found from the correlation developed for the Prius in Chapter 3 at an engine speed of 2000 RPM. The hydraulic diameter(D_h) of the flow was estimated using diagrams of engine cooling system configurations [51]. The dynamic viscosity(μ) was found from the properties of an ethylene glycol-water mixture. These values allowed the Reynolds number of the engine coolant flow to be calculated using Equation 6.4.

$$Re = \frac{4\dot{m}_{coolant}}{\pi D_h \mu} \tag{6.4}$$

The value of the Reynolds number estimate from Equation 6.4 was 1250, showing that the flow is laminar. An optimistic value for the Nusselt number was used for a situation in which there is a combined thermal and hydrodynamic entry length in parallel plates at a constant heat rate. This value was found to be 15.6 [52]. The Nusselt number correlation of the heat transfer coefficient is shown in Equation 6.5, where k is the thermal conductivity and htc is the heat transfer coefficient.

$$Nu = \frac{htcD_h}{k} \tag{6.5}$$

Evaluation of the heat transfer coefficient using these estimated values results in a value of 368 $\frac{W}{m^2-K}$. This value can be doubled to account for the surface roughness of the heat transfer area. Therefore, it is estimated that there is a heat transfer coefficient of 736 $\frac{W}{m^2-K}$ in a typical engine cooling system. The experimental data for the ethylene glycol-water mixture using the spray device resulted in heat transfer coefficients in the 3200 $\frac{W}{m^2-K}$ range, over four times as large as typical engine cooling systems. Therefore there is serious potential for the implementation of a new engine cooling system similar to the experimental design.

This experimental work exploring the application of spray cooling to engine cooling systems has shown potential for successful implementation. The results from the experimental work have demonstrated that high heat transfer coefficients can be attained using spray cooling, allowing for higher coolant temperatures. These higher coolant temperatures would provide increased opportunity for heat recovery from the coolant system as shown in Chapter 3.

Chapter 7

Conclusions and Recommendations

As found in the Literature Review (2), there are many different methods and designs that offer possibilities for energy recovery within a vehicle. There have been numerous attempts over the last century to develop a design for implementation into the vehicle fleet. Most of the research done related to energy recovery was either during the early development of the modern passenger vehicle in the early 1900s or during the times of high energy cost in the 1970s and currently. Energy predictions for the future show that the limit of energy resources will keep prices high and rising. The high cost of fuel, along with emissions concerns correlated to global warming and environmental sustainability, will create a prolonged interest in energy conservation and energy efficiency. The transportation industry is a significant portion of the energy consumption in the United States, thus requiring an increased importance of the efficiency of vehicles. Energy recovery from the waste heat of vehicles allows an option for increasing the overall system efficiency and will continue to be investigated as energy efficiency and energy consumption becomes more of a priority in our society.

Gasoline/electric hybrid vehicles offer advantages for energy recovery, as the storage battery provides a mechanism for which the recovered energy can be easily utilized to directly power the vehicle. Traditional gasoline-only vehicles only allow the recovered energy to be used to power the electronics, without significant modification to the drivetrain. Additionally, the gasoline/electric hybrid vehicles are designed for high efficiency, allowing a waste heat recovery system to assist in achieving a total system efficiency much higher than current typical vehicles.

This investigation has focused on the 2004 Toyota Prius gasoline/hybrid vehicle, as data for a typical driving cycle for this vehicle were available. The energy balance on the system

revealed that the exhaust gas temperatures and flow are lower than typical values, resulting in less energy available for recovery. An availability and finite time analysis on the data revealed that the potential for energy recovery from the exhaust system and engine cooling system is approximately the same. The finite time analysis showed that approximately 1.2% and 1.6% of the initial fuel energy can be recovered from the engine coolant system and exhaust system respectively. All of the values in this analysis were based on the percentage of initial fuel energy, which allows for simple application to other systems. These values cannot be directly compared to the typically reported results of analyses that base the percentage increase on an increase of the engine output power. For example, the above finite time results would translate to 3.6% and 4.8%, respectively, for an engine that is 33% efficient based on engine output power. Therefore, the 1.2% and 1.6% of fuel energy recovery rates are significant should they be attained.

The analysis continued with an evaluation of various heat recovery designs for both the engine coolant system and exhaust. The implementation of a turbine in the exhaust stream was explored in Chapter 4. The models in GT-Power showed that the backpressure imposed by the turbine on the internal combustion engine severely impacted the engine's performance. Many analyses for energy recovery from the exhaust system, including some of those referred to in Chapter 2, do not include this effect even though it is quite important. The examination of backpressure in the exhaust stream continued in Chapter 6 with an analysis of a compact heat exchanger. The backpressure from the compact heat exchanger was found to be not as significant as it was for the turbine in the exhaust. There does appear to be opportunity for heat recovery from the exhaust system utilizing a compact heat exchanger. However, the relatively low mass flow rates of the exhaust system of the Toyota Prius limit the amount of heat that can be recovered, especially at lower engine speeds. The results from the compact heat exchanger model show that there is some opportunity for heat recovery from the exhaust for a Toyota Prius, however, it does appear that exhaust system heat recovery may be offer

better results for different vehicle systems. The Literature Review in Chapter 2 includes some designs for energy recovery from the exhaust where the backpressure effects are not as significant. Many of these designs are applied to larger, Diesel engines which may be better suited for energy recovery from the exhaust stream, due to their higher exhaust flowrates and resistance to backpressure effects.

Energy extraction from the cooling system was explored in Chapter 6. A parametric analysis of the engine coolant temperature showed an increase in recoverable energy as the coolant temperature was increased. This motivated the investigation of different heat removal techniques within the engine coolant system to allow for higher coolant temperatures while extracting the necessary amount of heat for proper operation. An investigation of the use of spray cooling techniques in the cooling system showed that much higher heat transfer coefficients can be realized, than those in typical engine coolant systems. The higher heat transfer coefficients that can be attained with spray cooling enable the coolant temperature to be increased to $150°C$, which increases the finite time availability to 4.2% of the fuel energy. Converting this value to the typical format based on engine output power results in an increase of 12.6% for an engine that is 33% efficient. The implementation of this type of system would allow potential for energy recovery from the cooling system to be a viable option. Even if the energy recovery is not desired or determined not economical, this type of cooling system would also provide benefits over current systems. The spray cooling system would provide even cooling across the engine in an efficient manner. The system would allow engines to have a smaller and lighter design.

The optimization of the Toyota Prius system for efficiency appears to have reduced the opportunity for energy recovery. There are many engineering challenges that are encountered with designing a heat recovery system that is feasible for a vehicle such as the Toyota Prius due to the reduced quality of the waste energy sources. Unique designs and ideas, such as the use of spray cooling in the engine coolant system in Chapter 6, must be developed and

optimized for viable implementation into the Toyota Prius. The spray cooling system, along with other innovative energy recovery designs, should be actively pursued for the application to a gasoline/electric hybrid vehicle. Even though this type of vehicle has increased challenges for energy recovery, the benefits of providing even higher efficiency than the already efficient gas/electric hybrid vehicles could be substantial. Additionally, different types of vehicles should also be heavily explored for implementing energy recovery. The analysis in Chapters 3 - 6 and comparison to other results in the Literature Review (Chapter 2) show that smaller gasoline/electric vehicles, such as the Toyota Prius, are not the optimum system for energy recovery. Other analysis, such as those in Chapter 2, show greater potential for energy recovery in larger vehicles, especially Diesel powered vehicles.

Bibliography

[1] Toyota Motor Corporation Public Affairs Division. Toyota Hybrid System II - hybrid synergy drive. 4-8 Koraku 1-chome, Bunkyo-ku, Tokyo, 112-8701 Japan, May 2003.

[2] J. W. Mitchell O. M. Ibrahim, S. A. Klein. Effects of irreversibility and economics on the performance of a heat engine. *Journal of Solar Energy Engineering*, 114:267–271, 1992.

[3] Energy Information Administration United States Government. Annual energy outlook 2007. Technical report, Department of Energy, 2007.

[4] C.D. Keeling and T.P. Whorf. Atmospheric CO2 records from sites in the SIO air sampling network. In Trends: A compendium of data on global change. Technical report, Oak Ridge National Laboratory, U.S. Department of Energy, Oak Ridge, Tenn., U.S.A., 2005.

[5] United States Government National Climatic Data Center. Global surface temperatures. Technical report, National Climatic Data Center, United States Department of Commerce, 2005.

[6] J. B. Heywood. *Internal Combustion Engine Fundamentals*. McGraw-Hill Book Company, 1988.

[7] L. E. Hall. Back to the past: The history of hybrids. *MSN Autos*, 2005.

[8] J. Atkinson. The Atkinson cycle. *The Engineer*, LXIII, 1887.

[9] The Scuderi Group. Scuderi air-hybrid engine. 1111 Elm Street, Suite 4, West Springfield, MA 01089.

[10] M. J. Moran and H. N. Shapiro. *Fundamentals of Engineering Thermodynamics*. John Wiley and Sons, Inc., 4th edition, 2000.

[11] A. I. Kalina. Combined-cycle system with novel bottoming cycle. *Transactions of the ASME - Journal of Engineering for Gas Turbines and Power*, 106(4):737–742, October 1984.

[12] H. A. Mlcak. Kalina cycle concepts for low temperature geothermal. *Geothermal Resources Coucil Transactions*, 26:707–713, September 2002.

[13] S. Klopstein F. Koch P. Diehl, F. Haubner. Exhaust heat recovery sytem for modern cars. *Society of Automotive Engineers*, (2001-01-1020), 2001.

[14] G. Lin F. Yang, X. Yuan. Waste heat recovery using heat pipe heat exchanger for heating automobile using exhaust gas. *Applied Thermal Engineering*, (23 (2003) 367-372), 2002.

[15] A.G. Kulakov D.A. Mishkinis P.V. Bohan L.L. Vasiliev, V.S. Burak. Latent heat storage modules for preheating internal combustion engines: Application to a bus petrol engine. *Applied Thermal Engineering*, (20 (2000) 913-923), 1999.

[16] T. J. Hendricks and J. A. Lustbader. Advanced thermoelectric power system investigations for light-duty and heavy-duty applications: Part II. *XXI International Conference on Thermoelectrics*, pages 387–394, August 2002.

[17] K. Misawa N. Suzuki L.I. Anatychuk, Y. Y. Rozver. Thermal generators for waste heat utilization. *16th International Conference on Thermoelectrics*, pages 586–587, 1997.

[18] G. Jackson D. Crane and D. Holloway. Towards optimization of automotive waste heat recovery using thermoelectrics. *Society of Automotive Engineers*, (2001-01-1021), 2001.

[19] V. H. Johnson. Heat-generated cooling opportunities in vehicles. *Society of Automotive Engineers*, (2002-01-1969), 2002.

[20] R.P. Kapoor P.L. Ballaney, O.P. Grover. Air-conditioning of fiat car from waste heat energy. *IE - Journal - ME*, 57(UDC 629.1.06):342–345, May 1977.

[21] B. Agnew M. Talbi. Energy recovery from diesel engine exhaust gases for performance enhancement and air conditioning. *Applied Thermal Engineering*, (22 (2002) 693-702):693–702, 2001.

[22] B. Agnew M. Mostafavi, R. Atan. A theoretical investigation of the utilisation of a diesel engine exhaust waste heat for air conditioning and cooling purposes. *Institution of Mechanical Engineers*, (C495/004/94):159–172, 1994.

[23] M. Mostafavi B. Agnew, M. Talbi. Combined power and cooling, an analysis of the combined diesel-absorption cycle. *Applied Thermal Engineering*, (19 (1999) 1097-1105):1097–1105, 1998.

[24] B. Agnew M. Mostafavi. Thermodynamic analysis of combined diesel engine and absorption unit - turbocharged engine with intercooling. *Applied Thermal Engineering*, 16(8/9), 1996.

[25] B. Agnew M. Mostafavi. Thermodynamic analysis of combined diesel engine and absorption refrigeration unit - supercharged engine. *Applied Thermal Engineering*, 16(6), 1996.

[26] R. Atan. Heat recovery equipment (generator) in an automobile for an absorption air-conditioning system. *Society of Automotive Engineers*, (980062), 1998.

[27] J. R. Akerman. Automotive air conditioning systems with absorption refrigeration. *Society of Automotive Engineers*, (710037), 1971.

[28] D. Kapich. Turbo-hydraulic engine exhaust power recovery system. *Society of Automotive Engineers*, (2002-01-2731), 2002.

[29] Foresight Vehicle. Engineers tap into exhaust power. www.foresightvehicle.org.uk.

[30] BMW. BMW developing steam assist drive based on waste heat recovery. http://www.gizmag.com/go/4936/.

[31] A. Verneau. Recovery from exhaust gas on a diesel engine. *VDI Berichte*.

[32] S. E. Aly. Diesel engine waste-heat power cycle. *Applied Energy*, 29:179–189, 1988.

[33] M. M. Bailey. Comparative evaluation of three alternative power cycles for waste heat recovery from the exhaust of adiabatic diesel engines. Technical report, National Aeronautics and Space Administration, 1985.

[34] S. Kramer E. Doyle, L. DiNanno. Installation of a diesel-organic rankine compound engine in a class 8 truck for a single-vehicle test. *Society of Automotive Engineers*, (790646), 1979.

[35] S. Ogino H. Oomori. Waste heat recovery of passenger car using a combination of rankine bottoming cycel and evaporative engine cooling system. *Society of Automotive Engineers*, (930880), 1993.

[36] D. Clodic R. E. Chammas. Combined cycle for hybrid vehicles. *Society of Automotive Engineers*, (2005-01-1171), 2005.

[37] A. T. O'Neill H. S. Lee. Comparison of boiling curves between a standard S.I. engine and a flow loop for a mixture of ethylene glycol and water. *Society of Automotive Engineers*, (2006-01-1231), 2006.

[38] B. Ahlborn F. L. Curzon. Efficiency of a Carnot engine at maximum power output. *American Journal of Physics*, 43:22–24, 1975.

[39] www.flatplateselect.com. Gea flatplate inc.

[40] Morel. *GT-Power*. 2005.

[41] F. J. Vesper J. A. Bolt, S. P. Bergin. The influence of exhaust back pressure of a piston engine on air consumption, performance, and emissions. *Society of Automotive Engineers*, (730195), 1973.

[42] T. G. Adams. Effect of exhaust system design on engine performance. *Society of Automotive Engineers*, (800319), 1980.

[43] A. L. London W. M. Kays. *Compact Heat Exchangers*. Krieger Publishing Company, 3 edition, 1984.

[44] S. A. Klein. *Engineering Equation Solver*. F-Chart Software, 2006.

[45] A. McMahan. Design and optimization of organic Rankine cycle solar-thermal power-plants. Master's thesis, University of Wisconsin-Madison, 2006.

[46] ASHRAE. *2005 ASHRAE Handbook-Fundamentals*. 2005.

[47] A. C. Ashwood. Fluid property effects on spray cooling: An experimental and numerical study. Master's thesis, University of Wisconsin-Madison, 2006.

[48] A. G. Pautsch and T. A. Shedd. Spray impingement cooling with single- and multiple-nozzle arrays Part I: Heat transfer data using FC-72. *International Journal of Heat and Mass Transfer*, 48:3167–3175, 2005.

[49] R. F. Crook J. J. JuGer. Heat transfer performance of propylene glycol versus ethylene glycol coolant solutions in laboratory testing. *Society of Automotive Engineers*, (1999-01-0129), 1999.

[50] C. E. Kuyatt B. N. Taylor. Guidelines for evaluating and expressing the uncertainty of nist measurement results. *NIST Technical Note 1297*, 1994. National Institute of Standards and Technology Technical Note 1297.

[51] K. L. Hoag. *Vehicular Engine Design*. SAE International, 2006.

[52] B. Weigand W. Kays, M. Crawford. *Convective Heat and Mass Transfer*. McGraw-Hill, fourth edition, 2005.

===== Appendix

Appendix A

Compact Heat Exchanger Analysis Results

This appendix includes results for other compact heat exchanger configurations that were analyzed in a manner similar to the one in Chapter 5. Plots are shown for the Reynolds number, friction factor, effectiveness, heat transfer rate and pressure drop as a function of the engine speed. Also included are the plots that show the heat exchanger length optimization along with the power and percent power change as a function of the Rankine cycle efficiency. All of the heat exchanger configurations shown in the appendix are analyzed using water as the heat transfer fluid for comparison purposes.

A compact heat exchanger analysis was performed to provide a general relationship between heat recovered and pressure drop. The analysis was done using the equations, methods and tables from Kays and London [43]. The data from Kays and London [43] have been implemented as a routine in a software program called Engineering Equation Solver (EES) [44]. Additionally, a GT-Power model that examined the backpressure effects on engine performance was created. The resulting data from the compact heat exchanger analysis and GT-Power model were coupled to obtain a total system power. The total system power ($\dot{W}_{total}$) is the sum of the engine power for the given backpressure ($\dot{W}_{engine}$) and the resulting power generated from the heat recovered. The heat recovered is used to drive a Rankine cycle to produce usable power for the system. Thus, the power generated from the heat recovered is the product of the heat recovered from the compact heat exchanger ($\dot{W}_{CHE}$) and the Rankine cycle efficiency ($\eta_{Rankine}$). The equation for the total system power is shown in Equation A.1.

$$\dot{W}_{total} = \dot{W}_{engine} + \eta_{Rankine}\dot{W}_{CHE} \tag{A.1}$$

The total system power shown in Equation A.1 was then compared to the engine power computed without any heat recovery system in the exhaust system. This allows for a determination of the viability of a heat recovery system in the exhaust system.

There are some assumptions that need to be made for the geometry of the heat exchanger prior to the analysis. It is assumed that that frontal area of the heat exchanger is 0.0025 m^2, i.e. 0.05m $\times$ 0.05m. For frontal areas lower than this, the pressure drops across the heat exchanger approach values that significantly affect the engine performance. Frontal areas larger than the assumption result in minimal heat transfer due to the relatively small mass flow rate. The length of the heat exchanger is initially assumed to be 0.5 m and is optimized following the initial analysis of the heat exchanger coupled with the engine system. Also for this analysis, it was assumed that the fluid within the tubes is water with a mass flow rate of 0.1 kg/s. The Reynolds number for the water was then determined as shown in Equation A.2.

$$Re = \frac{GD_h}{\mu} \tag{A.2}$$

The mass flux of the water (G), viscosity (μ) and the hydraulic diameter (D_h) are needed for the Reynolds number equation. The mass flux of the water is calculated using the mass flow rate and the minimum free flow area (A_c) as shown in Equation A.3. The hydraulic diameter is found from the tables in Kays and London for each flow configuration.

$$G = \frac{\dot{m}}{A_c} \tag{A.3}$$

The Reynolds number for the exhaust stream was calculated using the same equations as shown for the water. The mass flow rate of the exhaust stream was found as a function of the engine speed from the Prius data. A linear fit for the mass flow rate of exhaust was calculated from the Prius data as shown in Figure A.1.

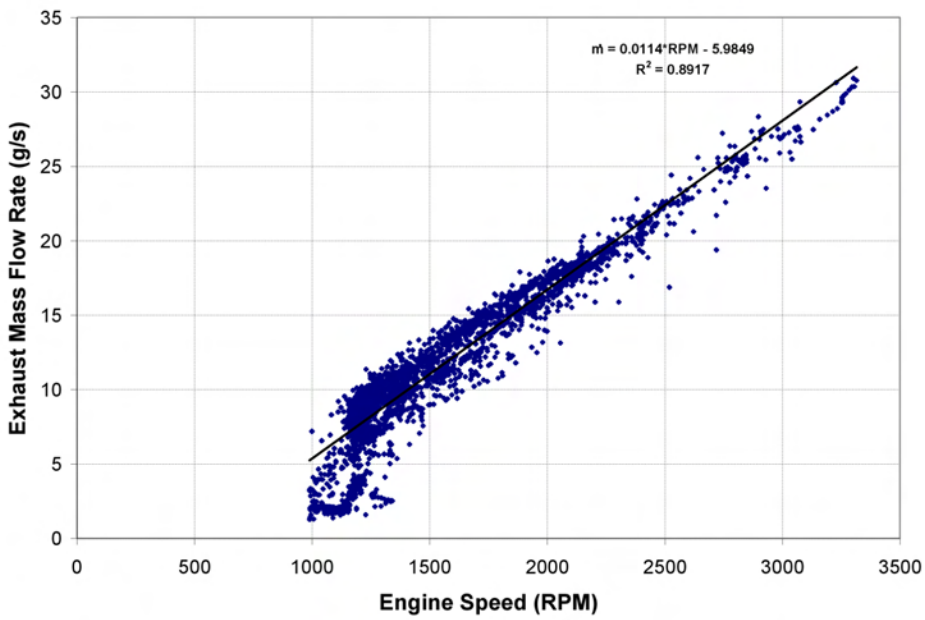

Figure A.1: Exhaust Mass Flow Rate as a Function of the Engine Speed for the Prius Data

The Reynolds numbers computed for the water and the exhaust were used to find the heat transfer rate and the pressure drop of the heat exchanger. Kays and London include tables that provide the friction factor (f) for a given Reynolds number for various geometries, which can be used to determine the pressure drop. The same tables that include the friction factor also include the product of the Prandtl number raised to the $\frac{2}{3}$ power and the Stanton number. This dimensionless number is used to find the heat transfer coefficient(htc). The Prandtl (Pr) and Stanton (St) dimensionless numbers are defined in Equations A.4 and A.5.

$$Pr = \frac{c_p \mu}{k} \tag{A.4}$$

$$St = \frac{htc}{\rho V c_p} \tag{A.5}$$

Previously undefined variables in Equations A.4 and A.5 include the thermal conductivity and the specific heat, which are denoted by k and c_p, respectively. Combining these dimensionless numbers into the form for which data is given results in Equation A.6.

$$StPr^{\frac{2}{3}} = \left(\frac{htc}{\rho V c_p}\right)\left(\frac{c_p \mu}{k}\right)^{\frac{2}{3}} \tag{A.6}$$

The left side of Equation A.6 is found from the tables in Kays and London [43] for a computed Reynolds number. The right side of Equation A.6 includes the velocity which is known and values which are properties of the fluid that can be found for the given conditions. The only unknown in Equation A.6 is the heat transfer coefficient, which can then be evaluated.

The heat transfer coefficient found by Equation A.6 was used to compute the overall heat transfer coefficient area product (UA). The thermal resistances (R) were calculated using the heat transfer coefficients found for the water and exhaust sides using Equation A.7.

$$R = \frac{1}{htcA_{ht}} \tag{A.7}$$

In Equation A.7, A_{ht} denotes the heat transfer area, or the contact area of the two fluids. The calculation of the thermal resistances allows for the computation of the overall heat transfer coefficient area product as shown in Equation A.8.

$$UA = \frac{1}{R_{water} + R_{wall} + R_{exhaust}} \tag{A.8}$$

The overall heat transfer coefficient area product was then applied to find the number of transfer units (NTU), as in Equation A.9.

$$NTU = \frac{UA}{\dot{C}_{min}} \tag{A.9}$$

In Equation A.9, the $\dot{C}_{min}$ term is the minimum of the exhaust and water heat capacity rates. The heat capacity rate is defined as the product of the mass flow rate and the specific heat of a fluid. Additionally, the heat capacity rate ratio CR was computed as in Equation A.10.

$$CR = \frac{\dot{C}_{min}}{\dot{C}_{max}} \tag{A.10}$$

The number of transfer units and heat capacity rate ratio were then used together to obtain the effectiveness (ϵ) by tables in Kays and London. The effectiveness is the ratio of the actual heat transfer rate ($\dot{Q}$) to the maximum possible heat transfer rate ($\dot{Q}_{max}$) for a given system, as shown in Equation A.11.

$$\epsilon = \frac{\dot{Q}}{\dot{Q}_{max}} \tag{A.11}$$

The maximum heat transfer rate is defined as the product of the minimum heat capacity rate and the difference of the temperatures of the inlet streams, as shown in Equation A.12.

$$\dot{Q}_{max} = \dot{C}_{min}(T_{exhaust,inlet} - T_{water,inlet}) \tag{A.12}$$

Thus, $\dot{Q}_{max}$ can be found since the variables in Equation A.12 are all known from the GT-Power model or the assumptions. Therefore, the heat transfer rate for the system can be computed using Equation A.11. This provides a solution for how much heat can be recovered utilizing a typical compact heat exchanger in the exhaust system.

The pressure drop on the exhaust side of the heat exchanger can then be calculated using the friction factor found from the tables in Kays and London that relate the Reynolds number to the friction factor for various heat exchanger types and geometries. The pressure drop equation is shown in Equation A.13.

$$\Delta P = \left(\frac{\dot{m}}{A_{xs,min}}\right)^2 (\nu)(f)2\left(\frac{L}{D_h}\right) \tag{A.13}$$

In Equation A.13, $A_{xs,min}$ is the minimum cross sectional area for the flow of exhaust gas and ν is the specific volume of the exhaust gas. The resulting pressure drop calculated from Equation A.13 is then compared to results from the GT-Power model to obtain correlations for the backpressure effects on the engine power. The GT-Power model used in this analysis was the same Detailed Prius model that was used in Chapter 4. The cross sectional area of an orifice in the exhaust system was modified until the backpressure was similar to the pressure drop obtained from Equation A.13. This provided an engine power given the backpressure constraints due to the compact heat exchanger in the exhaust system. The plot of engine power as a function of backpressure, as modeled in GT-Power for an engine speed of 2000 RPM is shown in Figure A.2.

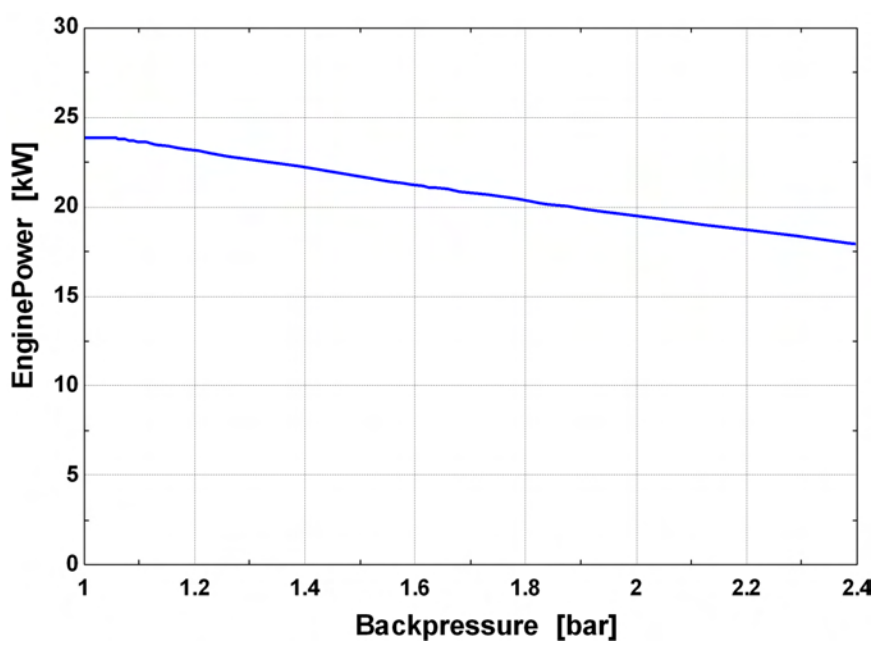

Figure A.2: Engine Power as a Function of the Backpressure at an Engine Speed of 2000 RPM

The engine power obtained from the GT-Power simulation was summed with the power that could be generated from the heat recovered from the compact heat exchanger. This total system power was then compared to the engine power that results without any heat recovery device obstruction in the exhaust stream to determine the practicality of heat recovery from the exhaust system.

The results for the total system power are then optimized by varying the length of the heat exchanger. The total system power requires the Rankine cycle efficiency, which was assumed to be 0.25. This value was used only in the optimization of the length. The average percent power difference is the percentage difference between the total system power (Engine and Heat Exchanger) and the engine without a heat exchanger.

The power that can be generated from the heat recovered was calculated as the product of the heat transfer rate found in Equation A.11 and a Rankine cycle efficiency. The Rankine cycle efficiency was estimated to be between 0.1 to 0.4, as this is a typical to optimistic range for efficiencies of the Rankine cycle. The total system power was calculated as a function of the Rankine cycle efficiency.

A.1 Finned-tube surface, Circular Tubes, Circular Fins - 'CF 8.72'

The following plots are for a compact heat exchanger with a finned-tube surface, circular tubes and circular fins and is denoted at the 'CF 8.72' configuration in Kays and London [52]. A schematic of the configuration is shown in Figure A.3.

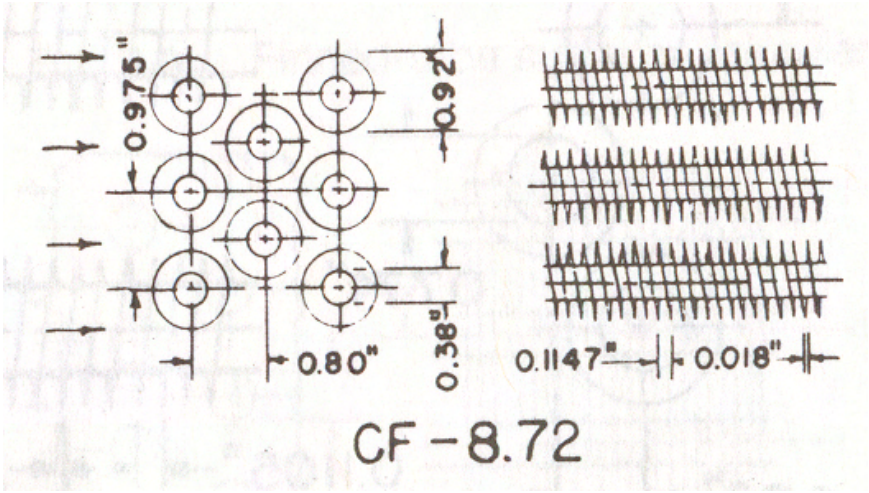

Figure A.3: Schematic of the 'CF-8.72' Compact Heat Exchanger Studied

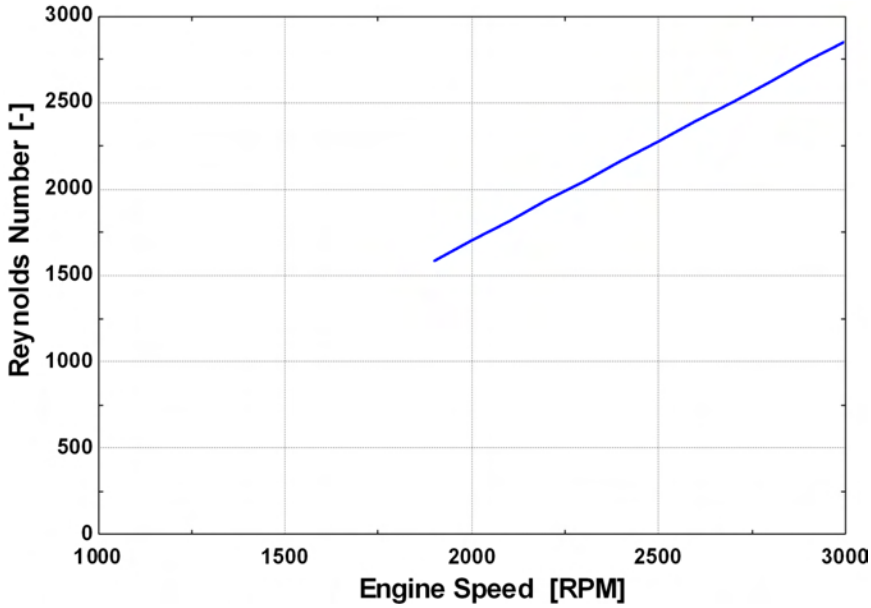

Figure A.4: Reynolds number as a Function of the Engine Speed for the 'CF-8.72' Compact Heat Exchanger

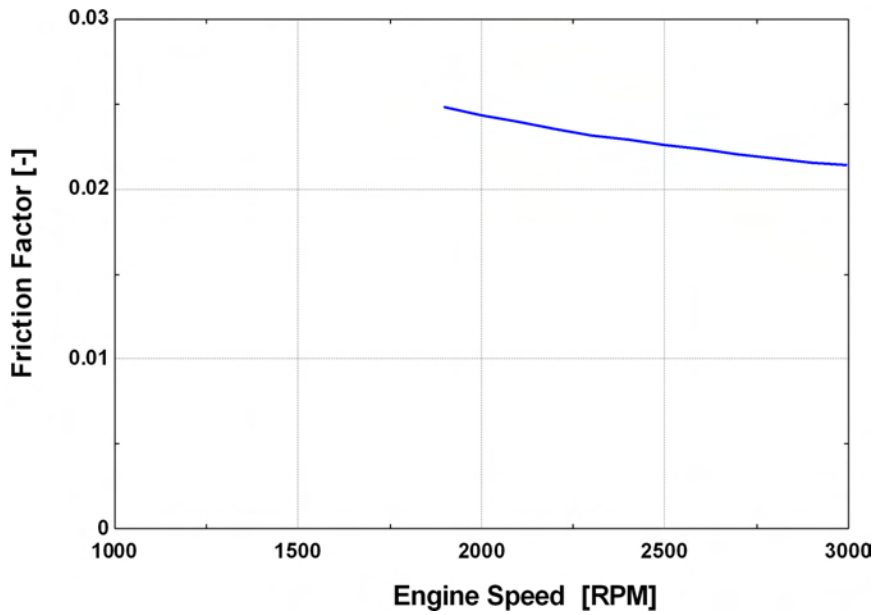

Figure A.5: Friction Factor as a Function of the Engine Speed for the 'CF-8.72' Compact Heat Exchanger

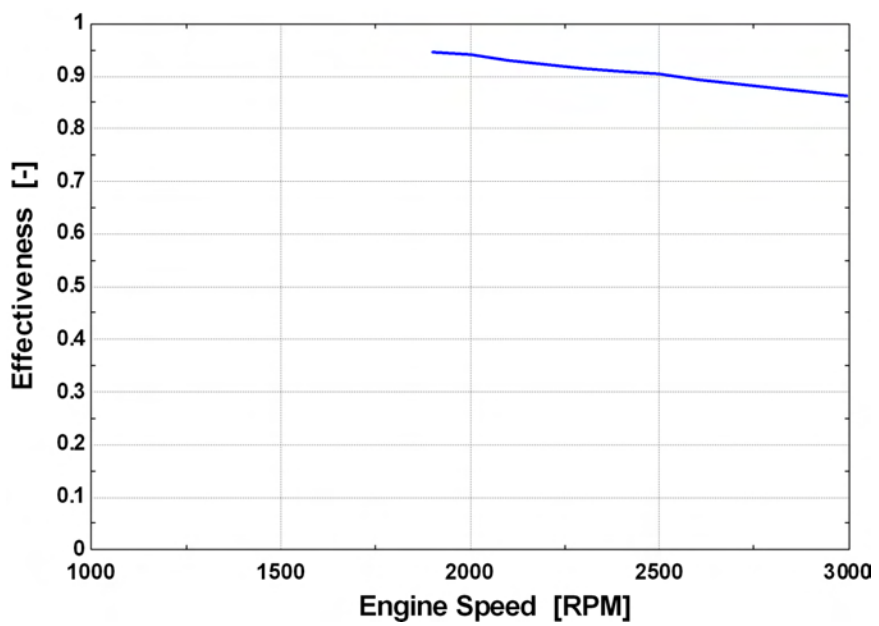

Figure A.6: Effectiveness as a Function of the Engine Speed for the 'CF-8.72' Compact Heat Exchanger

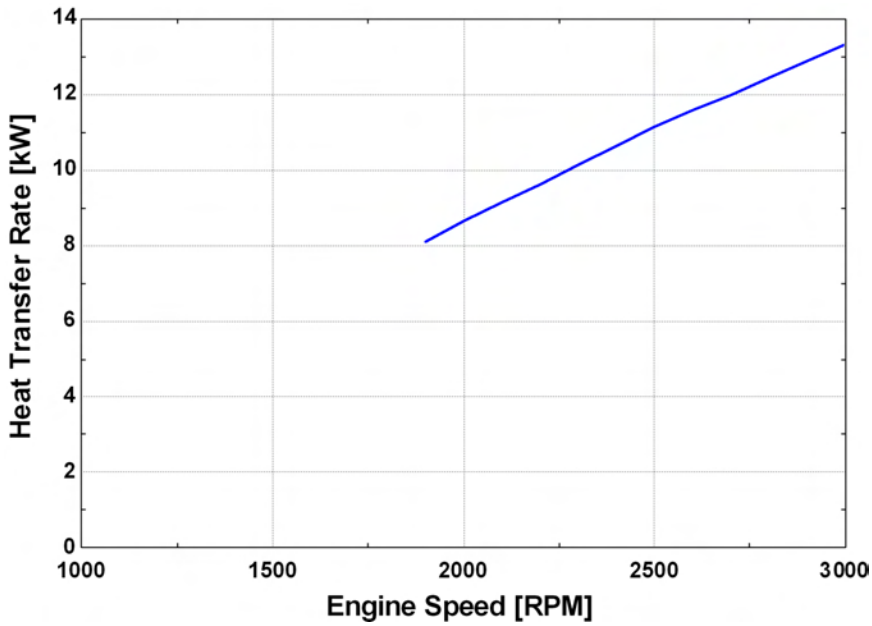

Figure A.7: Heat Transfer Rate as a Function of the Engine Speed for the 'CF-8.72' Compact Heat Exchanger

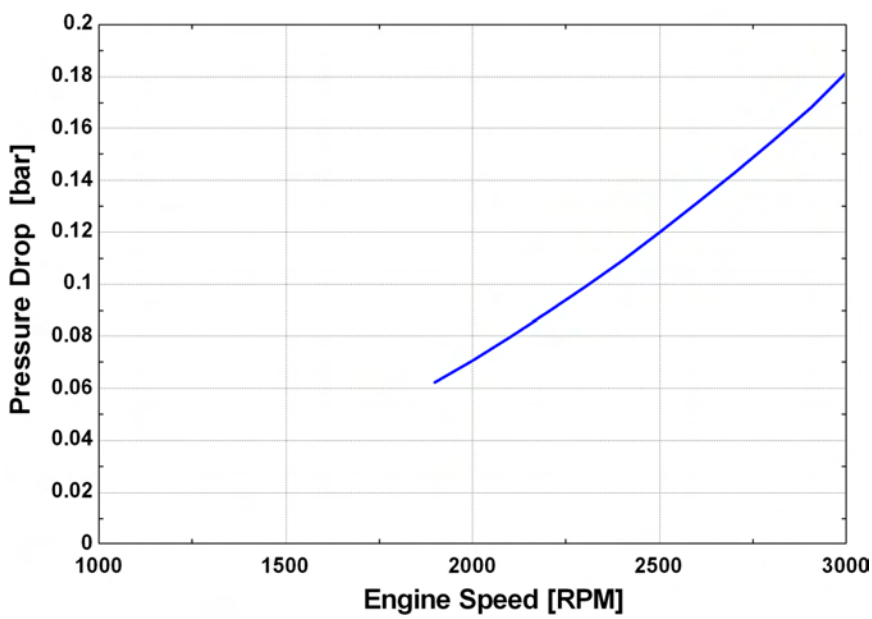

Figure A.8: Pressure Drop as a Function of the Engine Speed for the 'CF-8.72' Compact Heat Exchanger

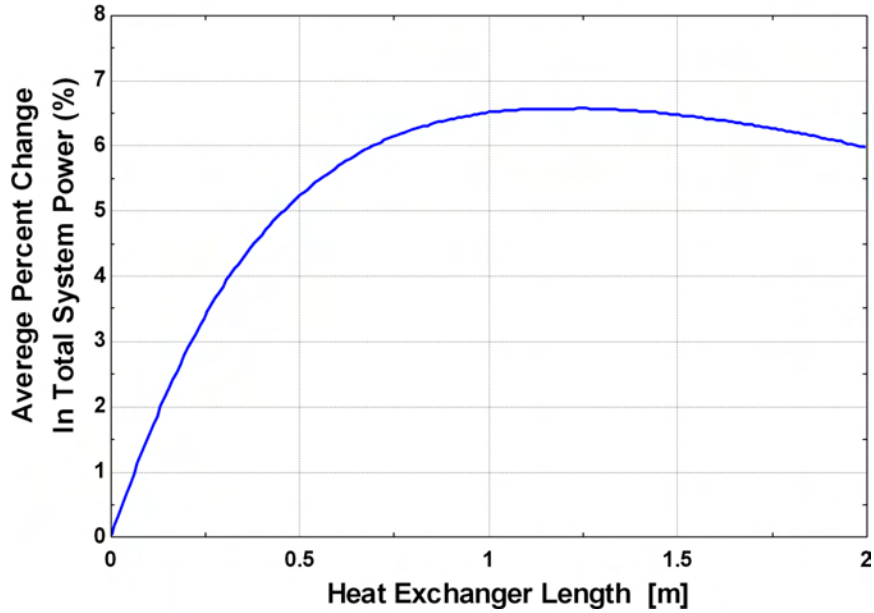

Figure A.9: Average Percent of Power Change as a Function of the Heat Exchanger Length for the 'CF-8.72' Compact Heat Exchanger

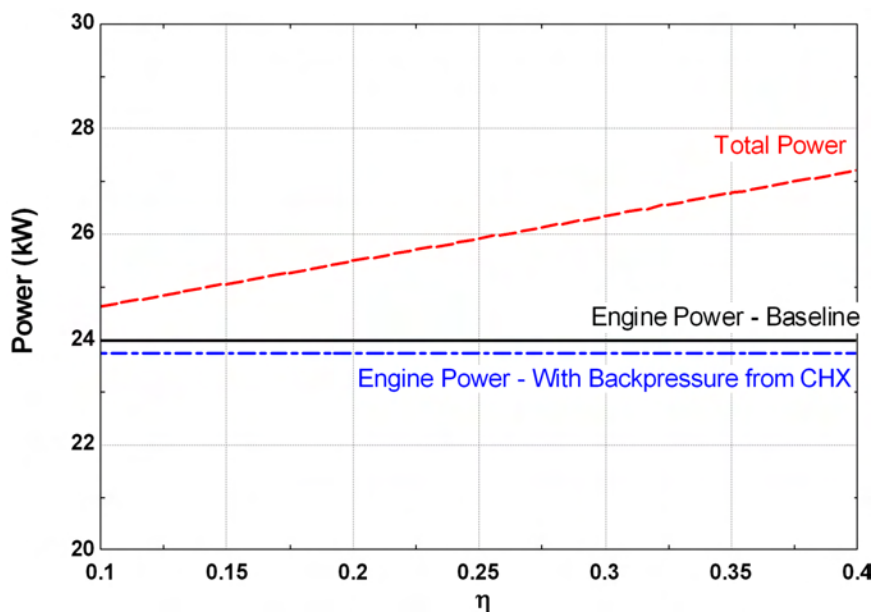

Figure A.10: Power as a Function of the Rankine Cycle Efficiency for the 'CF-8.72' Compact Heat Exchanger at an Engine Speed of 2000 RPM

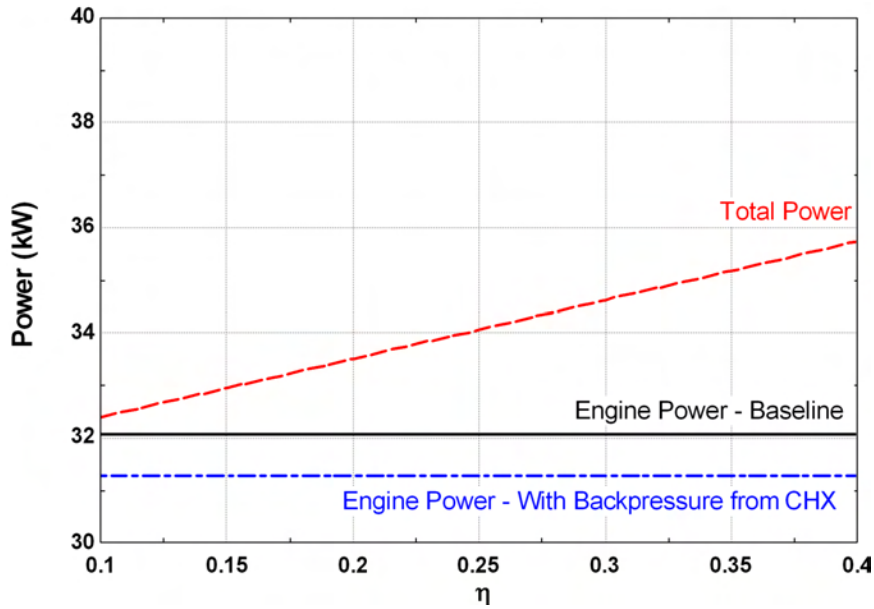

Figure A.11: Power as a Function of the Rankine Cycle Efficiency for the 'CF-8.72' Compact Heat Exchanger at an Engine Speed of 2500 RPM

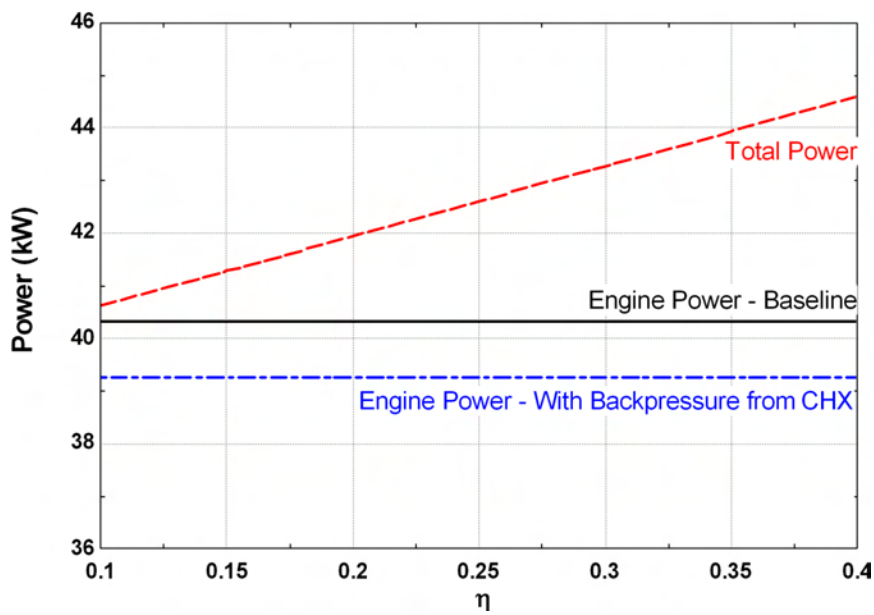

Figure A.12: Power as a Function of the Rankine Cycle Efficiency for the 'CF-8.72' Compact Heat Exchanger at an Engine Speed of 3000 RPM

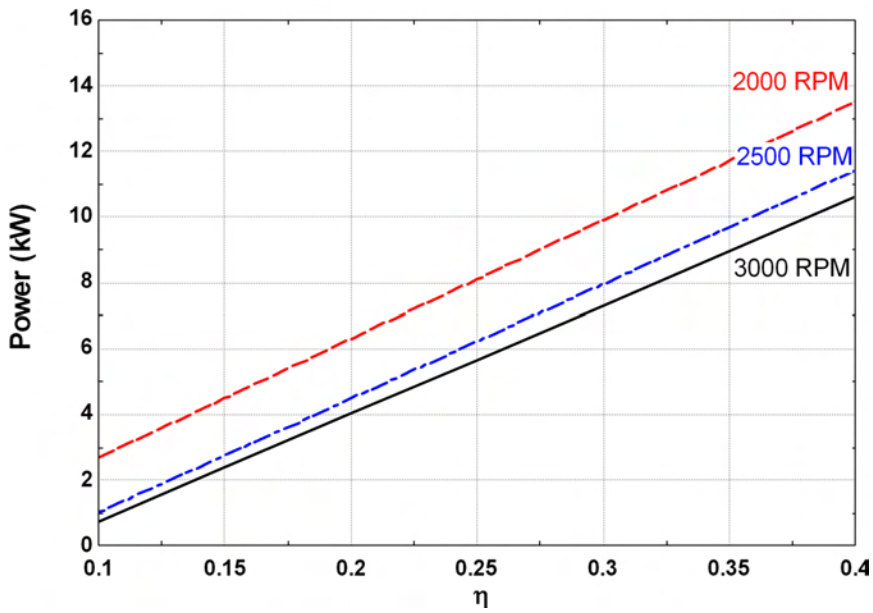

Figure A.13: Percent Power Change as a Function of the Rankine Cycle Efficiency for the 'CF-8.72' Compact Heat Exchanger

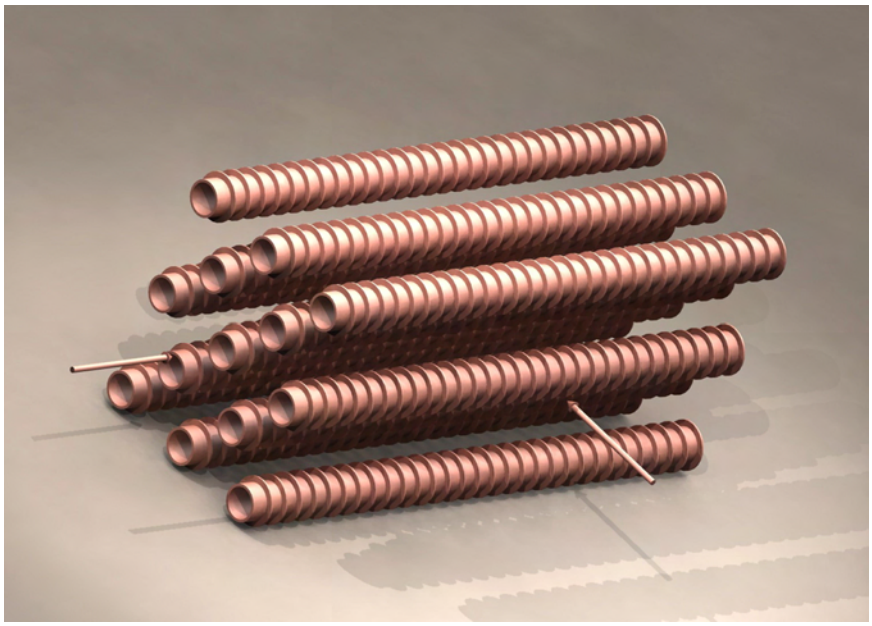

Figure A.14: Flow Configuration of Compact Heat Exchanger Studied

A.2 Finned-tube surface, Circular Tubes, Circular Fins - 'CF-7.34'

The following plots are for a compact heat exchanger with a finned-tube surface, circular tubes and circular fins and is denoted at the 'CF-7.34' configuration in Kays and London [52]. The flow configuration is shown in Figure A.14 and a schematic is shown in Figure A.15.

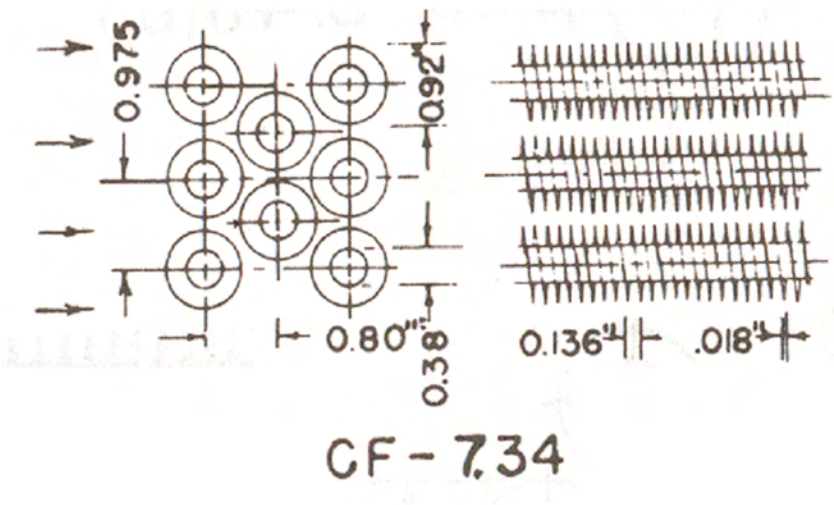

Figure A.15: Geometry of the Tubes in the Compact Heat Exchanger

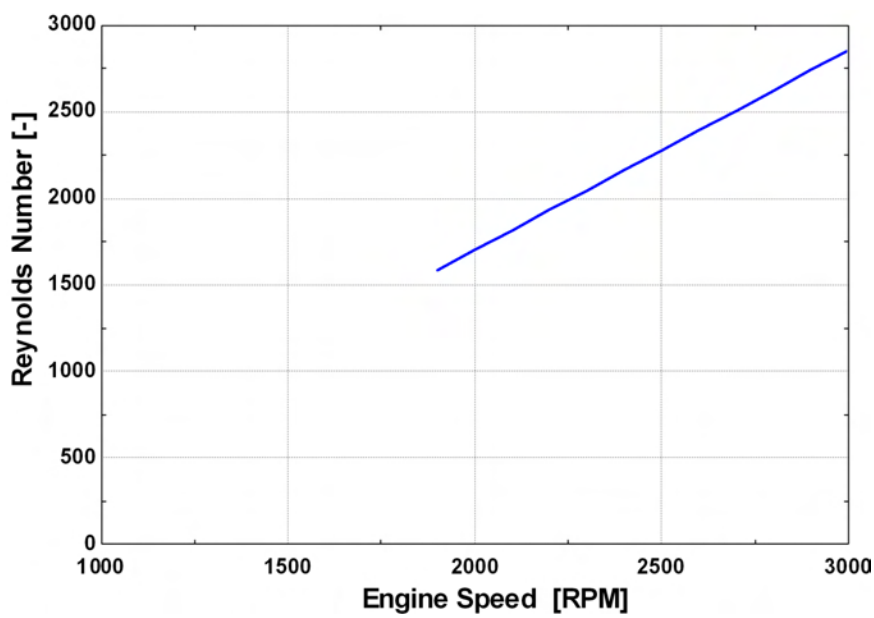

Figure A.16: Reynolds number for the Exhaust Gas as a Function of the Engine Speed for the 'CF-7.34' Compact Heat Exchanger

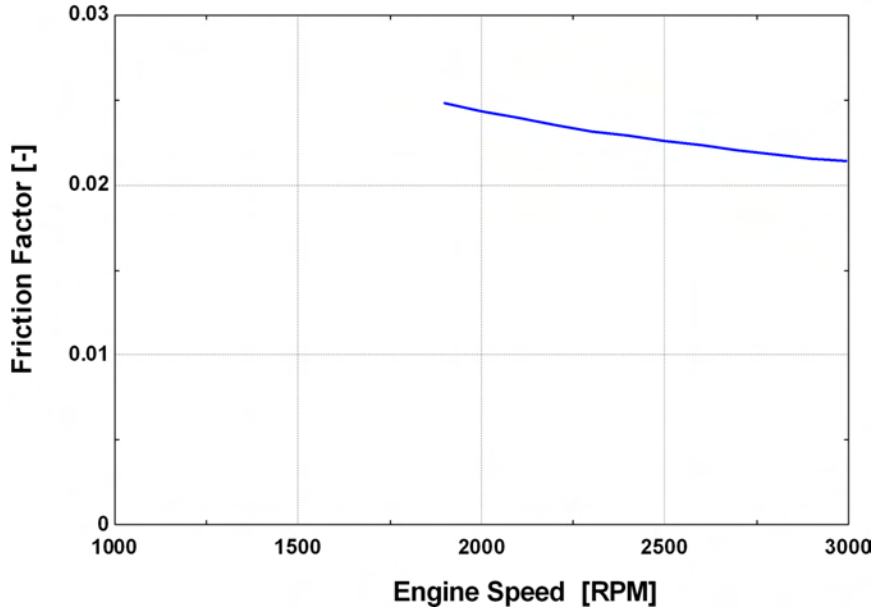

Figure A.17: Friction factor for the Exhaust Gas as a Function of the Engine Speed for the 'CF-7.34' Compact Heat Exchanger

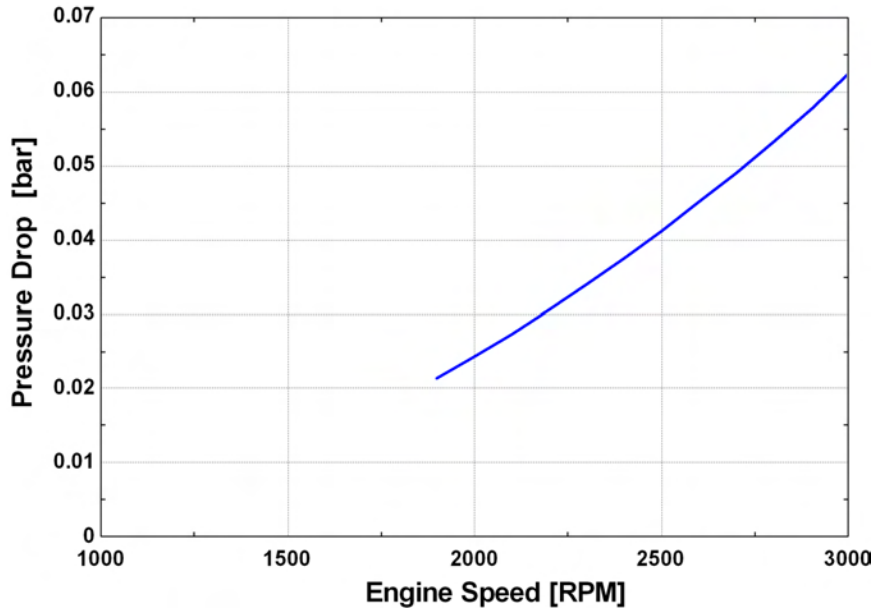

Figure A.18: Pressure Drop as a Function of the Engine Speed for the 'CF-7.34' Compact Heat Exchanger

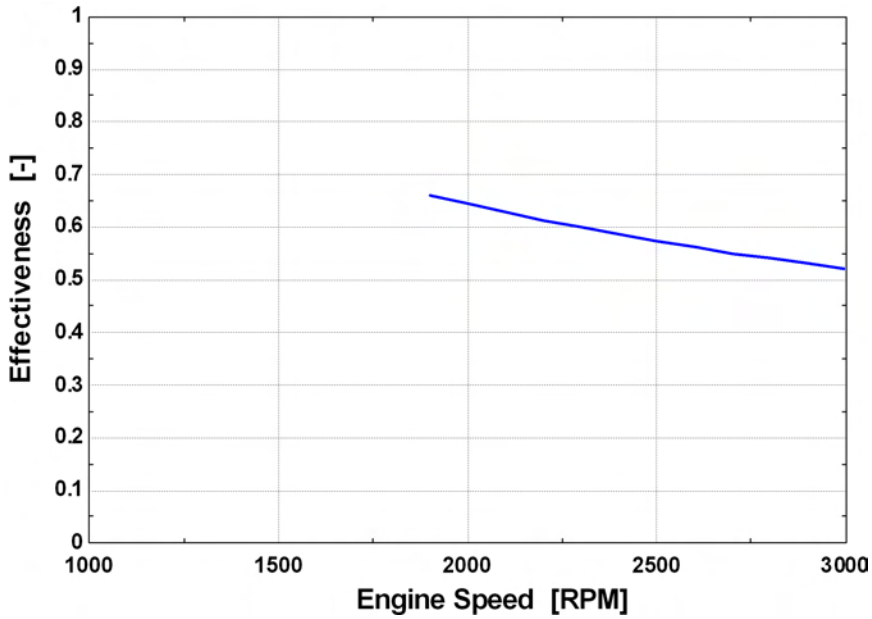

Figure A.19: Effectiveness for the Exhaust Gas Side as a Function of the Engine Speed for the 'CF-7.34' Compact Heat Exchanger

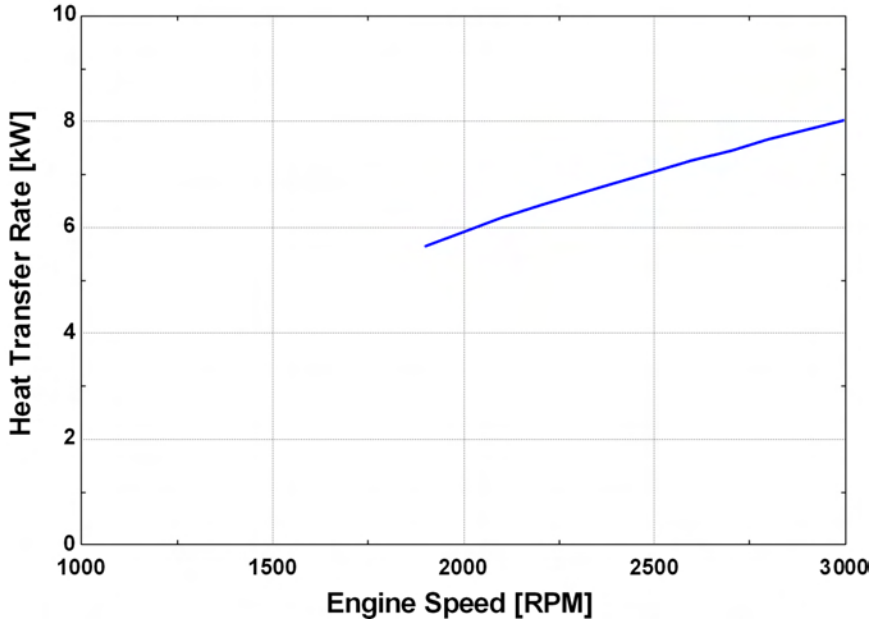

Figure A.20: Heat Transfer Rate as a Function of the Engine Speed for the 'CF-7.34' Compact Heat Exchanger

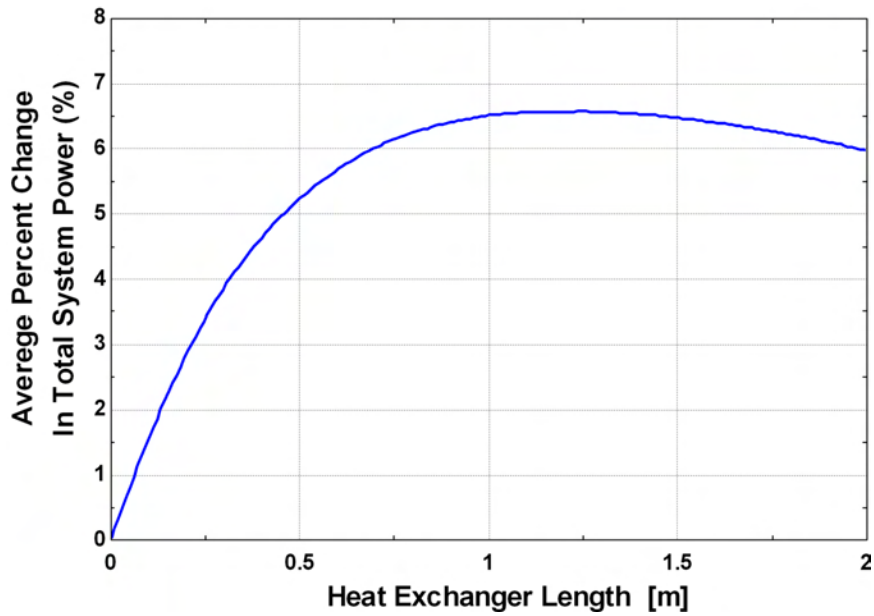

Figure A.21: Average Percent Power Difference as a Function of the Heat Exchanger Length for the 'CF-7.34' Compact Heat Exchanger

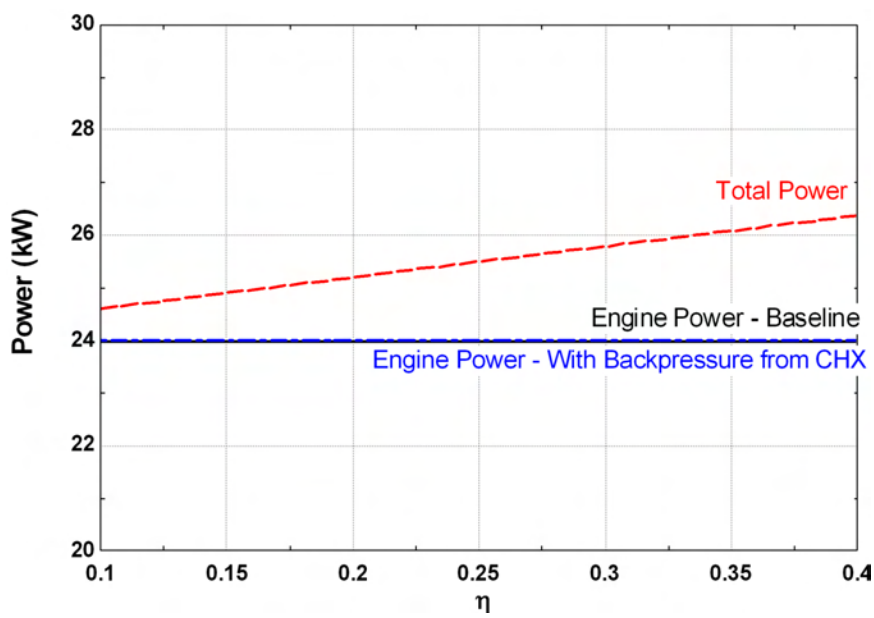

Figure A.22: Power vs. Rankine Cycle Efficiency for a Compact Heat Exchanger with Circular Fins ('CF-7.34') in the Exhaust System with an Engine Speed of 2000 RPM

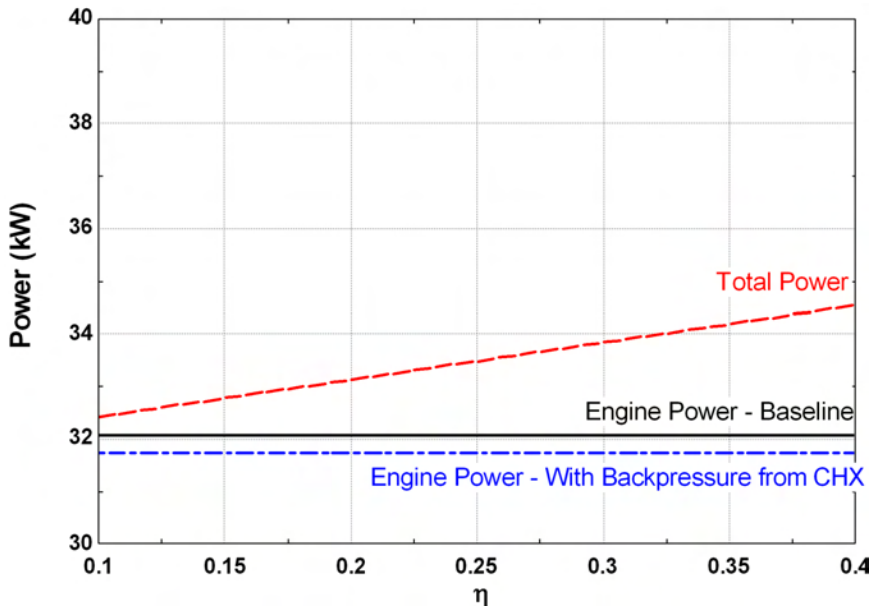

Figure A.23: Power vs. Rankine Cycle Efficiency for a Compact Heat Exchanger with Circular Fins ('CF-7.34') in the Exhaust System with an Engine Speed of 2500 RPM

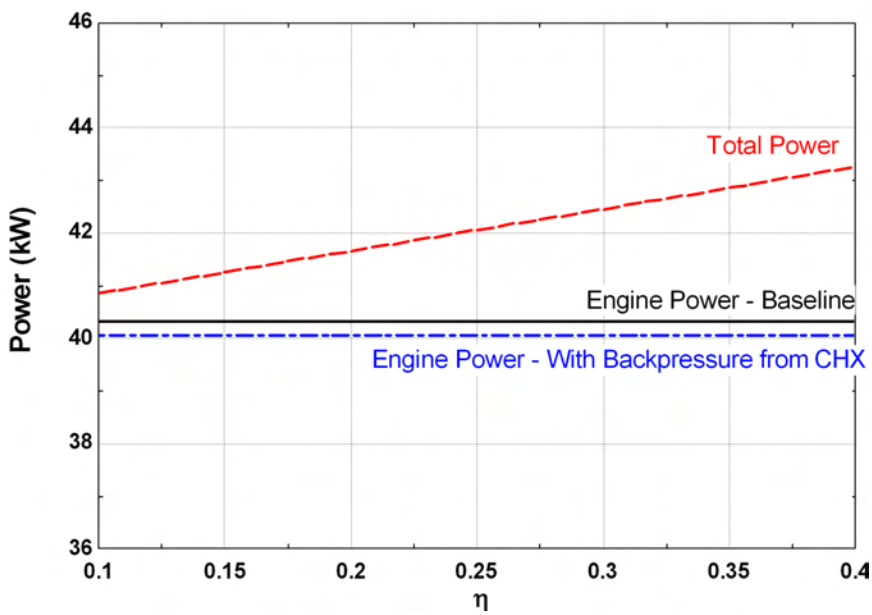

Figure A.24: Power vs. Rankine Cycle Efficiency for a Compact Heat Exchanger with Circular Fins ('CF-7.34') in the Exhaust System with an Engine Speed of 3000 RPM

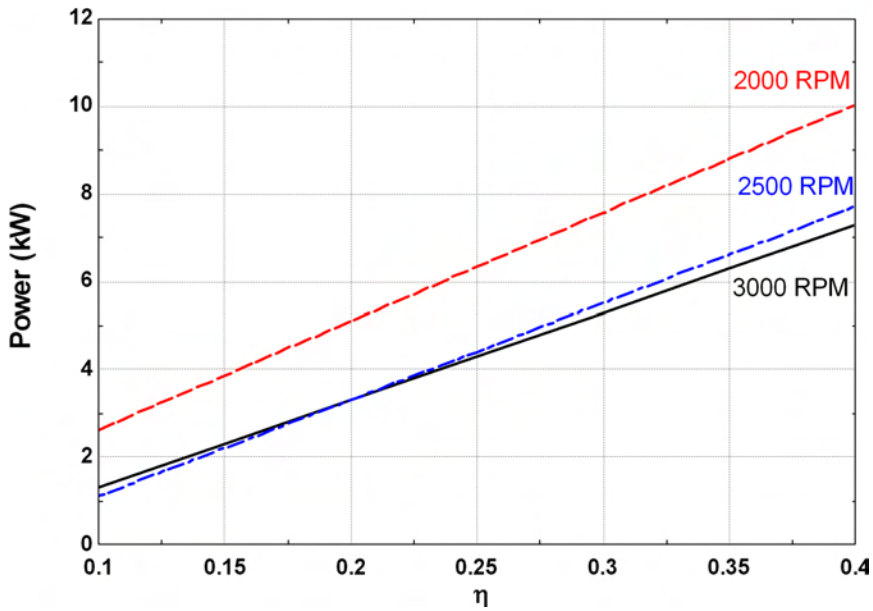

Figure A.25: Percent Change in Power vs. Rankine Cycle Efficiency for a Compact Heat Exchanger with Circular Fins ('CF-7.34') in the Exhaust System at the Precat location

A.3 Finned-tube surface, Circular Tubes, Continuous Fins - '7.75 - 5/8 T'

The following plots are for a compact heat exchanger with a finned-tube surface, circular tubes and continuous fins and is denoted at the '7.75-5/8T' configuration in Kays and London [52]. A schematic of the configuration is shown in Figure A.26.

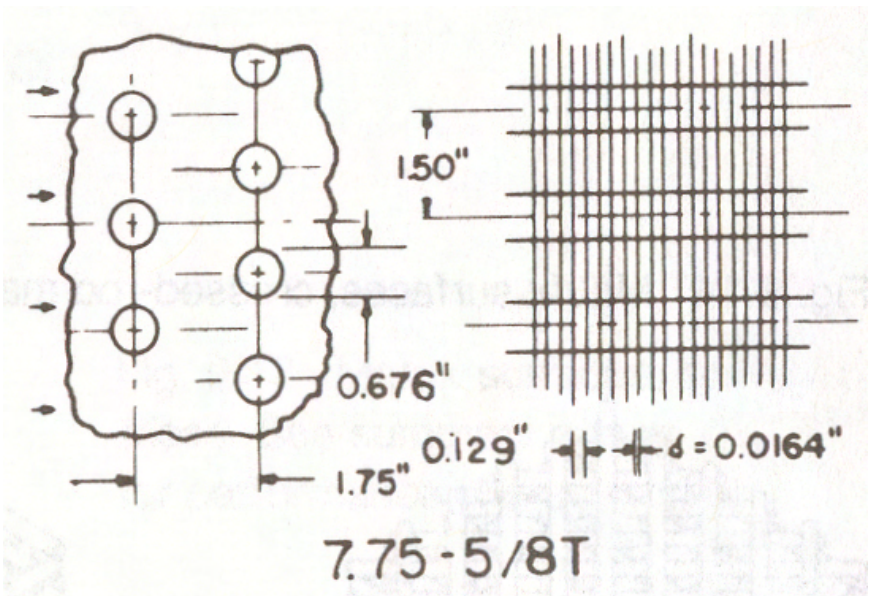

Figure A.26: Schematic of the '7.75-5/8T' Compact Heat Exchanger Studied

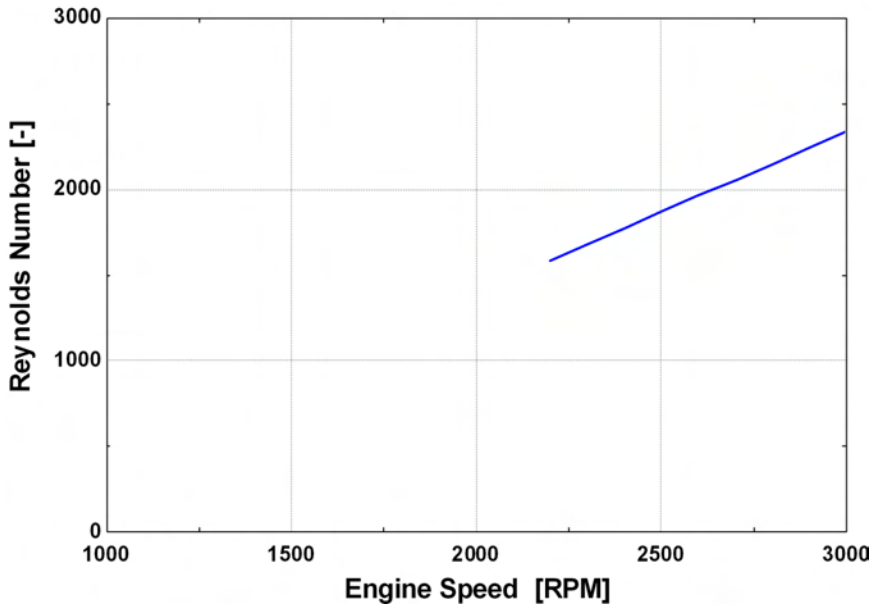

Figure A.27: Reynolds number as a Function of the Engine Speed for the '7.75-5/8T' Compact Heat Exchanger

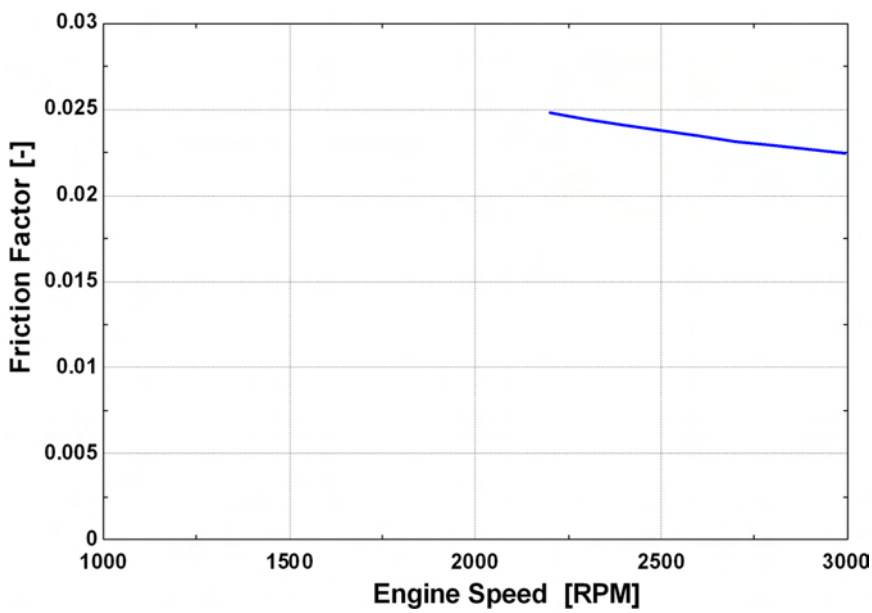

Figure A.28: Friction Factor as a Function of the Engine Speed for the '7.75-5/8T' Compact Heat Exchanger

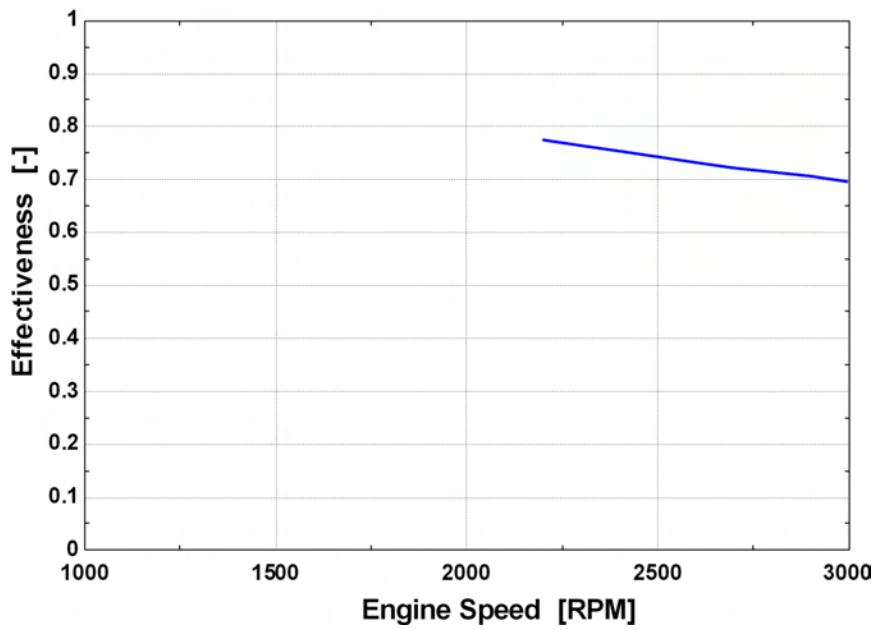

Figure A.29: Effectiveness as a Function of the Engine Speed for the '7.75-5/8T' Compact Heat Exchanger

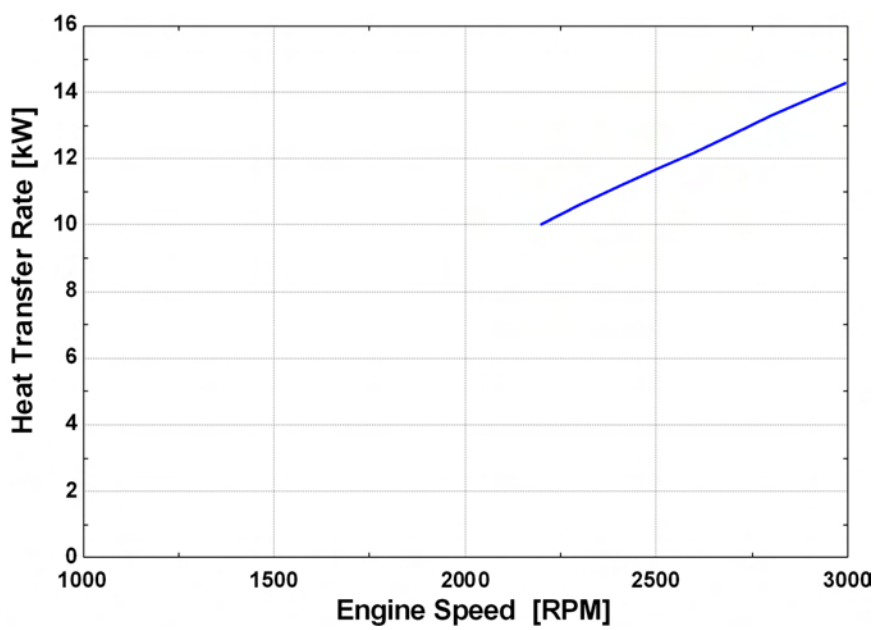

Figure A.30: Heat Transfer Rate as a Function of the Engine Speed for the '7.75-5/8T' Compact Heat Exchanger

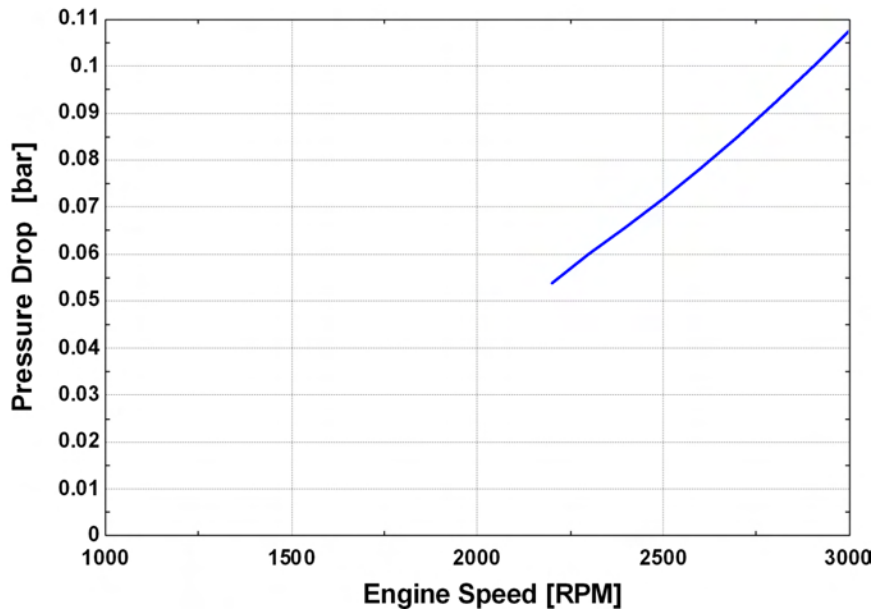

Figure A.31: Pressure Drop as a Function of the Engine Speed for the '7.75-5/8T' Compact Heat Exchanger

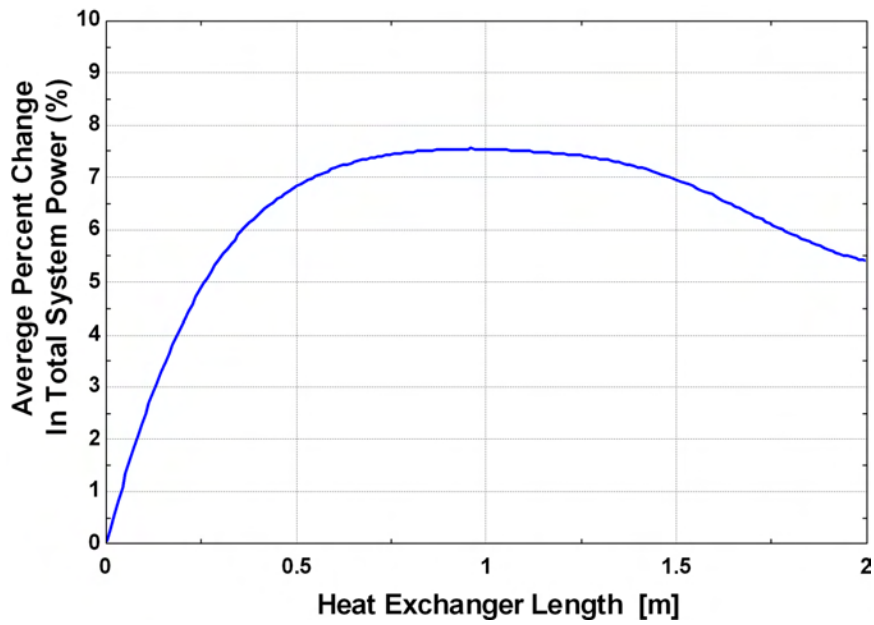

Figure A.32: Average Percent of Power Change as a Function of the Heat Exchanger Length for the '7.75-5/8T' Compact Heat Exchanger

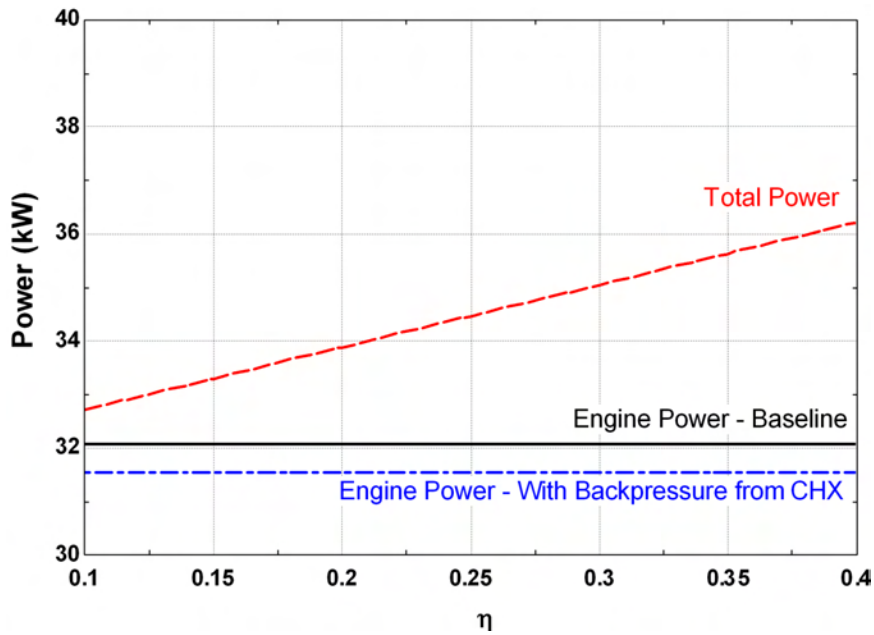

Figure A.33: Power as a Function of the Rankine Cycle Efficiency for the '7.75-5/8T' Compact Heat Exchanger at an Engine Speed of 2500 RPM

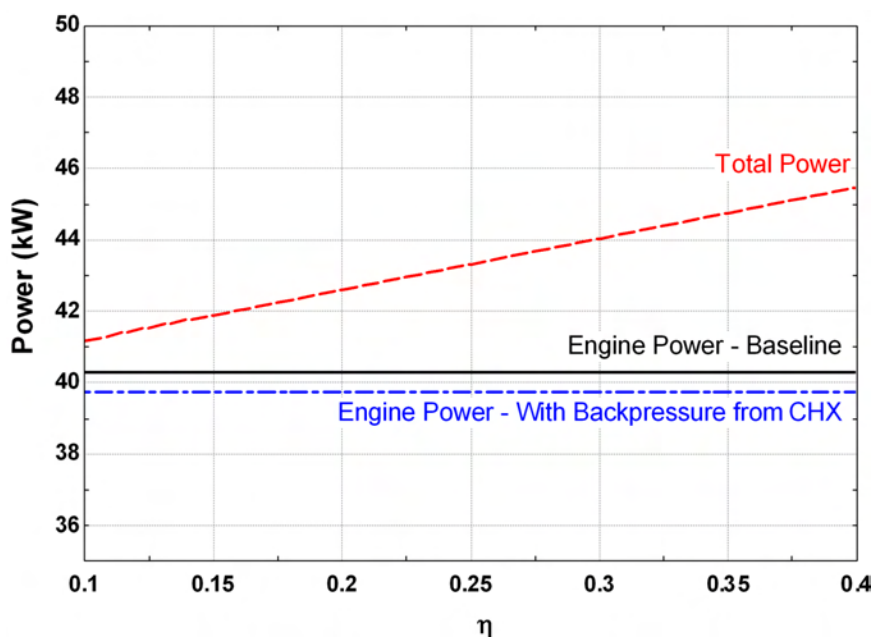

Figure A.34: Power as a Function of the Rankine Cycle Efficiency for the '7.75-5/8T' Compact Heat Exchanger at an Engine Speed of 3000 RPM

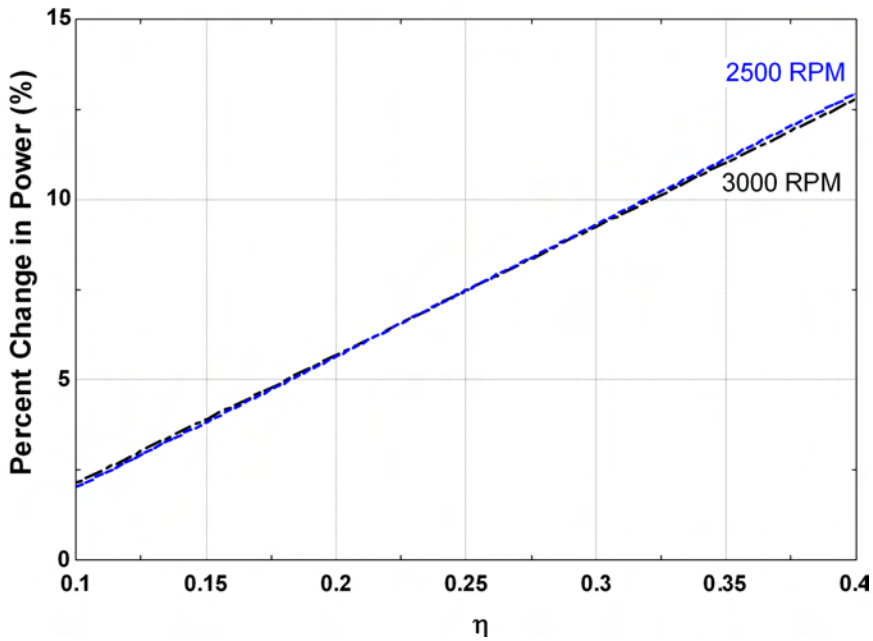

Figure A.35: Percent Power Change as a Function of the Rankine Cycle Efficiency for the '7.75-5/8T' Compact Heat Exchanger

A.4 Finned-tube surface, Flat Tubes, Continuous Fins - '9.29-0.737-SR'

The following plots are for a compact heat exchanger with a finned-tube surface, flat tubes and continuous fins and is denoted at the '9.29-0.737-SR' configuration in Kays and London [52]. A schematic of the configuration is shown in Figure A.36.

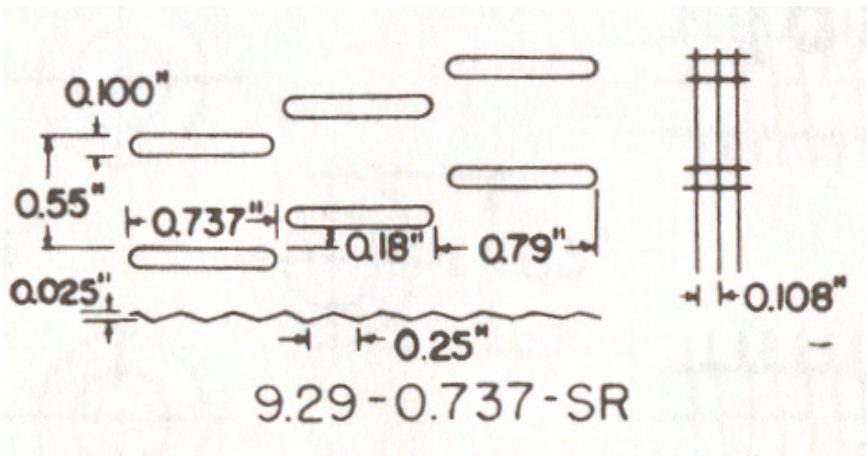

Figure A.36: Schematic of the '9.29-0.737-SR' Compact Heat Exchanger Studied

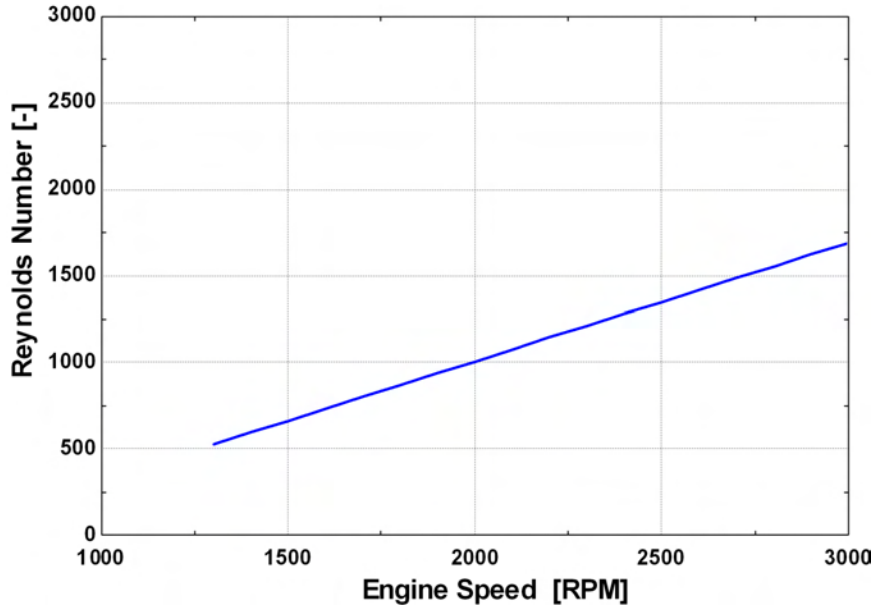

Figure A.37: Reynolds number as a Function of the Engine Speed for the '9.29-0.737-SR' Compact Heat Exchanger

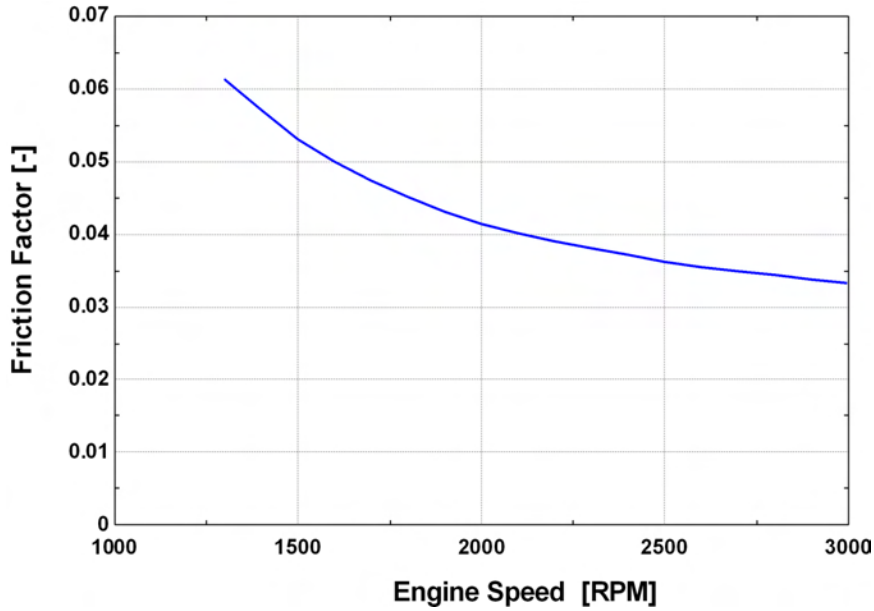

Figure A.38: Friction Factor as a Function of the Engine Speed for the '9.29-0.737-SR' Compact Heat Exchanger

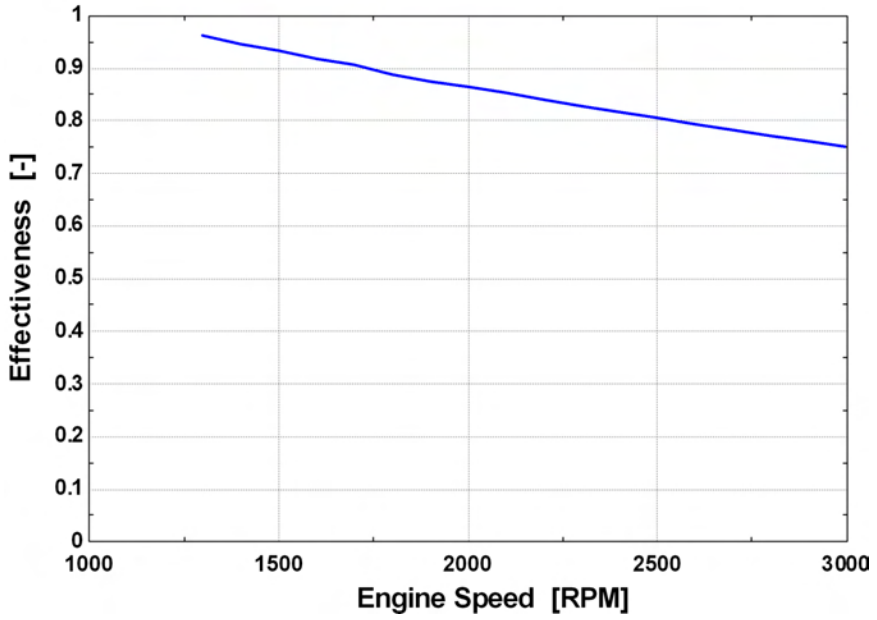

Figure A.39: Effectiveness as a Function of the Engine Speed for the '9.29-0.737-SR' Compact Heat Exchanger

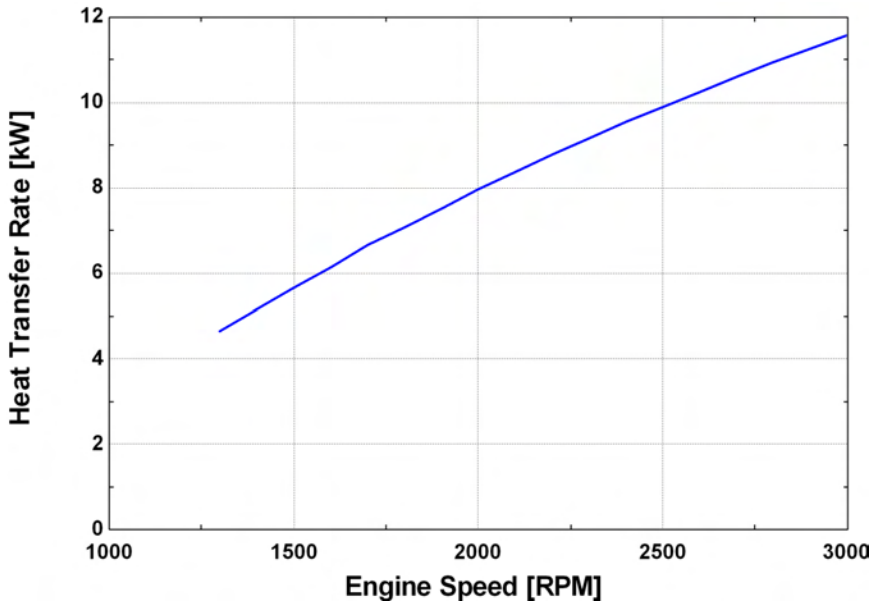

Figure A.40: Heat Transfer Rate as a Function of the Engine Speed for the '9.29-0.737-SR' Compact Heat Exchanger

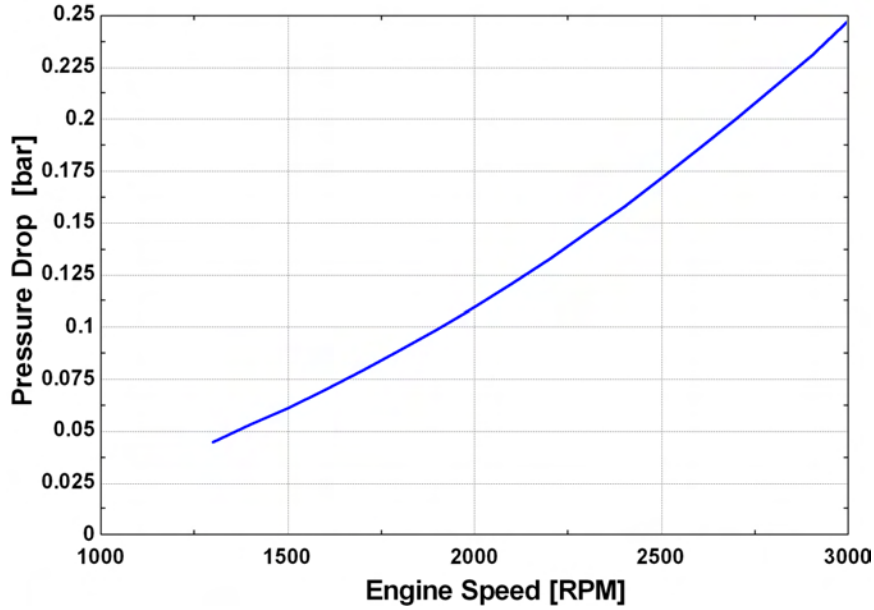

Figure A.41: Pressure Drop as a Function of the Engine Speed for the '9.29-0.737-SR' Compact Heat Exchanger

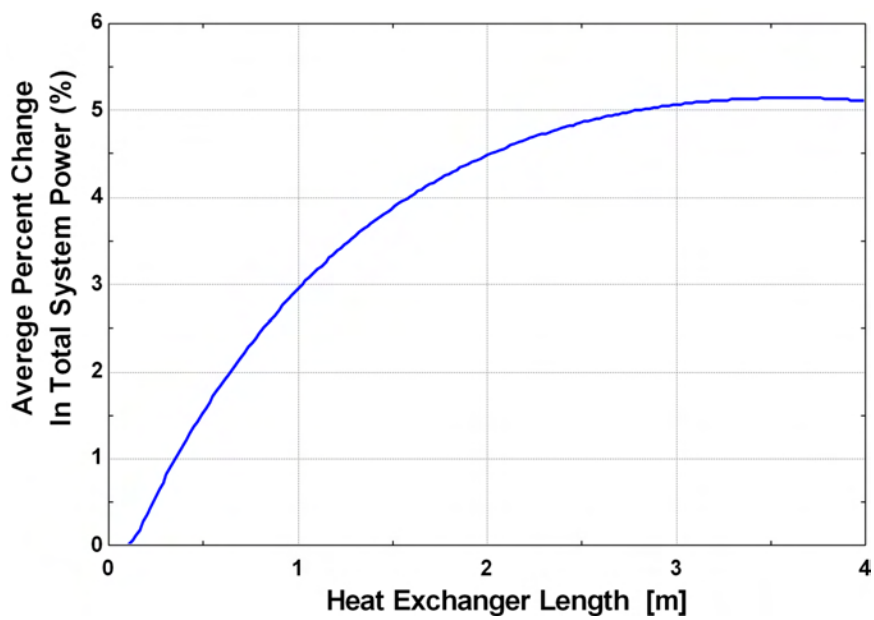

Figure A.42: Average Percent of Power Change as a Function of the Heat Exchanger Length for the '9.29-0.737-SR' Compact Heat Exchanger

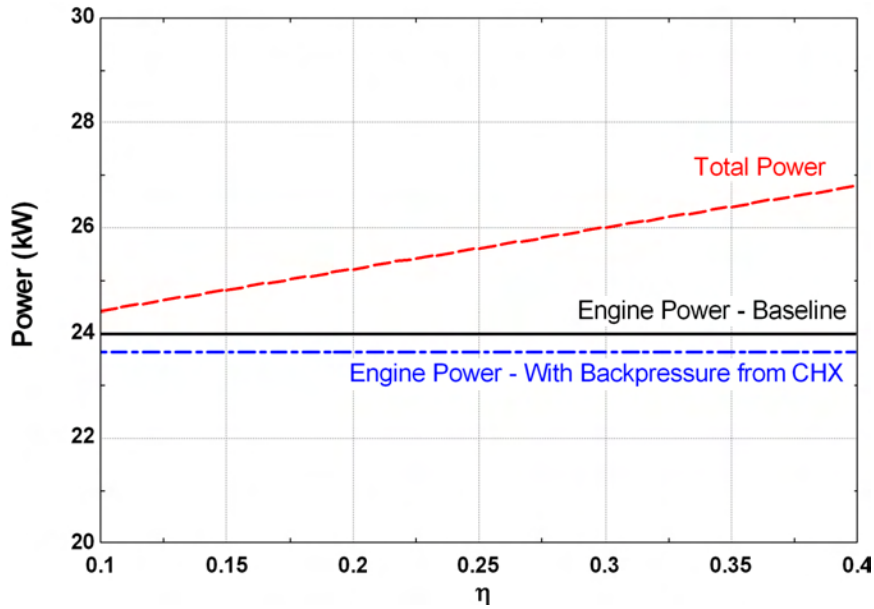

Figure A.43: Power as a Function of the Rankine Cycle Efficiency for the '9.29-0.737-SR' Compact Heat Exchanger at an Engine Speed of 2000 RPM

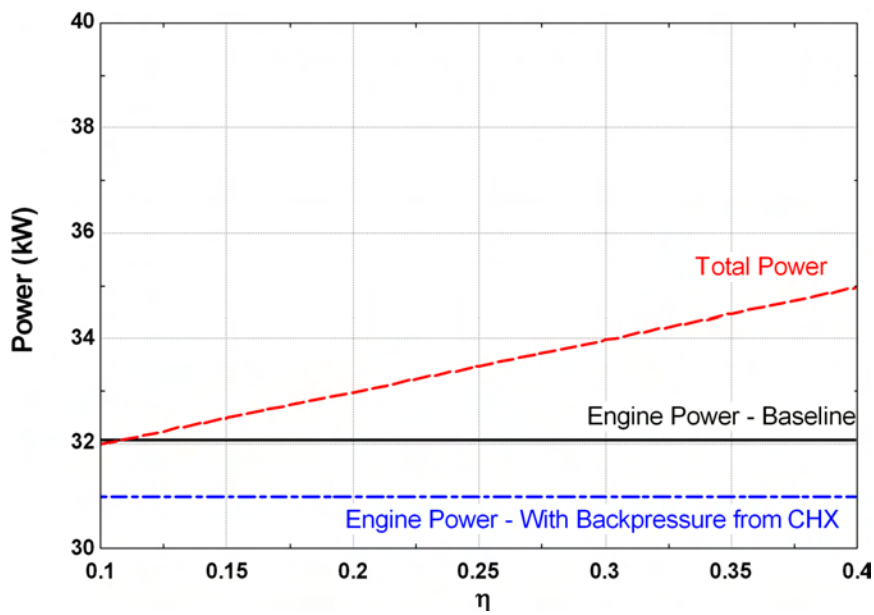

Figure A.44: Power as a Function of the Rankine Cycle Efficiency for the '9.29-0.737-SR' Compact Heat Exchanger at an Engine Speed of 2500 RPM

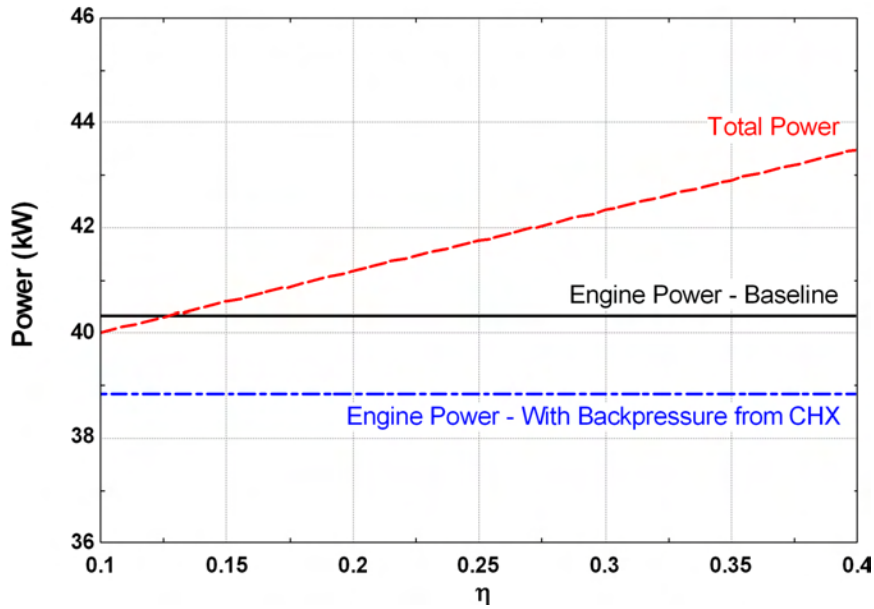

Figure A.45: Power as a Function of the Rankine Cycle Efficiency for the '9.29-0.737-SR' Compact Heat Exchanger at an Engine Speed of 3000 RPM

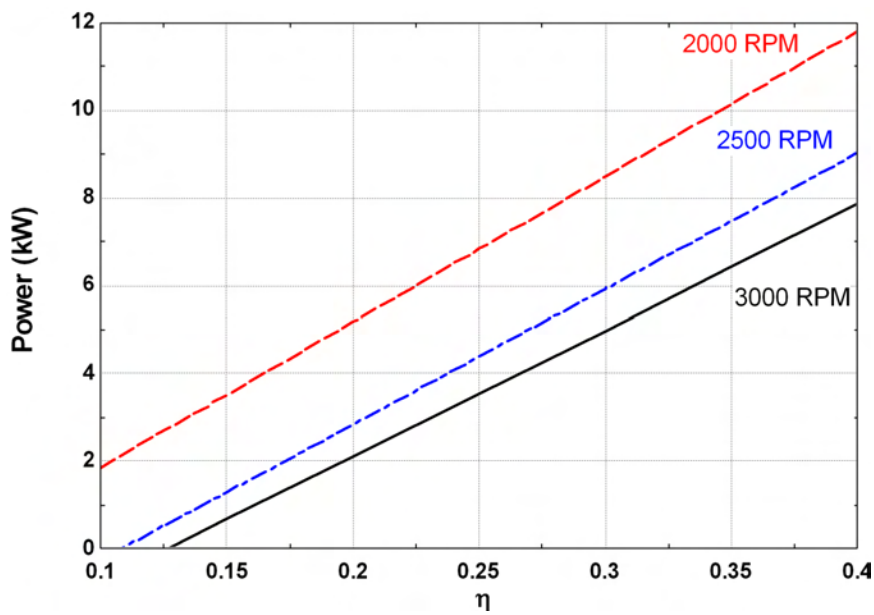

Figure A.46: Percent Power Change as a Function of the Rankine Cycle Efficiency for the '9.29-0.737-SR' Compact Heat Exchanger

Summary Page

This document has 0 figures.

This document has 0 tables.

This document has 0 equations.

There are 19 pages in the preamble.

There are 154 pages in the body of the paper.

There are 5 pages in the bibliography.

There are 27 pages in the Appendix